Three-Dimensional Finite-Volume Time-Domain Modeling of Graphitic Fault Zones in the Athabasca Basin Using Unstructured Grids

by

©Xushan Lu

A thesis submitted to the School of Graduate Studies in partial fulfillment of the

requirements for the degree of

Doctor of Philosophy

Department of Earth Sciences

Memorial University of Newfoundland

June, 2020

St. John's   Newfoundland & Labrador

Abstract

In this thesis, numerical modeling methods for geophysical time-domain electromagnetic (EM) problems and their applications in modeling graphitic faults in the Athabasca Basin are investigated. A finite-volume time-domain numerical modeling method is developed. The method uses unstructured Delaunay-Voronoï dual meshes. Such unstructured meshes are more flexible and efficient when models containing geological units with complex geometries and topography need to be considered. A model building procedure is established to construct arbitrarily complex models with topography. The procedure locally refines the mesh quality at certain areas such as loop sources and receivers in order to obtain better numerical results.

For modeling time-domain EM problems, two approaches are used: the electric field approach and the potential approach. The electric field method directly solves the electric field Helmholtz equation while the potential method solves the Helmholtz equation expressed using vector and scalar potentials. The electric field method is simpler in theory and results in a smaller linear system of equations compared to potential methods. The potential method, on the other hand, is more complex in

theory and a larger linear system of equations needs to be solved. However, using the potentials method enables the decomposition of the electric field into galvanic and inductive parts, which is helpful for understanding the physics behind the behaviour of the EM fields in the ground. In addition, the linear system of equations is better conditioned which potentially allows the use of iterative methods to solve it.

Both methods are validated by comparing the modeling results with analytic solutions for homogeneous half-space models and numerical results for models presented in the literature. The modeling methods developed in this thesis are then applied to the modeling of real EM data collected in the Athabasca Basin. Thin, steeply dipping graphitic fault systems, which are linked to the formation of uranium deposits are present in the basin and have a large conductivity contrast with the background host. Because of the close relationship between the graphitic faults and the uranium deposits, time-domain EM surveys are important tools for uranium exploration in the basin. Geological models of the graphitic fault systems are discretized with unstructured grids using the model building procedure developed in this thesis. Two real data sets that were previously collected from the Athabasca Basin are modeled and the modeling results are compared with the real data. The match between the calculated three-component responses and real data is good for models built based on geological information, drilling information, and trial-and-error. These models can help us to infer the complex geometry and conductivity features of the subsurface conductor beyond the areas targeted by drilling. Therefore, 3D modeling of realistic, complicated real-life conductive targets such as in the uranium exploration in the Athabasca Basin

or any other classic mineral exploration for a conductive target with complex shape is an important tool.

Acknowledgements

the project. Discussions with them also helped me to understand many aspects of geophysical electromagnetic exploration for uranium deposits in the Athabasca Basin.

I would like to thank Dr. Xiu Li, supervisor of my Master's program, for his support and encouragement for me doing a PhD program here in Canada. I am grateful to Dr. Huaifeng Sun who guided me though the early days of my Master program during which I gained a strong interest in numerical electromagnetic modeling methods. I deeply appreciate the unconditional support offered by my family throughout the entire period of my program. At last, I would like to express my gratitude to my fiancée, Miss Yixi Yang, for her encouragement and companionship without which I would not be able to finish this program.

Table of Contents

List of Tables

List of Figures

xxiii

Chapter 1

Introduction

Time-domain electromagnetic (TDEM) methods, or transient electromagnetic (TEM) methods, have been widely used in mineral explorations (Powell et al., 2007; Yang and Oldenburg, 2012), ground water detections (Young et al., 2004; Ezersky et al., 2011), hydrocarbon explorations (Um et al., 2010b; Commer et al., 2015; Um et al., 2015) and other investigations of the subsurface. Unlike frequency-domain electromagnetic (FDEM) methods, where measurements are made in the presence of the primary field, TDEM methods commonly measure the electromagnetic (EM) fields during the absence of the primary field. This means weak signals generated by the secondary field can be measured relatively accurately compared to FDEM methods (Everett, 2013). TDEM systems with loop sources are particularly popular in the mining industry such as the exploration of massive sulfide ore deposits (Vallée et al., 2011; Cox et al., 2012), and graphitic conductors (Powell et al., 2007; Zeng et al., 2019).

In TDEM methods, the magnetic field, B, and its time-derivative, dB/dt, are

commonly measured in time at different times. The field is recorded at a certain number of time channels or gates which are a short period of time during which the measurement is taken and averaged. Those channels or gates are denoted by the time instant centered at the short periods. By interpreting the measured data, one can get useful information about the subsurface conductivity variation. The interpretation of the measured data is commonly carried out by three different approaches: conductivity-depth imaging (Macnae et al., 1991), trial-and-error numerical modeling of the measured data (Zeng et al., 2019), and inversion (Yang and Oldenburg, 2012). Among the above methods, inversion is preferred because it can automatically search for subsurface conductivity models that have EM responses close enough to those measured in the field subject to some predefined constraints depending on the actual inversion algorithm used. For instance, when a minimum-structure inversion algorithm is used, the inverted conductivity models are normally smooth (Farquharson and Oldenburg, 2004).

A successful inversion requires running many forward modelings, i.e., computing the data for candidate models. In order to make the inversion reliable and feasible, one has to make sure the forward modeling solvers are fast and accurate enough, especially in three-dimensional cases. Although it is possible to analytically calculate the EM response of certain models such as a homogeneous half-space model or a model with a spherical anomalous body buried in a homogeneous half-space media, it is impossible to find the analytical solutions for models with irregularly shaped anomalous bodies. Thus, the 3D forward modeling of EM data is normally carried out numerically.

The numerical forward modeling problem involves numerically solving the underlying partial differential equations (PDEs) of EM problems, namely, Maxwell's equations.

The EM responses of one or multiple conductors with simple shapes such as plates can also be calculated approximately by the method of equivalent sources and the theory of Green's functions (Annan, 1974). The key idea is to characterize the induced currents inside the plate with either a discrete mesh (Lamontagne and West, 1971) or a continuous distribution of "eigencurrents" (Dyck and Vallee, 1980). An even simpler version of this method is developed by Lamontagne et al. (1988) where a plate is cut into a series of "ribbons" and it is assumed that there will be no current galvanically crossing from one ribbon to another. This simplified method later led to commercial software packages such as MultiLoop and Maxwell (Lamontagne et al., 1988; EMIT, 2005). However, these simplified algorithms have many limitations because of certain assumptions made about the subsurface Earth. Among them, the most restrictive assumption is that the host is perfectly resistive such that no current channeling (or current gathering, Duckworth et al., 2001) happens between the host and conductor. Although a horizontal plate can be placed in the model to account for the responses of a conductive background, only late-time data can be modeled with a relatively high accuracy (Lamontagne, 2007). Another restriction comes with the assumption that conductors are rectangular and plate-like which is an oversimplification of real-life geology in most cases. The ribbons placed inside the conductor to represent the actual eddy currents are fixed throughout the entire modeling process, which is not a good representation of the actual eddy currents induced in the conductor. In reality, the

actual eddy currents induced in the conductor change dynamically when the distance between the plate and the source changes or as the time changes after the source is turned off. By employing 2D meshes for thin plates, the MultiLoop III program removes the geometrical limitation that the target has to be thin plates, and bent or deformed sheets can also be modeled (Walker and Lamontagne, 2007). However, the other limitations still exist. Therefore, only three-dimensional numerical methods that fully discretize the entire region of interest in the Earth model can yield accurate enough modeling responses.

For numerically solving TDEM problems, there are three types of methods that are commonly used. First, time-domain problems can be solved in the frequency domain and then transformed into the time domain by Fourier transforms (e.g., Newman et al., 1986; Li et al., 2017). Second, the so-called polynomial or rational Krylov subspace method can be used where the semi-discretized time-domain problem is solved by approximating a matrix-exponential function (e.g., Börner et al., 2015; Qiu et al., 2019; Zhou et al., 2018). Lastly, the time-domain problem can be solved by time-stepping methods which contain two stages: semi-discretization and full discretization (e.g., Um et al., 2010b; Yin et al., 2016; Li et al., 2018, 2014). The semi-discretization is the spatial discretization which converts the PDE system into an ordinary differential equation (ODE) system. The full discretization then solves the ODE system by either an implicit or an explicit time-stepping method.

To accurately compute the time-domain responses by transforming the frequency-domain responses to the time domain, one would need to calculate the frequency-

domain EM responses at many different frequencies. For example, Jones et al. (2016) calculated the frequency-domain responses at 40 frequencies ranging from 0.01 to 100 MHz. A system of equation should be solved for each frequency. Considering the large number of frequencies needs to be solved, it can easily be more expensive to calculate than time-stepping methods when direct methods are used to solve the linear system of equations. This is because the factorization results can be reused as long as the time steps remain unchanged (Oldenburg et al., 2013), and the number of factorization needed to get the time-domain solutions via time-stepping can be significantly smaller than the number of frequencies required to get an accurate transformation response. The rational Krylov subspace method is efficient and accurate, but its ideas are much more complex than the time-stepping methods. Therefore, the time-stepping method is implemented in this thesis.

Normally, a mesh which discretizes the computational domain is needed for the spatial discretization. The unknown EM fields are usually defined on the edges or nodes of a mesh, and different regions in the computational domain are represented by different mesh cells. Structured rectilinear meshes, semi-structured OcTree meshes, and unstructured tetrahedral meshes are all commonly used meshes in geophysical EM modeling. Structured meshes are simple and easy to generate, but lack flexibility when dealing with complex geometries. On the other hand, unstructured meshes are difficult to generate but much more flexible than structured rectilinear meshes. Real-life geological models are commonly complex, and may have many different regions with irregular interfaces (Zanchi et al., 2009). Topography is commonly present

in real-life geological models and it can have a significant effect on the accuracy of the numerical modeling so that it should be reasonably well represented by the mesh (Yin et al., 2016). Although it is more difficult to generate unstructured meshes compared with structured rectilinear meshes or OcTree meshes, there have been multiple programs developed for this purpose. Programs such as TetGen (Si, 2015) and COMSOL Multiphysics® have been used for the mesh generation for EM modeling and inversion (see, e.g., Li et al., 2018; Jahandari and Farquharson, 2014; Um et al., 2010b). TetGen is especially popular because it is open source software, and offers many different options to control the quality of the generated mesh. It is also able to generate both Delaunay and Voronoï meshes. However, the interaction with the software can only be made via text files, which makes the mesh generation process less intuitive and difficult when complex geometries are involved. In order to mitigate this difficulty, Lelièvre et al. (2018a) developed software named FacetModeller which creates surface-based models in a graphical user interface (GUI) environment. The surface-based model can be later exported to a text file with the specific format that is required by TetGen in order to generate the final tetrahedral mesh.

With a given mesh, the semi-discretization of the time-domain Maxwell's equations can be carried out by numerical methods such as integral equation (IE) methods, finite-difference (FD) methods, finite-volume (FV) methods, and finite-element (FE) methods. IE methods only need to discretize the anomalous region in the entire computational domain and therefore require less memory compared to other methods (Newman and Hohmann, 1988; Farquharson et al., 2006). In early stages of 3D EM

6

modeling, IE methods were widely adopted because of the limited computing resources available at the time.

The FD method uses discrete difference operators based on Taylor series at individual mesh points to approximate the continuous differential operators in the PDE. The FD method uses Yee's staggered grid (Yee, 1966) where the electric field is defined at the edges of cells and the magnetic field is defined at the centers of cell faces. Consequently, the continuity of the tangential component of the electric field and the continuity of the normal component of the magnetic field are satisfied. Due to these attractive features, the FD methods have been very successful in EM modeling (see, e.g., Oristaglio and Hohmann, 1984; Wang and Hohmann, 1993; Newman and Alumbaugh, 1995; Li et al., 2014). However, the difference operators used in the FD methods require the mesh to be structured. Otherwise, the difference operators cannot be easily defined. It is then impossible to use unstructured grids, such as unstructured tetrahedral grids, which limits its use in the modeling of real-life geological models.

The FV method approximates the integral forms of Faraday's law and Ampère's law by integrating them over a certain volume called the control volume. The Yee's scheme that is used in the FD method is also widely used in the FV method. When integrating the PDE over the control volume, the surface and volume integrals are converted into line and surface integrals, respectively, based on Stokes theorem and the divergence theorem. Besides Yee's grids, the FV method can also use other staggered grids, for example, the Delaunay-Voronoï dual meshes (Jahandari and Farquharson,

2014; Weiss, 2010). Like Yee's grids, the edges and faces of the Delaunay-Voronoï dual meshes are mutually orthogonal to each other despite being unstructured, which means that similar discretization schemes can be adopted. Being able to use the unstructured Delaunay-Voronoï dual meshes greatly improves the flexibility of the FV method when dealing with complex geometries.

The FV method can be used to discretize the two first-order equations in Maxwell's equations, which yields an explicit time-stepping method (Sazonov et al., 2008). However, the explicit scheme requires an extremely high mesh quality. The unstructured Delaunay-Voronoï dual meshes can be said to have a high quality when its minimum dihedral angle (the angle between two faces that share an edge in a selected tetrahedron) is large and its maximum radius-edge ratio (the length ratio between the radius of the circumscribed sphere of a selected tetrahedron and the shortest tetrahedral edge in a selected tetrahedron) is small. A low quality mesh can lead to degeneracies when centroids of multiple tetrahedra coincide with each other, which leads to zero-length Voronoï edges (Xie et al., 2011). The zero-length of the Voronoï edge poses difficulties to satisfying the stability conditions of an explicit scheme. Thus, in the electrical engineering community, much effort has been devoted to generating high quality unstructured staggered dual meshes (Xie et al., 2011; Walton et al., 2017). The implicit FV method can easily handle these mesh degeneracies because they are unconditionally stable.

The FE method, unlike FV or FD methods, solves the PDE in a weak sense. Two commonly used methods are node-based scalar FE method and edge-based vector FE

method. For the scalar case, the three components of the electric field are defined on the mesh nodes. The electric field within a cell can then be approximated by a combination of nodal basis functions which are only non-zero within the cell. For the vector method, the vector electric field is defined on mesh edges and the electric field within a cell can be approximated by the combination of edge basis functions which are only non-zero inside the cell. Recently, more attention has been paid to the vector FE method because the scheme naturally satisfies the continuity of tangential component of the electric field and allows the jump of the normal component at conductivity interfaces. Moreover, the divergence of the electric field within a cell by construction is zero (Bossavit, 1988). Although the scalar FE method also guarantees the tangential continuity of the electric field between cells with possibly different conductivities, it cannot provide the normal continuity of the current density between these cells (Farquharson and Miensopust, 2011). After approximating the electric field with proper basis functions, the FE method then seeks to minimize the residual which is the error introduced by using an approximate electric field in Maxwell's equations. The weighted residual method, and in particular the Galerkin method, is commonly used to solve the minimization problem (Jin, 2015). Like FV methods, it is also possible for the FE method to use unstructured tetrahedral meshes and conventional structured rectilinear meshes.

All the numerical discretization methods mentioned above can be used to discretize discrete operators which approximate their continuous counterparts. The discrete operators are essentially sparse matrices that contain information about the

discretization mesh and physical property distributions across the mesh. The discrete operators can improve the code reusability (Haber, 2014) and have been widely used in the geophysical EM modeling literature. For example, Mackie et al. (1993) derived the compact forms of the FD operators based on a staggered Yee's grid discretization (Yee, 1966) to solve the magnetotelluric (MT) modeling problem. Haber (2014) derived different numerical discrete operators using the mimetic FV method on the staggered Yee's grid.

After the semi-discretization by one of the numerical methods discussed above, the full discretization solves the resulting ODE system by either an explicit or an implicit time-stepping method. The explicit method does not require solving a linear system of equations at each iteration step. Instead, only a matrix-vector product operation is required (Wang and Hohmann, 1993; Börner et al., 2015). The matrix-vector multiplication can be easily parallelized so that the modeling can be carried out on a massively parallel computer (Commer et al., 2008) or using accelerating devices such as graphical processing units (GPU) (Lu et al., 2013). However, the explicit method is only conditionally stable, meaning that the time steps should be small enough in order to satisfy the stability conditions of the explicit scheme. The time step is dictated partly by the minimum conductivity values in the model and smaller conductivity values require smaller time steps (Wang and Hohmann, 1993). Consequently, when the air layer is modeled or when the background of the model is very resisitive, it can easily lead to hundreds of thousands of iteration steps for a single modeling, making the method less efficient.

Implicit methods such as the commonly used first-order backward Euler method are unconditionally stable but require solving a linear system of equations at each iteration step. When the model is complex and contains a large number of cells, the linear system of equations will also be large, demanding a very large amount of memory to solve the problem when direct methods are used (Kordy et al., 2016). Iterative methods use less memory and thus can be used when available memory is limited (Jahandari and Farquharson, 2015).

EM modeling can be carried out by using either E-field methods or by using potential methods in which the magnetic vector potential ($\mathbf{A}$) and the electric scalar potential (ϕ) are commonly used (e.g., Jahandari and Farquharson, 2015; Ansari et al., 2017; Badea et al., 2001; Haber et al., 2002). The E-field modeling method can be accurate and efficient when direct methods are used to solve the linear system of equations that is generated but these linear systems can be difficult to solve with iterative methods. The $A - \phi$ approach, on the other hand, is more expensive to solve using direct solvers (in terms of both computational time and memory), but does result in a system that can be solved by iterative solvers (which can be more memory-efficient; Jahandari and Farquharson, 2015). Also, in the decomposition of the electric field in the $A - \phi$ method, the part associated with $\mathbf{A}$ is considered to be the part corresponding to "inductive" effects while the part associated with ϕ is considered to be the part corresponding to "galvanic" effects. Inductive behaviour is typically associated with the generation of an electric field (and currents) by a time-varying magnetic field (i.e., Faraday's law) while galvanic behaviour is associated

11

with charge buildups at interfaces between regions with different conductivities across which a current is flowing (Jiracek, 1990; West and Macnae, 1991). While the galvanic effect is widely studied in the field of magnetotellurics in order to make corrections for near-surface and topographic distortions (Jiracek, 1990; Nam et al., 2009), it is rarely discussed in TDEM problems. As mentioned earlier in this Chapter, those early, fast TDEM modeling algorithms, such as those described in Annan (1974), Lamontagne et al. (1988), Walker and Lamontagne (2007), and Dyck and Vallee (1980), often assume that the background is perfectly resistive such that there would be no currents flowing between the target conductor and background, and hence no galvanic effects. However, often the host is not perfectly resistive and the galvanic part can have a significant influence on measured data (Duckworth et al., 2001). The $\mathbf{A} - \phi$ decomposition of the electric field enables us to numerically examine how important the galvanic effects are for a given model and time-domain survey configuration.

Moreover, the magnetic field can be obtained directly from $\mathbf{A}$ using the potential method. By contrast, the E-field approach can only calculate dB/dt responses directly and B-field responses need be obtained by numerical integration. Although dB/dt sensors are still widely used in field surveys, there has been an increasing interest in B-field sensors because of certain advantages they have over dB/dt sensors. For example, Asten and Duncan (2012) quantitatively analyzed the advantages of B-field sensors over dB/dt ones. They found that, for targets in a conductive host or under a conductive overburden, the response of the target occurred earlier and with higher amplitude in the B-field measurements than in the dB/dt measurements. Also, B-field

12

sensors are more sensitive to the late time responses associated with deeply buried conductors compared to dB/dt sensors (Roux and Macnae, 2007). These features become increasingly attractive as exploration moves to deeper conductors. The numerical integration used to obtain the B field response from dB/dt responses normally requires an extrapolation of dB/dt responses to a later time based on the data from the last several channels, assuming that the responses from late-time channels have sufficiently decayed so that they can be treated as the homogeneous half-space response (Levy, 1984). The late time B-field responses will be smaller than the actual value if no such extrapolation is performed and no dB/dt data is available at later times. However, when there are strong conductors in the model, the late time responses may still be dominated by the response caused by the conductors and therefore the extrapolation cannot be carried out reliably. Extra numerical modeling is then required to get the dB/dt responses to a later time, which may be costly.

While frequency-domain EM problems have been widely solved using the $A - \phi$ approach (Badea et al., 2001; Ansari and Farquharson, 2014; Ansari et al., 2017; Jahandari and Farquharson, 2015; Weiss, 2013), there are significantly fewer studies on time-domain problems. Using FV methods with rectilinear meshes, Haber et al. (2002) discretized the Helmholtz equation and conservation of charge law both expressed by potentials. Haber et al. (2002) also added Faraday's law as a third equation in their system with which the solution for the magnetic field can be obtained, and used the backward Euler method as the time stepping to advance the potential solutions in time. Haber et al. (2002) used an iterative solver, with an incomplete LU factorization

(ILU) as the preconditioner, for solving the linear system of equations generated in each of the time-stepping steps. Um et al. (2010a) developed a vector FE method which solves the Helmholtz equation expressed in terms of $\mathbf{A} - \phi$, and which can work with unstructured tetrahedral grids. In both cases just mentioned, iterative solvers could be used to solve the linear system of equations because of the improved condition number of the system resulting from the use of potentials.

The electric and magnetic fields can be determined once solutions for the potentials are obtained. The $\mathbf{A} - \phi$ solutions can be non-unique if the system is not gauged properly. This is due to the existence of the null space of the curl operator. The null space essentially is the gradient of any scalar potential (Allaire and Kaber, 2008; Li et al., 2015). However, the solution for the magnetic field is still unique because the null space will be removed when calculating the magnetic field from the vector potential by taking the curl of the vector potential. Through gauging, a process in which the divergence of the vector potential is defined, the non-uniqueness can be removed. The Coulomb gauge condition and the Lorenz gauge condition are the two most commonly used gauge conditions for defining the divergence of the vector potential (Jackson, 2002). The divergence of the vector potential is set to zero for the Coulomb gauge condition while it is set to some terms expressed by the scalar potential for the Lorenz gauge.

The Lorenz gauge condition for EM wave problems relates the 'retarded' scalar and vector potentials to each other (Jackson, 2002). With this gauge, the solutions for the scalar and vector potentials in homogeneous media such as vacuum can be

shown to be caused by charge density and current density sources, respectively. The Lorenz gauge can be thought of as treating space and time equally, which makes it consistent with special relativity, and which results in both potentials propagating at the speed of light (Jackson, 1998). The Coulomb gauge condition, on the other hand, does not couple the scalar and vector potentials, and only requires the divergence of the vector potential to be zero. The solution of the scalar potential 'propagates' instantaneously (Chew, 2014). However, the EM fields calculated by applying the two gauge conditions are the same no matter how unphysical the gauge condition might be; the fields are, after all, unique (Jackson, 2002). For geophysical EM problems for which the quasi-static approximation is valid, the Lorenz gauge takes a different form compared to the one used for EM wave problems (Bryant et al., 1990). The Lorenz gauge condition still relates the two potentials to each other, but it does so through the conductivity rather than permittivity. One key motivation behind using the Lorenz gauge condition rather than the Coulomb gauge condition is to decouple the two potentials and eventually eliminate the scalar potential in order to reduce the size of the problem that needs to be solved (see, e.g., Bryant et al., 1990; Um et al., 2010a). However, the potentials can only be decoupled if the conductivity is homogeneous (Bíró and Preis, 1989, 1990). Bossavit (1999) proposed a variant of the Lorenz gauge condition used by Bryant et al. (1990) in the hope of removing the homogeneous conductivity restriction. But the method is hard to implement due to the boundary conditions needed at the conductivity jump interfaces. Weiss (2013) used a FV discretization to solve the frequency-domain EM problem using potentials.

The two potentials are not decoupled and are both kept in the discretized system. The resulting coefficient matrix is symmetric with the FV discretiztion while it loses the symmetry when nodal FE methods are used (Bíró and Preis, 1990).

The Coulomb gauge condition is the same for both EM wave and diffusion problems, and is free of the restrictions observed with the Lorenz gauge. It is also more straightforward to discretize by either nodal FE (see, e.g., Badea et al., 2001; Puzyrev et al., 2013; Ansari et al., 2017) or FV (Haber et al., 2002; Jahandari and Farquharson, 2015) methods. When edge-element FE methods are used, the divergence of the vector potential, by construction, is zero within element cells. However, as shown by Ansari et al. (2017), the system is still not completely gauged because the normal component of the vector potential across the element faces is not necessarily continuous. The implicit enforcement of the Coulomb gauge (Bíró and Preis, 1989) incorporates the divergence operator in the differential equation to be solved, which makes it hard to be descretized using an edge-element FE method (Li et al., 2015) while the nodal FE discretization has no such issue. Consequently, the so-called tree-cotree method has been widely used to enforce the Coulomb gauge condition in edge-element FE methods (Manges and Cendes, 1995; Bíró et al., 1996; Jin, 2015). This method is argued by Li et al. (2015) to be a non-optimal choice because it results in a coefficient matrix that is no longer highly sparse, and a good tree graph that leads to a fast convergence is hard to find. Li et al. (2015) instead formulated the divergence of the vector potential based on the space mapping between the Whitney forms by mathematical and Hodge operators while using edge elements for the expansion of

16

the vector potential. However, extra computational costs are required to calculate the matrix inverse and multiplication operations which arise with this method. To avoid these extra computational costs, Ansari et al. (2017) added the Coulomb gauge condition as an extra equation to be solved along with the Helmholtz equation and the conservation of charge equation both expressed in terms of potentials. Ansari et al. (2017) treated the divergence of the vector potential as a scalar field and weighted it with the nodal basis function as the test function. The FV method, as shown by Jahandari and Farquharson (2015), is free from these issues when it comes to the implicit enforcement of the Coulomb gauge condition. Moreover, the method developed by Ansari et al. (2017) can also be implemented because the divergence operator can be easily discretized with FV methods.

In this work, the FV method for unstructured Delaunay-Voronoï dual meshes of Jahandari and Farquharson (2014) and Jahandari and Farquharson (2015) from the frequency domain will be extended to the time domain and both the E-field and $A - \phi$ methods will be implemented. For the $A - \phi$ method, the Coulomb gauge condition will be enforced in order to get unique potential solutions. Unlike frequency-domain cases where gauge conditions are merely enforced for obtaining unique solutions for potentials, inconsistent solutions of potentials across different time steps would result in incorrect solutions for EM fields for time-domain problems if no gauge condition is enforced. The implicit enforcement adopted in Jahandari and Farquharson (2015) and the explicit method developed in Ansari et al. (2017) are both implemented in this work.

The uranium deposits in the Athabasca Basin in northern Saskatchewan, Canada, are found to be closely-related to graphitic fault zones. Common ore bodies are small in size, and are typically found around the graphitic fault, near the unconformity between the sandstone basin and the metamorphosed basement (Jefferson et al., 2007). Graphite is very conductive while the sandstone basin and the metamorphosed basement are significantly more resistive than graphite so that there exists a large conductivity contrast between the graphite concentrated in the fault zones and the surrounding geological units. The relatively small size of the ore body and its deep burial depth mean that direct detection methods such as gamma-ray spectrometry cannot be effectively used. Consequently, graphitic fault zones have been historically considered as the pathfinder to the uranium ore bodies (Jefferson et al., 2007).

So far, electrical methods such as DC resistivity methods, frequency- and time-domain EM methods have been preferred for targeting the graphitic faults in the exploration of the uranium deposits in the basin (Powell et al., 2007). TEM methods can detect deeper targets compared with other electrical methods, and therefore are the most commonly used method. At early stages of the exploration, airborne (fixed-wing and helicopter-borne) EM surveys are commonly used to detect the general conductor trend over a large area (Smith et al., 2011; Irvine and Witherly, 2006). For a better delineation of graphitic conductors, ground TEM surveys are required. The fixed-loop TEM survey is commonly used for the initial mapping of the conductor system due to its relatively lower costs and higher efficiency. A large rectangular transmitter loop is laid far enough from the conductor while the receiver is moved

around the conductor region to record the TEM response (Spies and Frischknecht, 1991). However, the response from the conductor can be easily masked by multiple factors such as a strong layered-Earth response or a conductive host (Powell et al., 2007).

Moving-loop (or Slingram-style) configurations have the transmitting loops and receivers located at a fixed distance, and they are moved at the same time along a survey profile. This configuration is commonly used in both the time- and frequency-domain surveys. In the frequency domain, the transmitters and receivers are normally made of small loops fixed with a short offset on the same device (see Figure 2 in Weymer et al., 2015). The frequency-domain Slingram configuration is a popular tool used in the hydrogeophysics applications where it is used to map the near-surface conductivities (see, e.g., Francés et al., 2014; Weymer et al., 2015, 2016). In the time domain, the loop sources are commonly significantly larger than those of the frequency domain and hence are deployed separately (Powell et al., 2007).

For the uranium exploration in the Athabasca Basin, the moving-loop TEM configuration is commonly used to supplement the fixed-loop surveys because of their improved ability to map conductors (Powell et al., 2007). Moving-loop survey configurations use a large rectangular transmitter loop as source and record the TEM response using a receiver placed outside the transmitter loop along the survey profile with a fixed offset. Moving-loop survey profiles are commonly several kilometers long and the station spacing can be tens or hundreds of meters. However, a fixed transmitter-receiver separation can also limit its ability to resolve complex multi-

conductor systems. The so-called stepwise moving-loop or step-loop method combines the fixed-loop and moving-loop methods into one method by using multiple receivers for a given loop while also moving the loop along the profile. The step-loop method provides different transmitter-receiver separations and contains significantly more data, which then inevitably leads to an increase in survey costs. This thesis is mainly concerned with the moving-loop configuration given the real data that will be modeled are all of moving-loop configurations.

Because of the small thickness and steep dip angles of the graphitic faults commonly seen in the Athabasca Basin, it is critically important for the interpretation of TEM data to accurately give the location of the graphitic faults. Three-dimensional minimum structure inversions generally yield models with smoothly varying structures in which sharp boundaries are suppressed. The inversion results normally show a conductivity anomaly which is much larger than the actual graphitic fault zone, which makes it very difficult to target the graphitic faults for drilling (Keller, 2019). Although by using the l_1 measures, one can get blocky, piece-wise constant models which are less smooth compared with the models recovered with an l_2-norm (Farquharson, 2008), it would probably still struggle to recover models with very thin structures.

Traditionally, the interpretation of the TEM data collected in the Athabasca Basin for the exploration of graphitic conductors is commonly based on trial-and-error modeling of thin, plate-like conductors using fast algorithms provided by programs such as Maxwell (EMIT, 2005) and MultiLoop (Lamontagne, 2007). As mentioned before,

20

these algorithms assume that the background is perfectly resistive and the layered Earth responses are only accounted for by adding another horizontal thin plate in the air, and no current gathering effect is considered. Therefore, they are only capable of modeling late-time responses (see, e.g, Irvine and Witherly, 2007; Lamontagne, 2007). Despite being fast, the interpretation based on these fast algorithms may miss important information contained in early-time responses. For example, a conductor with a limited depth extent or a relatively small conductivity can only cause anomalous responses observable in early- to middle-time channels. The interpretation based only on late-time responses would not be able to recover such conductors. Also, the conductivity of the plate is required to be uniform when using these fast algorithms, which is hardly true in reality. In fact, as can be seen later in this thesis for the modeling of the real data from the Close Lake Project, a good match between the modeled data and the real data normally requires the conductor to have varying conductivities with depth.

The moving-loop surveys normally record three-component B or dB/dt responses. Only the in-line and vertical responses are commonly interpreted via trial-and-error modeling with fast algorithms. This is because the strike of the conductor is commonly assumed to be perpendicular to the survey profile and the conductor strike is considered to be constant. Consequently, no cross-line response is expected. However, graphitic faults in the Athabasca Basin can bend frequently along its strike, which causes non-zero cross-line responses. Therefore, the cross-line responses are important information which can be used to interpret the strike of the conductor.

The FV method developed in this thesis is able to calculate three-component TEM responses from early to late times. Using unstructured Delaunay-Voronoï dual meshes, it can calculate the TEM responses of realistic Earth models which contain not only the conductor but every other geological unit that is present in reality. For the conductor itself, its variation in strike, burial depth, depth extent, and conductivity with location can also be honored faithfully. Consequently, through trial-and-error, a 3D Earth model can be obtained, with which a good match between the modeled data and real data can be achieved.

It is not uncommon for an exploration project area in the Athabasca Basin to go through multiple exploration campaigns with different focuses, lasting for several decades. Historical diamond drilling data and EM survey data may have coarse coverage over the area where the survey data to be modeled are collected. Nonetheless, they are still useful and can provide information on roughly how deep is the unconformity and where does the conductor extend to. Based on experience or trial-and-error modeling with the aforementioned fast algorithms on the survey data, one can also have a rough estimation on the location of the conductor along the profile. Physical property measurements at neighboring drill holes, when they exist, can be helpful in determining conductivities of the conductor and its adjacent geological units.

This thesis consists of seven chapters. Chapter 2 investigates the unstructured meshes that will be used in this thesis, how to create these meshes to represent real-life geological models, and the governing equations that are key to TEM modeling. The mesh building procedure developed in this chapter is specifically designed to suit

the needs of the FV modeling in this thesis. The procedure is easy to follow and can generate unstructured grids with high quality for key modeling areas while keeping the total number of cells under control. Chapter 3 discretizes all the partial differential operators present in Chapter 2 into discrete operators by using the FV method. The discretized operators are essentially sparse matrices which makes it possible to write highly modularized programs which can significantly increase the reusability of the programs. Chapter 4 solves the E-field Helmholtz equation while Chapter 5 solves the Helmholtz equation expressed by $\mathbf{A} - \phi$. Although the methods used in these two chapters have been developed for solving frequency-domain problems, they have never been tested for time-domain cases. The decomposition of the electric field presented in Chapter 5 enables us to visually examine the existence of the current gathering effects of a conductive host into the conductor. Chapter 6 uses the modeling algorithms developed in Chapter 4 and Chapter 5 to model field data sets collected from the Athabasca Basin for uranium exploration. Tests show that by using the trial-and-error modeling method, it is possible to match all three components of the field data using realistic 3D models at much broader time channel ranges. Finally, Chapter 7 summarizes this thesis.

Chapter 2

Numerical modeling of geophysical EM data on unstructured tetrahedral meshes

2.1   Introduction

The EM fields for a given model can be calculated analytically if the model is simple enough or numerically (Ward and Hohmann, 1988). Models with analytic solutions normally are restricted to whole-space or half-space homogeneous models, layered halfspace models, or an anomalous body of simple geometrical shape buried in a homogeneous half-space. When the model consists of irregularly shaped anomalous regions such as ore bodies, the EM responses cannot be calculated from analytic methods anymore and numerical methods have to be used.

Maxwell's equations are a set of PDEs that describe how the EM fields behave within a given model. Normally, these PDEs are considered to be linear, i.e., the coefficients in the PDEs do not change with the unknown EM fields. In the time domain case, the EM fields are functions of both space and time. Therefore, the numerical discretization normally involves two stages: semi-discretization which discretizes the continuous EM fields on a discrete mesh to form an initial value problem for a set of ordinary differential equations (ODEs) in time, and full discretization which discretizes the ODE in predefined time instants using existing methods developed for solving ODEs (Ascher, 2008).

The solution of the TDEM problems requires initial conditions for the EM fields. For example, the static electric field caused by the grounded wire source should be calculated prior to solving the TDEM problem. Also, when the scalar and vector potentials are used in modeling the TDEM data of a loop source, the static potential fields before the source is switched off should be calculated. These static fields can be calculated by solving the direct current resistivity (DCR) problem and the magnetometric resistivity (MMR) problem.

Unstructured tetrahedral meshes have been widely used in EM modeling because they can easily conform to complicated geometry such as topography and real-life geological units with a smaller number of cells than conventional structured, rectilinear meshes (Lelièvre et al., 2012). The quality of the unstructured mesh, especially at key areas such as sources and receivers, can significantly affect the accuracy of the numerical modeling.

In this chapter, the governing equations, Maxwell's equations, and a set of PDEs derived from Maxwell's equations, are firstly introduced. Secondly, a specific type of unstructured mesh, the Delaunay-Voronoï dual meshes used by the FV method developed here will be introduced. Finally, a three-step mesh building procedure that is used to generate high quality meshes with proper refinements specifically designed for the FV method will be developed and a detailed description of this mesh generation method will be given.

2.2   Maxwell's equations and constitutive relations

Maxwell's equations are a set of PDEs which describe how EM fields behave. The equations describe four fundamental physical laws: Gauss's law, Gauss's law for magnetism, Faraday's law and Ampère's law. For the geophysical applications that this thesis is mainly concerned with, namely ground TEM surveys, EM fields with a frequency higher than 10^5 Hz are negligible within the recorded data. Consequently, the quasi-static approximation, under which the displacement current is ignored, is valid (Spies and Frischknecht, 1991). The time-domain Maxwell's equations under quasi-static approximation can be written in a differential form as

$$\nabla \cdot \mathbf{D} = \rho, \tag{2.1}$$

$$\nabla \cdot \mathbf{B} = 0, \tag{2.2}$$

$$\nabla \times \mathbf{H} = \mathbf{J} + \mathbf{J}_s, \tag{2.3}$$

$$\nabla \times \mathbf{E} = -\frac{\partial \mathbf{B}}{\partial t}, \tag{2.4}$$

where $\mathbf{D} = \mathbf{D}(\mathbf{r}, t)$ is the electric displacement vector, $\mathbf{E} = \mathbf{E}(\mathbf{r}, t)$ is the electric field intensity, $\mathbf{B} = \mathbf{B}(\mathbf{r}, t)$ is the magnetic flux density, $\mathbf{H} = \mathbf{H}(\mathbf{r}, t)$ is the magnetic field intensity, $\rho = \rho(\mathbf{r}, t)$ is the charge density, $\mathbf{J} = \mathbf{J}(\mathbf{r}, t)$ is the current density which does not include the source, $\mathbf{J}_s = \mathbf{J}_s(\mathbf{r}, t)$ is the current density of the source, $\mathbf{r}$ is the position vector, and t is time. The relationships between $\mathbf{B}$ and $\mathbf{H}$, $\mathbf{D}$ and $\mathbf{E}$ are given by the constitutive relations:

$$\mathbf{B} = \mu \mathbf{H}, \tag{2.5}$$

$$\mathbf{D} = \varepsilon \mathbf{E}, \tag{2.6}$$

where μ and ε are the magnetic permeability and electric permittivity, respectively. In reality, both μ and ε are anisotropic, nonlinear functions of multiple factors (Ward and Hohmann, 1988). But here they are assumed to be constants which have the values of those of free space, μ_0 and ε_0, respectively. These approximations are appropriate for the applications considered in this thesis.

Ohm's law gives the relationship between $\mathbf{E}$ and $\mathbf{J}$:

$$\mathbf{J} = \sigma \mathbf{E}, \tag{2.7}$$

where $\sigma = \sigma(\mathbf{r})$ is the electrical conductivity which is considered to be only a function of $\mathbf{r}$ despite the fact that in reality it can also be a function of time, frequency, and the strength of the EM fields themselves. In this thesis, the electrical conductivity σ is the only variable that changes with space in the numerical modeling and what one intends to recover from measured field EM data.

2.2.1 E-field formulation of Helmholtz equation

Taking the curl of Equation 2.4 and substituting the subsequent equation into Equation 2.3 while also considering Ohm's law gives

$$\nabla \times \nabla \times \mathbf{E} + \mu_0 \sigma \frac{\partial \mathbf{E}}{\partial t} = -\mu_0 \frac{\partial \mathbf{J}_s}{\partial t}. \tag{2.8}$$

This equation is referred to as the electric field Helmholtz equation. It is a diffusion equation rather than a wave equation.

2.2.2 $\mathbf{A} - \phi$ formulation of Helmholtz equation

The EM fields can also be expressed in terms of the magnetic vector potential, $\mathbf{A}$, and the electric scalar potential, ϕ, as

$$\mathbf{E} = -\frac{\partial \mathbf{A}}{\partial t} - \nabla \phi, \tag{2.9}$$

$$\mu_0 \mathbf{H} = \nabla \times \mathbf{A}. \tag{2.10}$$

Substituting Equations 2.9 and 2.10 into Equation 2.3 and also considering Ohm's law (Equation 2.7) gives the Helmholtz equation for the potentials under quasi-static approximation:

$$\nabla \times \nabla \times \mathbf{A} + \mu_0 \sigma \left(\frac{\partial \mathbf{A}}{\partial t} + \nabla \phi \right) = \mu_0 \mathbf{J}_s. \tag{2.11}$$

Considering Ohm's law, the conservation of charge law can be written as

$$\nabla \cdot \sigma \mathbf{E} = -\nabla \cdot \mathbf{J}_s. \tag{2.12}$$

Replacing $\mathbf{E}$ with potentials, Equation 2.12 can be further written as

$$\nabla \cdot \sigma \left(\frac{\partial \mathbf{A}}{\partial t} + \nabla \phi \right) = \nabla \cdot \mathbf{J}_s. \tag{2.13}$$

Equations 2.11 and 2.13 can be solved together to obtain solutions for $\mathbf{A}$ and ϕ. After the solutions for $\mathbf{A}$ and ϕ are obtained, the electric and magnetic fields can be determined by Equations 2.9 and 2.10.

2.2.3 Direct current resistivity problem

For DCR problems, the electric field is static so that Equation 2.9 changes to

$$\mathbf{E} = -\nabla \phi. \tag{2.14}$$

Substituting Equation 2.14 into the conservation of charge law, i.e., Equation 2.12, gives

$$\nabla \cdot \sigma \nabla \phi = \nabla \cdot \mathbf{J}_s. \tag{2.15}$$

Once Equation 2.15 is solved and the solution for ϕ is obtained, the static electric field then can be determined by Equation 2.14.

2.2.4 Magnetometric resistivity problem

Like the DCR method, the MMR method also employs a grounded wire as its source. But it measures the horizontal magnetic field rather than the electric potential as is done in DCR surveys (Edwards, 1978). In order to calculate the magnetic field for such a configuration, the electric field of the electrostatic DCR problem should be solved first. Here, the same vector potential as in the TDEM case (Equation 2.10) is used to express the magnetic field. Therefore, substituting Equation 2.10 into Equation 2.3 and also considering Ohm's law (Equation 2.7) yields

$$\nabla \times \nabla \times \mathbf{A} = \mu_0 \mathbf{J}_s + \mu_0 \sigma \mathbf{E}, \tag{2.16}$$

where $\mathbf{E}$ can be obtained by solving the DCR problem as discussed in Section 2.2.3.

By solving Equation 2.15 and 2.16 one after another, the static electric and magnetic fields as well as the scalar and vector potential fields that are caused by a grounded-wire source can be obtained. Note that for a loop source, the static vector

potential can still be calculated using the above equation but without the electric field term on the right-hand side. These static EM fields together with the potential fields can be used as the initial conditions for solving the TEM problem using various methods that will be discussed later in Chapters 4 and 5.

2.3   Unstructured meshes

In this thesis, the unstructured Delaunay-Voronoï dual meshes (Figure 2.1) are used for the finite-volume time-domain (FVTD) method. For 3D problems, let Ω be the computational domain of the modeling. The Delaunay mesh discretizes Ω into a set of three-dimensional simplicial complexes (nodes, segments, triangles, and tetrahedra). For any tetrahedron in the mesh, all nodes except the four that comprise the tetrahedron are located outside the circumscribed sphere of that tetrahedron. The Voronoï mesh can be obtained by connecting the circumcenters of all the tetrahedra.

An important feature of the Delaunay-Voronoï dual meshes is that the edges and faces of the Delaunay and Voronoï meshes are mutually orthogonal to each other. Therefore, the dual meshes can be considered as a generalized staggered mesh to the rectilinear staggered Yee's grid (Yee, 1966).

For geophysical EM modeling under the quasi-static approximation, both conductivity and magnetic susceptibility of the Earth can be considered to be functions of spatial location. However, the effect of the inhomogeneity of the magnetic susceptibility is only obvious for certain types of TEM surveys such as the detection of
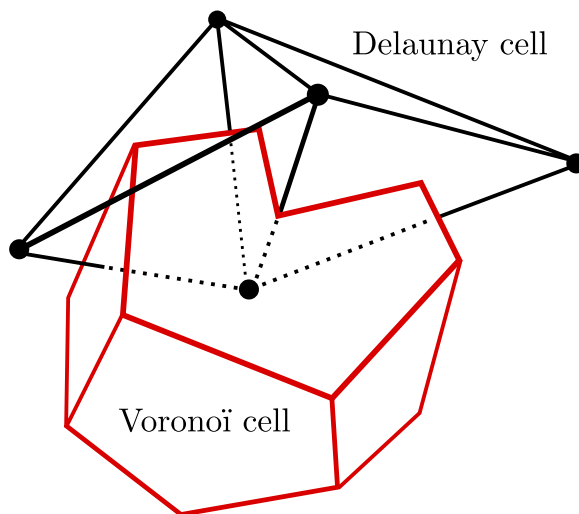
Figure 2.1: Delaunay (black) and Voronoï (red) dual meshes. The Voronoï mesh is obtained by connecting the circumcenters of the tetrahedra of the dual meshes. The Delaunay (Voronoï) edges are orthogonal to the Voronoï (Delaunay) faces (after Jahandari and Farquharson, 2014).

unexploded ordnances (UXOs; Pasion et al., 2007). The effect is negligible for applications that this thesis is concerned with so it is set to the same as that of free space. The variation of the subsurface conductivity is accounted for by assigning different values to different tetrahedral cells. Inside a tetrahedral cell, the conductivity is considered to be constant.

In reality, the subsurface of the Earth is filled with different geological units such as sediments deposited at different times. For each unit, the conductivity is normally varying continuously within certain ranges. Different geological units might possess similar conductivity values so that they can be considered as a single unit in the geophysical model. Also, the conductivity of the same geological unit can vary significantly when certain types of minerals with extremely large conductivities are not evenly distributed in that geological unit. Therefore, the geophysical model should be built based on the geological model but care must be taken in this process when deal-

ing with the possible inconsistency between the geological and geophysical models. For simplicity, Ω is normally divided into several different regions with each region representing a geological unit with a unique conductivity value. The variation of the conductivity inside these regions is not considered.

2.4 Mesh generation

In this work, a three-step procedure is developed and used for the generation of the unstructured Delaunay-Voronoï dual meshes that can be used by the FV method developed in this thesis. First, refinement points are generated for key areas such as the transmitting source and receivers. Then, the software called FacetModeller (Lelièvre et al., 2018a) is used to create a surface-based model which describes the regions and their geometries. Lastly, the software TetGen (Si, 2015) is used to generate the unstructured Delaunay-Voronoï dual meshes. The following sections describe these three steps in detail.

2.4.1 Surface mesh refinements

The quality of the mesh affects the numerical modeling results significantly (see, e.g., Jahandari and Farquharson, 2014; Li et al., 2018; Ansari and Farquharson, 2014). For example, the mesh around the receivers and transmitters should be refined properly in order to get accurate EM response. Also, when topography is present, the surface mesh around the source and receivers should also be refined in order to better account

for the effect of the topography. In addition, regions with small sizes but which represent key anomalies should also be refined with smaller cells.

A 2D surface mesh is created first which has the refinements needed for the source, receiver, and topography since they all appear at the Earth's surface for the ground Slingram-style surveys which are the major applications presented in this thesis. The topography data generally cannot be used directly for building the mesh due to its limited area coverage and relatively dense sampling. For example, Figure 2.2 shows the original topography data taken from the Voisey's Bay Ovoid massive sulphide ore deposit site located in Labrador, Canada. The data approximately covers an area of 2 km × 2 km, with a small area at the south-west corner not covered. The data are collected with a very small station spacing of 5 m in both the x and y directions, resulting in 159,084 nodes and 317,565 triangles. This data cannot be directly used to create the surface mesh because it is too dense, which causes the final tetrahedral mesh to have an extremely large number of cells. Also, although the area with topography data is large, it is not large enough to cover the entire area needed for building the 3D model. Normally, 3D models need a truncation boundary tens or even hundreds of kilometers away from the center of the mesh in order to be able to use the Dirichlet boundary condition (a detailed discussion can be found in Section 4.5.3). Therefore, we have to interpolate the topography data onto a coarser mesh and extrapolate it in areas where topography data are unavailable in order to form a complete ground surface in the model.

Firstly, a triangle mesh with its quality varying according to its actual location is
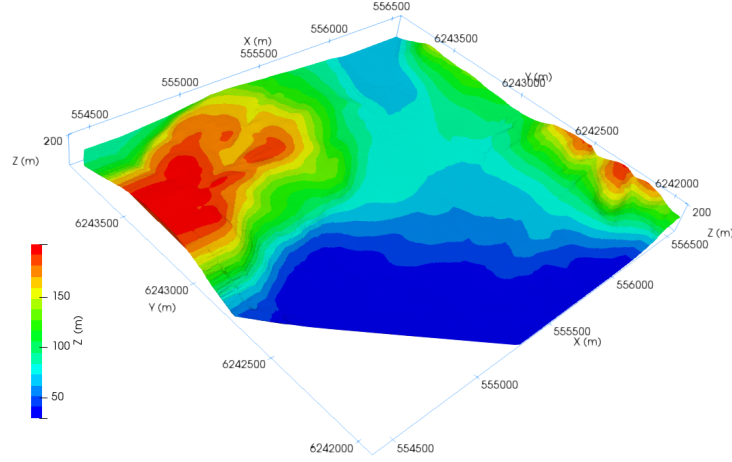
Figure 2.2: An example of the original topography data from the Ovoid massive sulphide ore deposit site located in Labrador, Canada.

created. Following the ideas developed by Williams (2008) and Lelièvre et al. (2018b), the 2D mesh is divided into multiple regions based on their locations. As shown in Figure 2.3, these regions include a core area of interest (COI), which is the area closest to the sources and receivers where a higher quality of the mesh is preferred, a regional area of interest (ROI), which is an area outside the COI where the topography data should also be available but the quality of the mesh does not need to be as high as that in the COI, and a padded regional area of interest (POI), which is an area outside the ROI that is used to extend the model to a reasonably far distance from the center of the mesh and no refinements are needed for it. All these regions can simply be defined by rectangles within which constraints of maximum area of triangles can be defined separately in order to specify different levels of refinements for the different regions. The 2D triangular mesh generation software called Triangle (Shewchuk, 1996) is used in generating the 2D triangle mesh. Figure 2.4 is the generated 2D triangle mesh

35
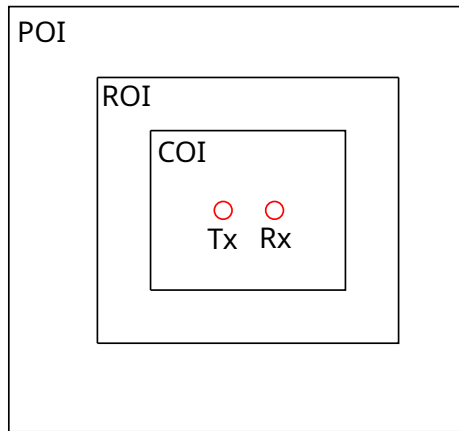
Figure 2.3: A schematic diagram showing the COI, ROI, and POI regions used in creating the surface mesh. The survey area should be located inside the COI and topography data should be interpolated onto a finer surface mesh inside this area. The surface mesh inside the ROI and outside COI does not need to be as refined as that inside the COI, and it can be unrefined for areas inside the POI and outside the ROI.

superimposed with the topography shown in Figure 2.2.

Inside the COI, as shown in Figure 2.5, regular triangles (denoted by the inside red nodes) are generated for each of the receivers with the observation points located at its circumcenters. The triangles will be used eventually to form two regular tetrahedra for each of the observation points, with one of them located above the surface and another located below the surface. The green tetrahedra shown in Figure 2.5 are the ones above the surface. The 2D coordinates of the three points which form the regular triangle were provided to program Triangle when generating the 2D triangle mesh. The coordinates of the other two points (one above and one below the surface) used in forming the two regular tetrahedra are written to a separate file so that later they can serve as input information for TetGen. Loop sources or grounded wire sources are considered in this thesis and their refinements differ between FV and FE methods. For FV methods, it is convenient to put the current wires on the tetrahedral edges so
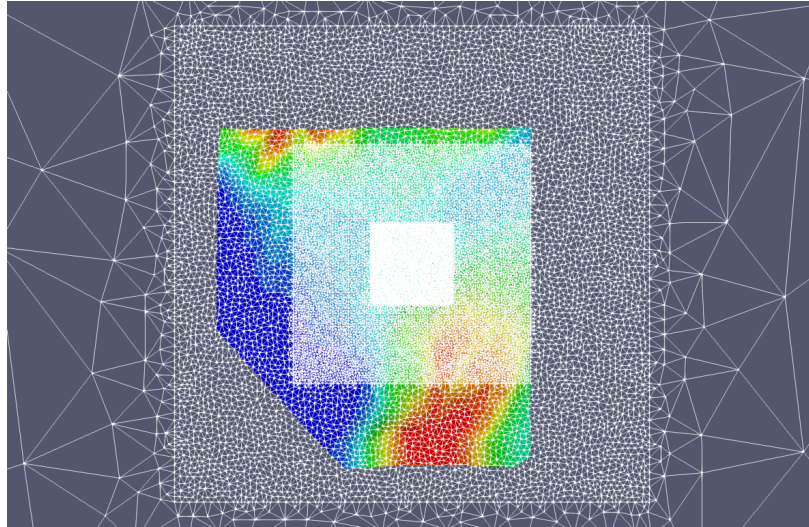
Figure 2.4: The topography data (in color) on which the 2D triangle mesh (gray) created for its later interpolation is superimposed. The innermost rectangle represents the refinements made for the transmitter and receivers. The rectangle enclosing the innermost rectangle is the COI area which is mostly refined and topography data is available everywhere inside it. The triangle mesh outside the COI is the ROI where only part of the topography data is available and the mesh is less refined compared with that of the COI. The outermost part is the POI and no topography data is available for which the mesh is the least refined.

a number of edges are inserted in the 2D mesh as the refinements for sources. The red nodes on the outer rectangle shown in Figure 2.5 were inserted to generate these edges in the surface mesh. For FE methods, although it is possible to use tetrahedral edges to represent current source wires (Yin et al., 2016), it is common to force the current wires inside tetrahedra (Ansari and Farquharson, 2014). The refinements then can be achieved simply by adding extra nodes above or below the current wire so that more tetrahedra will be generated around the source area. The inserted nodes do not appear in the 2D surface mesh and are written to files for later use by TetGen as well.

After the 2D triangle mesh is generated, topography is then interpolated to all the nodes of the 2D mesh. This gives the z coordinates of the nodes in the 2D mesh. The program PODIUM (Lelièvre et al., 2018b) is used to interpolate topography data onto
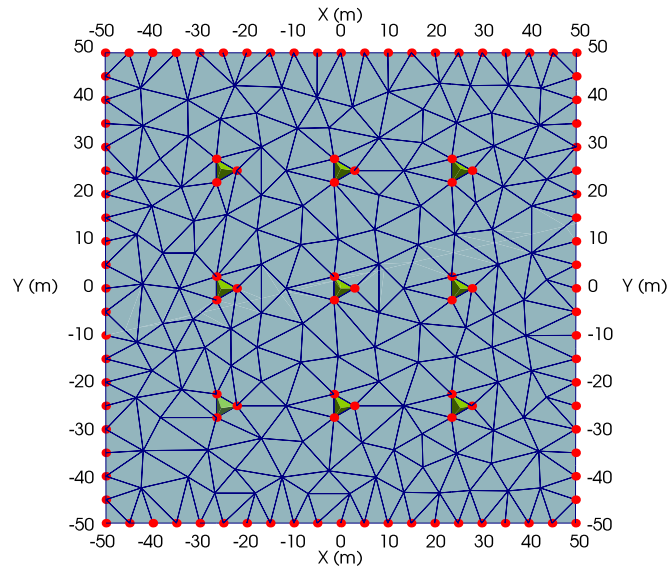
Figure 2.5: An example of surface mesh refinements for observation points and a loop transmitter. The outside red nodes are inserted for the refinement of the loop source and the inside red nodes are inserted to form regular triangles which eventually are used to form regular tetrahedra shown in green. The nine receivers are located at the circumcenters (center of the circumscribed circle) of the regular triangles on the surface.

the 2D surface mesh to create a 3D triangle mesh that will be incorporated into the 3D model later as the Earth's surface. It actually performs interpolation inside areas where topography data are available and extrapolation where topography data are unavailable. In addition to the 2D surface mesh, those nodes that were inserted for creating the regular tetrahedra for observation points refinements as well as the nodes inserted for FE source refinements also need to be interpolated to the topography data. They are firstly moved to the 2D flat surface and then moved up and down, respectively, after the interpolation, based on their original relative position to the 2D flat surface. Figure 2.6 shows an example of an interpolated surface mesh based on a given topography data-set. The regular tetrahedron is inserted for the refinement of an observation point. The segments below it which form a straight line are inserted
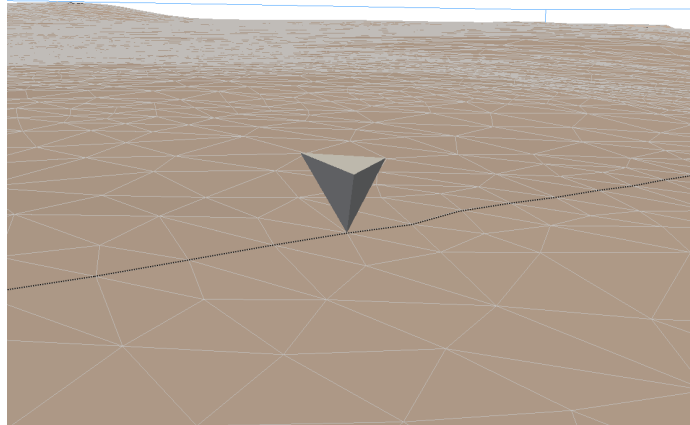
Figure 2.6: An example where the flat surface is interpolated based on a given topography data-set. The regular tetrahedron is inserted for the refinements of the observation point. The black dashed line represents the source wire and it is connected by tetrahedral edges inserted for the refinement of the source. These tetrahedral edges are firstly introduced into the 2D surface mesh and must be preserved in the final 3D tetrahedral mesh in order to calculate the right-hand sides of the linear system of equations for the FV method.

for the refinement of the loop source. This is an example taken from a Slingram type survey and the observation point happens to be located at the same location of a loop source from previous stations. Therefore, the regular tetrahedron is flipped upside down in order to avoid interference between the refinements inserted for the source and those for the receiver. The survey area shown is actually very flat (observation points on a frozen lake) and topography features can only be seen in areas far away from the survey area.

2.4.2 Surface-based model creation

Geological models are commonly surface-based, that is, a model contains different units which can be defined by surfaces shared by adjacent units (see, e.g., Figure 3 in Miorelli et al., 2019). A piecewise linear complex (PLC; Miller et al., 1996)
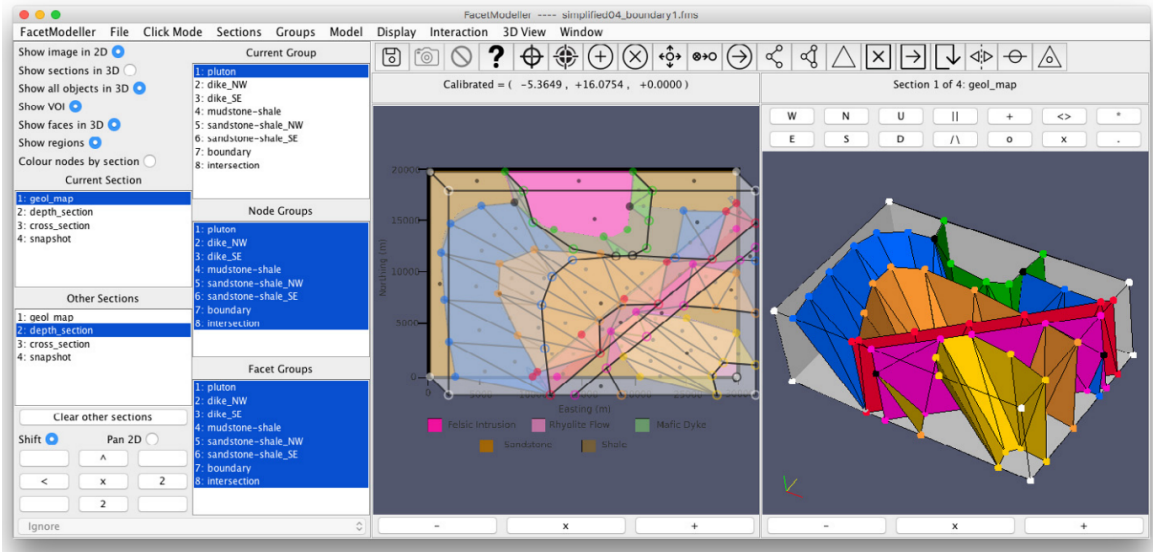
Figure 2.7: A screenshot from FacetModeller. The nodes and facets are defined based on a geological map and interpreted geological sections (Lelièvre et al., 2018a).

can be used to describe the surface-based models and it is widely used as input for mesh generation software packages (Lelièvre et al., 2018a). FacetModeller (Lelièvre et al., 2018a) is designed to generate a quality PLC (see Si, 2015, for more detailed information on PLCs) given a surface-based geological model. For creating a PLC with FacetModeller for a geological model, two types of data can be used as input data. The first type is digitized images such as geological maps, interpolated vertical cross sections or horizontal depth sections (Figure 2.7). The second type is a pre-defined 3D model surface which can be tessellated or just comprise unconnected nodes on that surface (Figure 2.8).

The interpolated surface mesh is essentially a 3D tessellation of the ground surface in the model, and can be readily taken in by FacetModeller as an input. For example, Figure 2.9 shows the screenshot of FacetModeller with the surface mesh interpolated from the 2D triangle mesh seen in Figure 2.4. Part of the POI, all of the ROI, and

40
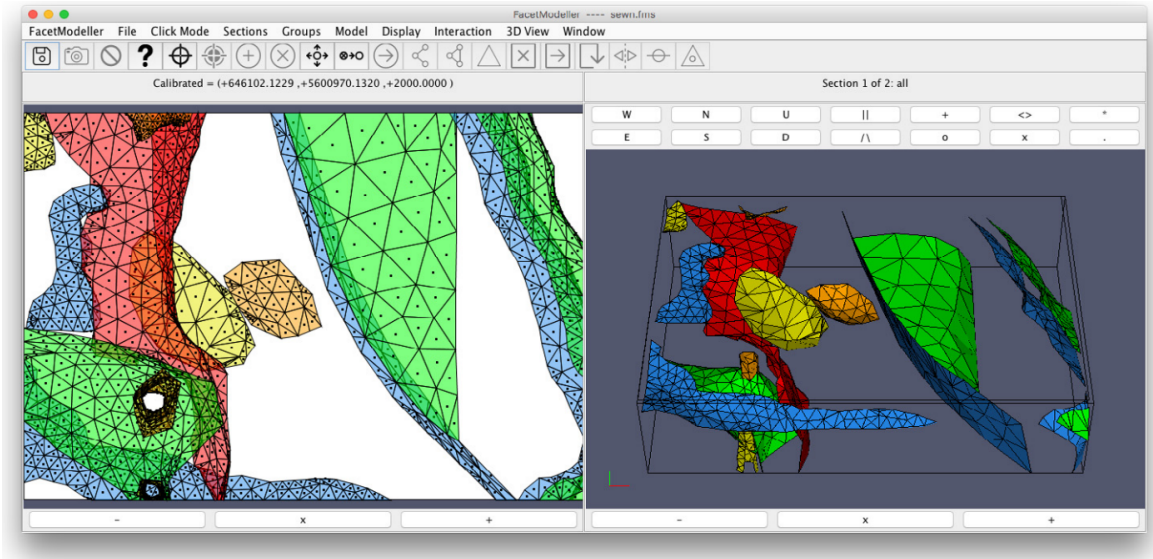
Figure 2.8: A screenshot from FacetModeller. The nodes and facets are defined based on surfaces built by Gocad and AutoDesk Meshmixer (see Lelièvre et al., 2018a and the references therein).

the COI can be seen in the 2D viewing panel on the left and the entire surface mesh can be seen in the 3D viewing panel on the right. After loading the surface mesh, other geological units can be built in FacetModeller.

For the graphitic fault models, the vertical cross sections derived from drilling data (see, e.g., Figure B.1) can be used to build the subsurface of the model Earth. Then FacetModeller can generate a PLC which describes the 3D model with watertight regions representing different geological units. Figure 2.10 shows a screenshot taken from FacetModeller during the building of a graphitic conductor model. On the 2D viewing panel, a sandstone layer (brown) is located below the overburden layer (green) and above the unconformity (not shown). The overburden, sandstone layer and a dipping conductor (blue) are shown in the 3D viewing panel. The gray triangle mesh above these regions is the interpolated 2D surface mesh. For the reason

41
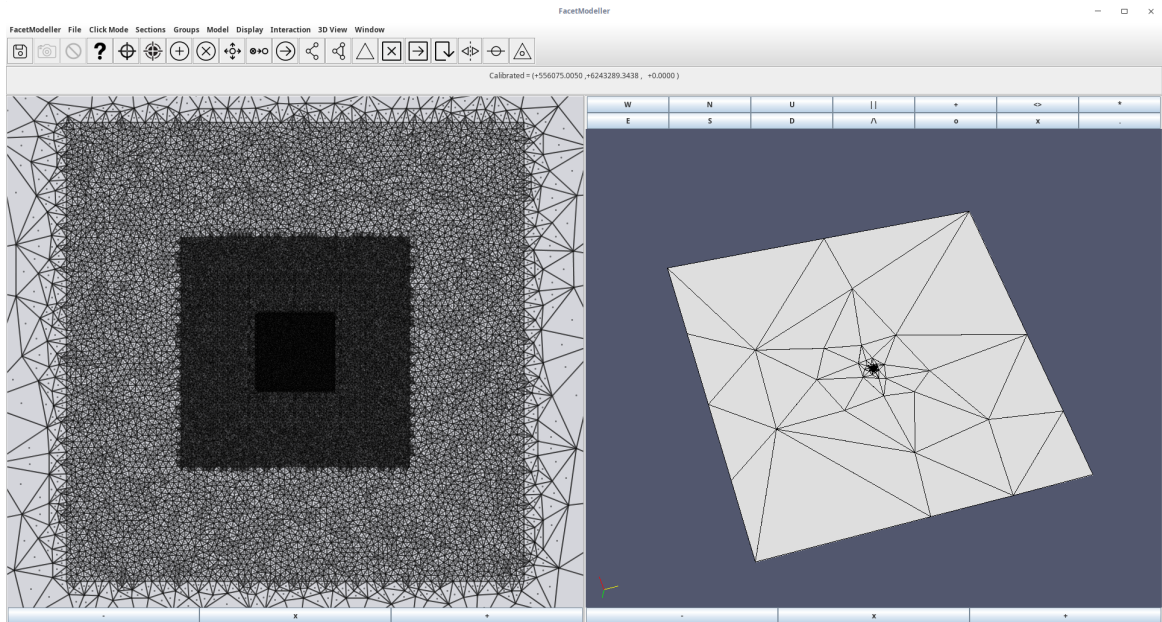
Figure 2.9: A screenshot of FacetModeller after the surface mesh created for the Ovoid model is loaded. The 2D viewing panel on the left shows the trianlges of the surface mesh which covers the area of the innermost part of the POI, the ROI, and the COI. The innermost region with the highest mesh density is the region inside the loop source where the refinements for receivers are made. The 3D viewing panel on the right shows the entire surface mesh and the region shown in the 2D viewing panel is concentrated in the center which can be barely seen.

of simplicity, these layers are commonly simplified into horizontal plates with regular geometry. In FacetModeller, for the plate, one only needs to define its eight corner nodes and then connect them into facets in order to get the watertight region to represent a geologically unique region. For geometrically more complex bodies such as the one shown in Figures 2.7 and 2.8, significantly more nodes need to be provided in order to better depict the complex geometry of the interfaces between different geological units. These nodes need to be eventually connected manually to form facets which form the surface of the watertight regions. If surface tessellations are available, then the amount of work needed in FacetModeller will be significantly reduced. For detailed information about how to use FacetModeller to create geometrically complex
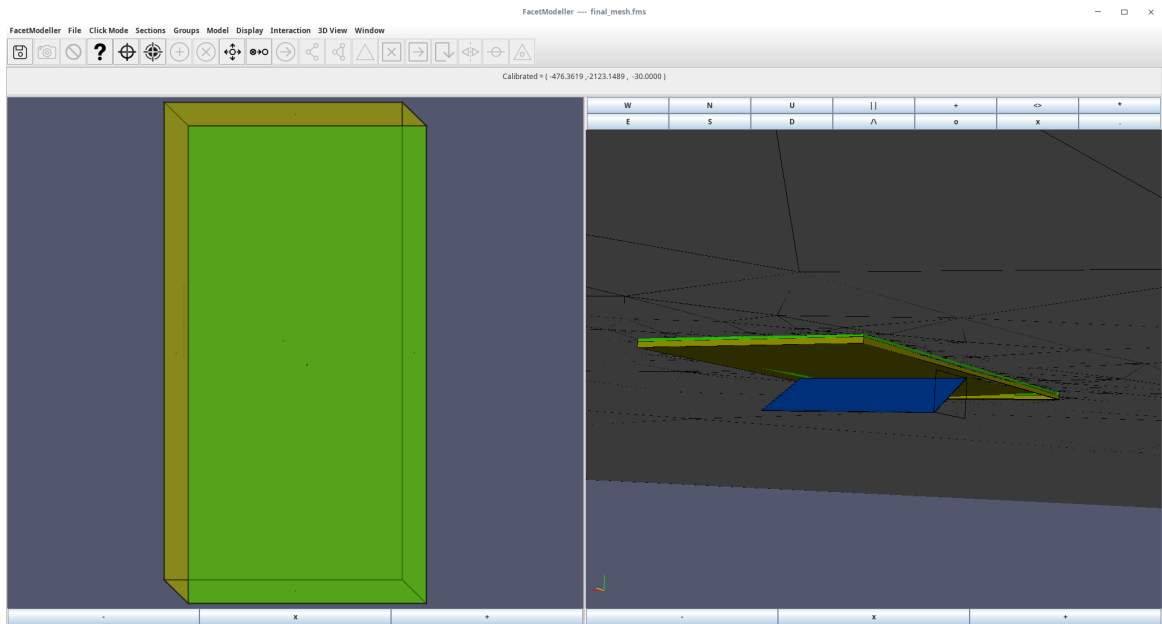
Figure 2.10: A screenshot of FacetModeller where a model representing the Athabasca graphitic conductor is shown. The 2D viewing panel (left) shows a watertight region which represent the sandstone layer (brown) below the overburden layer (green). The 3D viewing panel (right) shows the overburden and sandstone layers as well as a dipping conductor (blue).

models, the reader is referred to Lelièvre et al. (2018a).

Finally, after all watertight regions are formed in FacetModeller, the PLC can be exported to an ASCII text file which can be read in as an input for TetGen to generate the Delaunay-Voronoï dual meshes. The state of FacetModeller can also be exported and stored on the hard drive so that later the model building procedure can be quickly resumed.

2.4.3 Final mesh generation by TetGen

The PLC exported by FacetModeller and all the extra points generated in the surface mesh refinement process are the inputs for TetGen in generating the final Delaunay-Voronoï dual meshes. Beyond the measures taken in the surface mesh refinement,

43

TetGen allows one to further refine the mesh through various approaches.

The two most important constraints accepted by TetGen to control the quality of the mesh are the maximum radius-edge ratio bound and minimum dihedral angle bound. As explained in the Introduction of this thesis, the radius-edge ratio is the ratio between the radius of the circumscribed sphere of a tetrahedron and the shortest edge length in that tetrahedron, and the dihedral angle is the angle between two faces that share an edge in a tetrahedron. By enforcing a lower maximum radius-edge ratio and a higher minimum dihedral angle, TetGen can generate a mesh with higher quality. However, the number of cells would also be increased as the quality of the mesh improves, which would lead to longer computation times for the modeling. Therefore, an optimal trade-off between the mesh quality and the number of cells is important.

Besides the above two constraints, TetGen also allows one to specify a maximum volume constraint for a specific region and a maximum area constraint for a surface (described as a facet in the PLC). The maximum volume constraint is useful for regions with small volume but extraordinary physical properties. The graphitic faults in the Athabasca Basin are good examples where this constraint can be used. The fault commonly looks like a thin plate dipping with a steep angle and its conductivity can be several orders higher than that of the surrounding background rocks. If no maximum volume constraint is given, TetGen tends to generate a very course mesh for the region with a small number of cells. This would cause the modeling to give a less accurate modeling result.
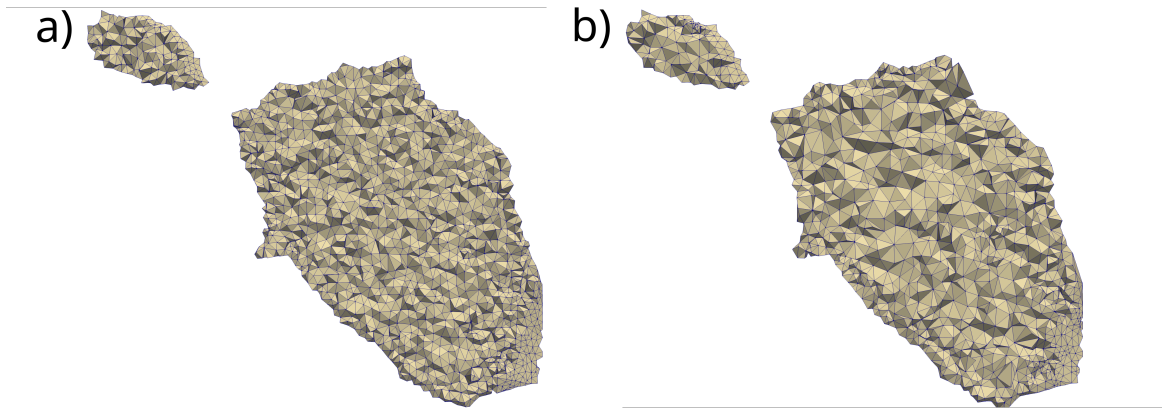
Figure 2.11: Horizontal cross sections of the mesh for the Ovoid massive sulphide ore body refined by a maximum area constraint of 50 m^2 for the facets that comprise the ore body surface, and additionally a maximum volume constraint of 200 m^3 (a) and 1000 m^3 (b), respectively, for the ore body.

The maximum area constraint for a facet can be used when the mesh quality over the surface of each region is important and the quality inside the region is not. This is true when one only wants to investigate the behaviour of the EM fields over the interfaces between different regions and the region has a round shape with a large volume. If maximum volume constraints are used for this scenario, an extremely large number of cells will be generated in the mesh and the quality of the mesh would be uniformly refined over the entire region, which is obviously unnecessary. For example, Figure 2.11 shows depth sections ($z = 20$ m) of the mesh generated by TetGen with different refinement strategies for the Ovoid model (Li et al., 2018). The facets which comprise the ore body for both panels are refined with a maximum area constraint of 50 m^2. The ore bodies in panels (a) and (b) are refined with a maximum volume constraint of 200 m^3 and 1000 m^3, respectively. Clearly, the mesh in panel (b) only tries to refine the boundary part since the maximum volume constraint is large while the mesh in panel (a) has both the boundary and interior parts well refined.

Chapter 3

Finite-volume discretization of differential operators

3.1 Introduction

The finite-volume method can be used to discretize the continuous partial differential operators such as $\nabla \times$, $\nabla \cdot$, and ∇. These partial differential operators are present in equations that were derived in Chapter 2. The concept of discrete operators are adopted. Discrete operators based on the FV method and the dual meshes are developed and described in detail in this chapter. These newly developed discrete operators are essentially matrices that, in addition to containing the information about the EM fields and how their gradients are related to one another, carry information about the mesh and physical property distributions across the mesh. These discrete operators can then be combined into a linear system of equations that is the discrete equivalent

of the Helmholtz (E-field method) or Helmholtz and conservation of charge ($A - \phi$ method) PDEs. Compared to directly discretizing PDEs, using discrete operators can improve the code reusability. Although the idea of presenting the FV discretization as discrete operators is not new, I believe, to the best of my knowledge, this is the first time that these discrete operators are presented for unstructured Delaunay-Voronoï dual meshes with the FV discretization. By solving the linear system of equations, the approximate EM fields on the edges and nodes of the mesh and at discrete time steps are obtained.

3.2 Definition of fields on the Delaunay-Voronoï meshes

As mentioned in Chapter 2, the conductivity is considered to only vary from one tetrahedral cell to the next, and be constant inside a tetrahedron. The interfaces between different regions where a physical property jump exists are comprised of tetrahedral faces. On the interface, the tangential component of the electric field is continuous and the normal component is discontinuous. Therefore it is convenient to define the electric field on the Delaunay edges so that the tangential continuity is preserved. The magnetic field is defined on the edges of the Voronoï mesh which guarantees its normal continuity across the interface (Figure 3.1).

Figure 3.2 shows an example of the Voronoï cell and the Delaunay edges corresponding to its faces. Scalar potentials are defined on the tetrahedral nodes so that
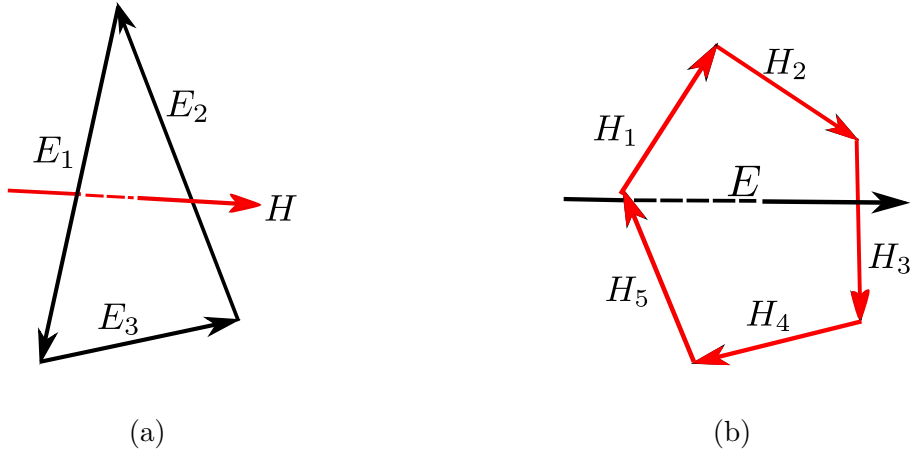
Figure 3.1: The locations where the electric and magnetic fields are defined on the Delaunay-Voronoï dual meshes (after Jahandari and Farquharson, 2014). Panel (a) shows the electric field defined on the Delaunay edges (black), and panel (b) shows the magnetic field defined on the Voronoï edges (red).

its gradient along an edge yields the electric field on that edge, which is consistent with the definition of the electric field on tetrahedral edges. The vector potential $\mathbf{A}$ is also defined on tetrahedral edges since its contribution to the electric field is just a scaling factor of itself (see Equation 2.9).

Here, n, e, f, c are used to denote the nodes, edges, faces, and cells of the dual meshes. Superscripts d and v, and subscripts i and j, are used to represent the Delaunay mesh and Voronoï mesh, respectively. The lengths, areas, and volumes of edges, faces, and cells are denoted by l, s, and ξ. When combined with different subscripts and superscripts, N is used to denote the number of nodes, edges, faces, and cells of the dual meshes.

For the discretization of the transmitting sources such as a grounded-wire source or a loop source, it is common to discretize the current density of the source rather than the current that is flowing in the wire. There are mainly two reasons for this choice.
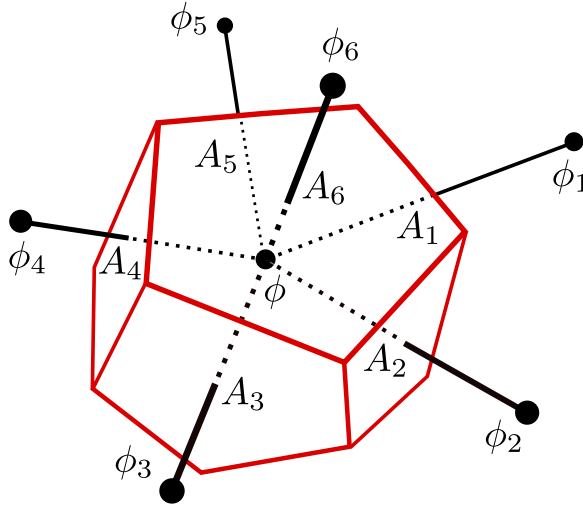
Figure 3.2: An example of a Voronoï cell and the Delaunay edges corresponding to its faces. Scalar potentials are defined on the black Delaunay nodes and vector potentials are defined on the red Delaunay edges (after Jahandari and Farquharson, 2015).

First, according to Ampère's law, the curl of the magnetic field is directly related to the current density. Second, although the current density is singular in the mesh, that is, a delta function is needed to describe the distribution of it in the mesh when the source wire is considered to be infinitely small, numerical methods such as finite-element and finite-volume only calculate the volume (FE, Ansari and Farquharson, 2014; Li et al., 2018) or area (FV, Jahandari and Farquharson, 2014; Haber et al., 2000) integral of the current density term. Thus, the difficulties involved in discretizing the singular current density term can be easily overcome. Here, following Jahandari and Farquharson (2014), the current density term is also defined on Delaunay edges.

3.3 Discretization of the curl operators

Considering Stokes' theorem, the surface integral of $\nabla \times \mathbf{E}$ over, for example, f_i^d as shown in Figure 3.1a, becomes

$$\iint_{f_i^d} \nabla \times \mathbf{E} \cdot d\mathbf{S} = \oint_{\partial f_i^d} \mathbf{E} \cdot d\mathbf{l}, \tag{3.1}$$

where ∂f_i^d is the boundary of face f_i^d. The line integral can be approximated by:

$$\oint_{\partial f_i^d} \mathbf{E} \cdot d\mathbf{l} \approx E_1 l_1^d + E_2 l_2^d + E_3 l_3^d. \tag{3.2}$$

Dividing by the area of f_i^d on both sides of Equation 3.2 leads to the matrix expression of $\mathbf{curl}_d$:

$$\mathbf{curl}_d = \boldsymbol{S}_d^{-1} \mathbf{C} \mathbf{L}_d, \tag{3.3}$$

where $\boldsymbol{S}_d = \text{diag}\{s_i^d\}$, $\mathbf{C}$ is a $N_f^d \times N_e^d$ matrix with only ± 1 on the entries corresponding to the global indices of the edges which comprise ∂f_i^d, and $\mathbf{L}_d = \text{diag}\{l_i^d\}$. Similarly, the surface integral of $\nabla \times \mathbf{H}$ over f_j^v as shown in Figure 3.1b can also be converted to a line integral:

$$\iint_{f_j^v} \nabla \times \mathbf{H} \cdot d\mathbf{S} = \oint_{\partial f_j^v} \mathbf{H} \cdot d\mathbf{l}, \tag{3.4}$$

where ∂f_j^v is the boundary of face f_j^v. Again, the line integral on the right-hand side can be approximated by

$$\oint_{\partial f_j^v} \mathbf{H} \cdot d\mathbf{l} \approx H_1 l_1^v + H_2 l_2^v + H_3 l_3^v + H_4 l_4^v + H_5 l_5^v. \tag{3.5}$$

Therefore, after dividing by the area of f_j^v on both sides of Equation 3.5, the matrix expression of $\mathbf{curl}_v$ is given by:

$$\mathbf{curl}_v = \mathbf{S}_v^{-1} \mathbf{K} \mathbf{L}_v, \tag{3.6}$$

where $\mathbf{S}_v = \mathrm{diag}\{s_j^v\}$, $\mathbf{K}$ is a $N_f^v \times N_e^v$ matrix with only ± 1 on the entries corresponding to the global indices of the edges which comprise ∂f_j^v, and $\mathbf{L}_v = \mathrm{diag}\{l_j^v\}$.

3.4 Discretization of the curl-curl operator

Now that the two operators which map functions from e^d to e_j^v and e^v to e_i^d have been constructed, it is possible to derive the discrete **curl-curl** operator corresponding to the continuous case in Equations 2.8 and 2.11. Note that in the mesh we have $N_e^d = N_f^v$ and $N_e^v = N_f^d$, thus the **curl-curl** operator can be directly obtained by multiplying the two curl operators, $\mathbf{curl}_d$ and $\mathbf{curl}_v$:

$$\nabla \times \nabla \times \approx \mathbf{curl}_v \, \mathbf{curl}_d = \mathbf{S}_v^{-1} \mathbf{K} \mathbf{L}_v \mathbf{S}_d^{-1} \mathbf{C} \mathbf{L}_d. \tag{3.7}$$

Each row of the matrix $\mathbf{curl}_v\,\mathbf{curl}_d$ only contains non-zero entries for tetrahedral edges that share common nodes with the edge whose index is the number of that row. Therefore, the edge that is orthogonal to the Voronoï face as shown in Figure 3.3 is coupled to other edges which share one common node with it.
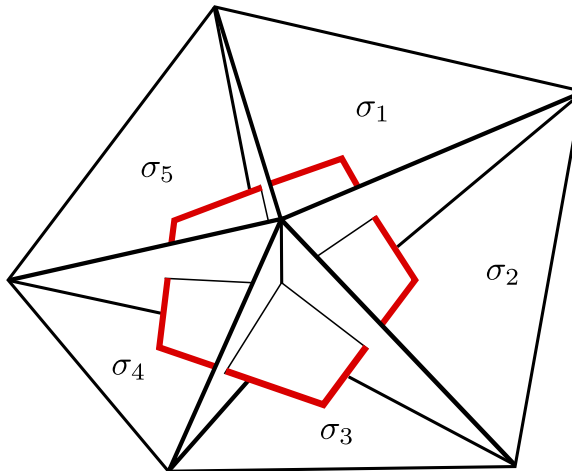
Figure 3.3: The Voronoï face (in red) and the tetrahedra (in black) related to it. The tetrahedral edge which is perpendicular to the Voronoï face is shared by the five tetrahedra. σ_1 to σ_5 are the conductivity values of the five tetrahedra. The conductivity value that is associated with the Voronoï cell can be evaluated by an area- or volume-weighted averaging method (after Jahandari and Farquharson, 2014).

3.5   Discretization of the gradient operator

The gradient of the scalar potential over a tetrahedral edge e_i^d can be approximated by:

$$\nabla\phi_{e_i^d} \approx \frac{\phi_{i_2} - \phi_{i_1}}{l_i^d}, \tag{3.8}$$

where ϕ_{i_1} and ϕ_{i_2} denote the approximate values of ϕ defined on the first and the second nodes of e_i^d. The matrix form of the discrete gradient operator is then given

by:

$$\mathbf{grad} = \mathbf{L}_d^{-1}\mathbf{G}, \tag{3.9}$$

where $\mathbf{L}_d = \mathrm{diag}\{l_i^d\}$, $\mathbf{G}$ is a matrix of size $N_e^d \times N_n^d$ and only consists of ± 1 as the non-zero entries. The first node in e_i^d corresponds to -1 while the second corresponds to 1.

3.6   Discretization of the divergence operator

The **div** operator can be obtained by integrating it over the Voronoï cell and then applying the divergence theorem. For example, the integral of $\nabla \cdot \mathbf{A}$ over a Voronoï cell c_j^v (Figure 3.2) can be calculated by:

$$\iiint_{c_j^v} \nabla \cdot \mathbf{A}\, dV = \oiint_{\partial c_j^v} \mathbf{A} \cdot \mathbf{n}dS, \tag{3.10}$$

where ∂c_j^v is the boundary of a Voronoï cell c_j^v. The surface integral can then be approximated by:

$$\oiint_{\partial c_j^v} \mathbf{A} \cdot \mathbf{n}dS \approx \sum_m A_m s_m^v. \tag{3.11}$$

The discrete operator **div** then can be derived as

$$\mathbf{div} = \mathbf{V}^{-1}\mathbf{DS}_v, \tag{3.12}$$

where $\mathbf{V} = \mathrm{diag}\{\xi_j^v\}$, $\mathbf{D}$ is a $N_c^v \times N_f^v$ matrix with only ± 1 on entries that correspond to the global indices of the Voronoï faces, and $\mathbf{S}_v = \mathrm{diag}\{s_j^v\}$.

3.7 Conductivity averaging

The coefficient σ in Equation 2.8 needs to be discretized before giving the final expression for the semi-discretizations. (See Figure 3.3 for conductivity values that are related to a Voronoï face.) In Equation 2.8, the conductivity is related to the tetrahedral edges (or Voronoï faces). However, as explained in Section 2.3, the conductivity in the mesh is associated with tetrahedral cells (see Figure 3.3). Therefore, the conductivity values of the tetrahedral cells need to be averaged in order to get the conductivity associated with the Delaunay edges.

Two methods can be used in the conductivity averaging: an area-weighted method and a volume-weighted method. Let $\mathbf{W}$ be the weighting matrix with a size of $N_e^d \times N_c^d$, then for the area-weighted method the entries of $\mathbf{W}$ can be calculated by

$$w_{mn} = \frac{\hat{a}_n^v}{a_m^v}, \tag{3.13}$$

where m and n are the row and column indices of $\mathbf{W}$, respectively, $\hat{a}_n^v$ is the area of the part of the Voronoï face that is between the two faces of the nth tetrahedron (the shaded area in Figure 3.4), and a_m^v is the area of the mth Voronoï face in the mesh. Note that the row and column indices, m and n, also correspond to the global indices
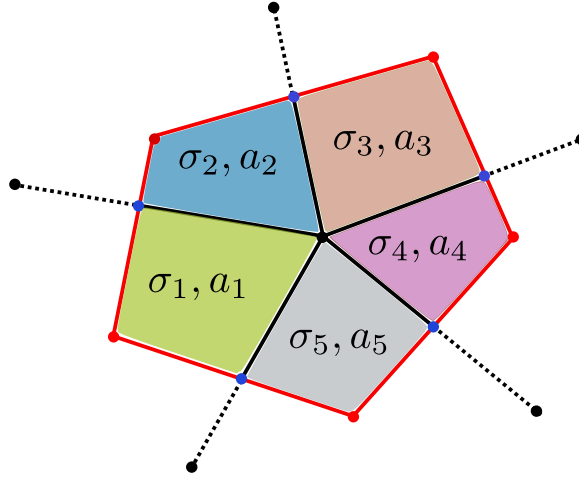
Figure 3.4: A 2D diagram showing the subareas used in calculating the weights for area-weighted conductivity. Each shaded area with a different color is the subarea which is associated with the tetrahedron enclosing it. The red dots and segments are the nodes and edges of the Voronoï face. The black segments are the intersecting segments between the Delaunay faces and the Voronoï face (see Figure 3.3). The blue dots are the intersections between the Voronoï face and the Delaunay faces. The conductivity values and the area of the shaded zones are denoted by σ_1 to σ_5 and a_1 to a_5, respectively.

of the Voronoï face and the Delaunay cells that are associated with it.

Alternatively, the entries of $\mathbf{W}$ for the volume-weighted method can be calculated by

$$w_{mn} = \frac{\hat{v}_n^d}{v_m^d}, \tag{3.14}$$

where v_m^d is the total volume of all the tetrahedra that are related to the mth Voronoï face, and $\hat{v}_n^d$ is the volume of the nth tetrahedron.

The $\mathbf{curl}_v$ operator is derived by integrating $\nabla \times \mathbf{H}$ over the Voronoï face so that the area-weighted conductivity is the method that should be used. Figure 3.4 shows an example of a Voronoï face that is cut into multiple pieces by the Delaunay faces that intersect with it when all the nodes of the Voronoï face sit in between the two faces of their corresponding tetrahedral cells. To calculate the area of each shaded

zone, the intersection between the tetrahedral edge and the Voronoï face should first be found. Then, the intersections between the Voronoï face and the tetrahedral faces as indicated by the blue dots in Figure 3.4 should be determined. The weights can then be calculated from the ratio between a_1 to a_5 and the area of the Voronoï face.

However, Figure 3.4 only shows an ideal case where the intersections between the Voronoï and Delaunay faces are all located inside the area between their corresponding Delaunay faces (between the intersecting segments in Figure 3.4). This can only happen when all the tetrahedra related to the Voronoï face are of high quality so that their circumcenters stay inside themselves. In reality, the circumcenter of a tetrahedron in the mesh are often found to be outside it, and this makes it nontrivial to find the intersections between the Voronoï face and Delaunay faces. Thus, **W** becomes very difficult to calculate for the area-weighted method. Practically, the area-weighted method is only used for those Voronoï faces with all the intersections between Delaunay faces and the Voronoï edges within the corresponding Voronoï edges. The volume-weighted method is used when any of these intersections are outside their corresponding Voronoï edges.

Through numerical experiments, it is found that for frequency-domain problems and when the receiver is far away from the source (e.g., the model shown in Figure 8 in Jahandari and Farquharson, 2014), a smoother and more accurate response can be obtained with the area-weighted method. When the volume-weighted method is used, the result is generally less smooth and less accurate. However, the effect of conductivity averaging algorithms for time-domain modeling is not as obvious as for

frequency-domain modeling, and comparisons will be presented in Section 4.5.

Chapter 4

Finite-volume modeling using the E-field method

4.1 Introduction

In the previous chapter, discrete partial differential operators were derived using the finite-volume method. In this chapter, the discrete double curl operator will be used to solve the electric field Helmholtz equation. The equation will first be discretized in space and then it will be discretized in time by time stepping. The initial and boundary conditions will also be discussed. Some of the parameters which can significantly affect the accuracy and efficiency of the method such as the distance to the truncation boundary, the mesh refinement schemes, and the time-stepping schemes are also discussed in the examples section. This work is an extension of previously developed frequency-domain methods in the literature. To the best of my knowledge,

58

this is the first application of the FV method using Delaunay-Voronoï duel meshes for solving time-domain electric field Helmholtz equation with a time-stepping method.

4.2 Semi-discretization of the Helmholtz equations

From now on, vectors with a tilde symbol will represent the discrete functions on the mesh. Substituting the discrete double curl operator into Equation 2.8 yields its semi-discretization:

$$\mathbf{curl_v}\ \mathbf{curl_d}\tilde{\boldsymbol{E}} + \mu_0 \mathbf{Q}\tilde{\boldsymbol{E}}_t = -\mu_0 \tilde{\mathbf{J}}_{s_t}, \tag{4.1}$$

where $\tilde{\boldsymbol{E}}_t$ and $\tilde{\mathbf{J}}_{\boldsymbol{s}t}$ are the temporal derivatives of the discrete electric field and source current density, respectively; $\mathbf{Q} = \mathrm{diag}\{\mathbf{W}\boldsymbol{\sigma}\}$, and $\boldsymbol{\sigma}$ is a N_c^d long vector with its entries being the conductivities of all the Delaunay cells, and $\mathbf{W}$ is the conductivity averaging weighting matrix discussed in Section 3.7.

4.3 Full discretization of the Helmholtz equations

The backward Euler method is chosen for the discretization of the temporal derivatives in Equation 4.1. The time period during which the EM field response should be calculated can be discretized using a series of time instants, $t_0, t_1, \cdots, t_{N_t-1}$, where N_t is the total number of time instants and $\Delta t_k = t_k - t_{k-1}$. The ordinary time derivatives of a function, taking $\tilde{\mathbf{E}}_t$ for example, can be approximated by (Iserles, 2009):

$$\tilde{\mathbf{E}}_t^k \approx \frac{\tilde{\mathbf{E}}^k - \tilde{\mathbf{E}}^{k-1}}{\Delta t_k}. \tag{4.2}$$

Substituting Equation 4.2 into Equation 4.1, the full discretization of Equation 2.8 can be obtained as:

$$(\Delta t_k \mathbf{curl}_v \mathbf{curl}_d + \mu_0 \mathbf{Q}) \tilde{\mathbf{E}}^k = \mu_0 \mathbf{Q} \tilde{\mathbf{E}}^{k-1} - \mu_0 \tilde{\mathbf{J}}_s^k + \mu_0 \tilde{\mathbf{J}}_s^{k-1}. \tag{4.3}$$

Equations 4.3 can now be solved iteratively with proper initial and boundary conditions.

4.4 Boundary and initial conditions

4.4.1 Boundary conditions

It is important to maintain the uniqueness of the solution to the boundary value problem by applying proper boundary conditions (Harrington, 2001). The Dirichlet boundary condition is typically used in geophysical EM modeling and it is also used here. Specifically, the tangential component of the electric field on $\partial\Omega$ is set to zero: $\mathbf{E}_\Gamma = 0$. In order to reasonably approximate the homogeneous conditions at infinity, the computational domain should be set large enough. The domain size depends on the conductivity model and also the length of time for which the secondary field is to be simulated. When the background of the model is resistive and there does not

exist a relatively large conductive region inside the model, a larger size is needed in order to get accurate responses in late times because the EM field diffuses faster in a more resistive medium. Also, the longer the time period for which the modeling is to be carried out, the larger the domain size needs to be simply because the EM fields can diffuse further away from the center given a longer time.

4.4.2 Initial conditions

The initial condition that is needed for solving the E-field Helmholtz equation depends on the type of the excitation source. The two most commonly used sources are grounded-wire (galvanic) and loop sources. For grounded-wire sources, at the time when the source is switched off, electric and magnetic fields exist. For loop sources, there only exists the magnetic field assuming that the current in the source is kept constant after it is switched on.

The DCR problem, which was described in Section 2.2.3, needs to be solved in order to obtain the initial electric field for grounded-wire sources. Using the finite-volume discrete operators **div** and **grad** developed in Chapter 3, Equation 2.15 can be discretized as

$$\textbf{div}\textbf{Q}\textbf{grad}\tilde{\phi} = \textbf{div}\tilde{\textbf{J}}_\textbf{s}. \tag{4.4}$$

Once the solution for ϕ is obtained, the electric field can be determined by calculating

the gradient of the scalar potential over each edge in the Delaunay mesh:

$$\tilde{\mathbf{E}} = \mathbf{grad}\tilde{\phi}. \tag{4.5}$$

4.4.3 Solution of the problem

Equation 4.3 can be solved iteratively to advance the solutions for the electric field in time once the initial condition is determined. For each iteration, a linear system of equations needs to be solved. The system is near-singular especially for areas where the conductivity is very small such as in the air, which poses serious difficulties for iterative solvers (Haber and Ascher, 2001; Haber et al., 2000). Therefore, direct solvers such as MUMPS (Amestoy et al., 2006) are commonly used in solving the linear systems resulting from finite-element (e.g., Um et al., 2010b; Yin et al., 2016; Li et al., 2018) or finite-volume methods (Oldenburg et al., 2013).

Generally, direct solvers solve the linear system of equations in three steps: analysis, factorization, and solve. The analysis phase analyzes the coefficient matrix and chooses pivots from the diagonal. The factorization phase factorizes the coefficient matrix based on the analysis results from the analysis phase. The solve phase computes the solution based on the right-hand sides and the factors obtained from the factorization phase. Among the three phases, the factorization usually takes the longest time, but once it is finished it can be reused as long as the coefficient matrix remains the same. This means problems with many different right-hand sides can be

solved efficiently by reusing the factorization results (Oldenburg et al., 2013). For example, the right-hand side will be updated for each iteration step when solving the TDEM problem but the factorization can still be used provided the time step remains the same from one iteration to another. The solutions can be quickly obtained from backward substitution with the factorization results and the new right-hand side. Direct solvers are robust and the solutions are accurate. Despite all these advantages, it uses larger amounts of memory compared to iterative solvers, which can restrict its applicability.

For TDEM modelings, the coefficient matrix remains the same as long as the time step is unchanged, which makes direct solvers very attractive. For the Slingram-style survey, there are multiple sources in a profile, and the factorization can also be reused for solving the responses excited by different transmitting sources if a single mesh is used to discretize the entire model. Therefore, the direct solver MUMPS (Amestoy et al., 2006) is used here to solve the linear system of equations encountered in the FVTD modeling.

The electric field changes rapidly in early times after switching off the source. Smaller time steps have to be used for early times to capture this rapid variation. For later times, the EM field changes less rapidly and larger time steps can be used. Given that the coefficient matrix will remain unchanged if the time step is not changed, the same time step would normally be used multiple times once the factorization is finished for that step. Then, the time step would be increased after a certain number of iterations have finished. Two common strategies have been used in updating time

steps. The first strategy was proposed by Um et al. (2010b) where the time step is automatically doubled when the difference in solutions from a larger time step is close to that of a smaller time step within a given threshold. A predefined number of steps will be calculated before the time step is doubled and solutions are compared. If the difference is smaller than the threshold then the doubled time step would be used for the next stage. In Li et al. (2018), a second strategy is used where the time step increases m times after n steps, that is, m and n are the time-stepping multiplier and the number of iterations for a same-sized time step, respectively.

In practice, the second strategy is more efficient compared to the first one but the accuracy can be worse depending on the values used for m and n. Moreover, for the first strategy it is hard to give a unified threshold for all the transmitter and receiver pairs (referred to as TR pairs in the remainder of this thesis) when multiple transmitters and receivers exist in the survey. Thus the second strategy is adopted here and optimal values for m and n are investigated in Section 4.5.

As explained in Section 2.4.1, the observation points are located inside tetrahedra. The solutions of Equation 4.3 are the electric fields on tetrahedral edges. The electric field and the dB/dt response at the observation points can be determined from the electric field on the edges which comprise the tetrahedra that the observation points are located in through interpolation using vector interpolation functions. Here, the first-order vector basis function defined on tetrahedral edges are used (see Jin, 2015 for details of these functions). However, the B-field responses cannot be obtained from the electric field solution directly using interpolation. One commonly used method to

obtain the magnetic field is numerically integrating the dB/dt response backward in time from the very last time step (Levy, 1984).

4.5 Examples

4.5.1 Introduction

In this section, the responses of the FVTD method developed here for different models are compared with analytic solutions and solutions from other numerical methods from the literature. Also, influences of various parameters such as the mesh quality and time-stepping schemes to the accuracy of the method will also be investigated through a series of models.

4.5.2 Initial time steps

In this section, the current in the source is switched off in an extremely short period of time in order to approximate a step-off source. As mentioned before, the time step at early times should be small in order to catch the rapid change of the electric field. Here, the current is assumed to vanish from its initial value to zero in a single step. Three different values, 10^{-8} s, 10^{-7} s, and 10^{-6} s, are used as the initial time step length in order to analyze its effect on the accuracy of the modeling.

Figures 4.1 and 4.2 show, respectively, the results of the FVTD modeling and the analytic solution for 0.1 and 0.001 S/m half-space models with a 100×100 m loop

source. The computation domain is set to $50 \times 50 \times 50$ km for the 0.1 S/m model and $200 \times 200 \times 200$ km for the 0.001 S/m model. A relatively conservative time-stepping scheme where the time step is doubled every 200 steps is used for the two half-space models to reduce the modeling errors caused by increasing time steps too fast. A detailed study of the effects of time-stepping schemes will be presented later in this chapter. The numbers of steps required for the above three initial time steps in order to cover 50 ms of secondary field simulation are 1,593, 2,245, and 2,906, respectively.

For the 0.1 S/m half-space model, the relative errors become less than 3% around 10^{-5} s after the source is turned off. The responses of the three initial time steps are close to each other except that the response generated by an initial step of 10^{-6} s has a higher relative error compared with the other two. When the conductivity of the half-space is decreased to 0.001 S/m, the responses generated by the three initial time steps become more distinctive before 10^{-4} s compared with the 0.1 S/m model. The initial time step 10^{-6} s failed to give an accurate modeling response at times earlier than 10^{-4} s after the source is switched off. Considering that many EM instrument systems have their first time channels earlier than or around 10^{-4} s, an initial time step which is smaller than 10^{-6} s should be considered when modeling such resistive models.

Although the initial time step 10^{-8} s gives the best modeling result in terms of accuracy, it requires more time to calculate the responses because more time steps are needed to cover the same period of time for the secondary field. For example, the 0.1 S/m half-space model is discretized by a mesh with 99,427 tetrahedral edges, and it
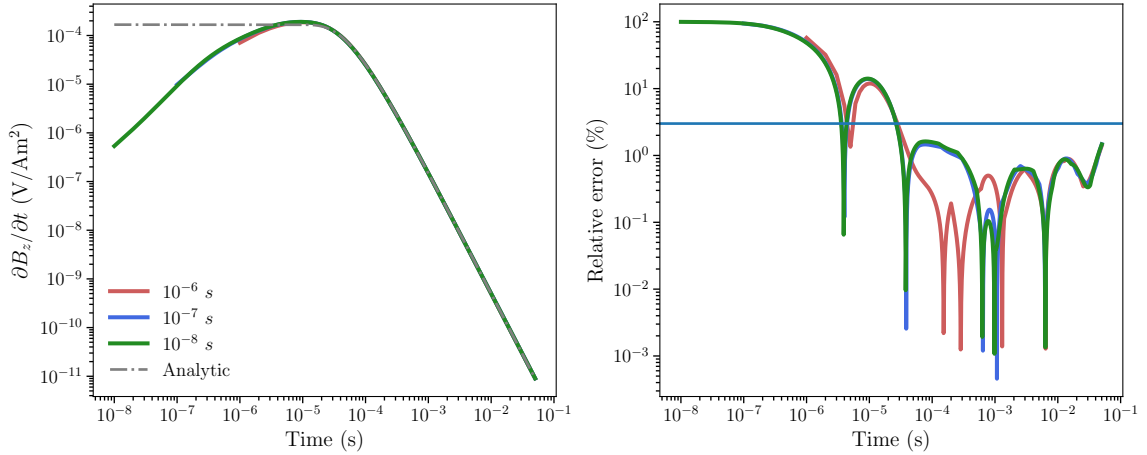
Figure 4.1: Comparison of the FVTD results for a 0.1 S/m half-space model with a 100×100 m loop source. The left panel shows the $\partial B_z/\partial t$ responses of the FVTD modeling with intial time steps of 10^{-6}, 10^{-7}, and 10^{-8} s, and the analytic solution. The right panel shows relative errors between the FVTD and the analytic solutions, with a horizontal line marking the 3% relative error.

takes approximately 301 seconds to finish the modeling on a Linux workstation with two Intel® Xeon® E5-2650 v4 12-core processors running at 2.2 GHz with 256 GB of RAM. Meanwhile, it only takes 219 s and 235 s, respectively, for initial time steps of 10^{-6} s and 10^{-7} s. Therefore, based on the above analyses, the initial time step is set to 10^{-7} s for all the modeling examples in this chapter unless otherwise stated.

4.5.3   Truncation boundaries

As mentioned before, the Dirichlet boundary condition is used for the FVTD modeling where a truncation boundary for the computational domain is set far away from the center of the mesh. In this thesis, the term truncation distance means the distance between the mesh center and the truncation boundary. For frequency-domain problems, the truncation distance is normally set to several times the skin depth for the modeling frequency (see, e.g., Ren et al., 2013; Li et al., 2017). For time-domain

67
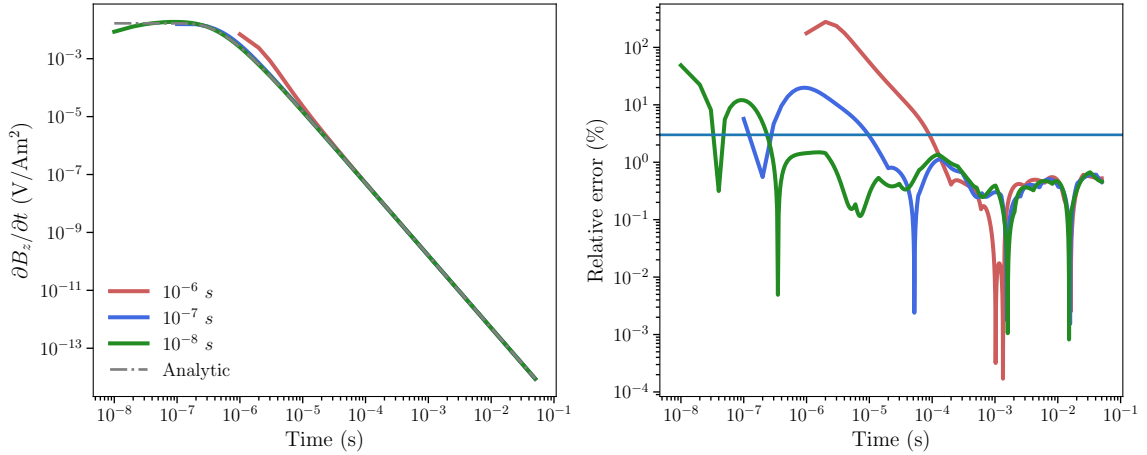
Figure 4.2: Comparison of the FVTD results for a 0.001 S/m half-space model with a 100×100 m loop source. The left panel shows the $\partial B_z / \partial t$ responses of the FVTD modeling with initial time steps of 10^{-6}, 10^{-7}, and 10^{-8} s, and the analytic solution. The right panel shows relative errors between the FVTD and the analytic solutions, with a horizontal line marking the 3% relative error.

problems, the truncation boundaries are set to 30 to 100 km away from the center of the mesh by Um et al. (2010b) for different marine time-domain controlled-source electromagnetic (TDCSEM) models. Li et al. (2018) set the truncation distance to four times the skin depth for a 1Hz EM field and achieved good accuracy in their modeling of half-space models with different conductivities. Here, the effects of the truncation boundary on various models with different background conductivities are investigated in order to find out the optimal values that can be used in general modelings.

The number of channels (or the duration of the secondary field) of data that are collected in the field are determined by the main target burial depth and the conductivity of the subsurface Earth. Normally, with deeper targets and larger background conductivities, a lower frequency transmitting waveform (a longer measurement period) and larger transmitting loop sources will be considered, and vice versa. A large transmitting loop source and a long measurement time would allow the EM fields to

diffuse further away from the source thus a larger truncation distance would be needed in order to satisfy the assumptions made for using the Dirichlet boundary condition.

Figure 4.3 shows the dB/dt responses (left panel) of three different models with different truncation distances for a 0.01 S/m half-space and the errors (right panel) relative to the analytic solution. The size of the loop is 100×100 m and the time steps are doubled every 200 steps. The modeling is carried out until 0.1 s after the source is turned off. The truncation distances are set to one, two, and three times the skin depth of a 1 Hz EM field in the model. For the reminder of this chapter, δ is used to denote the skin depth of a 1 Hz EM wave field for a given homogeneous half-space model. As can be seen in the figure, the results for the model with a truncation distance of 1 δ differ from the analytic solution noticeably at late times and the relative error reaches to almost 100 %. The models with truncation distances of 2 δ and 3 δ have responses close to the analytic solution until the end of the simulation, with the relative error of the former starting to grow above 3 % in the end. Despite the significant increase in the truncation distance from the first model to the third model, the increase in the number of tetrahedral edges in the mesh is not great. As shown in Table 4.1, for the 100×100 m loop source, the mesh size and the computation time only increase around 11 % from the first to the third model compared with a 200 % increase in the truncation distance. The relatively small increases in both mesh size and computation time can be attributed to using unstructured meshes whose cell sizes increase rapidly in areas far away from the domain center.

When a 400×400 m loop source is used, the truncation boundary needs to be at
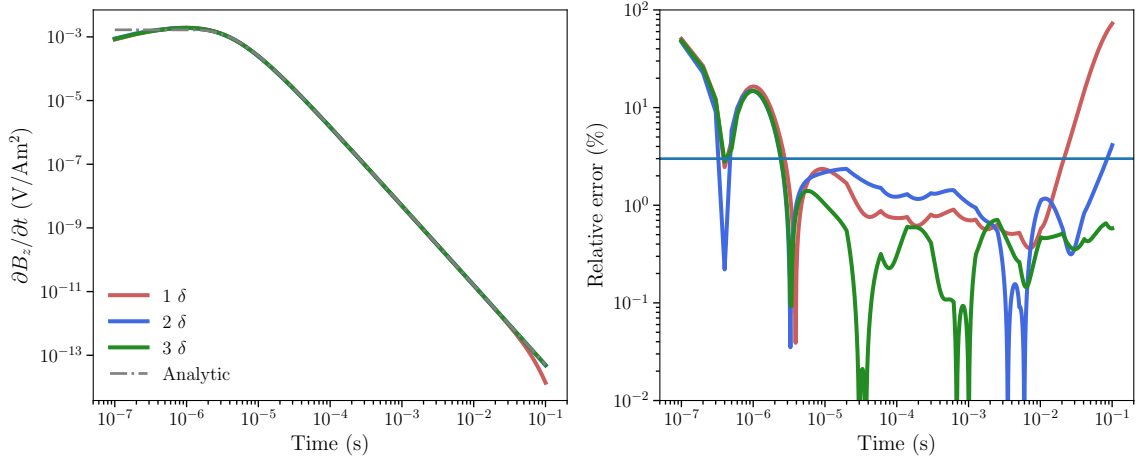
Figure 4.3: Comparison of the FVTD results for a 0.01 S/m half-space model with a 100×100 m loop source. The left panel shows the $\partial B_z/\partial t$ responses of the FVTD modeling with truncation boundaries of 1, 2, and 3 times of the skin depth of a 1 Hz EM wave, and the analytic solution. The right panel shows relative errors between the FVTD and analytic solutions, with the 3 % relative error marked by a horizontal line.

least 7 δ to get the relative error below 3 % at the latest time in the simulation (Figure 4.4). This is mainly caused by the extension of the modeled data from 0.1 s to 0.5 s after the source is turned off. The EM field has diffused further away from the source during this time so that a larger truncation boundary is needed to guarantee that the field on the domain boundary can still be treated as zero for enforcing the Dirichlet boundary condition. The increase in the loop size does not have a noticeable effect because the skin depth is considerably larger than the size of the loop source. This can also be observed from Figure 4.4 where the relative error at $t = 0.1$ s for the 3δ model is also well below 3 %. The increase in the number of edges in the mesh and the computation time from the first to the third model, as shown in Table 4.1, are 14.4 % and 16.4 %, respectively. These increases are also minor compared with the increase in the domain size from the first to the third model.

70
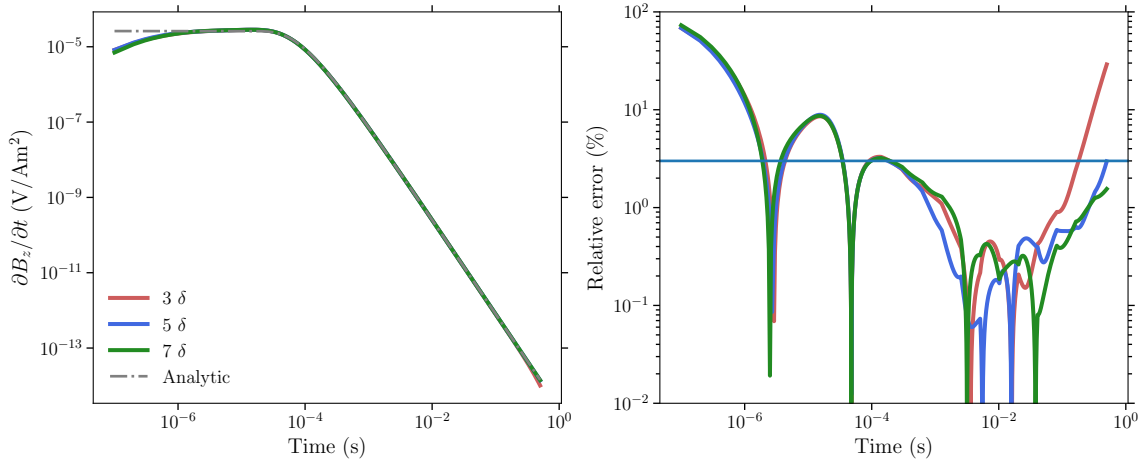
Figure 4.4: Comparison of the FVTD results for a 0.01 S/m half-space model with a 400×400 m loop source. The left panel shows the $\partial B_z / \partial t$ responses of FVTD modeling with truncation boundaries of 3, 5, and 7 times the skin depth of a 1 Hz EM wave, and the analytic solution. The right panel shows the relative errors between the FVTD and analytic solutions, with the 3 % relative error marked by a horizontal line.

For the modeling of TEM data collected in the Athabasca Basin, it is common to find models with highly resistive background. To investigate whether the conclusions obtained from the analysis of the 0.01 S/m model are applicable to models with significantly smaller conductivity, the same experiments were carried out for a 0.0002 S/m half-space model. The skin depth of the 1 Hz EM field increased from approximately 5,033 m for the 0.01 S/m half-space to 35,588 m for the 0.0002 S/m half-space. Figure 4.5 shows the comparison of the FVTD responses for models with different truncation boundaries and the analytical solution for 100×100 m and 400×400 loop sources. The results are very similar to the results shown in Figures 4.3 and 4.4, which means that the conclusions drawn for the 0.01 S/m half-space are also applicable here for the 0.0002 S/m half-space model.

Realistic models may contain localized conductors that are more conductive than

71

Table 4.1: Comparison of mesh sizes and computing efficiency for models with different truncation boundaries. The number of Delaunay edges (N_e^d) and computation time (T) only increase slightly as the truncation boundary increases.

Loop size (m)	Truncation distance (δ)	N_e^d	T (s)	N_e^d increase (%)	T increase (%)
100	1	79,480	278	-	-
100	2	86,528	301	8.8	8.3
100	3	88,890	310	11.8	11.5
400	3	138,066	579	-	-
400	5	140,056	580	1.4	0.1
400	7	158,006	674	14.4	16.4

the hosting half-space. The abrupt changing of the magnetic field caused by a rapid turn off of the loop source induces eddy currents inside these conductors. The EM fields therefore would persist longer inside the conductors compared with the half-space model and the diffusion of the EM fields thus becomes slower compared with half-space models. This means when setting the truncation boundaries for models with conductors located inside a homogeneous half-space, the truncation distances can be smaller than those determined for the homogeneous half-space models.

To verify this, a model with a vertical conductive plate inside a 0.01 S/m half-space was created and modeled. As shown in Figure 4.6, the top center of the plate is located at (0, 100, -100) m. The thickness and strike length of the plate are 40 and 1,000 m, respectively. The conductivity of the background half-space is kept at 0.01 S/m as in the model shown in Figure 4.3 while the conductivity of the plate is set to 1 S/m. Figure 4.7 shows the comparison of the plate model responses modeled by the FVTD code and the analytic solution for the half-space model and the relative
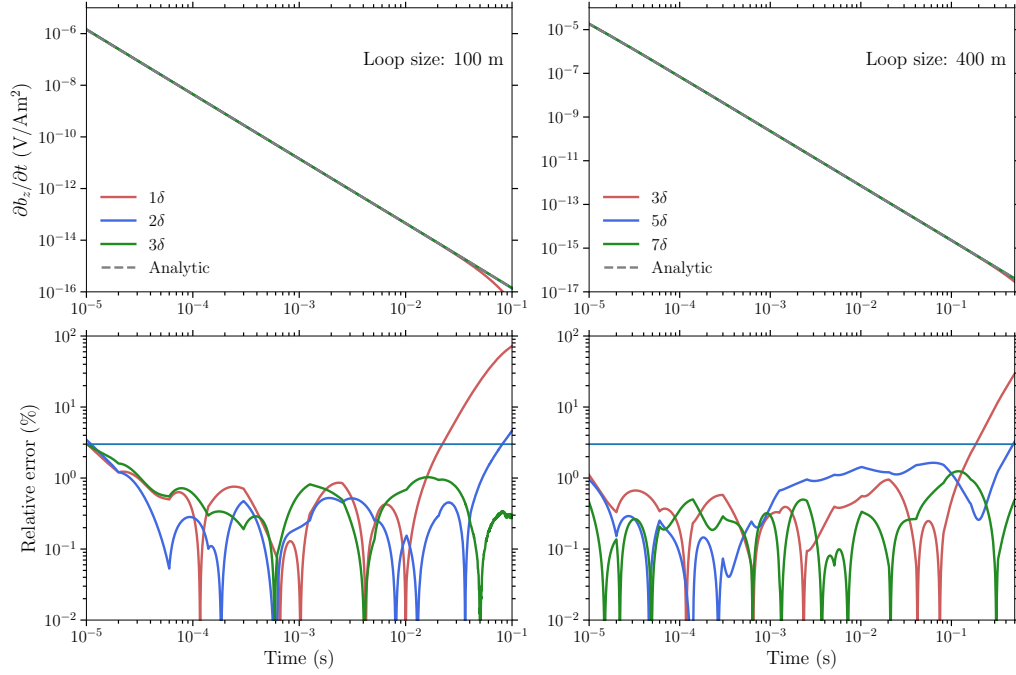
Figure 4.5: The dB/dt responses of models with different truncation boundaries for a 0.0002 S/m half-space model with 100×100 m (top left) and 400×400 m (top right) loop sources. Relative errors between the FVTD results and the analytic solutions are shown in the bottom panels.

errors between them. Due to the existence of the plate, the response of the plate model is higher than that of the analytic solution of the half-space model between approximately 5×10^{-4} s and 0.01 s. Afterwards, the 3D responses and the 1D solution coincide with each other until the very late time where the model with the shortest truncation distance is observed to have a smaller response than that of the analytic solution. At the late times, it is found that the relative error of the model with a 2δ truncation distance is smaller than that shown in Figure 4.3. Thus, it is more than sufficient to use a truncation distance of 3δ when there are regions more conductive than any background part of the model. Therefore, the skin depth of the 1 Hz EM field can be used as a good reference for setting the truncation boundaries of a model
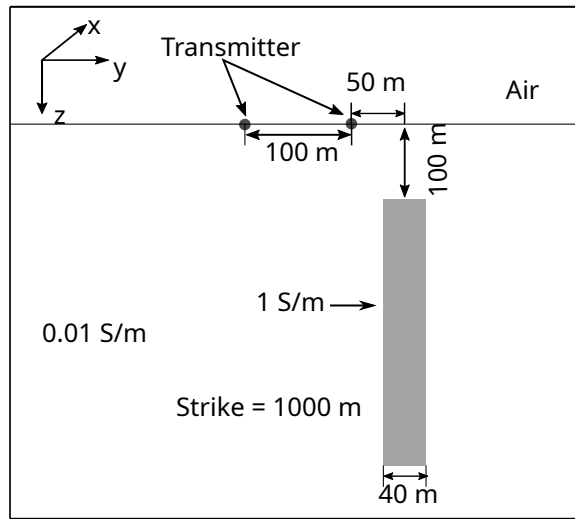
Figure 4.6: Vertical section of a model with a conductive plate buried in a homogeneous half-space. The transmitter is a 100×100 m loop source with its center located at $(0, 0, 0)$ m. The top center of the plate is located at $(0, 100, -100)$ m and the depth extension is 500 m. The thickness and the strike length of the plate are 40 and 1,000 m, respectively.

in order to get accurate responses at late times. The conclusions drawn here are used as guidelines for setting truncation boundaries for all the later modelings in this thesis.

4.5.4 Mesh quality

The quality of the unstructured mesh significantly affects the accuracy of the modeling of TEM data. By properly refining the mesh in key areas such as places where the transmitting source and receiver are located by inserting more edges and restricting the maximum radius-edge ratio and minimum dihedral angles (as discussed in Section 2.4.3) of the entire mesh, a higher accuracy of the modeling can be achieved. However, the refinement of the mesh can lead to a large number of cells in the mesh so that the modeling becomes expensive to compute. Therefore, compromises need to be made
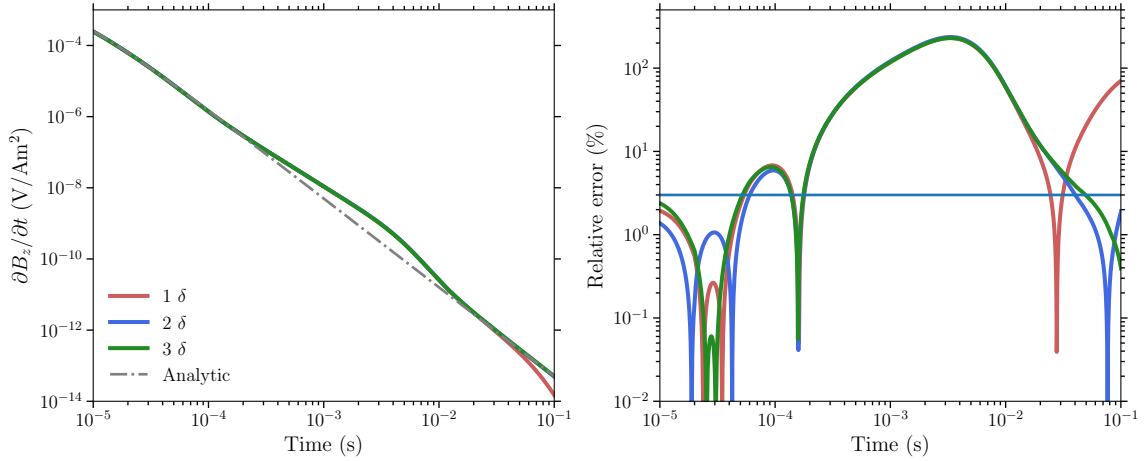
Figure 4.7: Comparison of the FVTD results for the plate model shown in Figure 4.6 and the analytic response of a 0.01 S/m homogeneous half-space model. The left panel shows the $\partial B_z/\partial t$ responses of plate model's calculated by the FVTD method and the analytic solution. The plate model's truncation boundaries are set to 1, 2, and 3 δ. The right panel shows the relative errors between the FVTD and analytic solutions, with the 3 % relative error marked by a horizontal line.

during mesh refinements. In order to better understand what kinds of refinements are necessary and what are not, an investigation on how the mesh refinement affects the accuracy of simple half-space models is presented here.

4.5.4.1 Refinement at the source

As discussed in Section 3.2, small edges are inserted in the mesh to represent the source wires for both galvanic and loop sources in the FV method. If the size of the edge is too large then fewer edges will be coupled with source edges in the coefficient matrix obtained by the FV discretization, which can potentially reduce the accuracy of the computed response. Depending on how far away the source is from the receiver, the effects of the refinement edge size can also be different. Here, half-space models with conductivity values of 0.01 S/m and 0.0002 S/m are selected for the investigation.

75

For both half-spaces, two different transmitter loops, 100×100 m and 400×400 m, are used for the models. Two observation points are considered for each loop: one is located at the center of the loop and another is located outside the loop with an offset. The second observation point corresponds to the configuration of a Slingram type survey. For models with 100×100 m and 400×400 m loops, the truncation boundary will be set to 3 δ and 7 δ, respectively.

Table 4.2 lists four refinement schemes used to refine the 100×100 m loop source, with each of the schemes having a unique combination of the inserted edge length and maximum area constraints. The edge length is the length of the tetrahedral edges that are inserted for the refinement of the source. The maximum area is the allowed maximum area for triangles inside the loop in the surface mesh. Figure 4.8 shows the comparison of the relative errors between the FVTD modeling results and the analytic solution. A larger constraint has to be used for schemes with longer source refinement edges because otherwise the connections of these edges will be destroyed by the program Triangle in order to enforce the area constraint. As shown in Figure 4.8, the four refinement schemes can all generate responses with relative errors below 3 % after a certain period of early time. For the examples shown here, these correspond roughly to the time earlier than 10^{-5} s for the central receiver and 10^{-4} s for the outside receiver (after the sign reversal). At early times, the error decreases with the inserted segment sizes as expected, and it can be seen from the decay curves that it takes longer for the modeled response to get close to the analytic solution in early times if the refinement edges are larger. This is probably caused by the fact that the

76

Table 4.2: The refinement schemes used for half-space models with a 100×100 m loop source. The schemes are characterized by different sizes of source refinement segments and maximum area constraints.

Scheme	Segment length (m)	Max. area (m^2)
1	2.5	100
2	5	100
3	10	100
4	20	250

cell sizes are larger than the dominant high-frequency EM fields' skin depth so that the mesh is incapable of catching the rapidly changing EM fields. For later times, the cell sizes are all small enough to catch the diffusive EM fields and the relative errors are all smaller than 3 %.

Generally speaking, a more refined mesh leads to a smaller relative error. However, the relative errors do not follow this pattern strictly. This might be explained by the fact that the refinement of the 3D mesh is first introduced into the 2D surface mesh and the 2D mesh is used as input information for generating the 3D mesh, and a good refinement for the 2D surface mesh may not be a good refinement for the 3D mesh. As shown in Figure 4.9, the 3D mesh (the blue triangles) on the air-Earth interface all have extra points inserted which result in extra triangles compared with the 2D mesh (red dots). The refinements for sources and receivers in the final 3D mesh, that is, the edges which comprise the source loop and the regular triangle which forms one face of a regular tetrahedron designed for the receiver refinement, are all preserved from the 2D mesh. The extra inserted points and triangles are the result of TetGen

trying to satisfy the mesh generation constraints such as the minimum dihedral angle and maximum edge-radius ratio during the generation of the 3D tetrahedral mesh while preserving the existing 2D points and edges. Unfortunately, a higher quality 2D mesh does not necessarily lead to a higher quality 3D mesh generated by the method described above, and this brings in extra complications for obtaining a high quality 3D mesh.

Table 4.3 shows that the number of tetrahedral edges and the computation time increase as smaller edges are inserted for source refinements. Although the refinement is only applied locally to the source area, it is clear that it can lead to a significant increase in the size of the mesh and consequently the computation time. The data at another observation point which is 200 m to the right (positive x) of the loop center are shown in the right panel of Figure 4.8. The responses calculated by the FVTD code are generally close to the analytic solution with comparable relative errors as for the observation point at the center of the loop. The largest error happens at the time when the response changes sign.

Depending on the receiver location where the data are collected in the field, optimal choices can be made to obtain a good accuracy of the modeling while using the mesh with the smallest number of cells. For instance, if both inside and outside receivers are used then Scheme 1 should be considered. However, if only the outside receiver is relevant like in the Slingram style survey then Scheme 4 should be used.

For the 400×400 m source, refinements using 5, 10, 20, and 40 m edges are investigated. As listed in Table 4.4, the smallest maximum area constraint used

Figure 4.8: The relative errors between the FVTD modeling results and those for the 1D analytic solution for the 0.01 S/m half-space model with a 100×100 m loop. Different refinement schemes for the source are used and the comparison for results at the center of the loop and 200 m to the positive x direction of the loop are shown in the left and right panels, respectively. The refinement schemes are detailed in Table 4.2.

Table 4.3: The number of edges (N_e) and computation times (T_c) as the mesh is more refined for the 100×100 m loop source. The refinement schemes are listed in Table 4.2.

Refinement scheme	N_e	T_c (s)	N_e increase (%)	T_c increase (%)
4	62,426	241	-	-
3	73,112	277	17.12	14.94
2	93,232	377	49.35	56.43
1	142,055	596	127.56	147.30

in refining the 2D mesh inside the loop can only be set to 250 m^2 for the 20 m refinement and 5,000 m^2 for the 40 m refinement. A smaller area constraint would break the connections of the inserted points to form an edge. However, it is possible to use smaller constraints such as 100 m^2 for the 5 m refinement. Figure 4.10 shows the relative errors of the FVTD solutions with different refinement schemes (listed in Table 4.4) compared to the analytic solution. The left panel shows the relative errors calculated for the inside receiver located at the loop center and the right panel shows
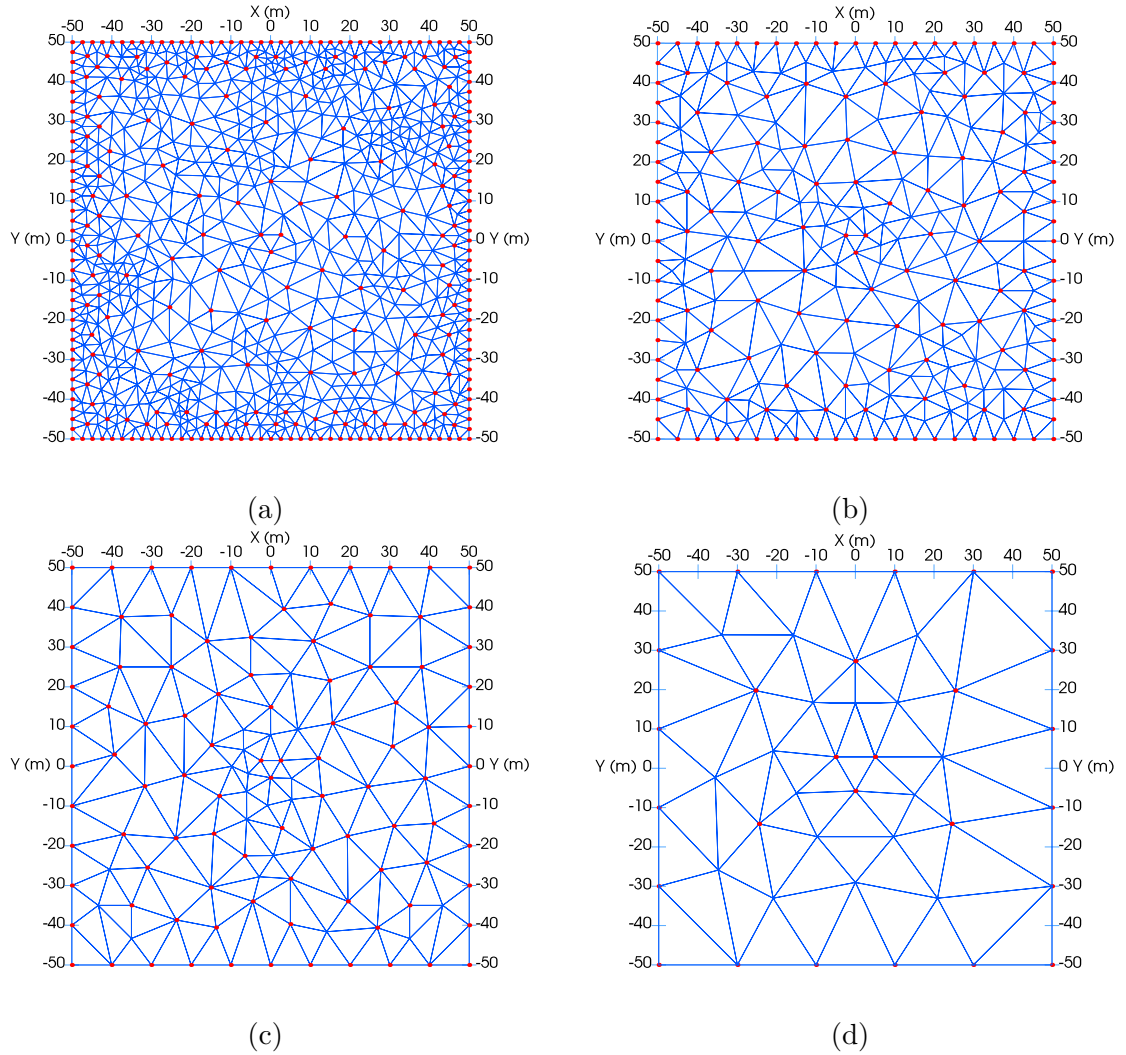
Figure 4.9: The surface mesh inside the 100×100 m loop source for different refinement schemes as listed in Table 4.2. The blue triangles are from the 3D tetrahedral mesh generated by TetGen and the red points are from the 2D triangle mesh generated by Triangle. The lengths of the refinement edges for the loop source are (a) 2.5 m, (b) 5 m, (c) 10 m, and (d) 20 m, respectively. The maximum area constraint for the 2D mesh inside the loop is 100 m^2 for panels (a), (b), and (c), and 500 m^2 for panel (d).

Table 4.4: The refinement schemes used for the 0.01 S/m half-space model with a 400×400 m loop source. Differences of the schemes lie in the length of the source refinement segments and the maximum area constraints of the 2D surface triangle mesh. Two regular tetrahedra with 5 m length edges are inserted for the refinement of the observation points.

Scheme	Segment length (m)	Max. area (m^2)
1	5	100
2	10	250
3	20	250
4	40	5,000

Table 4.5: The number of edges (N_e) in the mesh and the computation time (T_c) for models refined with different schemes for the 400×400 m loop source.

Scheme	N_e	T_c (s)	N_e increase (%)	T_c increase (%)
4	92,489	460.86	-	-
3	144,820	601.30	56.58	30.47
2	163,968	905.1	77.28	96.39
1	236,427	985.6	155.63	113.86

the relative errors of the outside receiver located at 800 m to the right of the loop center for the 0.01 S/m half-space model. Scheme 4, with the largest segments for refinements, gives the largest relative error for both receivers. The results generated by other refinement schemes are close to each other for the inside receiver while Schemes 2 and 3 seem to be giving the best results for the outside receiver. Based on the relative error values given in Figure 4.10 and the computational time listed in Table 4.5, Scheme 3 seems to be the best choice if only the outside receiver is considered.

Figure 4.10: The relative errors between the FVTD modeling results compared with the 1D analytic solution for the 0.01 S/m half-space model with a 400×400 m loop. Different refinement schemes for the source are used and the comparison for results at the center of the loop and 800 m to the positive x direction of the loop are shown in panels (a) and (b), respectively. The refinement schemes are detailed in Table 4.4.

4.5.4.2   Refinement of the observation points

In the previous subsection, only the tetrahedron with a 5 m edge length is considered for observation point refinements. Here, tetrahedra with different edge sizes are inserted to investigate how the observation point refinements affect both the accuracy of the calculated responses and the efficiency of the modeling.

First, regular tetrahedra with edge lengths of 2.5, 5, 10, and 20 m are inserted for the refinement of the observation points both inside and outside a 100×100 m loop source for the 0.01 S/m homogeneous half-space model. The length of the segments inserted for the refinement of the loop source is fixed at 10 m and the maximum area constraint for triangles inside the loop source region is 500 m^2. These numbers

are chosen in order to make sure that the shape of these regular tetrahedra can be preserved by TetGen while generating the mesh. Smaller numbers make it impossible to preserve the shape of the larger regular tetrahedra because the mesh around the source is better refined and the level of refinement tends to extend to the center of the loop source so that extra points would be inserted inside the predefined regular tetrahedron.

Figure 4.11 shows the relative errors between the dB/dt responses calculated by the 3D FVTD method and the analytic solution. The left and right panels show the relative errors of the inside and outside receivers compared to analytic solutions, respectively. Each curve corresponds to a different refinement scheme. From the figure it can be seen that the four refinement schemes give similar results for the inside receiver. For the outside receiver, the 20 m refinement scheme failed to yield accurate results around the time when the sign reversal happens but after $t = 10^{-3}$ s, the 20 m scheme can also generate results with a relative error smaller than 1 %. This implies that extremely small regular tetrahedra such as the one with an edge length of 2.5 m is unnecessary when refining the mesh for observation points but if the outside receiver is used it would be better to use regular tetrahedra with an edge length smaller than 20 m.

Table 4.6 lists five refinement schemes for the same 0.01 S/m half-space model when a 400×400 m loop source is used. The lengths of the segments used to refine the source are all 20 m except the fifth scheme. This is because if the 20 m edge is used, the shape of the regular tetrahedron intended for the refinement of the observation

83
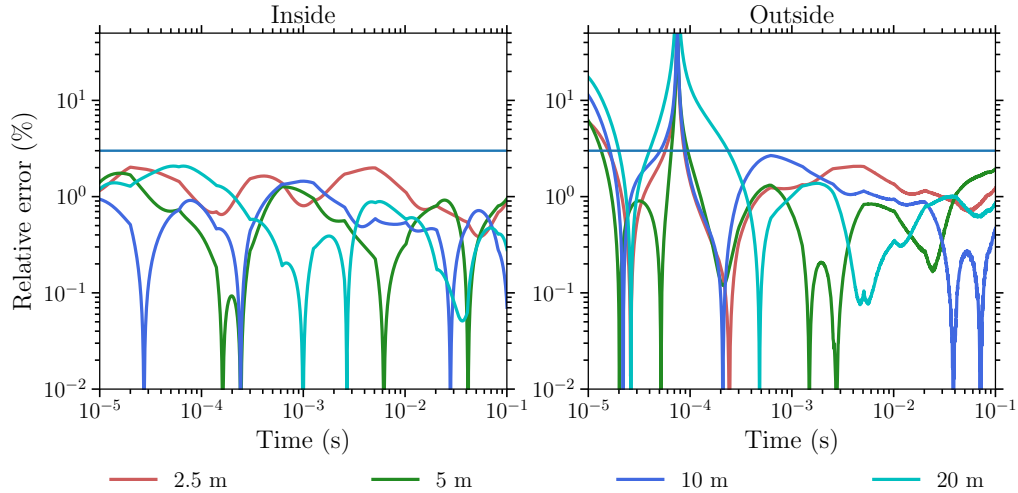
Figure 4.11: The relative errors between the FVTD modeling results and the 1D analytic solution for the 0.01 S/m half-space model with a 100×100 m loop source. Each curve corresponds to a different edge length of the regular tetrahedron inserted for the refinement of the observation point. The left and right panels show comparisons of the inside and outside receivers, respectively.

point cannot be preserved by TetGen. The maximum area constraint for triangles inside the loop region inside the 2D triangle mesh is 1,000 m^2. Figure 4.12 shows the relative errors of the dB/dt responses calculated by the FVTD method and the analytic solution. It can be seen that for the inside receiver the first four schemes are all able to yield results that have relative errors smaller than 3 % just after $t = 10^{-4}$ s. The fifth scheme failed to generate results with relative errors smaller than 3 % at times just earlier than 10^{-3} s. For the outside receiver, although the fifth scheme generates results with small relative errors that are comparable with others, it has the largest error at times just after $t = 10^{-4}$ s. Also, the fourth scheme also takes a long time to get the relative error to drop below 3 % after the sign reversal. Therefore, when 400×400 m loop sources are used, it is good to use regular tetrahedra with an

Table 4.6: The observation point refinement schemes used for the 0.01 S/m half-space model with a 400×400 m loop source. Each scheme uses a regular tetrahedron with different edge sizes for the refinement. The source segment length of Scheme 5 has to be increased to 25 m in order to maintain the shape of the regular tetrahedron for the observation point refinement.

Scheme	Edge length of obs. tet. (m)	Source segment length (m)
1	5	20
2	10	20
3	20	20
4	40	20
5	60	25

edge length smaller than or equal to 20 m for the refinement of receivers.

4.5.4.3   Constraints on maximum radius-edge ratio

All the previous tests use a small number, 1.15, as the maximum radius-edge ratio constraint for TetGen. This number is relatively conservative and normally leads to a mesh with a good quality and hence an accurate modeling result. Also, the minimum dihedral angle constraint was all set to the default value, 0, which means that no constraint on the dihedral angle was considered.

In this section, the 0.01 S/m half-space model with 100×100 m and 400×400 m loop sources will be tested again to find out optimal maximum radius-edge ratio constraints. Figure 4.13 shows the relative errors between the numerical dB/dt responses and the analytic solution for the 0.01 S/m half-space model with a 100×100 m loop source. Each curve corresponds to a unique maximum edge-radius ratio constraint. It can be seen that for the inside receiver, the largest value that can be used is $\alpha = 1.15$ and when $\alpha > 1.15$ the relative error becomes larger than 3 %, especially at earlier

Figure 4.12: The relative errors between the FVTD modeling results compared with the 1D analytic solution for the 0.01 S/m half-space model with a 400×400 m loop. Each curve corresponds to a unique refinement scheme listed in Table 4.6. The left and right panels show comparisons of the inside and outside receivers, respectively.

times. For the outside receiver, the relative errors remain under 3 % for most of the times when $\alpha \leqslant 1.2$. Table 4.7 shows that the number of edges in the mesh as well as the computational time increase steadily as α decreases from 1.25 to 1.15. A dramatic increase happens when α further decreases from 1.15 to 1.125.

Figure 4.14 shows the relative errors between the numerical dB/dt responses and

Table 4.7: The number of edges in the mesh (N_e) and the computation time (T_c) increase as the maximum radius-edge ratio decreases for the half-space model with a 100×100 m loop source.

Scheme	α	N_e	T_c (s)	N_e increase (%)	T_c increase (%)
1	1.25	25,452	100.7	-	-
2	1.2	37,130	147.4	45.88	46.38
3	1.175	46,562	172.9	82.94	71.70
4	1.15	60,171	236.8	136.41	135.15
5	1.125	110,959	453.1	335.95	349.95

Figure 4.13: The relative error between the FVTD modeling results and the 1D analytic solution for the 0.01 S/m half-space model with a 100×100 m loop. Each curve corresponds to a unique maximum edge-radius ratio constraint.

the analytic solution for the 0.01 S/m half-space models with a 400×400 m loop source. Compared to the 100×100 m loop source, the majority of the relative errors are smaller than 3 % for the inside receiver when $\alpha \leqslant 1.25$. For the outside receiver, the majority of the responses have a relative error smaller than 3 % if $\alpha \leqslant 1.3$. Table 4.8 lists the number of edges and computation times for each constraint.

4.5.4.4 Constraints on minimum dihedral angle

While investigating the maximum radius-edge ratio constraint in the previous subsection, the minimum dihedral angle constraint is set to the default value 0 which means that TetGen only focuses on refining the mesh to meet the criterion set by the maximum radius-edge ratio constraint. In this subsection, the effects of the minimum dihedral angle are investigated by fixing the maximum radius-edge ratio constraint to

87
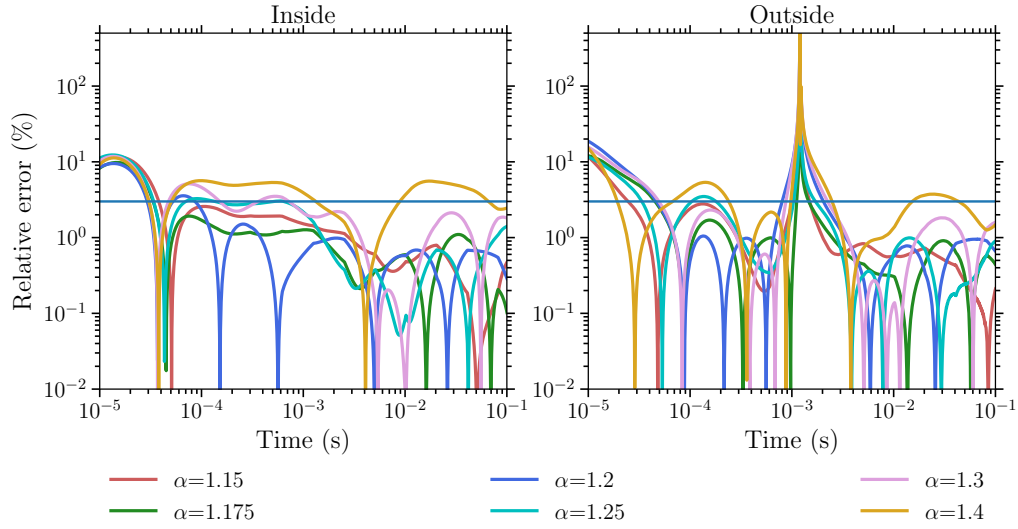
Figure 4.14: The relative errors between the FVTD modeling results and the 1D analytic solution for the 0.01 S/m half-space model with a 400×400 m loop. Each curve corresponds to a unique maximum edge-radius ratio constraint.

the default value of 2.

Figure 4.15 shows the relative errors between the FVTD results and the analytic solution for the 0.01 S/m half-space model with a 100×100 m loop source. Each curve corresponds to a unique minimum dihedral angle (β) constraint while α is fixed at 2. From the figure it can be seen that the numerical results are only accurate enough when $\beta \geqslant 18$ and meshes generated with a smaller minimum dihedral angle constraint all failed in giving responses with relative errors smaller than 3 %. The relative error is generally smaller for the outside receiver compared to the inside receiver when the same constraint is used.

Table 4.9 lists the number of edges in the mesh generated by different minimum dihedral angle constraints for the 0.01 S/m half-space model with a 100×100 m loop source. It also lists the computation time required by the FVTD modeling for each

Table 4.8: The number of edges in the mesh (N_e) and the computation time (T_c) increase as the maximum radius-edge ratio decreases for the 0.01 S/m half-space model with a 400×400 m loop source.

Scheme	α	N_e	T_c (s)	N_e increase (%)	T_c increase (%)
1	1.4	36,460	138.2	-	-
2	1.3	48,067	184.2	31.83	33.29
3	1.25	59,079	226.2	62.04	63.68
4	1.2	79,915	289.1	119.19	109.19
5	1.175	94,302	380.2	158.65	175.11
6	1.15	125,266	521.8	243.57	277.57
7	1.13	192,659	775.9	428.41	461.43

mesh. It can be seen that the increase of the edge number in a mesh is not linear to the increase of β. Once β reaches 19, the mesh size grows rapidly even just with an increase in β by 0.1. The number of edges for Scheme 5 in both Table 4.7 and Table 4.9 are very close to each other (110,959 vs 127,461) and the relative errors of their responses are also very close. However, when comparing Scheme 3 in Table 4.9 and Scheme 2 in Table 4.7, despite having similar numbers of edges, the former Scheme has the majority of the relative error below 3 %, which is better than the later Scheme.

Figure 4.16 shows the relative error of the dB/dt responses between the numerical solution and the analytic solution for the 0.01 S/m half-space model with a 400×400 m loop source. Similar to what is observed in the previous section, when the source is larger, the results are generally better, especially when large β is used. The number of edges is also rising rapidly when $\beta \geqslant 19$.

Table 4.9: The number of edges in the mesh (N_e) and computation time (T_c) for meshes generated with different maximum radius-edge ratio constraints for the 0.01 S/m half-space model with a 100×100 m loop source.

Scheme	β	N_e	T_c (s)	N_e increase (%)	T_c increase (%)
1	16	14,836	52.8	-	-
2	17	19,450	66.9	31.10	26.70
3	18	37,050	134.8	149.73	155.30
4	19	55,035	205.8	270.96	289.77
5	19.6	127,461	526.8	759.13	897.73

Table 4.10: The number of edges in the mesh (N_e) and computation time (T_c) for meshes generated with different maximum radius-edge ratio constraints for the 0.01 S/m half-space model with a 400×400 m loop source.

Scheme	β	N_e	T_c (s)	N_e increase (%)	T_c increase (%)
1	16	56,496	223.5	-	-
2	17	67,384	263.7	19.27	17.99
3	18	110,727	453.2	95.99	102.77
4	19	167,371	732.0	196.25	227.52
5	19.5	362,582	1491.4	541.78	567.29
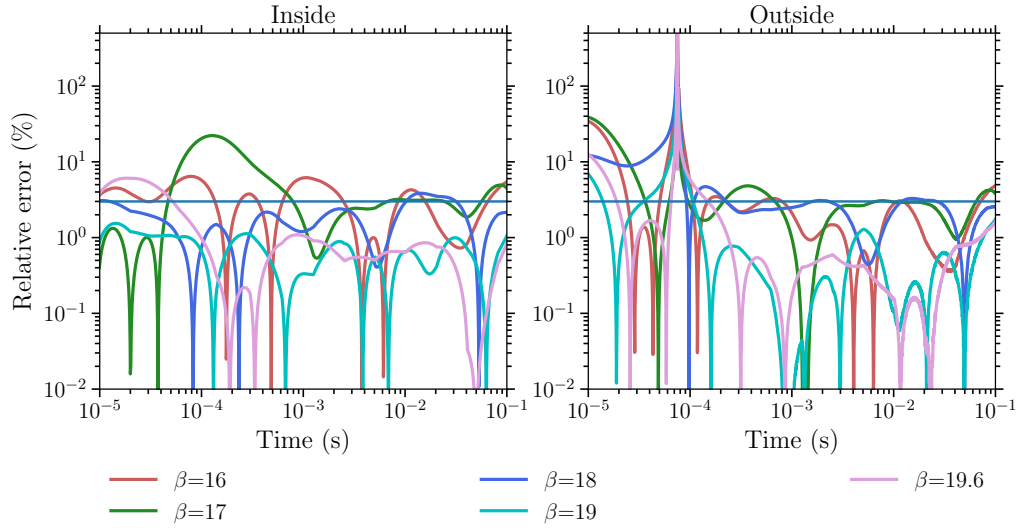
Figure 4.15: The relative error between the FVTD modeling results and the 1D analytic solution for the 0.01 S/m half-space model with a 100×100 m loop. Each curve corresponds to a unique minimum dihedral angle constraint as shown in Table 4.9. The maximum edge-radius ratio constraint is fixed to 2.

4.5.4.5 Constraints on both maximum radius-edge ratio and minimum dihedral angle

According to the previous two subsections, a good accuracy of the modeling can be achieved by constraining either α or β. Meanwhile, these two constraints can also be combined and the subsequent mesh would possess a good quality in both corresponding criteria. In this section, an investigation is carried out to find out the possible benefits of constraining α and β at the same time.

Figure 4.17 shows the relative errors between the numerical solution and the analytic solution for the 0.01 S/m half-space model with a 100×100 m loop source. Different combinations of α and β were used in generating the mesh. Edges of 5 m length were inserted for the refinement of the loop source and two regular tetrahedra

91
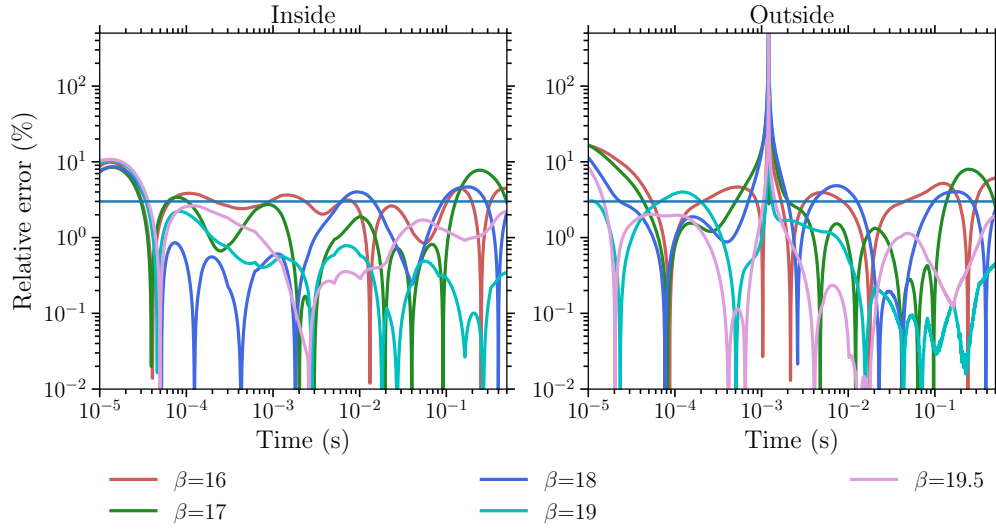
Figure 4.16: The relative errors between the FVTD modeling results and the 1D analytic solution for the 0.01 S/m half-space model with a 400×400 m loop. Each curve corresponds to a unique minimum dihedral angle constraint as shown in Table 4.10. The maximum edge-radius ratio constraint is fixed to 2.

with an edge length of 5 m were inserted for the refinement at each receiver. The maximum area constraint for areas inside the loop used in generating the 2D surface mesh was set to 100 m^2. Scheme 0 is a conservative scheme with α being set to 1.15 and β set to 0. It is used as a benchmark against which to compare all the other 16 schemes in order to get a sense of optimal combinations of α and β. Table 4.11 lists the number of edges (N_e) in the mesh generated by each scheme, the computational time (Tc), and the percentage of these two values relative to those of Scheme 0. Also, the last column concludes whether the current scheme is better than Scheme 0 in terms of both computational efficiency and accuracy. This conclusion is relatively subjective since the relative errors are smaller than 3 % for most of the schemes and they can vary from early times to late times. The main criteria used here are whether

or not the scheme can give a relative error that is smaller than 3 % for the majority of the times and whether or not the computational time is shorter than that of Scheme 0, then the current scheme is considered to be better than Scheme 0.

It can be seen, both from Figure 4.17 and Table 4.11, that it is possible for a scheme with a larger α to outperform Scheme 0 as long as a proper value is picked for β. For example, Scheme 7 generates a mesh with the number of edges only 44% of that of Scheme 0 and it only takes 37% of the time that is required for Scheme 0 to finish the modeling. However, the relative errors for both the inside and outside receiver are only larger than that of Scheme 0 at earlier times, and are smaller than 3 % for almost all the times.

When a large β is used, it is then possible to use a larger α in order to generate a mesh with a smaller number of cells while keeping the relative errors small. For example, α is set to 1.4 in Scheme 16 and it is still able to generate a response with the majority of relative errors smaller than 3 % while Scheme 12 failed to give good results for the outside receiver. For Schemes 1 to 8, even smaller α cannot give good results for the outside receiver because β is too small.
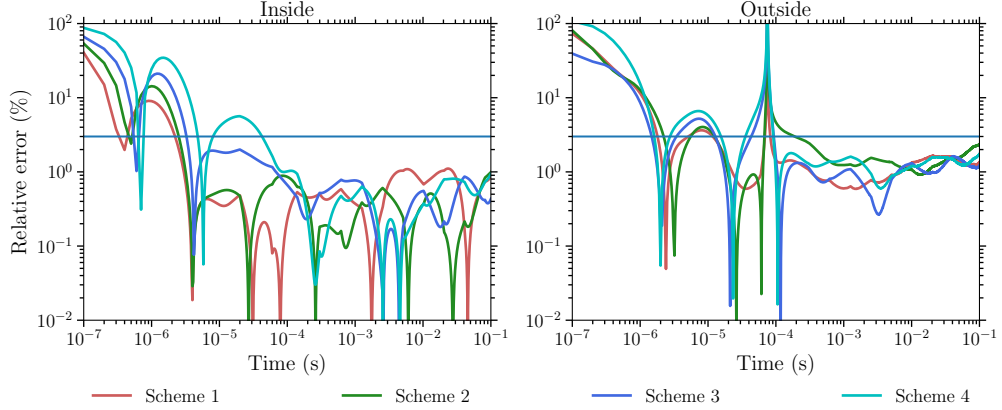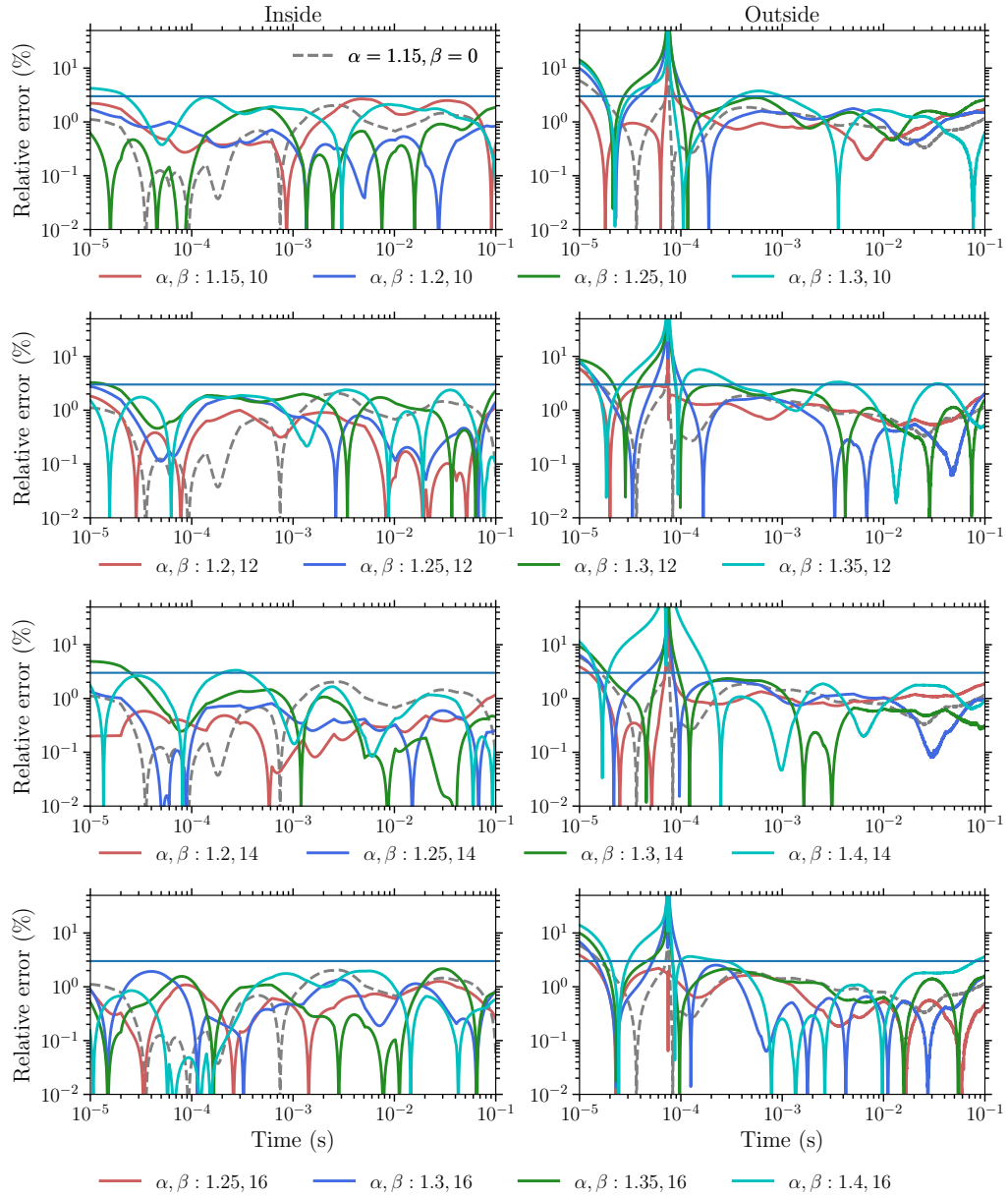
Figure 4.17: The relative errors between the FVTD modeling results and the 1D analytic solution for the 0.01 S/m half-space model with a 100×100 m loop. There are 16 combination of α and β as listed in Table 4.11 for generating the mesh using TetGen.

Figure 4.18 shows the relative errors between the numerical solutions calculated by FVTD and the analytic solution for the 0.01 S/m half-space model with a 400×400 m loop source. Again, the numerical responses are calculated using 16 different meshes

94

Table 4.11: The number of edges in the mesh (N_e), the computation time, and the percentage of their increases compared to Scheme 0 for 16 schemes with different combinations of α and β for the 0.01 S/m half-space model with a 100×100 m loop source. The last column shows whether the scheme is better than the standard one based on its efficiency and accuracy (as indicated in Figure).

Scheme	α	β	N_e	T_c (s)	N_e * (%)	T_c * (%)	Better
0	1.15	0	110,971	557.13	-	-	-
1	1.15	10	237,422	1,202.54	213.95	215.85	no
2	1.2	10	93,358	431.85	84.13	77.51	yes
3	1.25	10	54,712	261.14	49.30	46.87	yes
4	1.3	10	41,290	190.72	37.21	34.23	no
5	1.2	12	104,761	515.91	94.40	92.60	yes
6	1.25	12	64,966	295.00	58.54	52.95	yes
7	1.3	12	48,609	206.96	43.80	37.15	yes
8	1.4	12	40,897	183.86	36.85	33.00	no
9	1.2	14	245,060	1162.69	220.83	208.69	no
10	1.25	14	92,905	445.18	83.72	79.91	yes
11	1.3	14	61,632	287.90	55.54	51.68	yes
12	1.4	14	41,042	181.88	36.98	32.65	no
13	1.25	16	152,675	733.21	137.58	131.60	no
14	1.3	16	98,066	476.82	88.37	85.59	yes
15	1.35	16	68,837	313.63	62.03	56.29	yes
16	1.4	16	60,382	268.45	54.41	48.18	no

generated by 16 different combinations of α and β. Table 4.12 lists all the 16 schemes, including the corresponding number of edges of the mesh, computation times needed for the modeling, and the percentage of the number of edges and the computation times of each scheme relative to those of Scheme 0. Regular tetrahedra of 10 m edge length were used in the refinement of loop sources and observation points. The maximum area constraint for the area inside the loop was set to 250 m^2. The 16 schemes, when used for the 400×400 m loop source, behave similarly to those of the 100×100 m loop source case. Specifically, the relative error for the inside receiver at times around 10^{-4} s can briefly exceed 3 % for most of the schemes when $\beta \leqslant 12$, but it becomes smaller than 3 % when $\beta \geqslant 14$.
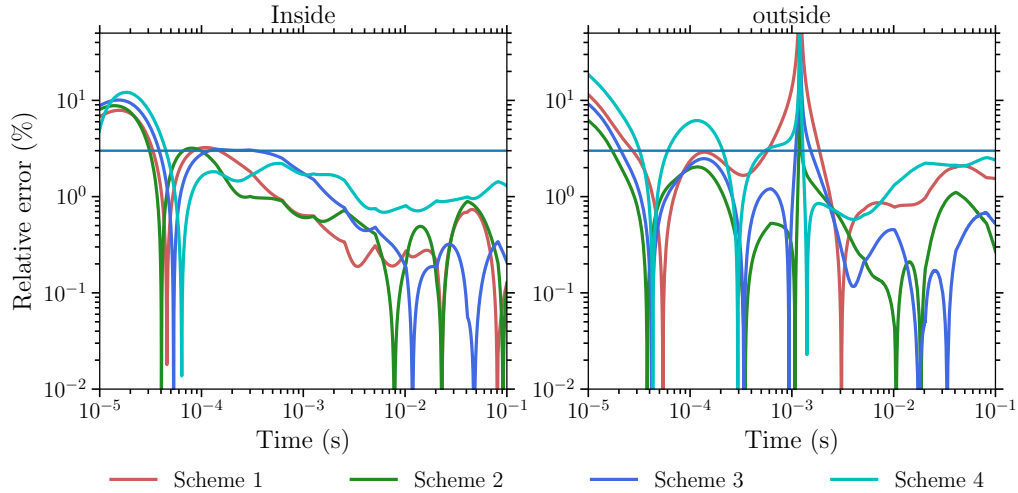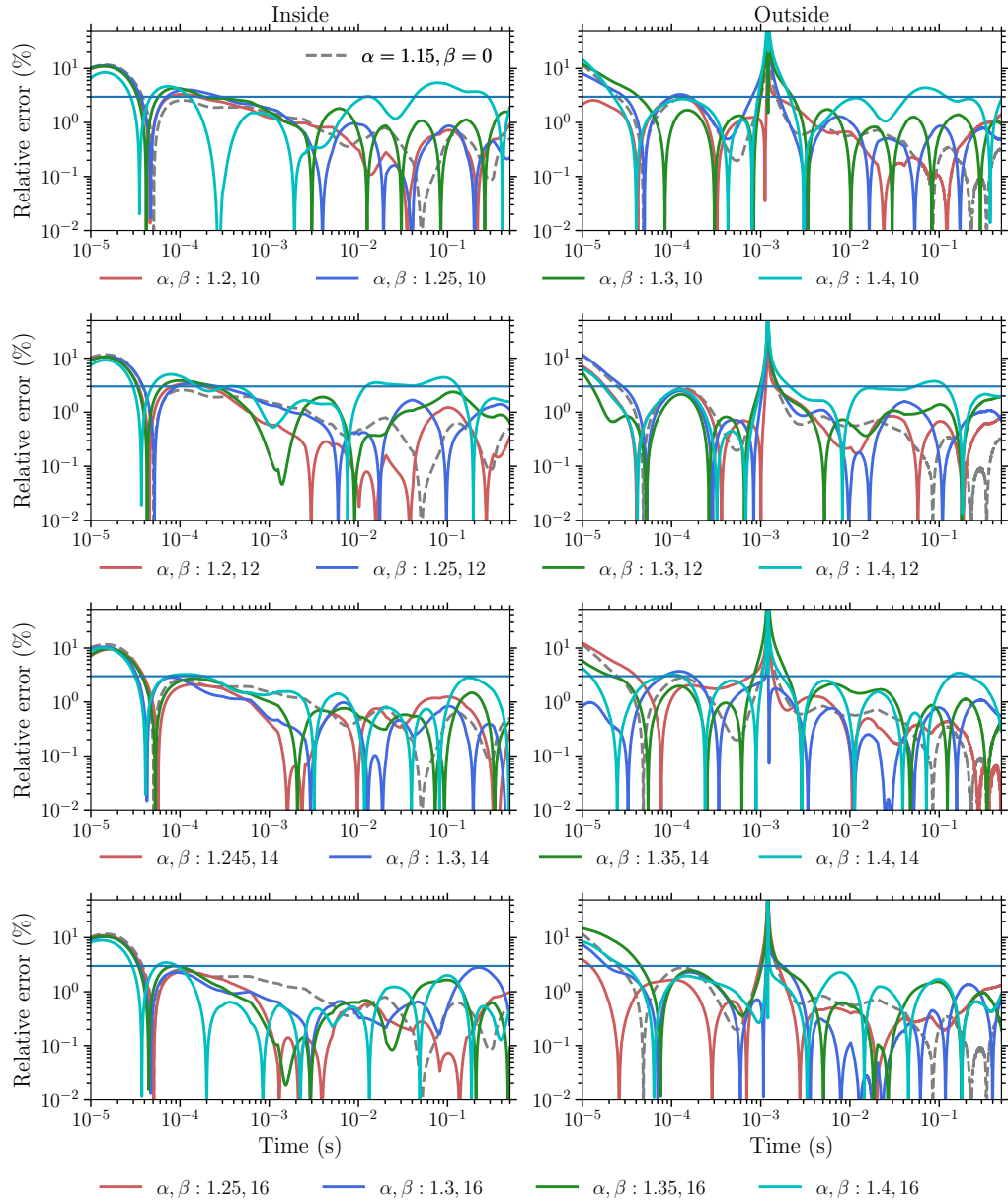
Figure 4.18: The relative error between the FVTD modeling results compared with the 1D analytic solution for the 0.01 S/m half-space model with a 400×400 m loop. There are 16 combination of α and β as listed in Table 4.12 for generating the mesh using TetGen.

It should be noted that the performance of the 16 schemes is only applicable to the mesh (source and observation points) refinements specified above which is relatively well refined. A better efficiency cannot be easily achieved by combining α and β when

97

Table 4.12: The number of edges in the mesh (N_e), the computation time, and the percentage of their increases compared to Scheme 0 for the 16 schemes with different combinations of α and β for the 0.01 S/m half-space model with a 400×400 m loop source. The last column shows whether the scheme is better than the standard one based on its efficiency and accuracy (as indicated in Figure 4.18).

Scheme	α	β	N_e	T_c (s)	N_e * (%)	T_c * (%)	Better
1	1.15	0	185,071	938.24	-	-	-
2	1.15	10	319,258	1,472.43	172.51	156.94	no
3	1.2	10	144,732	708.11	78.20	75.47	yes
4	1.25	10	107,431	509.12	58.05	54.26	yes
5	1.3	10	86,517	379.11	46.75	40.41	no
6	1.2	12	193,900	939.38	104.77	100.12	no
7	1.25	12	121,837	586.50	65.83	62.51	yes
8	1.3	12	100,247	469.83	54.17	50.08	yes
9	1.35	12	80,349	381.38	43.42	40.65	no
10	1.2	14	278,659	1,369.54	150.57	145.97	no
11	1.25	14	162,889	767.52	88.01	81.80	yes
12	1.3	14	117,287	561.63	63.37	59.86	yes
13	1.4	14	83,198	417.94	44.95	44.55	no
14	1.25	16	244,395	1,098.69	132.05	117.10	no
15	1.3	16	175,251	832.69	94.69	88.75	yes
16	1.35	16	137,400	667.49	74.24	71.14	yes
17	1.4	16	112,391	476.64	60.73	50.80	yes

the source and observation points are not well refined. Nonetheless, it is still good to generate the mesh by providing TetGen with a combination of α and β constraints which can lead to a better efficiency and a higher accuracy.

4.5.5 Time-stepping schemes

Another factor that can affect the accuracy and the efficiency of the FVTD modeling is the time-stepping scheme. Following Li et al. (2018), the time steps are increased m times every n steps, where m is the time-stepping multiplier and the n steps comprise a section within which the time step is kept unchanged. A scheme with a larger m and a smaller n leads to higher efficiency but normally lower accuracy, and vice versa. In this section, numerical experiments using half-space models will be carried out to investigate the influences of time-stepping schemes to the accuracy and efficiency of the FVTD method.

Figure 4.19 shows the relative error between the FVTD modeling results for the time-stepping schemes listed in Table 4.13 and the analytical solution for the 0.01 S/m half-space model. The number of sections and iteration steps are the minimum number required to guarantee the simulation reaches 100 ms. The loop sources used for the left and right panels are 100×100 m and 400×400 m, respectively. As can be seen from the figure, Scheme 3 gives overall the smallest relative error for both the 100×100 m loop and the 400×400 m loop while it also takes the longest time to compute (Table 4.13). Schemes 6 and 9 perform similarly to Scheme 2, with Scheme 2 being slightly more stable. Among the above three schemes, Scheme 6 takes the

99

Table 4.13: The time-stepping schemes and the corresponding computational times. The initial time step is set to 10^{-7} s. The model is a 0.01 S/m homogeneous half-space with 100×100 m and 400×400 m loop sources.

Scheme	Multiplier	# of steps per sec.	# of sections	# of iterations	T_c (100 m loop)	T_c (400 m loop)
1	2	50	15	712	62.5	186.4
2	2	100	14	1323	91.15	302.5
3	2	200	13	2445	146.5	523.4
4	4	50	8	395	29.5	110.3
5	4	100	8	728	53.6	164.3
6	4	200	7	1378	87.0	287.2
7	6	100	7	602	44.1	142.7
8	6	200	6	1089	69.6	236.5
9	6	300	6	1569	101.1	325.6

least time to finish for both sources, and Scheme 9 requires the longest time to run. Therefore, Scheme 6 should be used based on accuracy and efficiency.

Here, only one transmitter is considered which means that there will only be one right-hand side when solving the equations. Therefore, the time spent in factorization at the beginning of each section is significantly longer than the time spent in updating the right-hand side or backward substitution. However, when Slingram-style surveys are modeled, due to the large numbers of right-hand sides, the time required to update the right-hand side and to obtain solutions through backward substitution become considerably longer than the above case where only one source is considered. The proportion of time spent in factorization then becomes less significant. Consequently, schemes with a smaller number of iterations in one section which have similar accuracy levels compared to those with a larger number of iterations in one section should
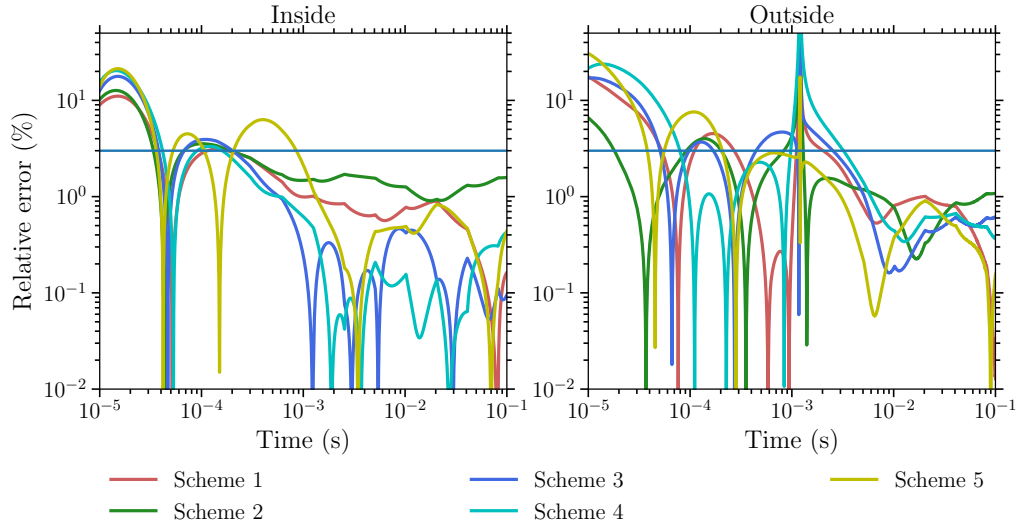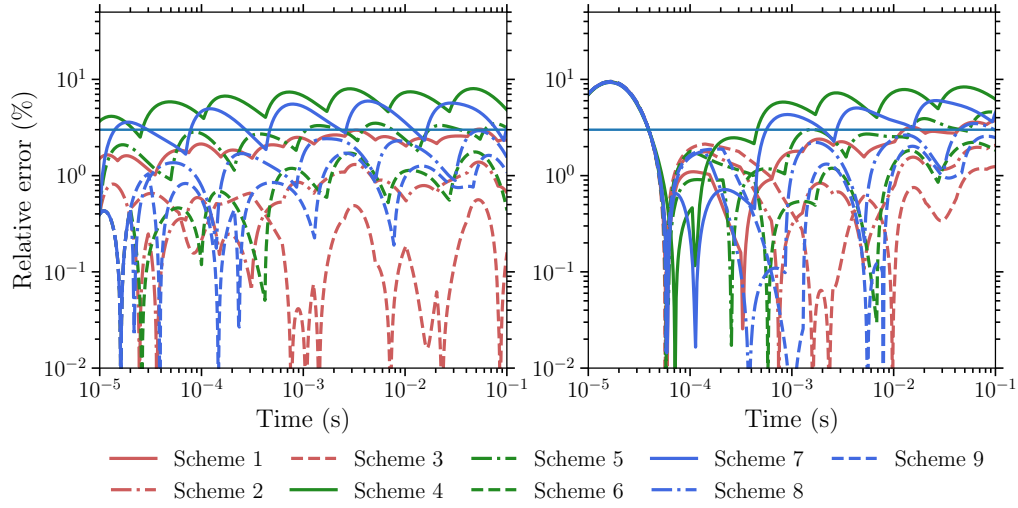
Figure 4.19: The relative errors between the FVTD modeling results and the analytic solution for the 0.01 S/m half-space with loop sources of 100×100 m and 400×400 m shown in the left and right panels, respectively. The time-stepping schemes are listed in Table 4.13.
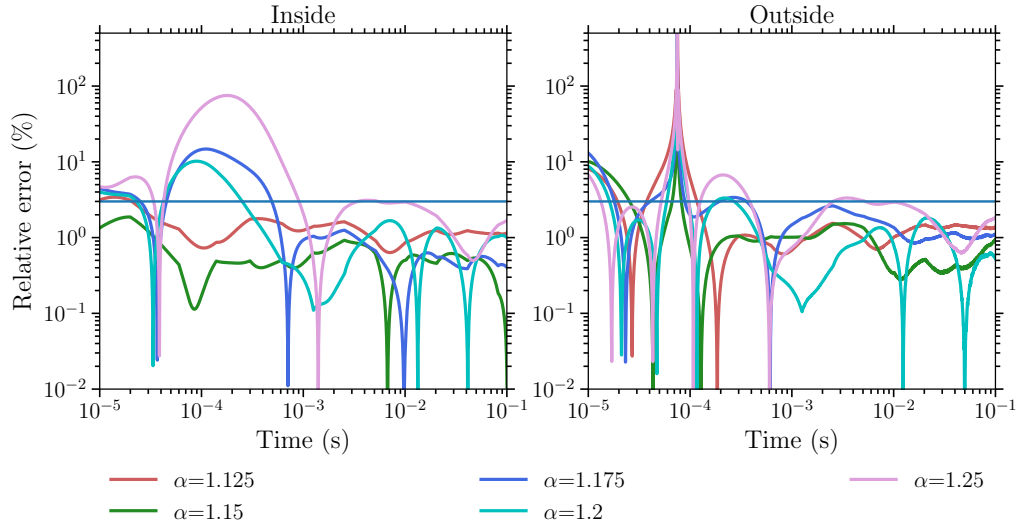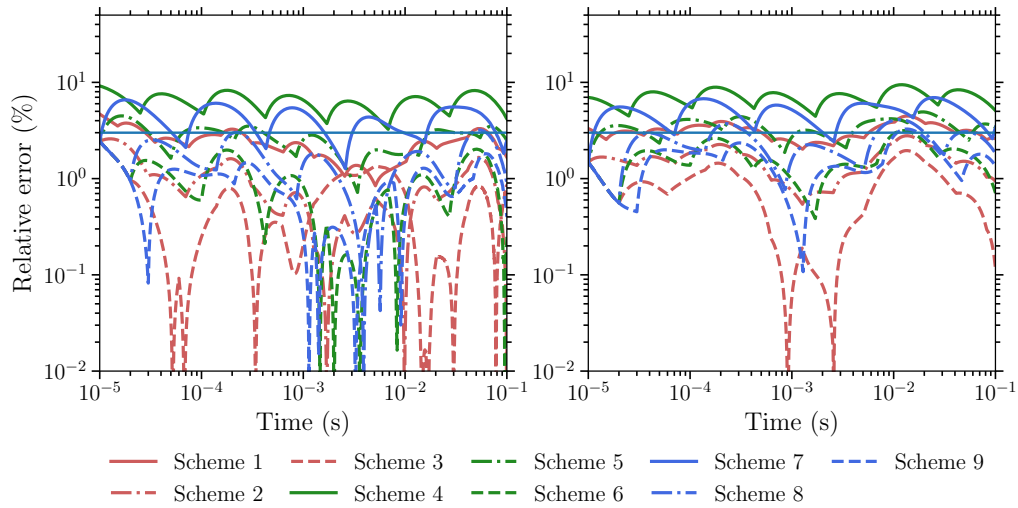

Figure 4.20: The relative errors between the FVTD modeling results and the analytic solution for the 0.0002 S/m half-space with loop sources of 100×100 m and 400×400 m shown in the left and right panels, respectively. The time-stepping schemes are listed in Table 4.13.

be preferred. For the schemes listed in Table 4.13, for modeling the Slingram-style surveys, Scheme 2 should be used to improve the efficiency.

4.5.6 A conductive block in a homogeneous halfspace

In the above sections, various factors such as truncation boundary, time-stepping schemes, and mesh quality that can affect the modeling accuracy were examined through a series of numerical modeling experiments. In this section, the responses calculated by the FVTD modeling method are compared with the results calculated by other numerical methods for a model that was first presented by Newman et al. (1986) where an IE approach was developed and used. It has since been used as a benchmark model by many authors. Here, the FVTD method is also used to calculate the response of the model and the result is compared with the results calculated by IE (Newman et al., 1986), FDTD (Wang and Hohmann, 1993) and finite-element time-domain (FETD; Li et al., 2017) codes.

As shown in Figure 4.21, this model consists of a small conductive block buried inside a relatively more resistive homogeneous half-space Earth. The transmitter is a 100×100 m square loop. The center of the 3D block is $(0, 50, 45)$ m and the block is $100 \times 40 \times 30$ m in the x-, y-, and z-directions, respectively. The conductivities of the air, background Earth, and the block are set to 10^{-8} S/m, 0.1 S/m, and 2 S/m, respectively. A receiver is placed at the center of the loop source.

Both area-weighted and volume-weighted methods were used for the conductivity averaging. It is possible for the FETD code to use the mesh designed for the FVTD code. Here, the mesh used was designed for the FVTD code and it used Scheme 2 in Table 4.2 to refine the mesh around the source and receivers. The values for α and β
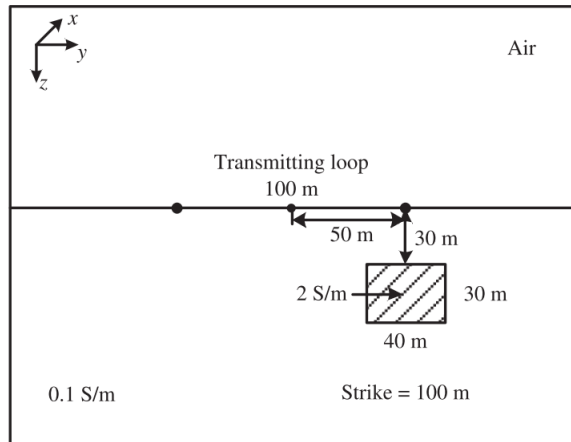
Figure 4.21: The $y - z$ section ($x = 0$ m) of the 3D block model (after Li et al., 2017).

were set to 1.19 and 10, respectively. The number of edges generated by TetGen in the mesh was 131,313.

The dB/dt responses calculated by IE (Newman et al., 1986), FDTD (Wang and Hohmann, 1993), FETD (Li et al., 2018) and the FVTD method developed here are presented in Figure 4.22. The figure also shows the relative errors between the FETD and FVTD (both volume- and area-weighted conductivity) methods. It can be seen that the solutions calculated by FVTD and FETD agree with each other very well, with the relative errors between the FVTD method and FETD method below 1%. The FDTD solution is slightly larger than the solutions for FETD and FVTD at early times but gradually becomes closer to the others as time progresses. The IE solutions are generally smaller than the FETD and FVTD solutions.
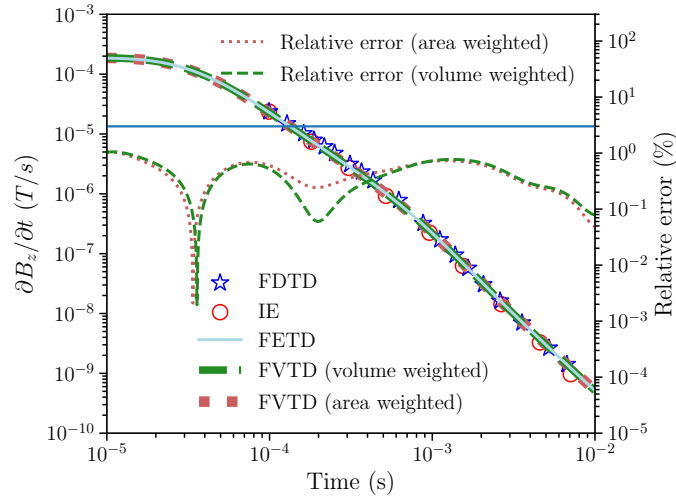
Figure 4.22: The numerical solutions for the 3D block model (Figure 4.21) calculated by the IE method (Newman et al., 1986), the FDTD method (Wang and Hohmann, 1993), the FETD method (Li et al., 2018), and the FVTD method in this paper. The relative errors between the FVTD and FETD responses are also presented.

4.5.7   A massive sulfide ore deposit model

The Ovoid massive sulfide deposit is located at Voisey's Bay, Labrador, Canada. The ore deposit itself has a complex geometry which has been well recovered by drilling data and geophysical surveys (Balch et al., 1998). The model has been used as an example for testing different methods both in the time domain (Li et al., 2017) and the frequency domain (Jahandari and Farquharson, 2014, 2015; Ansari et al., 2017). Here, it is used for the FVTD method following Li et al. (2018). Despite the fact that the shape of the ore body and the topography data were taken from field data, this model is still only a synthetic study since there exists no real TEM survey data. The geometry of the ore body is shown in panels (a) to (c) of Figure 4.23. The transmitter loop is 500×500 m, which is first laid on a flat hypothetical surface at an elevation
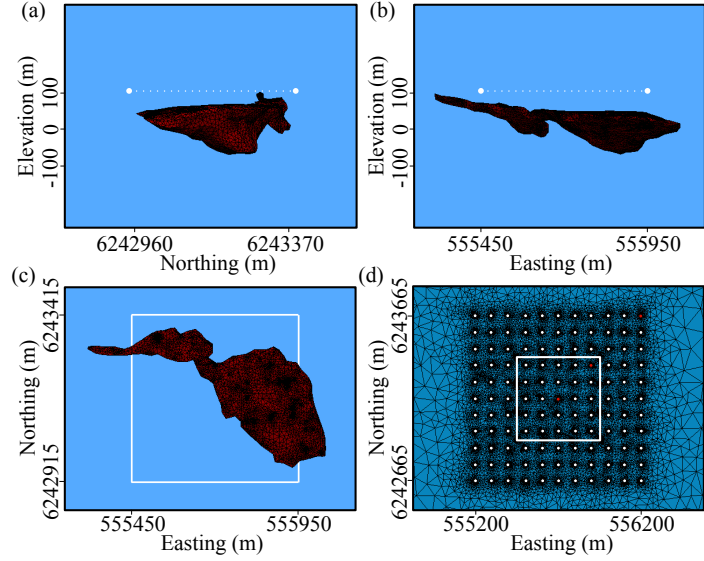
Figure 4.23: The tetrahedral grids for the Ovoid model used by Li et al. (2017). Panels (a-c) are the section views of the ore body from different directions, and panel (d) is the mesh of the air-Earth interface. The white rectangle marks the location of the 500×500 m loop source. The white and red dots represent the 121 observation points. The xy coordinates of the red dots relative to the loop center are (0, 0) m, (200, 200) m, and (500, 500) m (after Li et al., 2017).

of 110 m (Li et al., 2018). There are 121 receivers both inside and outside the loop.

The 500×500 m loop source is refined with 400 segments each with a length of 5 m. The mesh at each of the receivers is refined with two regular tetrahedra with 5 m edge length. The mesh is generated by TetGen with α and β being set to 1.2 and 10, respectively. The number of edges in the mesh is 1,220,478. The computation times for the FETD and FVTD methods were 2220.75 and 2242.82 s, respectively.

Three receivers are picked to compare the numerical solutions of the FETD method and the FVTD method developed in this thesis. Figure 4.24 shows the numerical solutions for the selected receivers. The responses from the (0, 0) m (relative to the source center, same for the following observation points) receiver match the best, and there is no sign reversal. Both the FETD and the FVTD responses of receivers (200,

105
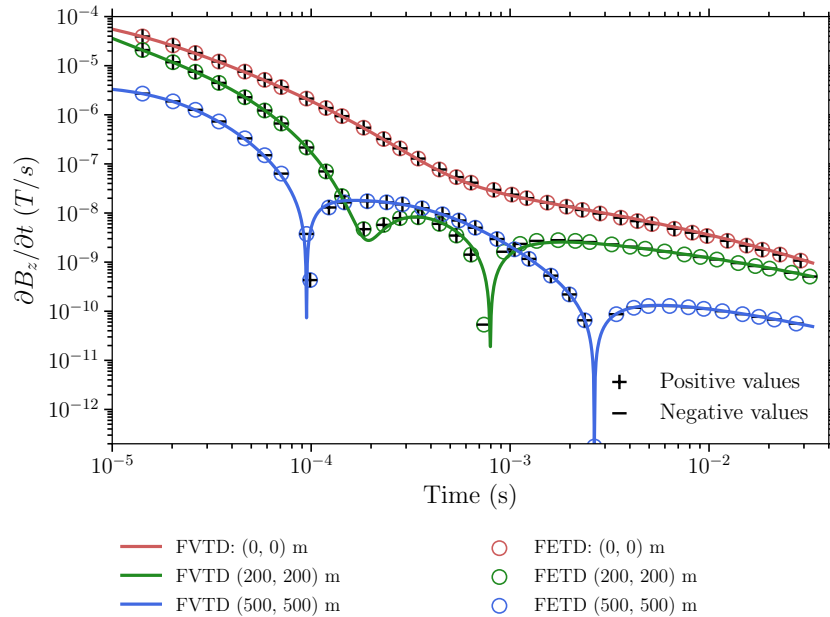
Figure 4.24: The dB/dt responses calculated by the FETD and the FVTD methods. The solid lines are responses of the FVTD method and the circles are responses of the FETD method. The responses at (200, 200) m and (500, 500) m both show sign reversal phenomena. The positive and negative responses are marked with $+$ and $-$ symbols, respectively.

200) m and (500, 500) m show sign reversals, and for the (500, 500) m receiver there are two. The most obvious discrepancies between the two numerical methods come at times close to sign reversals although generally the responses of the two numerical methods agree well with each other.

Topography data is also available over the survey area and can be incorporated easily into the modeling. Figure 4.25 shows the available elevation map over the survey area with the white rectangle representing the 500×500 m loop source. Although the loop source was laid at a relatively flat area, it sits right beside a hill which rises above the area for nearly 100 m. The topography data was interpolated and extrapolated to create a triangulated surface which represents the ground surface using the method
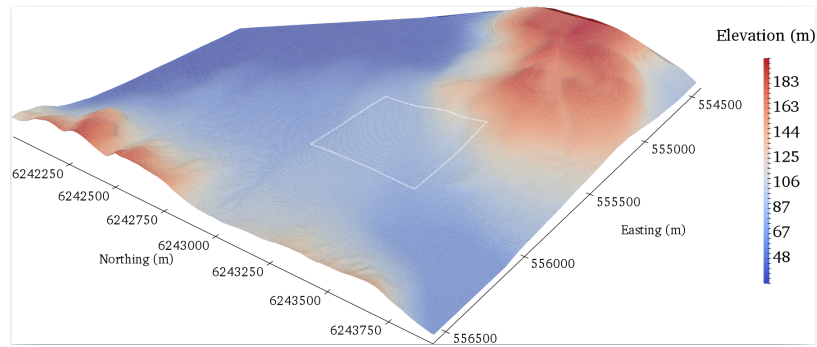
Figure 4.25: The topography over the Ovoid ore deposit site.

described in Section 2.4.1. The surface mesh generated by Triangle contains 14,079 nodes and 28,146 triangles. In order to make the modeling faster, only 11 receivers were considered for the model with topography. One hundred edges with an edge length of 5 m were inserted for the refinement at the loop source. The edge length of the tetrahedra inserted for the refinement of observation points was also 5 m. The numbers of elements and edges of the final tetrahedral mesh were 724,187 and 840,083, respectively. Note that the numbers of edges and cells are smaller than those of the flat surface model due to the reduction of the number of observation points.

The model has been used by Li et al. (2018) for a FE solver where the same topography data was used to construct the mesh. The method Li et al. (2018) used for creating the surface mesh was different from that used here. Instead of using Triangle to generate a 2D triangle mesh where refinements over certain areas are more flexible, Li et al. (2018) used a regular rectilinear surface mesh for the interpolation and extrapolation of the topography data. The mesh created with their method contained 1,873,344 tetrahedral edges, which is significantly larger than what is created using the method given in Section 2.4.1.

107
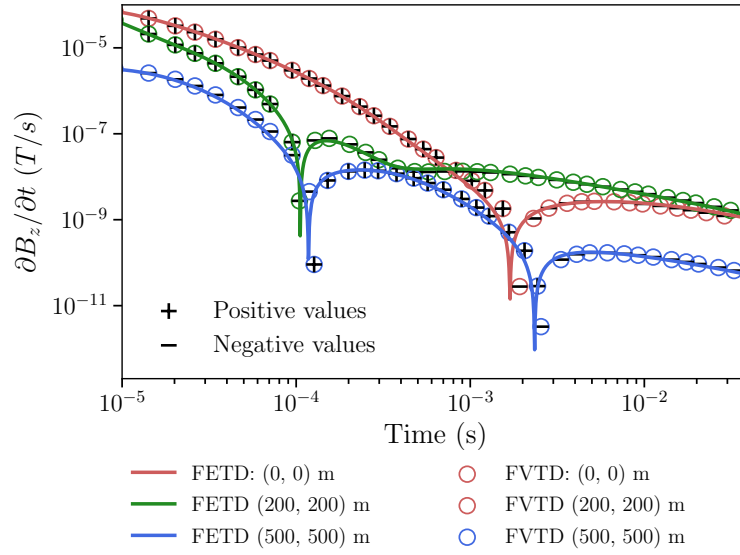
Figure 4.26: Comparison between the FVTD and the FETD results for the Ovoid model with topography.

Figure 4.26 shows the comparison between the results calculated by the E-field FVTD code presented in this chapter and the results from Li et al. (2018) for the three observation points as used in Figure 4.24. It can be seen that the two sets of results are generally very close to each other except at times where the sign reversal happens. The close match between the E-field FVTD method and the FETD method indicates that the E-field FVTD method can also be used to calculate models where topography exists. Also, the mesh generation method used here is able to generate meshes with a smaller number of cells and edges compared to the method used in Li et al. (2018) while giving comparable simulation results.

Chapter 5

Finite-volume modeling using $\mathbf{A} - \phi$ potentials

5.1 Introduction

In Chapter 4, the E-field Helmholtz equation was solved successfully using the FV method. However, as described in Section 2.2.2, it is also possible to express the EM fields in terms of $\mathbf{A} - \phi$ potentials and consequently the Helmholtz equation can also be expressed in terms of $\mathbf{A} - \phi$ potentials. Together with the conservation law of charge, solutions for $\mathbf{A} - \phi$ potentials can be calculated. Then the EM field solution can be derived from the potential solutions. The galvanic and inductive parts of the electric field are available from the computed potentials when the $A - \phi$ method is used. In this chapter, the FV method developed in Chapter 3 will be applied to solving the Helmholtz equation expressed by $\mathbf{A} - \phi$ potentials.

5.2 Gauge conditions

As given in Chapter 2 Section 2.2, the equations that need to be solved when using the $\mathbf{A} - \phi$ potentials are

$$\nabla \times \nabla \times \mathbf{A} + \mu_0 \sigma (\frac{\partial \mathbf{A}}{\partial t} + \nabla \phi) = \mu_0 \mathbf{J}_s, \tag{5.1a}$$

$$\nabla \cdot \sigma (\frac{\partial \mathbf{A}}{\partial t} + \nabla \phi) = \nabla \cdot \mathbf{J}_s. \tag{5.1b}$$

Solving the above system does not yield unique potential solutions although unique solutions of $\mathbf{E}$ and $\mathbf{H}$ can be derived from the $\mathbf{A} - \phi$ solutions (Jahandari and Farquharson, 2015; Ansari et al., 2017). To get unique solutions of $\mathbf{A}$ and ϕ, one must make sure that the vector potential $\mathbf{A}$ is gauged properly (Ward and Hohmann, 1988). For reasons discussed in Chapter 1, the Coulomb gauge is considered here. Two different methods are used to enforce the Coulomb gauge condition in the system in Equation 5.1. First, the Coulomb gauge can be enforced implicitly by adding $-\nabla(\nabla \cdot \mathbf{A})$ to the left-hand side of Equation 5.1a, which gives

$$\nabla \times \nabla \times \mathbf{A} - \nabla(\nabla \cdot \mathbf{A}) + \mu_0 \sigma (\frac{\partial \mathbf{A}}{\partial t} + \nabla \phi) = \mu_0 \mathbf{J}_s. \tag{5.2}$$

Taking the divergence of Equation 5.2 and considering Equation 5.1b gives

$$\nabla^2 (\nabla \cdot \mathbf{A}) = 0. \tag{5.3}$$

Equation 5.3 indicates that, as explained in Jahandari and Farquharson (2015), if $\nabla \cdot \mathbf{A}$ is zero on the boundary of our computational domain, then the Coulomb gauge condition holds everywhere inside the domain. As will be discussed later in Section 5.4, $\nabla \cdot \mathbf{A}$ will be zero when the homogeneous Dirichlet boundary condition is used. Thus, the Coulomb gauge condition holds everywhere in our computational domain if Equation 5.1 is solved.

Another method of enforcing the Coulomb gauge condition has been investigated by Ansari et al. (2017) for solving frequency-domain EM problems using FE methods. The method adds the Coulomb gauge term as a third equation to Equation 5.1 and also adds the gradient of the Lagrange multiplier into Equation 5.1a:

$$\nabla \times \nabla \times \mathbf{A} + \mu_0 \sigma (\frac{\partial \mathbf{A}}{\partial t} + \nabla \phi) + \nabla \lambda = \mu_0 \mathbf{J}_s, \tag{5.4a}$$

$$\nabla \cdot \sigma (\frac{\partial \mathbf{A}}{\partial t} + \nabla \phi) = \nabla \cdot \mathbf{J}_s, \tag{5.4b}$$

$$\nabla \cdot \mathbf{A} = 0. \tag{5.4c}$$

Since the Coulomb gauge condition is explicitly introduced into Equation 5.4, it will hold everywhere in our computational domain once Equation 5.4 is solved. Note that the introduction of λ is just for having enough unknowns so that the three equations in Equation 5.1a can be solved, and nothing in particular is done to analyze the value of λ.

5.3 Semi- and full discretizations

Let $\tilde{\mathbf{A}}$, $\tilde{\phi}$, $\tilde{\boldsymbol{\lambda}}$, and $\tilde{\mathbf{J}}_s$ represent the discrete fields defined on the Delaunay edges and nodes. Using the discrete operators developed in Chapter 3, the semi-discretization of Equation 5.4 can be written as

$$\mathbf{curl_v}\mathbf{curl_d}\tilde{\mathbf{A}} + \mu_0\mathbf{Q}(\tilde{\mathbf{A}}_t + \mathbf{grad}\tilde{\phi}) + \mathbf{grad}\tilde{\boldsymbol{\lambda}} = \mu_0\tilde{\mathbf{J}}_s, \tag{5.5a}$$

$$\mathbf{div}\mathbf{Q}(\tilde{\mathbf{A}}_t + \mathbf{grad}\tilde{\phi}) = \mathbf{div}\tilde{\mathbf{J}}_s, \tag{5.5b}$$

$$\mathbf{div}\tilde{\mathbf{A}} = 0, \tag{5.5c}$$

where $\tilde{\mathbf{A}}_t = \dfrac{d\tilde{\mathbf{A}}}{dt}$. Similarly, the semi-discretization of Equation 5.2 can be written as

$$\mathbf{curl_v}\mathbf{curl_d}\tilde{\mathbf{A}} - \mathbf{grad\ div A} + \mu_0\mathbf{Q}(\tilde{\mathbf{A}}_t + \mathbf{grad}\tilde{\phi}) = \mu_0\tilde{\mathbf{J}}_s, \tag{5.6a}$$

$$\mathbf{div}\mathbf{Q}(\tilde{\mathbf{A}}_t + \mathbf{grad}\tilde{\phi}) = \mathbf{div}\tilde{\mathbf{J}}_s. \tag{5.6b}$$

As in Chapter 4, the first-order backward Euler method is used to discretize $\tilde{\mathbf{A}}_t$. Therefore, Equation 5.5 changes to

$$\left(\frac{\Delta t_k}{\mu_0}\mathbf{curl_v}\mathbf{curl_d} + \mathbf{Q}\right)\tilde{\mathbf{A}}^k + \Delta t_k\mathbf{Q}\mathbf{grad}\phi^k + \frac{\Delta t_k}{\mu_0}\mathbf{grad}\boldsymbol{\lambda}^k = \mathbf{Q}\tilde{\mathbf{A}}^{k-1} + \Delta t_k\tilde{\mathbf{J}}_s^k, \tag{5.7a}$$

$$\mathbf{div}\mathbf{Q}(\tilde{\mathbf{A}}^k + \Delta t_k\mathbf{grad}\tilde{\phi}^k) = \mathbf{div}(\mathbf{Q}\tilde{\mathbf{A}}^{k-1} + \Delta t_k\tilde{\mathbf{J}}_s^k), \tag{5.7b}$$

112

$$\mathbf{div}\tilde{\mathbf{A}}^k = 0, \tag{5.7c}$$

where Δt_k is the time step used for the k th iteration. Similarly, Equation 5.6 becomes

$$\Big(\frac{\Delta t_k}{\mu_0}(\mathbf{curl}_v\mathbf{curl}_d - \mathbf{grad\ div}) + \mathbf{Q}\Big)\tilde{\mathbf{A}}^k + \Delta t_k\mathbf{Qgrad}\phi^k = \mathbf{Q}\tilde{\mathbf{A}}^{k-1} + \Delta t_k\tilde{\mathbf{J}}^k_s, \tag{5.8a}$$

$$\mathbf{div}\mathbf{Q}(\tilde{\mathbf{A}}^k + \Delta t_k\mathbf{grad}\tilde{\phi}^k) = \mathbf{div}(\mathbf{Q}\tilde{\mathbf{A}}^{k-1} + \Delta t_k\tilde{\mathbf{J}}^k_s). \tag{5.8b}$$

5.4 Boundary and initial conditions

EM fields and potentials would be vanishingly small at the boundary far enough from the center of the mesh since they are all caused by the source in the center of the mesh. Thus, like the E-field method, the homogeneous Dirichlet boundary conditions for both potentials are chosen. Specifically, $(\mathbf{n} \times \mathbf{A})_\Gamma = 0$ and $\phi_\Gamma = 0$, where Γ represents the outer boundary of the computational domain. Also, following Ansari et al. (2017), the same boundary condition is also used for λ.

The vector potential field exists for both galvanic and loop sources before the current in the transmitter loop is turned off. As indicated by both Equation 5.7 and 5.8, the solutions for the vector potential field should be calculated and used as part of the initial condition. The solutions for the initial value of the vector potential can be obtained by solving the MMR problem as discussed in Section 2.2.4. For galvanic sources, the solution has to be calculated numerically but for the loop sources it is

possible to calculate it analytically.

When loop sources are used, the electric field only exists in the source wires and therefore the MMR problem becomes the magnetostatic problem and Equation 2.16 becomes

$$\nabla \times \nabla \times \mathbf{A} = \mu_0 \mathbf{J}_s. \tag{5.9}$$

Considering the Coulomb gauge, $\nabla \cdot \mathbf{A} = 0$, and also considering the vector calculus identity, $-\nabla(\nabla \cdot \mathbf{A}) + \nabla \times (\nabla \times \mathbf{A}) = -\nabla^2\mathbf{A}$, Equation 5.9 becomes

$$-\nabla^2\mathbf{A} = \mu_0 \mathbf{J}_s. \tag{5.10}$$

For a given current distribution at location $\mathbf{r}'$, the solution of the vector potential caused by the current distribution at the observation point $\mathbf{r}$ is (Feynman et al., 2010)

$$\mathbf{A}(\mathbf{r}) = \frac{\mu_0}{4\pi} \iiint_V \frac{\mathbf{J}_s(\mathbf{r}')}{|\mathbf{r} - \mathbf{r}'|} dV. \tag{5.11}$$

By integrating over the entire source wire, the solution of $\mathbf{A}$ can be calculated analytically at any given observation point. The calculation of the analytic solution can take a long time to finish especially when the number of edges in the mesh is large. This is because the source wires need to be divided into small electric dipoles whose solutions need to be evaluated over all the edges in the mesh and eventually summed together. Alternatively, the initial solutions for $\mathbf{A}$ can be obtained numerically using the FV method developed in this thesis.

For galvanic sources, the DCR problem should be solved first in order to get the initial electric field and later the MMR problem should then be solved to get the solutions for $\mathbf{A}$. When solving the double curl equation for $\mathbf{A}$, the Coulomb gauge condition should also be enforced in order to get a unique solution, and the same method as discussed in Section 5.2 can also be used here. Using the operators derived in Chapter 3, Equation 2.15 can be written as

$$\mathbf{divQgrad}\phi = \mathbf{divJ}_s. \tag{5.12}$$

Equation 5.9 can also be gauged by either of the two gauge enforcement methods. When the explicit method is used, the following two equations need to be solved:

$$\nabla \times \nabla \times \mathbf{A} + \nabla\lambda = \mu_0\mathbf{J}_s + \mu_0\sigma\mathbf{E}, \tag{5.13a}$$

$$\nabla \cdot \mathbf{A} = 0. \tag{5.13b}$$

Alternatively, when the implicit method is used, the following equation needs to be solved:

$$\nabla \times \nabla \times \mathbf{A} - \nabla(\nabla \cdot \mathbf{A}) = \mu_0\mathbf{J}_s + \mu_0\sigma\mathbf{E}. \tag{5.14}$$

Using discrete operators from Chapter 3, Equation 5.13 becomes

$$\mathbf{curl_v curl_d}\tilde{\mathbf{A}} + \mathbf{grad}\tilde{\lambda} = \mu_0\tilde{\mathbf{J}}_s + \mu_0\mathbf{Q}\tilde{\mathbf{E}}, \tag{5.15a}$$

$$\mathbf{div\tilde{A}} = 0. \tag{5.15b}$$

Similarly, Equation 5.14 can be rewritten as

$$\mathbf{curl_v curl_d \tilde{A}} - \mathbf{grad\ div\tilde{A}} = \mu_0 \mathbf{\tilde{J}}_s + \mu_0 \mathbf{Q\tilde{E}}. \tag{5.16}$$

5.5 Examples

5.5.1 Introduction

In this section, the block-in-halfspace model used in Section 4.5.6 will be used again to validate the newly developed $A - \phi$ method. Then, the massive sulfide ore deposit model that was used in Section 4.5.7 will also be used here to analyze the B-field response. Lastly, a horizontal plate model and a vertical plate model are used to investigate the galvanic and inductive parts of the electric field. As for the E-field method, the modeling results of the $A - \phi$ method can also be affected by many factors such as those investigated for the E-field method in Section 4.5. Homogeneous half-space examples were used to investigate how those factors affect the $A - \phi$ method and the conclusions are generally similar to those for the E-field method. Therefore, those half-space models are not presented here.

5.5.2   A 3D block in half-space

The first example is the same 3D conductive block as used in Section 4.5.6 and shown in Figure 4.21. The same mesh as used in Section 4.5.6 is used here. We first calculated the B-field response of the homogeneous half-space without the conductive 3D block. The $A - \phi$ system is gauged with the Coulomb gauge both explicitly and implicitly. The B-field response calculated by the E-field method was obtained by integrating the dB/dt response backward in time. As in Section 4.5.6, a step-off waveform was considered for the modeling and the source is turned off within one iteration step. The initial time step was set to 10^{-7} s and was doubled every 200 steps for this example. In total, 12 sections and 2,245 steps were required to calculate the EM responses to $t = 50$ ms, which is later than most commonly used TDEM systems with a 100×100 m loop source. With this time range, the late time performance of the forward modeling algorithm can be tested.

Figure 5.1 shows the responses calculated by the $A - \phi$ methods match the analytic solution very well except at very early times. The relative errors between the responses calculated by the two $A - \phi$ methods and by the analytic solution are very close to each other. This indicates that the explicit and implicit methods of the Coulomb gauge enforcement lead to very similar solutions. The B-field response calculated by the E-field method through numerical integration has an obvious mismatch at late times. The mismatch is caused by the numerical integration. The modeling is only calculated up to $t = 50$ ms and so the calculated dB/dt response stops at this time.

This causes the significantly smaller B-field response computed through integration as seen in Figure 5.1. The problem can be mitigated by an extrapolation of the dB/dt response to later times based on the assumption that the late-time response mainly comes from a background half-space. A linear decay of the dB/dt response is then expected in log-log space so that one can easily extrapolate the dB/dt response to later times (Levy, 1984). However, this assumption is simply not valid when there are strong conductors such as high-grade graphite, nickel, and copper deposits present in the model because the late-time responses may still be dominated by the response from the conductor (Smiarowski and Macnae, 2013). The late-time mismatch can also be avoided if the forward modeling is carried out to a later time and then the numerical integration started from that time. Unfortunately, this can increase the computation costs of the modeling, and a suitable value for the latest time that the modeling should reach is difficult to determine prior to the modeling. For example, the B-field response calculated by numerical integration of dB/dt responses calculated until $t = 200$ ms still has a relative error greater than 10% at $t = 50$ ms. The relative error at $t = 50$ ms only becomes smaller than 3% when the dB/dt response is calculated to $t = 500$ ms. The computation times required for calculating the dB/dt responses to 50 ms, 200 ms, and 500 ms are approximately 680 s, 875 s, and 920 s, respectively, on a Linux workstation equipped with 2 Intel Xeon E5 2650 v4 CPUs (each CPU has 12 cores) running at 2.2 GHz and with 256 GB of RAM. This means 35% more computational time is needed to accurately calculate B-field responses from the numerical integration of dB/dt responses, compared to only calculating dB/dt
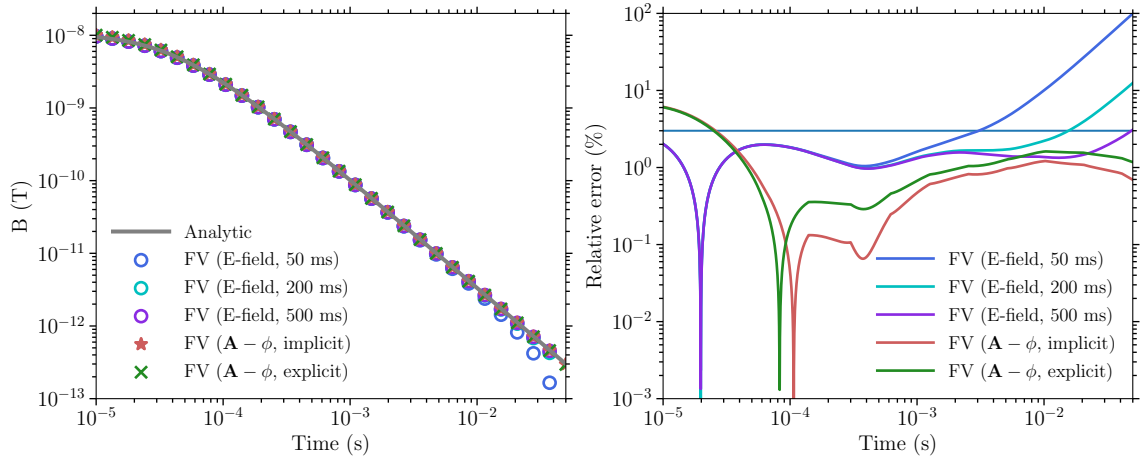
Figure 5.1: Comparison of the dB/dt responses calculated by analytic methods and FV methods for the half-space model (left panel) and relative errors of FV methods with respect to the analytic solution.

responses. The computational times for the explicitly and implicitly gauged B-field methods are 981 s and 1,256 s, respectively. Therefore, for the model shown here, the B-field method has a comparable computational time with the E-field method when B-field data are calculated.

The dB/dt responses computed using the FV methods developed here are compared against my independent implementation of the FE method of Li et al. (2018). The FE implementation shares many common components with the FV implementation here so that a relatively subjective comparison of the efficiencies of the two methods can be made. Figure 5.2 shows the dB/dt responses calculated by the FE and FV methods (left panel) and the relative errors between the responses calculated by the FV and FE methods (right panel) for the block-in-halfspace model as shown in Figure 4.21. From Figure 5.2 we can see that all four responses agree with each other very well. From the error plot, we can see that, again, the explicit and implicit
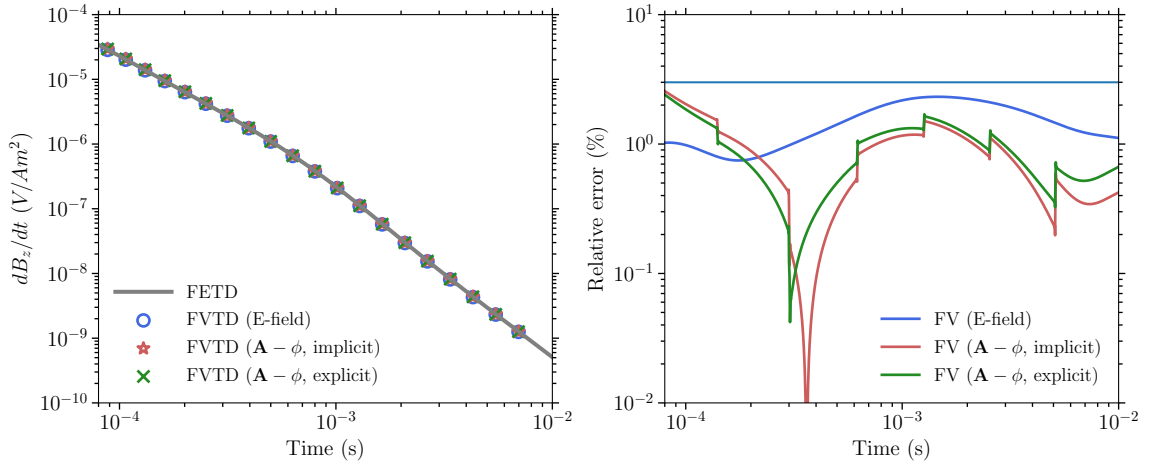
Figure 5.2: The dB/dt responses calculated by different numerical methods (left panel), and the relative errors between FV and FE methods (right panel) for the block-in-halfspace model as shown in Figure 4.21. Explicit and implicit gauging methods are both used for the $A - \phi$ method.

gauge enforcement methods give very close responses. The E-field FV method has the smallest relative error at early times but this error becomes slightly larger at later times compared to that of the $A - \phi$ method. All FV responses have a larger relative error at middle times which correspond to the time periods when the anomalous responses of the 3D conductive block are the largest.

The computing times and memory usage of the four numerical methods for this example are listed in Table 5.1. All computations were done on the same Linux workstation as described before. It can be seen that the E-field FE method requires the shortest time and the least memory while the implicit $A - \phi$ FV method requires the longest running time and needs the largest amount of memory. This is because FE methods generate a symmetric positive definite coefficient matrix while FV methods do not when unstructured grids are used. The symmetry of the coefficient matrix makes the FE method more efficient memory-wise despite the fact that FE methods

Table 5.1: Comparison of the computational efficiency for different numerical methods considered in this thesis.

Method name	Ave. Fact. tims (s)	Ave. RHS update time (s)	Ave. sol. time (s)	Tot. comp. time (s)	Memory (MB)
FE	4.281	0.035	0.244	687.114	1121
FV (E-field)	5.509	0.004	0.265	688.876	1754
FV ($A - \phi$, implicit)	16.976	0.009	0.362	1083.219	5781
FV ($A - \phi$, explicit)	13.909	0.008	0.355	1025.809	4549

have more non-zero elements in a row than FV methods because more edges are coupled in FE methods (Jahandari et al., 2017). However, the actual computation time of the E-field FV method is almost the same as that of the FE method. This is because when updating the right-hand side for each iteration in the time-stepping process, FV methods only require calculating the product of two diagonal matrices while FE methods require the calculation of a matrix-vector product. As can be seen from Table 5.1, the FE method requires on average 0.035 s to update the right-hand side term for a new iteration step while it only takes 0.004 s for the E-field FV method. For the factorization task, it takes 5.51 s for the E-field FV method while it only takes the FE method 4.28 s. However, there are only 12 sections in the modeling which corresponds to 12 factorization operations, and there are 2,245 iteration steps which all require an update of the right-hand side term. The average time spent in the solution stage for the FV method is only 0.021 s longer than the time spent in the FE method. Consequently, the computation times of the FE method and the E-field FV

method are almost the same for this model.

The $A - \phi$ methods require significantly larger amounts of memory partly because of the increased number of degrees of freedom (from only unknowns on the tetrahedral edges to unknowns both on the tetrahedral edges and nodes) and partly because the increased number of equations (increased number of rows in the coefficient matrix). The enforcement of the Coulomb gauge condition by either the explicit or the implicit methods also introduces more non-zero elements into the coefficient matrix. The implicit enforcement method, despite having only two equations, demands the largest amount of memory. This is caused by the **grad div** operator coupling many edges together. However, the significant increase of memory consumption (more than three times) by $A - \phi$ methods over E-field methods only increases the computation time by approximately 50%, and the exact reason for this is unknown.

5.5.3 Massive sulfide ore deposit model

This example was presented in Chapter 4 where its dB/dt responses were modeled with the E-field method. Here, the $A - \phi$ method is used to model the B-field response of the same model. Again, the same mesh as used in Section 4.5.7 for the flat air-Earth surface example is used here. Figure 5.3 shows the B-field responses from three receiver locations, which are calculated by the $A - \phi$ code and the E-field code. The receivers' coordinates relative to the center of the loop source are (0, 0, 0) m, (200, 200, 0) m, and (500, 500, 0) m. The dB/dt responses calculated by the E-field code were integrated backward from $t = 0.2$ s to $t = 10^{-7}$ s in order to get the B-field response.

The B-field responses calculated by the $A-\phi$ code and the E-field code agree with each other very well except for the responses close to sign changes when the field values are changing rapidly, which poses difficulties for the numerical methods since they all use relatively large time steps. The two responses all go through sign changes for receivers close to or outside the loop source, with sign changes in the B-field response happening much earlier. Also, the characteristics of the B-field response of the (200, 200) m receiver is simpler compared to that of the dB/dt response. The dB/dt field response first decreases with time and then increases before the sign reversal. The dynamic range of the B-field response is significantly smaller than that of the dB/dt response. Taking the (0, 0) m receiver for example, the dB/dt response decreases almost 5 orders of magnitude while the B-field response only decreases slightly more than one order.

It should be noted that the dB/dt response calculated by the E-field code should be calculated at least to 200 ms after the source is turned off in order to achieve an accurate B-field response from the numerical integration. Otherwise, the integrated B-field response would be smaller than that calculated by the $A-\phi$ method (similar to what was observed in Figure 5.1). A total number of 1,162 iteration steps was used to calculate the B-field response by the $A-\phi$ code from 10^{-7} s to 3.316×10^{-2} s while the number of iterations was 1,262 for the E-field code to get the modeling result from 10^{-7} s to 0.2 s. The computation times for the E-field and $A-\phi$ codes were approximately 2,512 s and 4,565 s, respectively, with the E-field code still being more efficient.
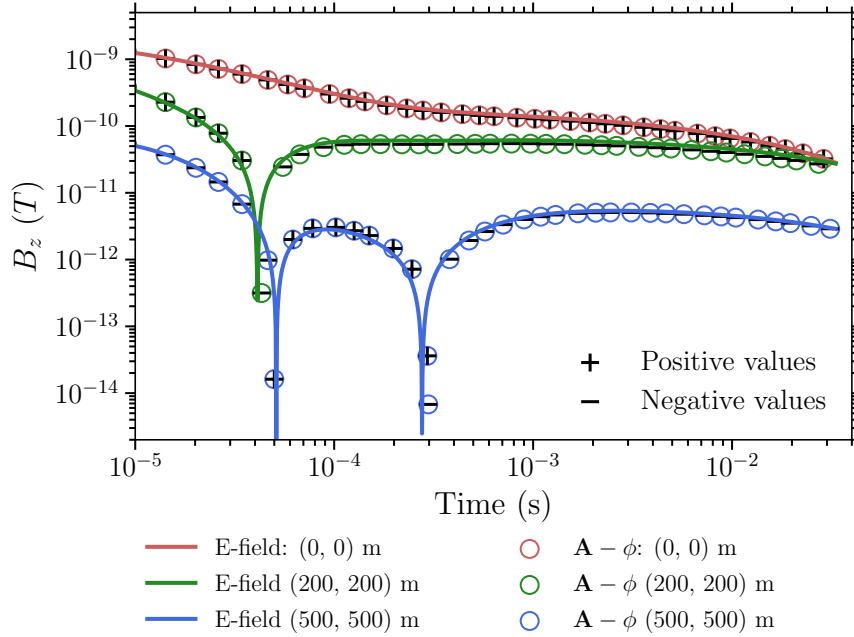
Figure 5.3: B-field responses of the massive sulfide ore deposit model with a hypothetical flat surface at $z = 110$ m (Figure 4.23).

5.5.4 A horizontal conductive slab model

This example considers a horizontal conductive slab buried in a homogeneous half-space. As depicted in Figure 5.4, the conductive slab is 30 m thick with a dimension of 200 m in both the x and y directions. A 100×100 m loop source is laid on the ground. The conductivity values of the slab and homogeneous half-space are 1 S/m and 0.01 S/m, respectively. The center of the source is 50 m above the center of the conductor. In order to study the EM field response within the slab, a grid of 1,296 receivers both inside and outside the slab was placed on the plane $z = -65$ m. To refine the mesh quality around these receivers, regular tetrahedra with an edge length of 2 m were inserted. These receivers cover an area of 350×350 m^2. The distances
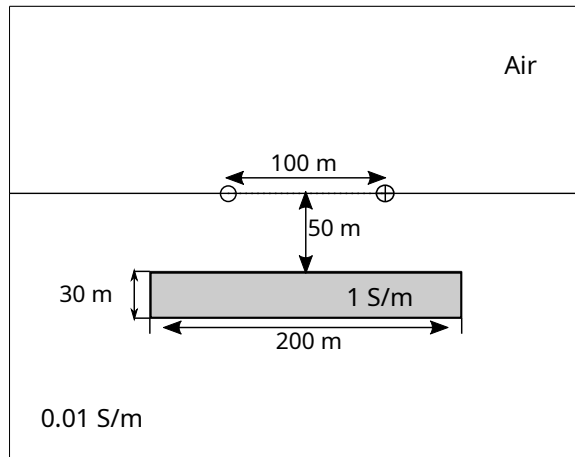
Figure 5.4: Diagram of the horizontal slab model.

between adjacent receivers in the x and y directions are all equal to 10 m.

The mesh along each side of the loop source was refined by inserting 20 edges each with a length of 5 m along the source wire location. In total, TetGen generated a mesh with 1,133,463 edges and 974,791 elements. The relatively large number of edges is mainly caused by the refinement of the 1,296 receivers. The modeling considers a step-off transmitter waveform, with the source amplitude decreasing from 1 A to 0 within 10^{-8} s. The modeling was carried out until $t = 100$ ms. The initial time step was 10^{-8} s and it was doubled after every 200 steps. In total, 16 sections and 3,106 iteration steps were required to finish the modeling. The modeling took approximately three hours and 19 minutes to finish on the same workstation as described before.

Figure 5.5 shows the horizontal components of the electric field (left column), the part of the electric field that is associated with $\mathbf{A}$ (middle column) and the part of the electric field that is associated with ϕ (right column), respectively, over the horizontal plane of receivers. The electric field is predominantly horizontal on this plane because

125

of the geometry of the conductor and the location of the transmitter. Figure 5.6 shows the corresponding current densities.

The **A** part of the electric field would be thought of as the inductive part if the conductor were in free space and hence the coupling between transmitter and slab were via the time-varying magnetic field only and there was no flow of current between the slab and host. The ϕ part of the electric field would be considered as the galvanic part for DC problems because there is no change in the magnetic field with time and thus no coupling between different parts of the domain via a time-varying magnetic field. However, for the general case, the **A** and ϕ parts cannot be decoupled. Consequently, it is unclear whether the solenoidal part of the electric field, $-\partial \mathbf{A}/\partial t$, and the irrotational part of the electric field, $-\nabla\phi$, can be identified with purely inductive and galvanic phenomena respectively. Nonetheless, the solenoidal and irrotational parts of the electric field will be referred to here as inductive and galvanic parts.

The electric fields and current densities come from three times: $t = 0.0178$ ms, $t = 1.0000$ ms, and $t = 31.6228$ ms. At the earliest time, the total electric field is just starting to penetrate into the conductive slab, and with the expected circular pattern. The corresponding total current density is relatively weak inside the slab (compared to later times) and clearly is strongest right at the edge of the slab. Also, the total electric field and current density show subtle current channelling behaviour into and out of the slab at the slab corners, which distorts the field and current in the host from being purely circular.

126
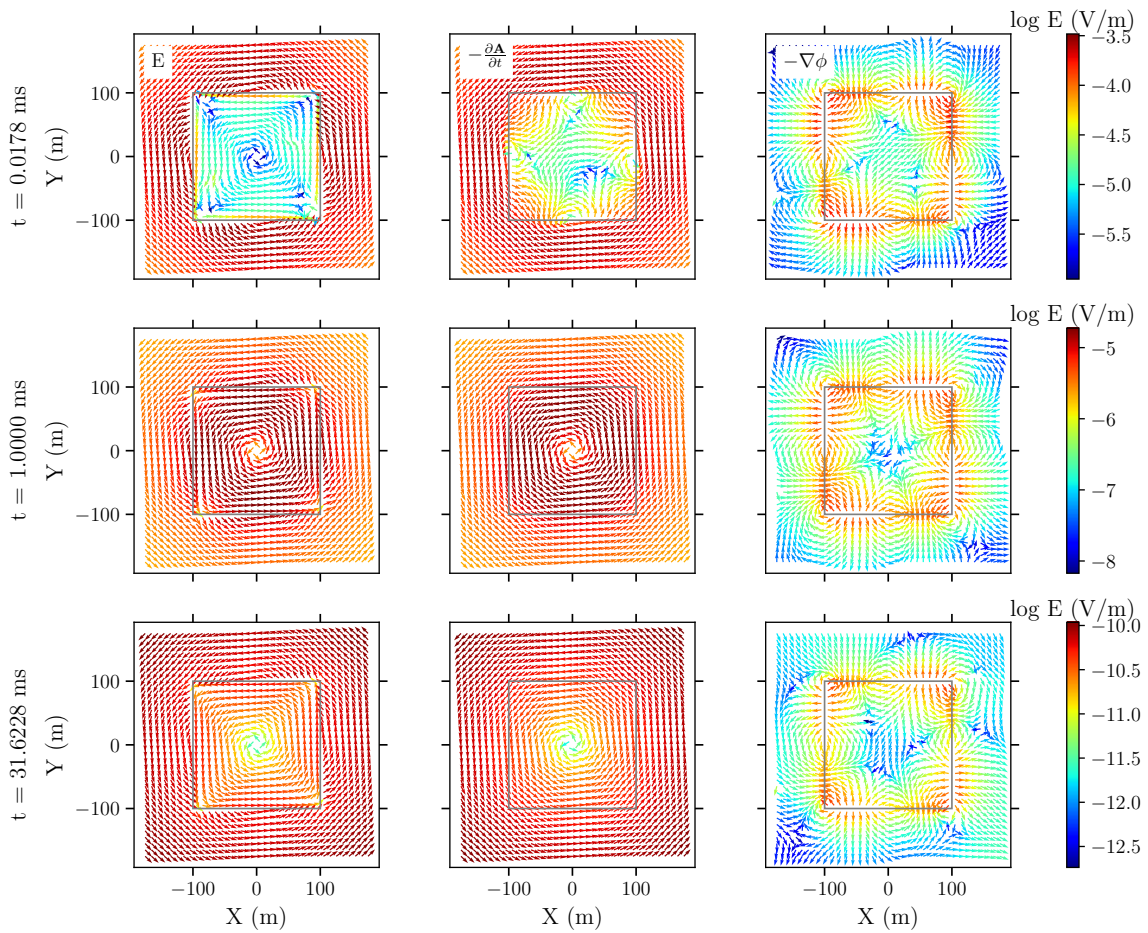
Figure 5.5: The horizontal component of the total electric field and its inductive and galvanic parts (from left to right) at three different times on a horizontal slice through the conductive slab of the example shown in Figure 5.4, and for the transmitter symmetrically above the slab. The gray square marks the boundary of the conductive slab. Note the different color scales for the three different times.

The inductive and galvanic parts of the electric field have a more complicated pattern compared to the electric field itself. The galvanic part has the pattern of a DCR-like field generated by charges on the edges of the slab, with opposite charges on the first and second halves of each edge. The inductive part loops into and out of the slab at the corners. The normal components of the two parts generally have opposite directions and similar magnitude such that their summation becomes largely

127
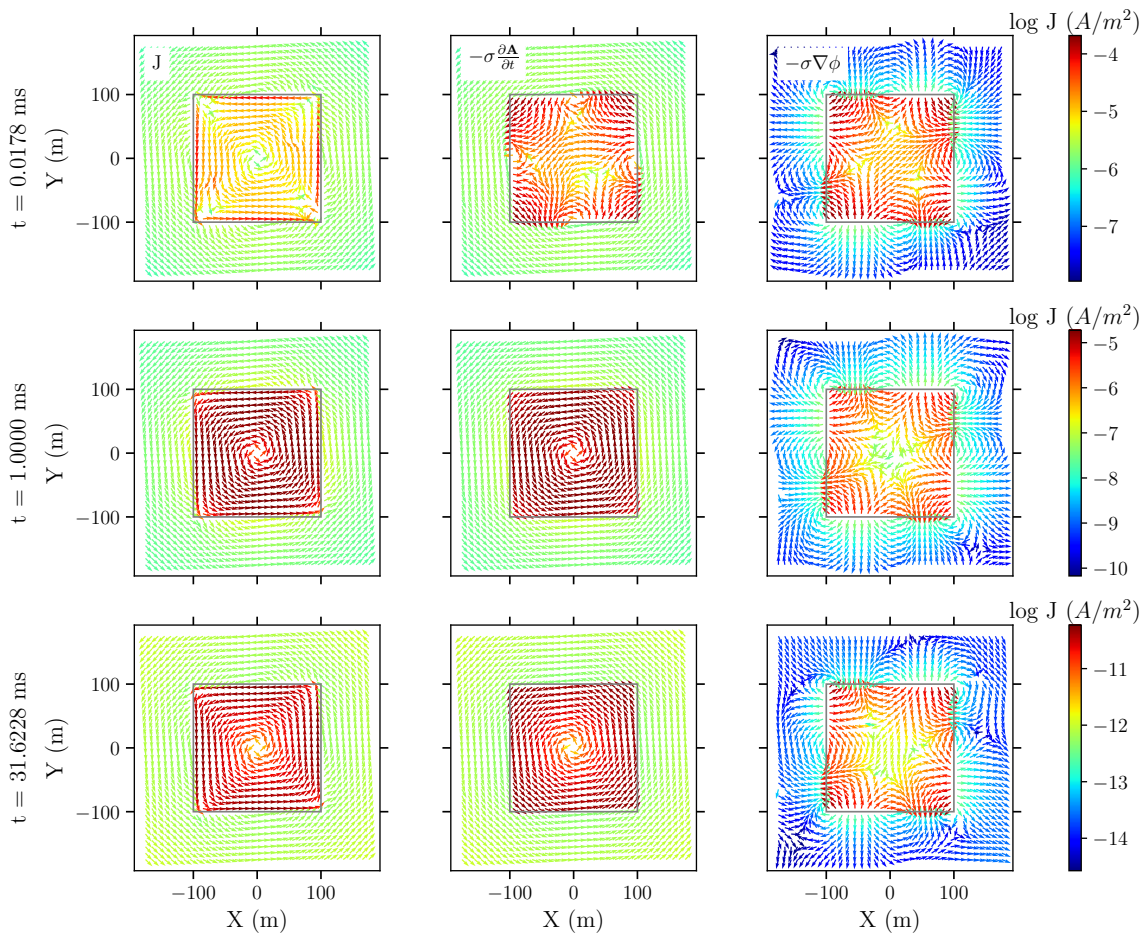
Figure 5.6: The horizontal component of the total current density field and its inductive and galvanic parts (from left to right) at three different times on a horizontal slice through the conductive slab of the example shown in Figure 5.4, and for the transmitter symmetrically above the slab. The gray square marks the boundary of the conductive slab. Note the different color scales for the three different times.

tangential to the edge of the slab. Also, the inductive and galvanic parts cancel each other out within most of the slab to give the weak internal field at this early time. The galvanic part is large close in to the edges of the slab, but rapidly becomes small away from the edges. The inductive part dominates in the host, consistent with the total field being essentially circulatory in the background.

The total electric field and current at $t = 1$ ms have become more evenly dis-

tributed inside the conductor, with the current in the slab now much stronger than in the background. The inductive part has now become dominant, and with the expected circulatory pattern. The galvanic part has the same pattern as for the previous time, namely, a DCR-like field generated by charges on the edges of the slab. Again, the galvanic part is only strong close to the edges of the block, especially around the four corners. Current channeling into and out of the slab can be seen at its corners. The total electric field and current density at the edges of the slab more closely follow the square shape of the slab than the inductive parts themselves. The total electric field and current at this time are predominantly circulatory and inductive, with a small galvanic, DCR-like contribution from current flowing in and out of the corners of the slab. The fields and currents behave similarly at $t = 31.6228$ ms except that the magnitude has decreased significantly.

The electric field and current density, and the inductive and galvanic parts, shown in Figures 5.6 and 5.5 are symmetrical because the source was deliberately placed symmetrically above the center of the plate. With this particular geometry, the electric field and current density are predominantly inductive, with the galvanic part only contributing at the edges of the slab. However, when the symmetry of the configuration is removed, the galvanic part of the electric field can end up contributing more to the total electric field than in the symmetric case. Consider the same conductor model as shown in Figure 5.4, but with the source moved so that its center is now located over the center of the conductor's left edge. The electric field and currents on the horizontal plane through the center of the slab at three different times, and
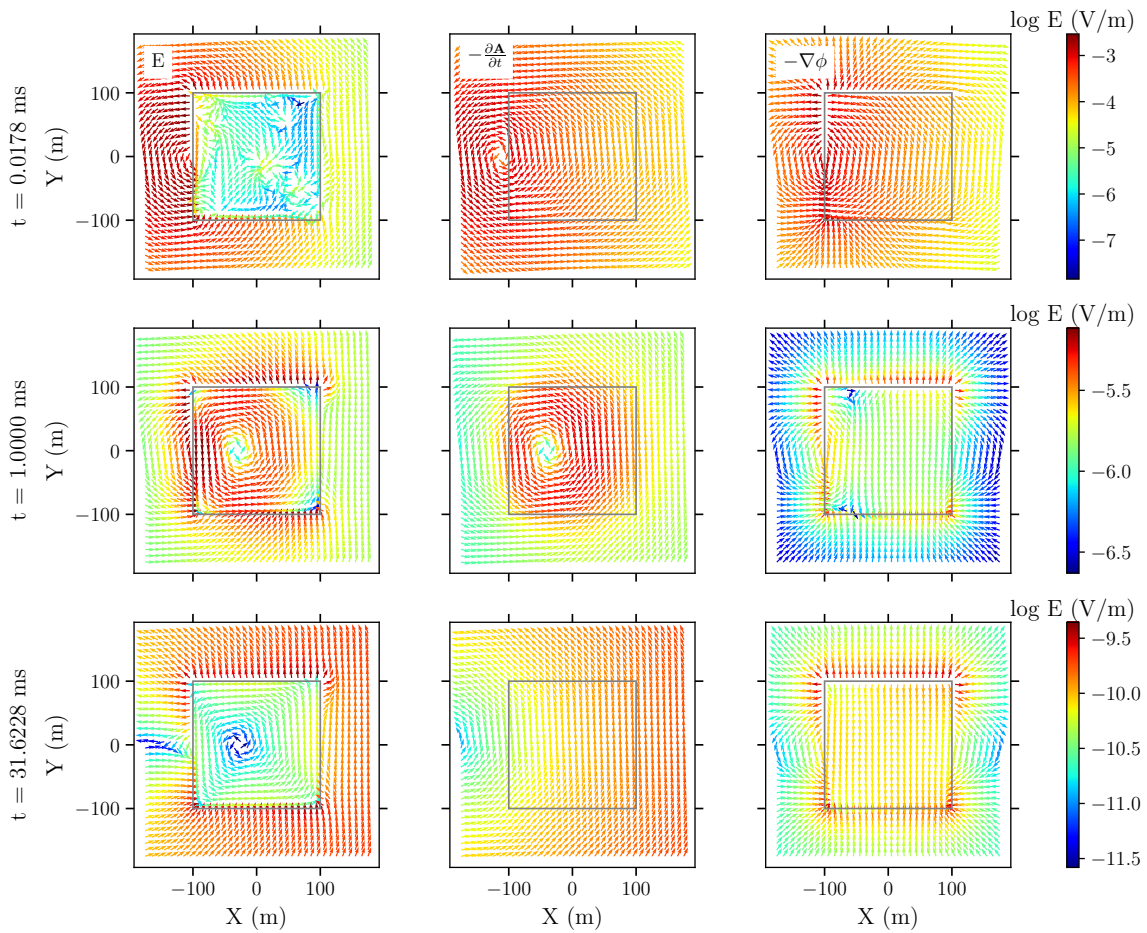
Figure 5.7: The horizontal component of the total electric field and its inductive and galvanic parts (from left to right) at three different times on a horizontal slice through the conductive slab of the example shown in Figure 5.4, and for the transmitter centerd above the left boundary of the slab. The gray square marks the boundary of the conductive slab. Note the different color scales for the three different times.

corresponding inductive and galvanic parts, for this asymmetrical situation are given

in Figures 5.7 and 5.8.

It can be seen from Figure 5.7 that at the earliest time shown ($t = 0.0178$ ms) the

total electric field in the background is rather circular and centered on the horizontal

location of the center of the source. The inductive part has a clear pattern centerd on

the transmitter, and somewhat resembles what one would expect for the total field if
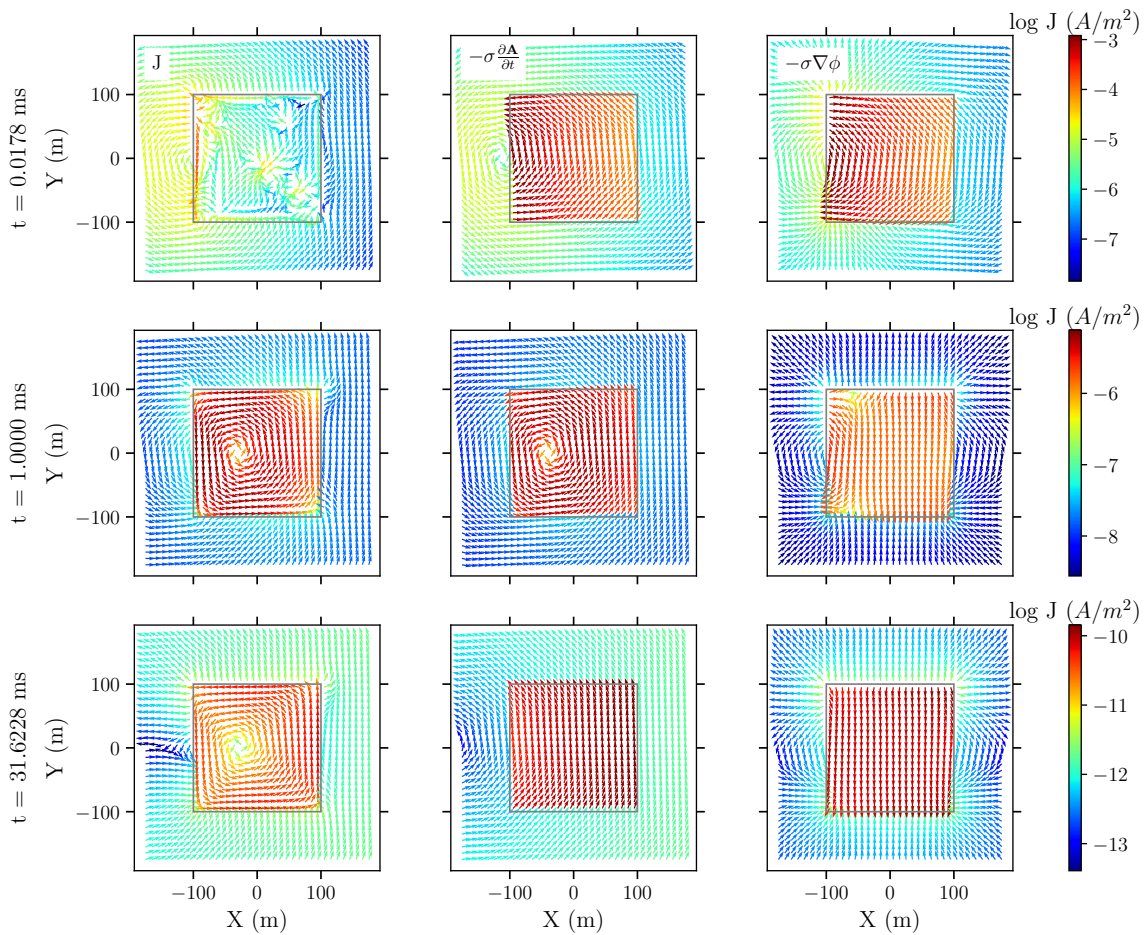
Figure 5.8: The horizontal component of the total current density field and its inductive and galvanic parts (from left to right) at three different times on a horizontal slice through the conductive slab of the example shown in Figure 5.4, and for the transmitter centerd at the left boundary of the slab. The gray square marks the boundary of the conductive slab. Note the different color scales for the three different times.

the slab were not there. The galvanic part is like a bipolar DCR field with a positive charge source at the top left corner of the slab and a negative charge source at the bottom left corner of the slab. The combination of the inductive and galvanic parts however results in a very small electric field and hence current density pointing into the slab at the bottom (in terms of the figure) and out of the slab at the top. At $t = 1$ ms, the total electric field and its inductive part become very similar inside the

conductor with a clear circular pattern centerd just to the left of the center of the slab. The galvanic part is like a DCR field for charge accumulations on the top and bottom edges of the slab, and, as for the symmetric case, decreases very rapidly away from the edges of the slab. Outside the conductor the total electric field with its mostly circulatory pattern is similar to the inductive part, except around the four corners of the slab where the behavior of the electric field is closer to that of the galvanic part. At $t = 31.6228$ ms, the inductive part looks like it is circulating around a point somewhere to the left of the conductor and its maximum magnitude has already moved away to the right of the conductor: it resembles the field that would exist if the slab were not present. The galvanic part is similar to that for t=1 ms, i.e., a DCR-like field for charge concentrations on the upper and lower edges of the slab (in relation to the figure), but which does not fall off as rapidly away from the slab. However, the combination of the inductive and galvanic parts result in clear circulation of the total electric field, and current density, localized within the conductor, that is, the galvanic part (the part associated with ϕ and charges on conductivity jumps) is critical in producing what would be considered the circulatory, "inductive" pattern of the total electric field and current in the conductor. This example shows that the galvanic part of the electric field is certainly not negligible when there is flow of current from a host into a conductive anomaly, and hence charges created on the conductivity discontinuity, even for a clearly inductive source.

5.5.5   A vertical conductive plate model

This example is a vertical thin conductor buried in a less conductive homogeneous half-space. As shown in Figure 5.9, the configuration used here is a loop source laid out on the Earth's surface to the left of the conductor. This configuration is similar to the Slingram configuration for a single station. The loop source is centered at (0, 0, 0) m and the top center of the conductor is located at (600, 0, -100) m. The conductor is 50 m thick and its strike length and depth extent were both set to 400 m. The conductivities of the conductor and background half-space are 100 S/m and 0.01 S/m, respectively. The air is considered to be very resistive with a conductivity of 10^{-8} S/m. A grid of 1,886 receivers (46 in the x direction and 41 in the z direction) was placed in the xz plane which cuts through the center of the conductor in the y direction. Also, two grids of receivers (361 in each grid, 19 in both y and z directions) were placed 0.1 m both inside and outside the conductor's boundary where $x = 575$ m. The horizontal and vertical spacings of the receivers on these grids were all set to 25 m and 21 m in the xz plane and yz planes, respectively. Regular tetrahedra with 5 m edge length were inserted around the receiver locations in order to get accurate fields at the receivers. In total, TetGen generated a mesh with 1,104,165 edges and 952,037 elements.

As for the previous examples, a step-off waveform was considered. The initial time step was 10^{-7} s and the time step was doubled every 100 steps. A total of 1423 steps and 15 sections were needed to simulate responses out to 200 ms. Figures 5.10 to
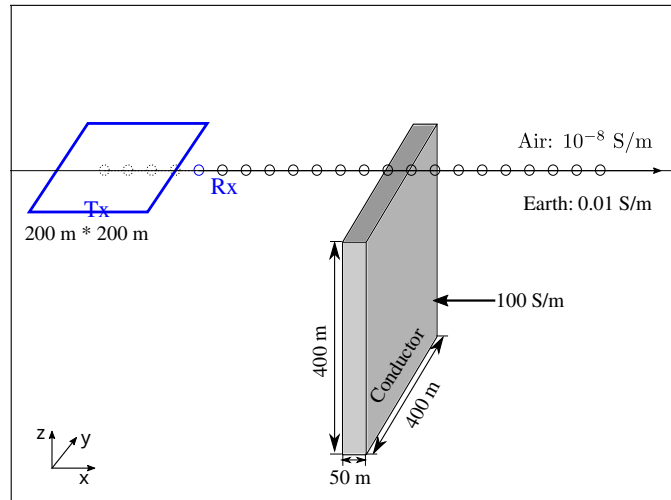
Figure 5.9: A diagram showing the configuration of a loop source survey for a vertical conductor model in a homogeneous half-space. The center of the loop source is located at (0, 0, 0) m and the top center of the conductor is located at (600, 0, -100) m. There are 1,886 receivers placed on the vertical plane along the x direction at $y = 0$ both above and below the ground.

5.12 show the total electric field, inductive and galvanic parts, and the magnetic field calculated over the grid of receivers over the xz plane at three different times. Figures 5.13 and 5.14 show the electric field and its galvanic and inductive parts calculated over the yz plane 0.1 m to the right (inside the conductor) and left (outside the conductor) of the conductor's left boundary ($x = 575$ m) at the three different times.

As can be seen from Figure 5.10, the magnetic field at $t = 0.4472$ ms still has its largest magnitude immediately below the source. However, there clearly exists a vortex around the top part of the conductor. This vortex corresponds to current flowing along the top of the conductor even at this relatively early time. The total electric field (top right panel of Figure 5.10) does exhibit a circulation within the vertical conductor, although at this early time the electric field is dominated by the

134

"smoke ring" up close to the source. The inductive part of the electric field (bottom right of Figure 5.10) resembles the large-scale smoke-ring pattern in the background with minimal indication of any effect of the conductor. The galvanic part (bottom left of Figure 5.10) is strongest in the vicinity of the conductor. As Figure 5.13 shows, the total electric field within the conductor is relatively weak at this early time and is fairly uniformly pointed in the negative y-direction throughout the conductor. Figure 5.13 also shows that the inductive and galvanic parts are close to being equal and opposite within the conductor. The large-scale circulatory flow of current in the background creates charges on the extremities of the conductor in the y-direction, and these charges then create the galvanic field pointed in the opposite direction in the conductor. The net effect is a weak electric field within the conductor that is strongest along the top of the conductor. The total electric field and its galvanic part outside the conductor, as shown in Figure 5.14, are very different from those within the conductor. While the electric fields are predominantly tangential inside the conductor, the total electric field and its galvanic part outside the conductor exhibit strong normal component. The total electric field is in line with the large-scale smoke-ring pattern in the background. The galvanic part, especially around the extremities in the y-direction, is normal to the conductor boundary and largely responsible for the normal total electric field seen in the total electric field. The inductive part, largely being tangential, is very similar to the inductive part within the conductor.

Later at $t = 9.4574$ ms (Figure 5.11), it can be seen that the magnetic field is

135

strongest around the conductor, and has a pattern consistent with circulating current within the conductor. This current in the plate can be seen in Figure 5.11, flowing in the negative y-direction in the top of the plate and in the positive y-direction in the bottom of the plate. The middle panel in Figure 5.13 clearly shows this circulating electric field within the conductor. Compared to the earlier time shown in Figure 5.10, the smoke ring of electric field and current density in the background has moved further away from the source both vertically and horizontally. This background smoke ring behavior dominates the inductive part of the electric field (bottom right image in Figure 5.11). The galvanic part (bottom left, Figure 5.11) is still a maximum at the slab. Just as for the earlier time, the inductive and galvanic parts in the slab are in mostly opposite directions. However, unlike the earlier time, they combine to give clear circulation of the electric field in the slab. The total electric field outside the conductor, as shown in the middle rows in Figure 5.14, starts to show the circulatory pattern just like what is observed for the total electric within the conductor (Figure 5.13), despite that the normal component is still strong in the extremities of the y-direction.

At the later time $t = 200$ ms (Figure 5.12 and bottom row of images in Figure 5.13), the eddy currents inside the conductor, which are causing the remaining magnetic field at this time, have become obvious. The smoke-ring field seen previously in the background half-space has vanished and the total electric field is a result of the currents inside the conductor. The inductive part is now very similar to the total electric field and the galvanic part is now very weak. At this time the situation is

essentially that of a purely inductive field created in the homogeneous half-space by a current source located in the conductive slab. The only hint of a galvanic part is at the corners of the slab as shown in the bottom row of Figure 5.13 (just like for the previous example: see, e.g, Figure 5.5). At this time, the total electric field and its inductive and galvanic parts, both inside and outside the conductor (Figures 5.13 and 5.14), have become mostly tangential and therefore continuous across the conductor boundary.

Although the total electric fields inside and outside the conductor look very different for the first two times shown in Figures 5.13 and 5.14, their tangential components, as shown in Figures 5.15 and 5.16, are continuous across the left boundary of the conductor. The normal components are clearly discontinuous across the interface because of the conductivity jump. Also, the normal component of the total electric field is very weak compared to the tangential component within the conductor for both times shown in the two figures.
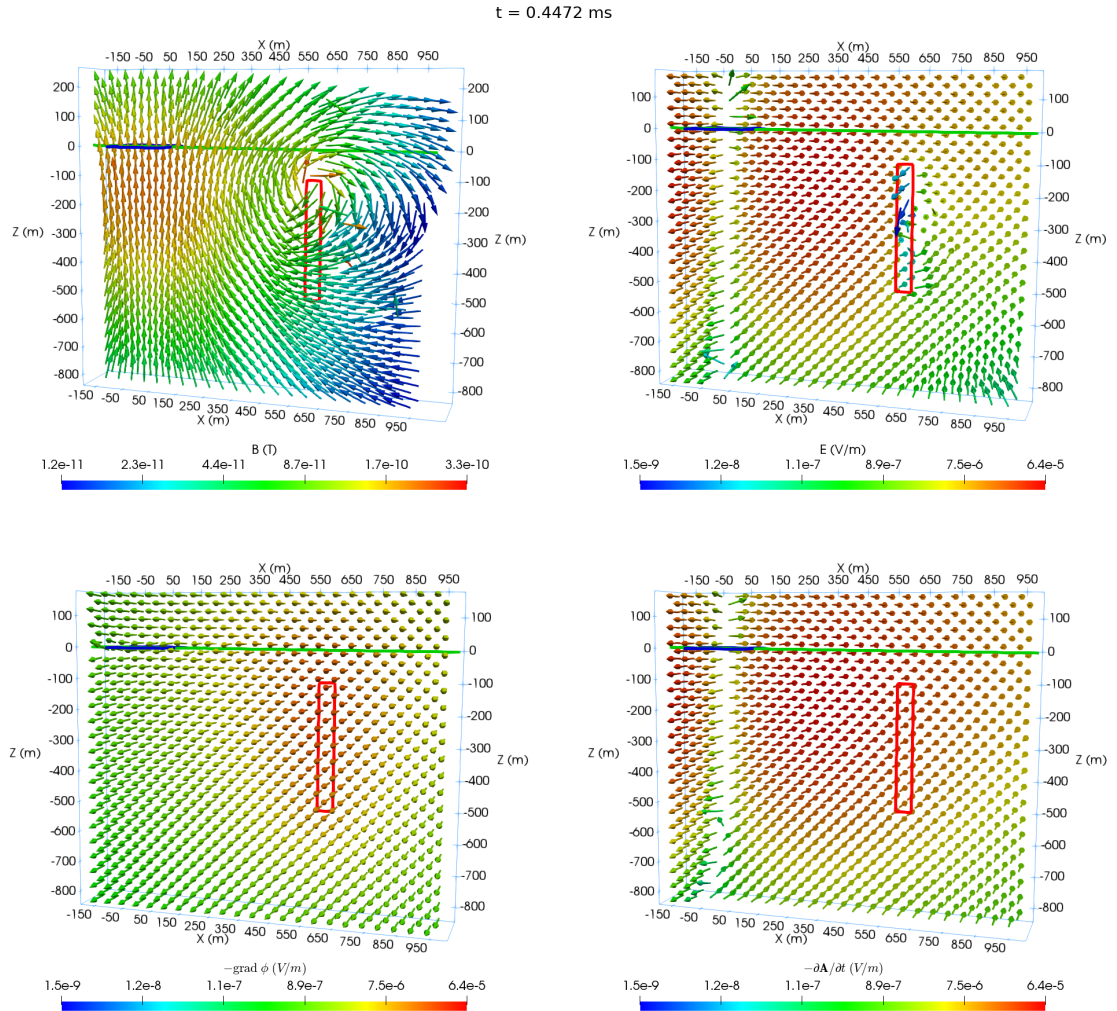
Figure 5.10: Perspective view of the EM fields at $t = 0.4472$ ms calculated at the 1,886 receivers over the $y = 0$ plane. The red rectangle marks the boundary of the conductor. The horizontal blue rectangle marks the location of the transmitting source. The green line shows the ground surface. The same colorbar is used for the electric field and its galvanic and inductive parts for the same time instant.
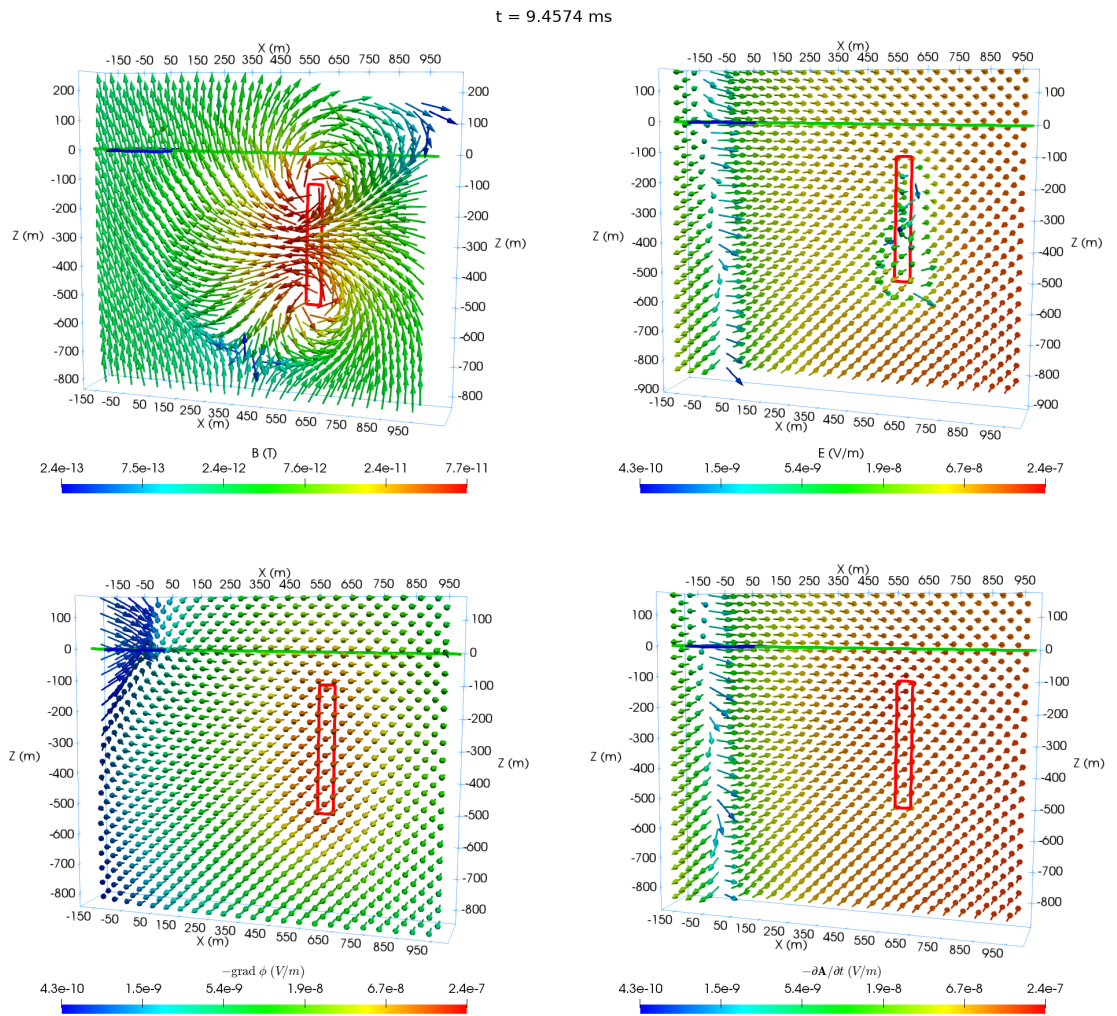
Figure 5.11: Same as Figure 5.10 but $t = 9.4574$ ms.
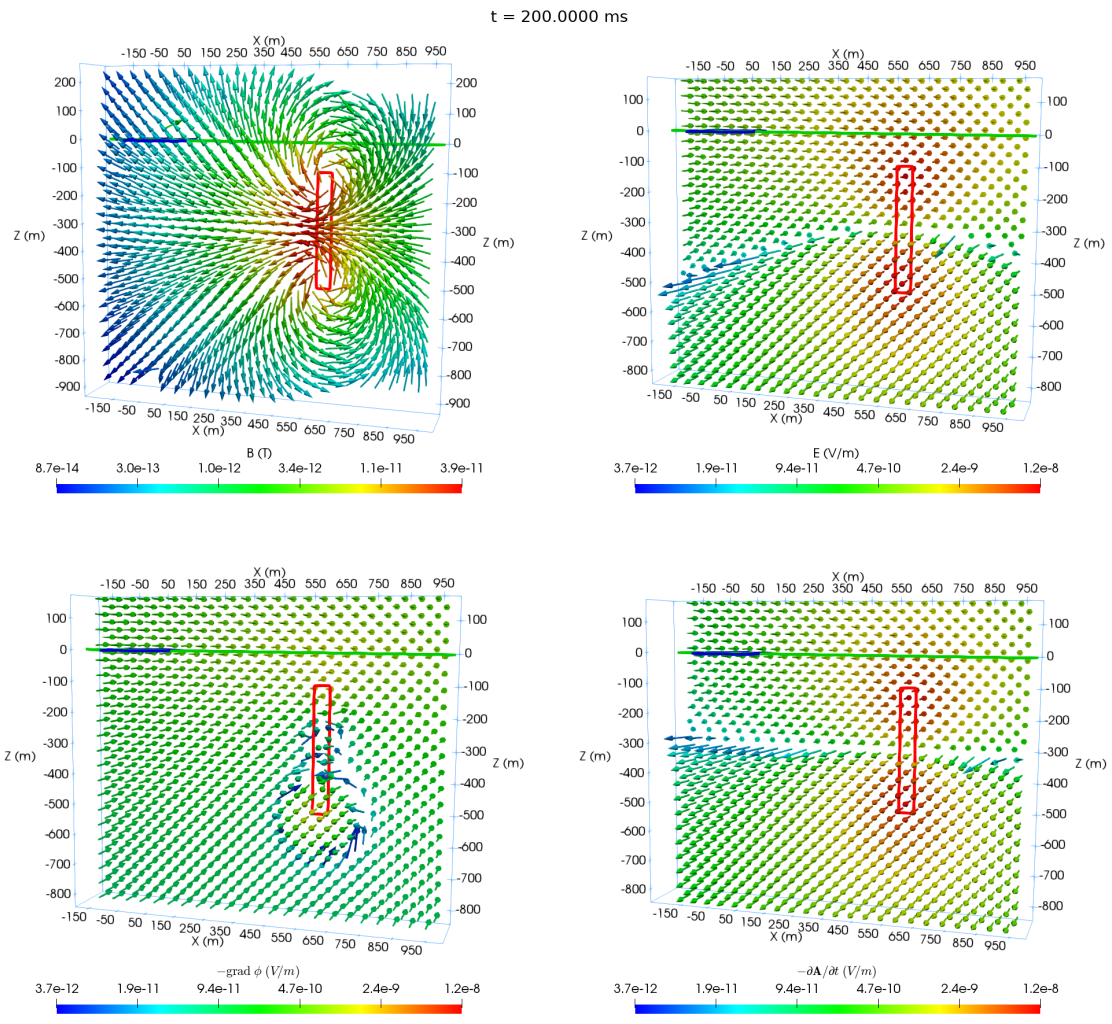
Figure 5.12: Same as Figure 5.10 but $t = 200$ ms.
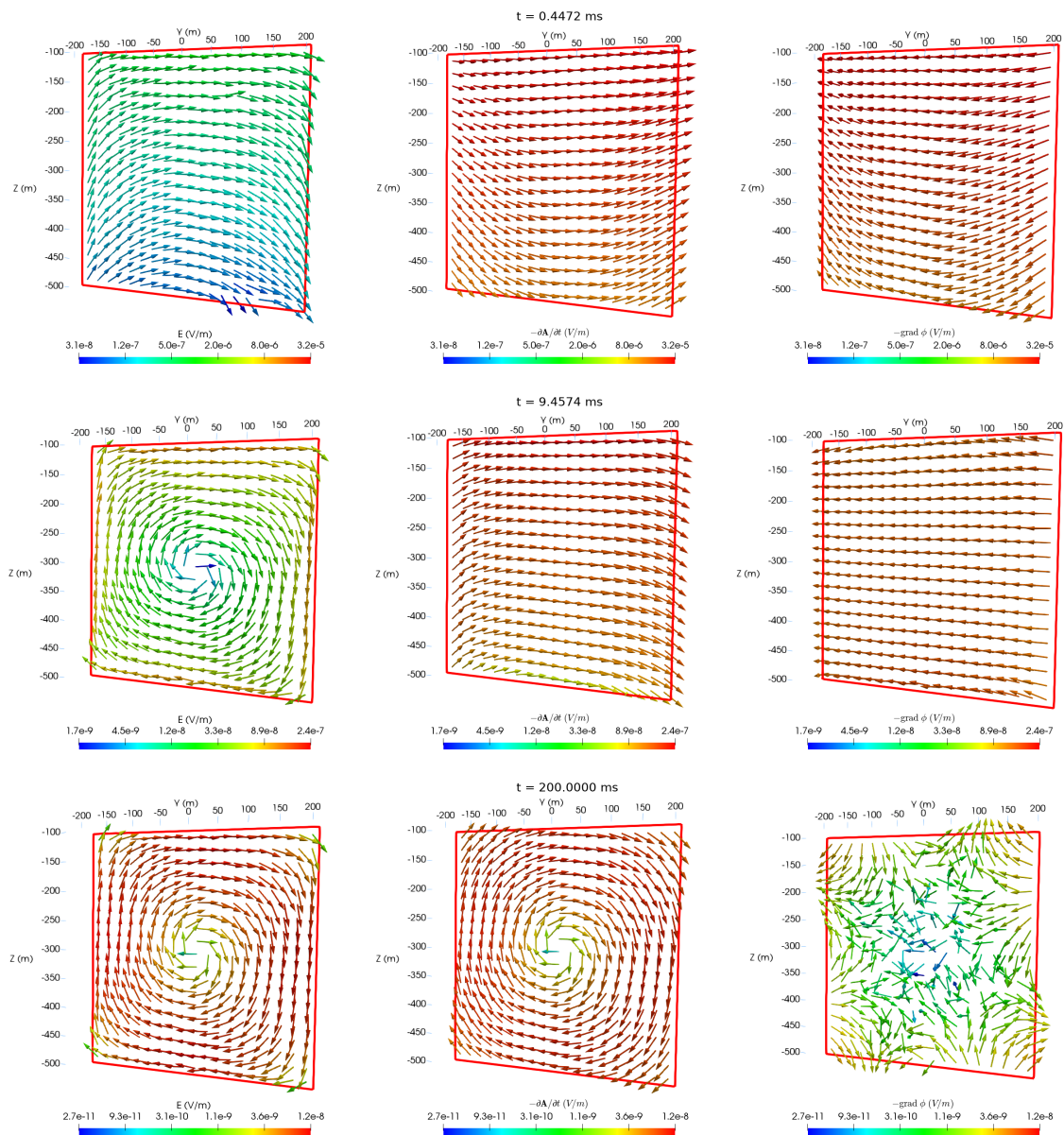
Figure 5.13: The electric field (left panel) and its inductive (middle panel) and galvanic (right panel) parts at receivers placed just inside the left boundary of the conductor at $t = 0.4472$ ms (upper), $t = 9.4574$ ms (middle), and $t = 200$ ms (lower). The conductor is marked by the red rectangle.
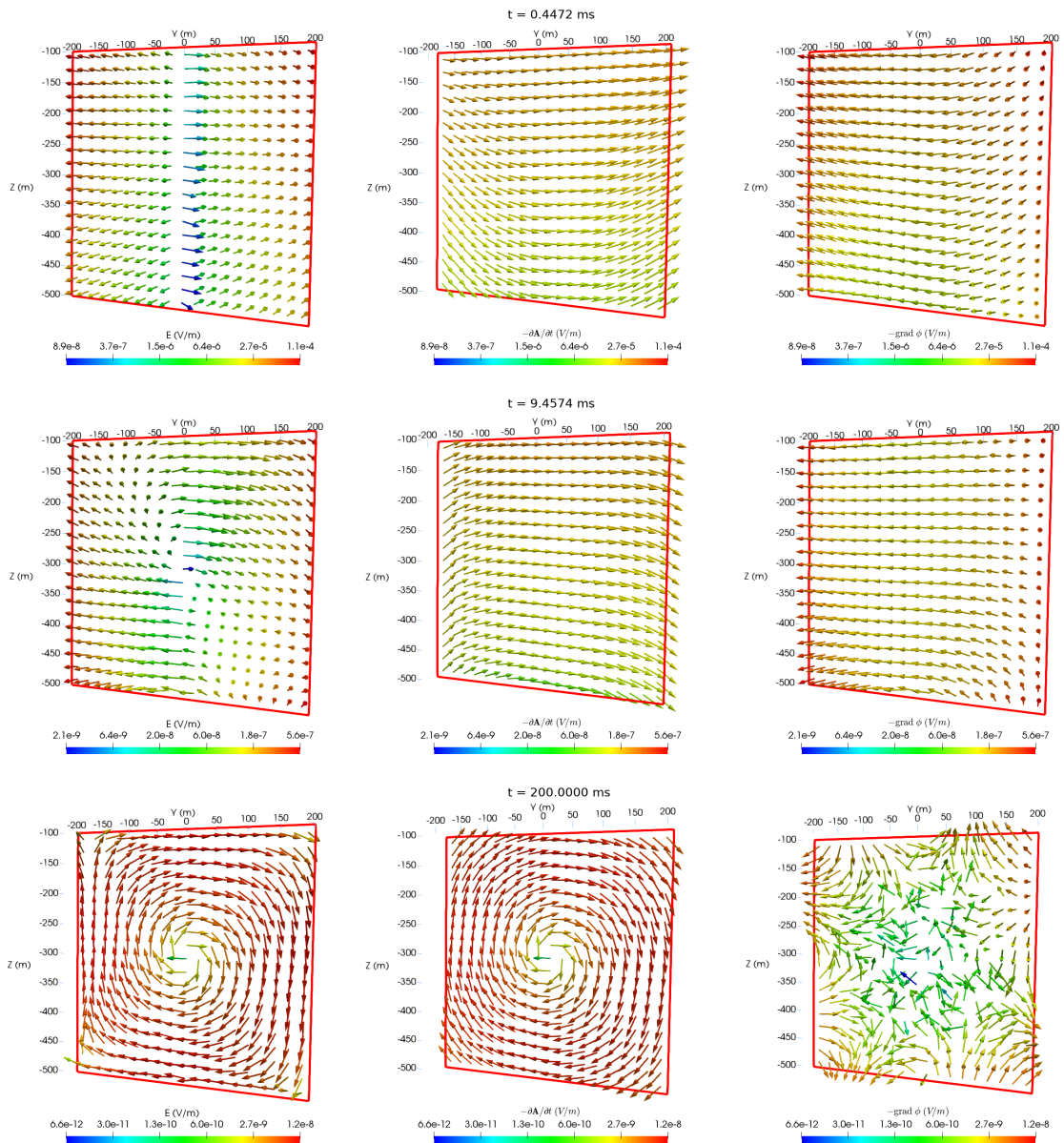
Figure 5.14: The electric field (left panel) and its inductive (middle panel) and galvanic (right panel) parts at receivers placed just outside the left boundary of the conductor at $t = 0.4472$ ms (upper), $t = 9.4574$ ms (middle), and $t = 200$ ms (lower). The conductor is marked by the red rectangle.
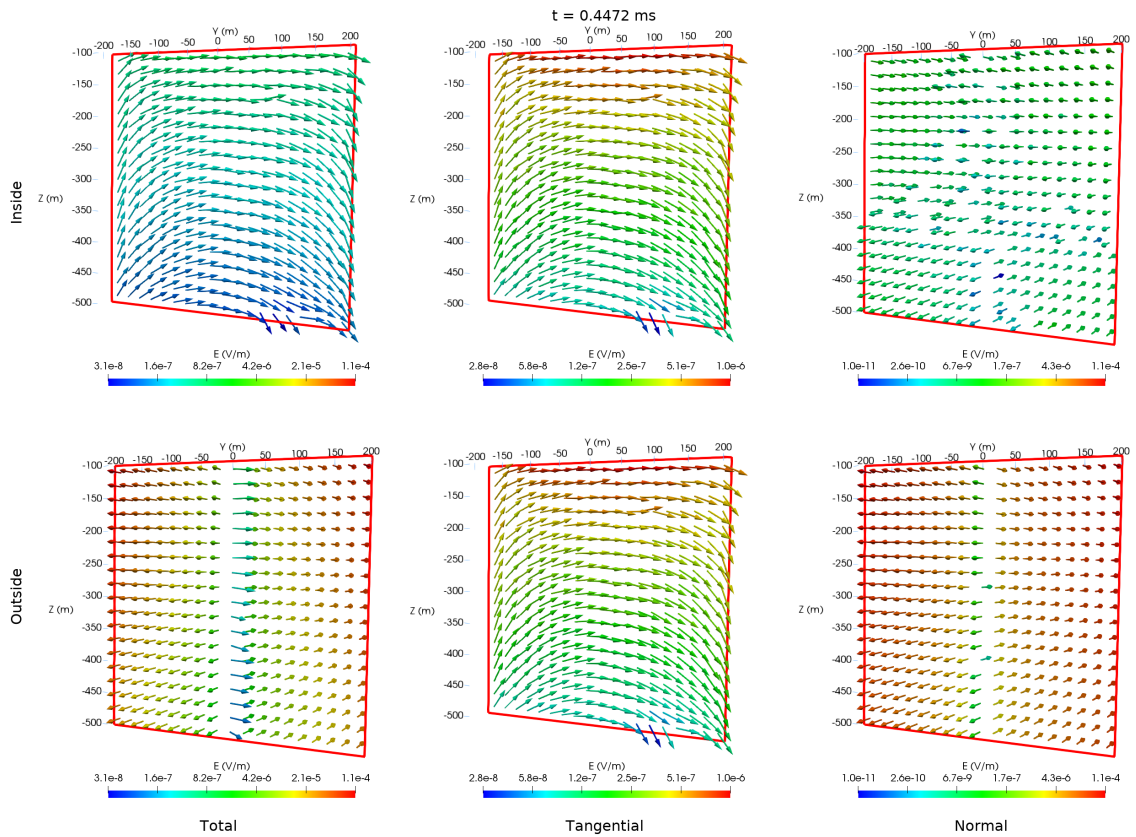
Figure 5.15: The total electric field (left panel) and its tangential (middle panel) and normal (right panel) components at receivers placed just inside (top) and outside (bottom) the left boundary of the conductor at $t = 0.4472$ ms. The conductor is marked by the red rectangle. The same colorbar is used for each column of plots.
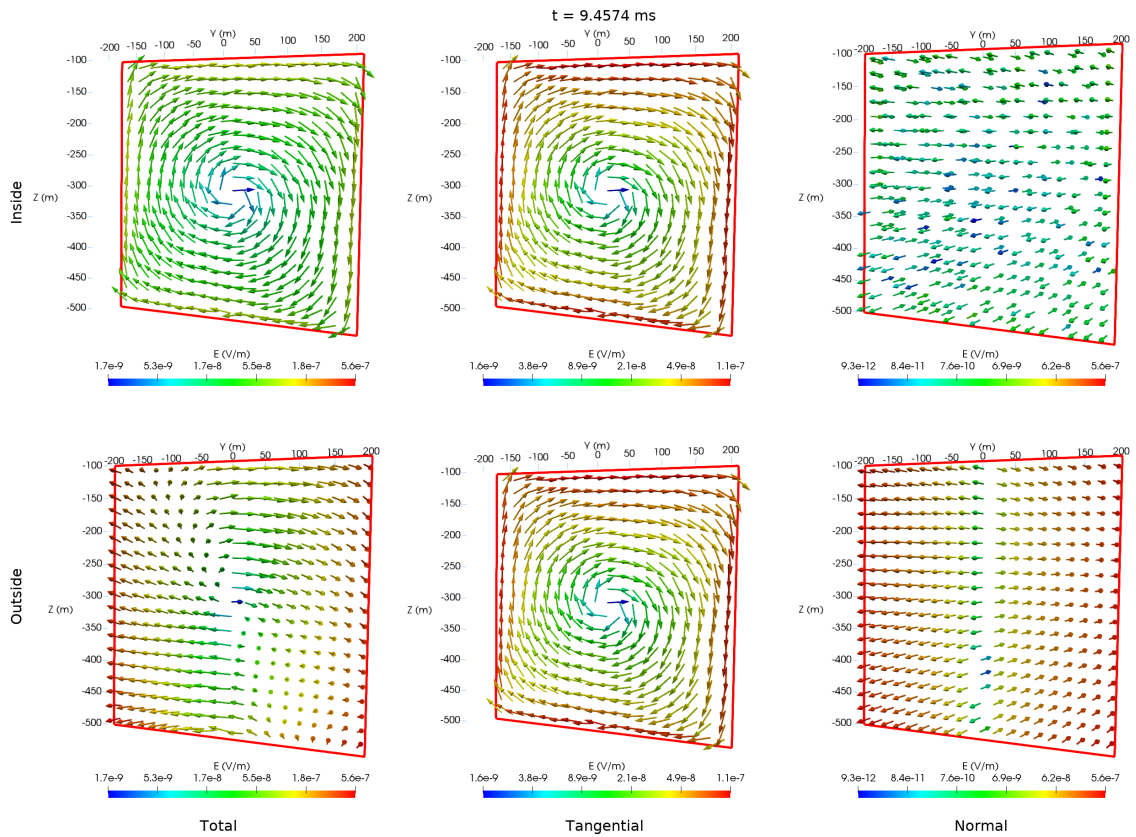
Figure 5.16: The total electric field (left panel) and its tangential (middle panel) and normal (right panel) components at receivers placed just inside (top) and outside (bottom) the left boundary of the conductor at $t = 9.4574$ ms. The conductor is marked by the red rectangle. The same colorbar is used for each column of plots.

Chapter 6

Modeling of graphitic fault zones in the Athabasca Basin

6.1 Introduction

The thin, sometimes steeply dipping graphitic conductors are the primary targets for time-domain EM surveys in the exploration for uranium in the Athabasca Basin. For these conductors, the inverted model from traditional minimum-structure inversion algorithms is normally smooth which does not show a clear boundary between the graphitic shear zones and the surrounding basin and basement units. Trial-and-error type of numerical modeling, especially using those fast algorithms such as Maxwell (EMIT, 2005), is therefore heavily relied on in the interpretation of the TEM data. As discussed in the Introduction chapter of this thesis, modeling based on those fast algorithms make many assumptions and can only obtain reliable responses at

late times, which may cause problems for the data interpretation. The FV methods developed in the previous two chapters overcome many of the existing disadvantages of those fast algorithms and can be used to accurately model three-component responses of TDEM data for realistic geological models from early to late times.

It is well known that transmitting waveforms of the source can have a significant effect on TEM responses (Fitterman and Anderson, 1987; Asten, 1987; Liu, 1998). The transmitting waveform typically consists of three stages: turn-on, steady, and turn-off. The current in the turn-on stage gradually increases from zero to a certain value which would be maintained during the entire steady stage. Then the current in the source rapidly reduces to zero during the turn-off stage. Figure 6.1 shows a "bipolar" cycle of a typical transmitting waveform which contains two transmitting and two measurement stages. The currents of the two transmitting stages have opposite directions in order to mitigate system noise.

Recently, Zeng et al. (2019) analyzed the full waveform effects on TEM responses of half-space models and a real-life data-set collected over a graphite ore deposit using their FETD solver. The authors analyzed the effects of the turn-on, steady, and turn-off stages of a full waveform. It is found that the effect of the turn-on stage is generally smaller than the other two stages. A steady stage that is not long enough will cause the late-time responses to be smaller than that of the analytic solution for resistive half-space models (0.0004 S/m). For a conductive half-space model (25 S/m), the responses can be smaller than the analytic solution for all time gates including the early-time responses. The length of the ramp-off stage only affects early-time

146
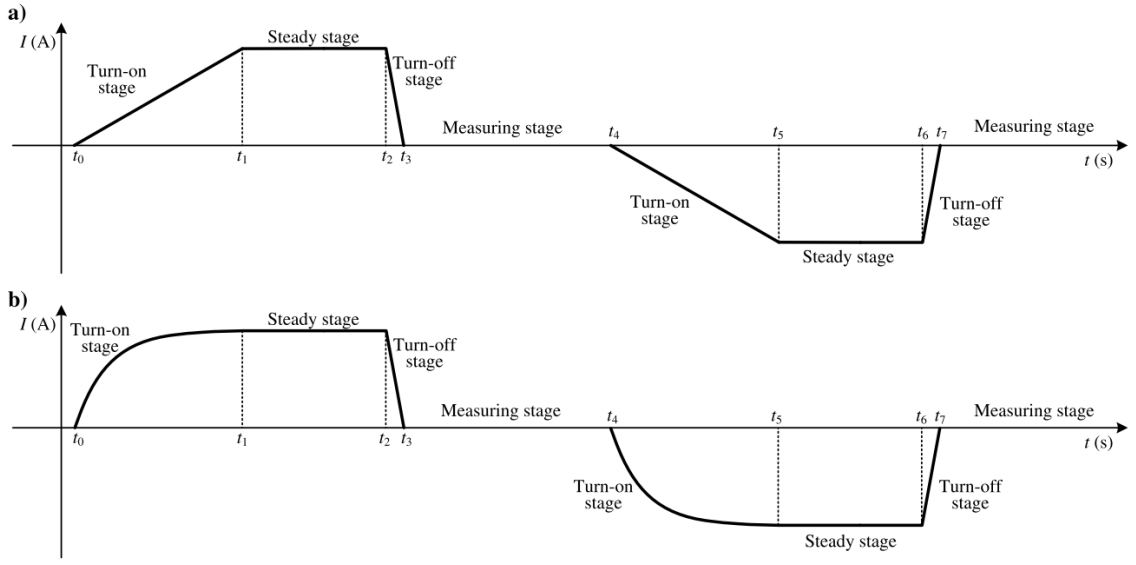
Figure 6.1: A schematic diagram of a bi-polar transmitting-current waveform. The turn-on edge is linear in (a) and non-linear in (b) (after Zeng et al. 2019).

responses for both conductive and resistive half-space models. A longer ramp-off stage leads to a weaker response in early times.

To understand how the waveform is affecting the measured response, it is necessary to investigate how the field changes with time during the transmitting and measurement stages. The turn-on and turn-off stages induce secondary magnetic fields with opposite directions which decay during the steady and measurement stages. The steady stage should be long enough so that the secondary magnetic field generated during the turn-on stage has vanished once it reaches the measurement stage. Otherwise, the measured secondary field can be smaller than the real value because the secondary field from the turn-on stage has an opposite sign to that of the turn-off stage. The length of the steady stage should be determined by the conductivity of the subsurface model. A more conductive model requires a longer steady stage sim-

ply because the decay of the secondary magnetic field generated by the turn-on stage takes longer to vanish compared to that of a more resistive model. The reason why a longer turn-off time leads to a smaller response is that by the time the measurement starts the secondary magnetic field has already decayed for a while. Also, the electromotive force generated by the sudden change of the magnetic field due to the turn-off of the source is inversely proportional to the turn-off time. Thus, a longer turn-off stage generates a smaller electromotive force which in turn causes the response in the early time to be smaller.

For modeling real data, it is therefore important to consider the actual transmitting waveform that is used in the data acquisition. Up until now, only step-off response is considered for all the models presented in this thesis. The step-off source is switched off instantaneously at $t = 0$ s and its response is approximated by reducing the initial value of the current density (always assumed to be 1 A/m^2) to zero within one iteration step which is normally extremely short (e.g., 10^{-7} s). Therefore, a shorter initial time step would lead to a more accurate approximation of the step-off response and generally it is set to a value at least four orders smaller than the time period of the measured data. For example, if the data is measured until 10 ms after the source is switched off, then the largest initial step that can be used is 10^{-6} s. To achieve the full-waveform modeling, there are two methods commonly used: one is to model the response from the beginning of the waveform through time-stepping, and the other is to convolve the step-off response with the actual waveform. The two methods, in theory, give the same result, however the computational resources

required can be very different.

In this chapter, a brief introduction to the incorporation of transmitting waveforms into the FVTD time-stepping modeling and the implementation of the convolution method will be given first. The responses calculated using the time-stepping process are then compared to those of the convolution method. Then, real data from the Preston Lake Project and the Close Lake Project will be modeled.

6.2 Incorporation of transmitting waveforms

To incorporate the waveform through time-stepping, the transmitting waveform should be discretized into a series of current density values. Smaller time steps are used for the turn-on and turn-off stages due to their relatively short lengths. Meanwhile, larger time steps can be used for the steady stage because the EM field is steady. Larger time steps can also lead to a more efficient modeling given that the steady stage is significantly longer than the lengths of turn-on and turn-off stages. Time steps in the turn-on and turn-off stages are generally set to 10^{-7} s and they should be at least one order smaller than the turn-on or turn-off stages. The time step for the steady stage is set to 10^{-5} s at the beginning and then gradually increases to larger values before it decreases to 10^{-5} s again at the end of the steady stage.

After the discretization of the current density, its derivative with respect to time is calculated using the first-order difference scheme. The initial conditions as described in Sections 4.4.2 and 5.4 are all set to zero when full waveforms are used, and the

149

initial value for the current density is also set to zero. Equation 4.3 for the E-field method and Equations 5.7 and 5.8 for the $A - \phi$ method are calculated iteratively with the discretized current density terms to get the full waveform response.

It is also possible to calculate the response of a step-off waveform with a ramp-off edge, that is, the current is assumed to have been turned on from negative infinity and gradually turns off starting at $t = 0$ within a short period of time. The initial conditions are the same as those in the modeling of the step-off responses. The current density then reduces to zero during multiple time steps discretizing the ramp-off stage. While normally non-linear turn-on and turn-off edges are used for EM transmitting systems, here they are considered to be linearly changing for simplicity.

Another commonly used method for calculating the full waveform response is through convolution. Let $f_s(t)$ and $f_w(t)$ be the step-off and full waveform responses, respectively, then $f_w(t)$ can be obtained by

$$f_w(t) = -\int_{-\infty}^{\infty} f_s(t - \tau)\frac{dI(\tau)}{d\tau}d\tau, \tag{6.1}$$

where $I(t)$ is the current density function of the waveform.

To calculate Equation 6.1, interpolation and possibly extrapolation of the step-off response is required. As shown in Figure 6.2, a trapezoidal transmitting waveform is considered and plotted left of the origin of the x-coordinate. The secondary field calculation starts at $t = 0$ and ends at $t = t_s$. Based on Equation 6.1, only the two shaded areas in the trapezoidal wave will have contributions for the full-waveform
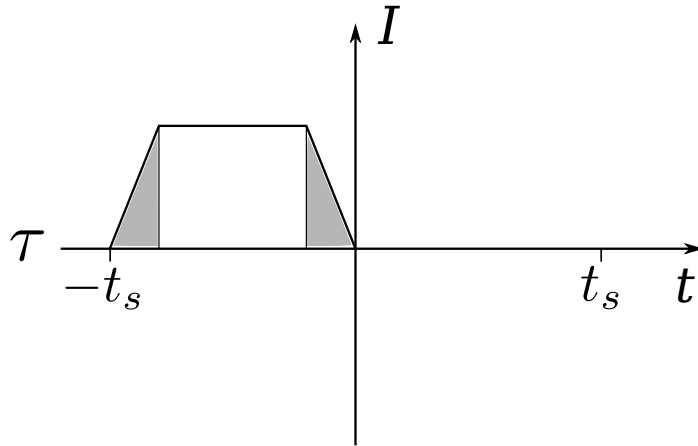
Figure 6.2: A diagram demonstrating how to calculate the convolution.

response since the time derivative of the transmitting current is zero for the steady stage. It is obvious that $t-\tau$ can be larger than t_s such that extrapolation of the step-off response is required if the forward modeling only calculated responses for $t < t_s$. When $t - \tau < t_s$, interpolation is likely required to get the step-off response for the exact time $t - \tau$. Also, when calculating the integration of Equation 6.1 numerically, turn-on and turn-off stages need to be discretized and optimal number of steps for the discretization of each stage should be sought in order to achieve satisfactory accuracy and efficiency. This will be investigated later using different examples.

Figure 6.3 shows various dB/dt responses calculated for a 0.01 S/m half-space model with a 100×100 m loop source. These responses are calculated using different waveforms by time stepping. The full-waveform response is also calculated by the convolution method based on the step-off response obtained from time stepping. The lengths of the turn-on, steady, and turn-off stages are 1, 10, and 0.01 ms, respectively, for the full waveform. All responses are calculated for 50 ms after the source is turned

off. Again, one receiver is located at the center of the source and the other is located at 200 m to the right side of the source center.

It can be seen that the full waveform responses calculated by time stepping and the convolution method have a good agreement for both receivers. At very early and late times, the full waveform solution is obviously smaller than the step-off and analytic solutions. The ramp-off response, that is, the response calculated by only considering the turn-off stage of the waveform, is very close to that of the full waveform response at earlier times and it becomes closer to the step-off and analytic responses at late times. This indicates the turn-off stage has a strong influence on the EM response over early times and the smaller values at late times observed from the full-waveform responses are mainly caused by the turn-on stage.

For convolution calculations, interpolation and extrapolation operations are needed in order to get the step-off response at specific times which can be later than the latest time of the secondary field modeled for the step-off response. Responses within the secondary field period can be calculated by spline interpolation and responses later than the end of the secondary field can be obtained by linear extrapolation of the step-off response in log-log space. For the extrapolation, a line fitting problem is first solved by the least squares method based on late time step-off responses in log-log space. It should be noted that the selected data points for the least squares problem should be late enough so that responses of conductive anomalies have already vanished. As explained in Section 5.5.2, if strong conductors exist in the model, the responses caused by the conductor still exist and the extrapolation method would not
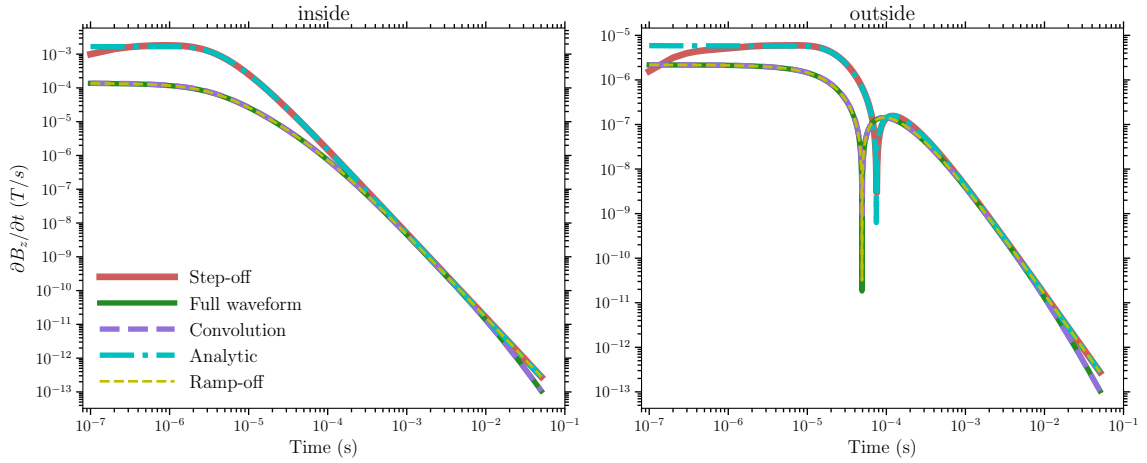
Figure 6.3: The dB/dt responses of the analytic, step-off, full waveform, ramp-off, and convolution solutions for a 0.01 S/m half-space model with a 100×100 m loop source. The left and right panels show the responses of the inside and outside receivers, respectively.

be able to give accurate enough result. Consequently, the modeling should be carried out to a time that is longer than the sum of the lengths of the secondary field and the waveform.

Figure 6.4 shows the responses for the same model as shown in Figure 6.3 but with a 400×400 m loop source. The transmitting waveform consists of 2 ms linear turn-on stage, 47.58 ms steady stage, and 0.42 ms turn-off stage. It can be seen that the convolution solutions for both the inside and outside receivers agree well with the full waveform solutions. At late times, the full waveform response is close to that of the step-off response due to a relatively longer steady stage so that the responses caused by the turn-on stage has already become small. Still, the ramp-off response is closer to the step-off response than the full waveform response, which means the influence of the turn-on stage still exists.

The time steps used in the discretization of the turn-on and turn-off stages in
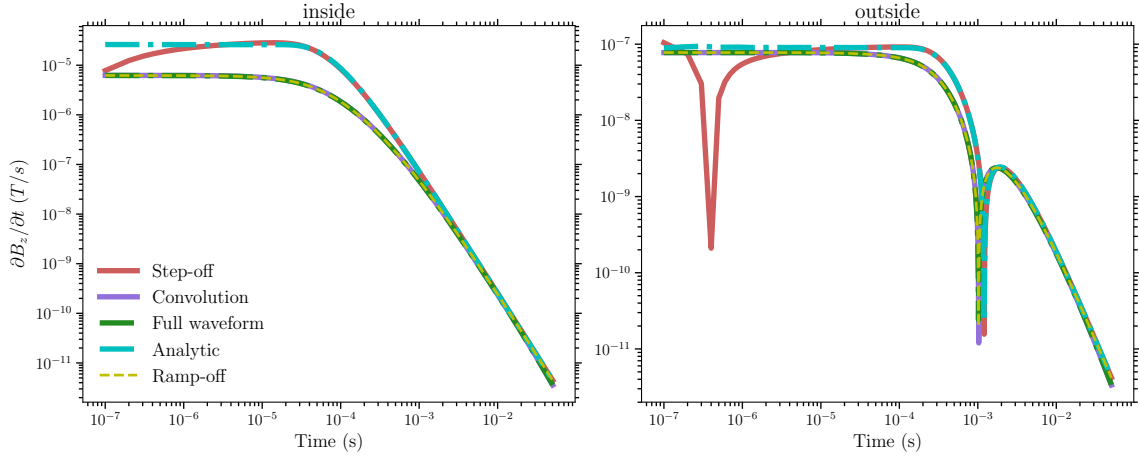
Figure 6.4: The dB/dt responses of the analytic, step-off, full waveform, ramp-off, and convolution solutions for a 0.01 S/m half-space model with a 400×400 m loop source. The left and right panels show the responses of the inside and outside receivers, respectively.

calculating the convolution response affect the accuracy of the convolution operation. The time steps used in Figures 6.3 and 6.4 were 10^{-8} s and 10^{-7} s, respectively. These values are very small which result in good accuracy but can take a long time to calculate especially when there are many receivers in a survey. Figure 6.5 shows the relative errors between responses calculated by the convolution and time-stepping methods for different schemes used in the discretization of the turn-on and turn-off stages. The model is the 0.01 S/m homogeneous half-space with a 100×100 m loop source. The detailed information about these schemes and their respective calculation times are given in Table 6.1. From Figure 6.5, it can be seen that shorter time steps lead to a closer match between the convolution and time-stepping methods. Meanwhile, shorter time steps also result in larger numbers of time steps which require longer computational time. Schemes 3 and 4 give very similar results but Scheme 4 requires much longer computation time. Comparing Schemes 3 and 5, 4 and 6, which

154
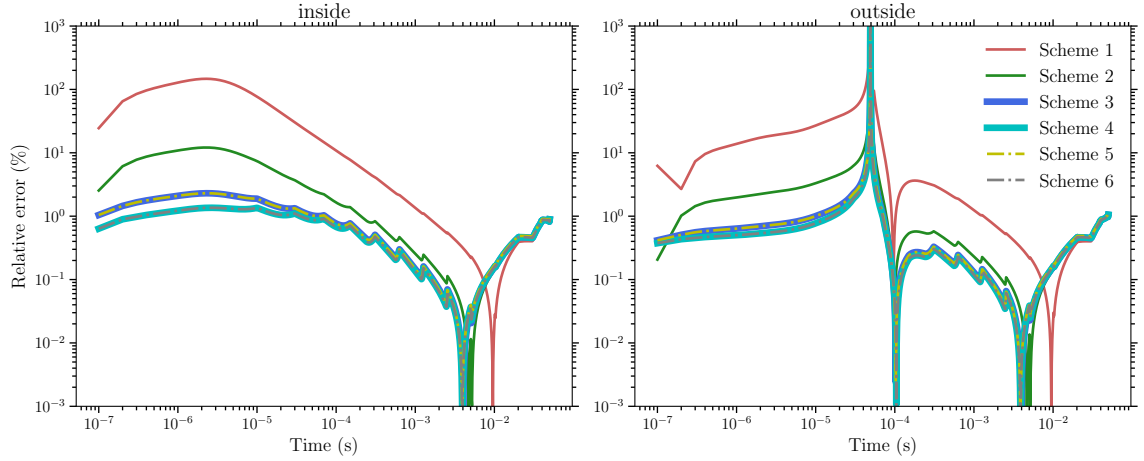
Figure 6.5: The relative errors between responses calculated by convolution and time-stepping methods for different discretization schemes of the 0.01 S/m homogeneous model with a 100×100 m loop source. Detailed information about the schemes is listed in Table 6.1.

Table 6.1: Discretization schemes used in the convolution calculation for the full waveform responses shown in Figure 6.3 and their corresponding computation times (T_c).

Scheme	Δt_{on} (s)	Δt_{off} (s)	N_{on}	N_{off}	T_c (s)
1	10^{-5}	10^{-5}	100	8	0.38
2	10^{-6}	10^{-6}	1000	80	1.48
3	10^{-7}	10^{-7}	10,000	800	9.19
4	10^{-8}	10^{-8}	100,000	8,000	84.54
5	10^{-5}	10^{-7}	100	800	1.14
6	10^{-6}	10^{-8}	1,000	8,000	6.89

have the same time steps for the turn-off stage, it is found that the influences of time step lengths of the turn-off stage are more significant than those of the turn-on stage. This is because the responses of the turn-on stage can be significantly smaller than those of the turn-off stage, depending on the length of the steady stage, at a given time when calculating the convolution. Based on the relative errors and computation times of all the schemes, Scheme 5 gives the best result and is used in future modelings.

155
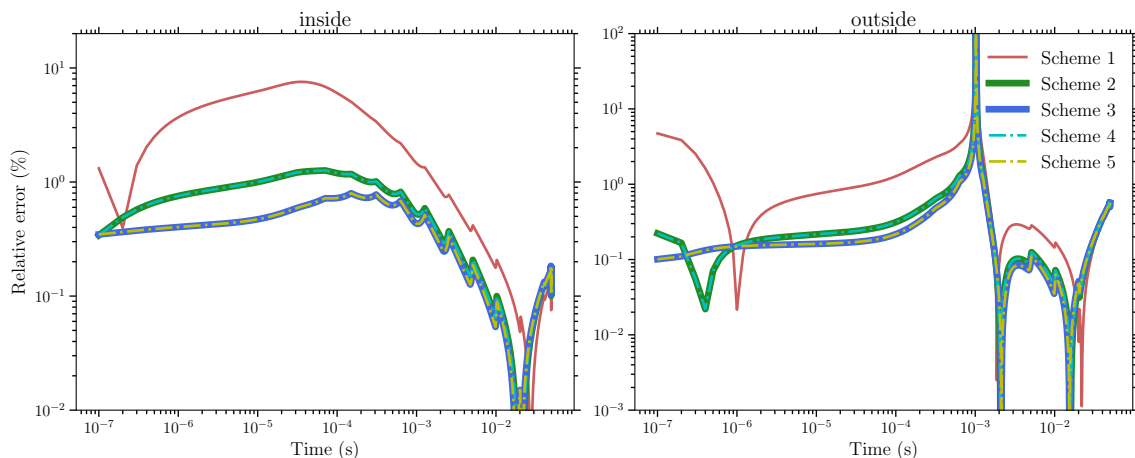
Figure 6.6: The relative errors between responses calculated by convolution and time-stepping methods for different discretization schemes of the 0.01 S/m homogeneous model with a 400×400 m loop source. Detailed information about the schemes is given in Table 6.2.

Table 6.2: Discretization schemes used in the convolution calculation for the full waveform responses shown in Figure 6.4 and their corresponding computation times (T_c).

Scheme	Δt_{on} (s)	Δt_{off} (s)	N_{on}	N_{off}	T_c (s)
1	10^{-5}	10^{-5}	200	42	0.39
2	10^{-6}	10^{-6}	2000	420	1.76
3	10^{-7}	10^{-7}	20000	4200	13.95
4	10^{-5}	10^{-6}	200	420	0.6
5	10^{-6}	10^{-7}	2000	4200	4.13

Figure 6.6 shows relative errors between responses of the convolution and time-stepping methods for the 0.01 S/m homogeneous model with a 400×400 m loop source. Detailed information and computation times of the five different discretization schemes are given in Table 6.2. Similar observations can be made as when a 100×100 m loop source is used except that the match between the convolution response and the time-stepping response is closer when the same time steps are used (e.g., Scheme 3 for both cases). Scheme 4 gives the best result in terms of both accuracy and efficiency.

6.3 Preston Lake project

6.3.1 Project introduction

The Preston Lake Project area (Figure 6.7) is located about 35 km south of the southwestern edge of the Athabasca Basin in northern Saskatchewan, Canada. In December, 2017, a Moving-Loop TEM survey was conducted in the northern part of the area west of Preston Lake by Abitibi Geophysics. This survey was designed to target conductor trends identified from the 2013 VTEM data (Figure 6.8). There were two survey grids, North Grid and South Grid, and 13 lines surveyed with a total length of 38 km. The size of the transmitter loop was 100×100 m and the receiver offset was 200 m. The survey used GEONICS TEM57 MK2 as the transmitter which utilizes a bipolar waveform (50% duty cycle) with a frequency of 31.25 Hz. The turn-off time was 80 μs while the lengths for turn-on and steady stages were unspecified. Three-component dB/dt and B-field data were collected simultaneously using the ARMIT MK2 sensor. In total, 20 channels of data ranging from 0.1042 ms to 6.0928 ms were collected. The elevation around the project area is 500 to 550 m above sea level.

For the project area, a drilling program was conducted in the winter of 2018 but the drilling data are not available. Only one line of data will be modeled here due to the lack of detailed drilling data and physical property measurements. The data come from Line 4800E in North Grid. The survey profile was 3 km long. The station spacing was 50 m and there were 61 stations in Line 4800E.
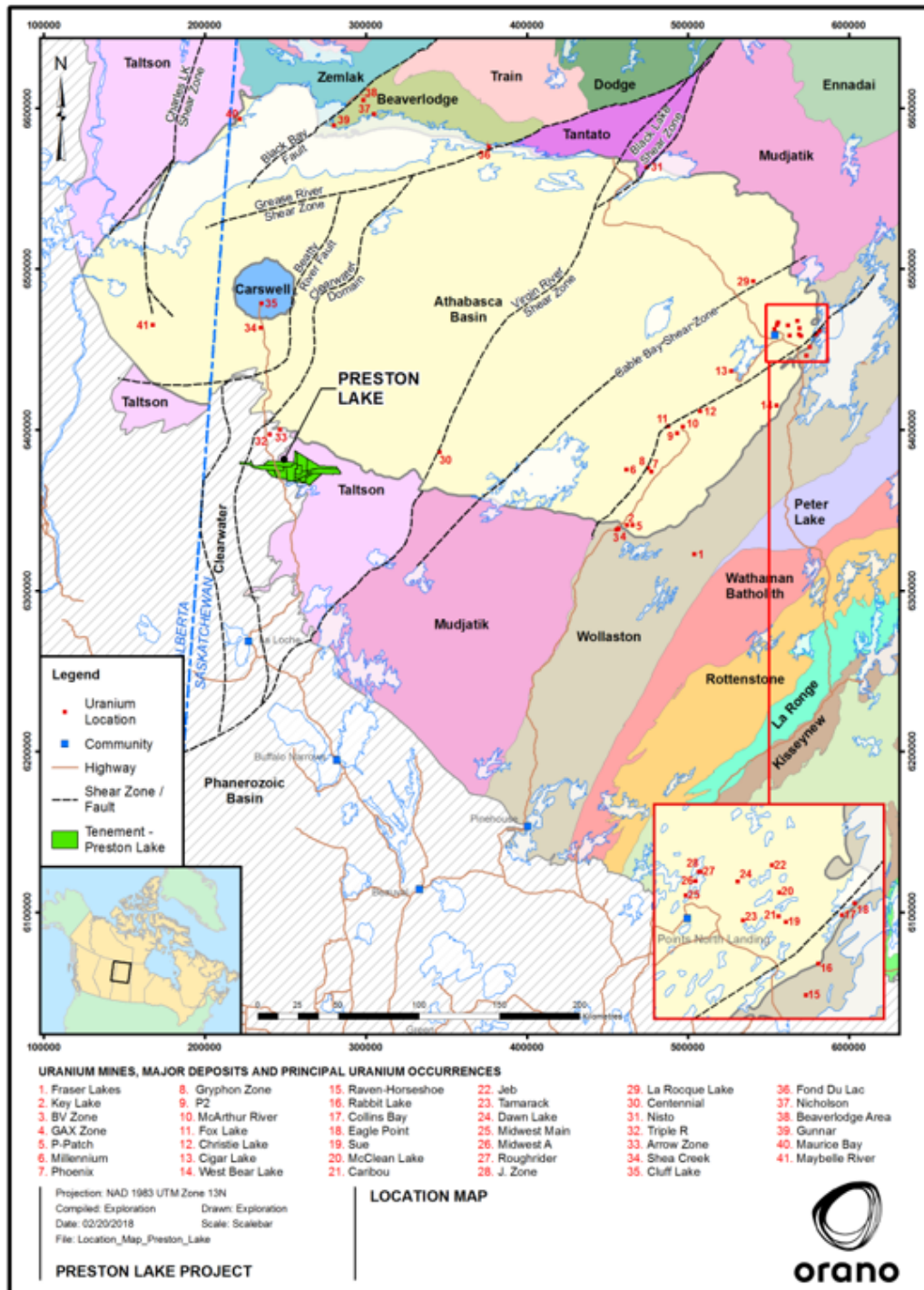
Figure 6.7: The location (green shaded area) of the Preston Lake Project survey (courtesy Orano Canada Inc.).
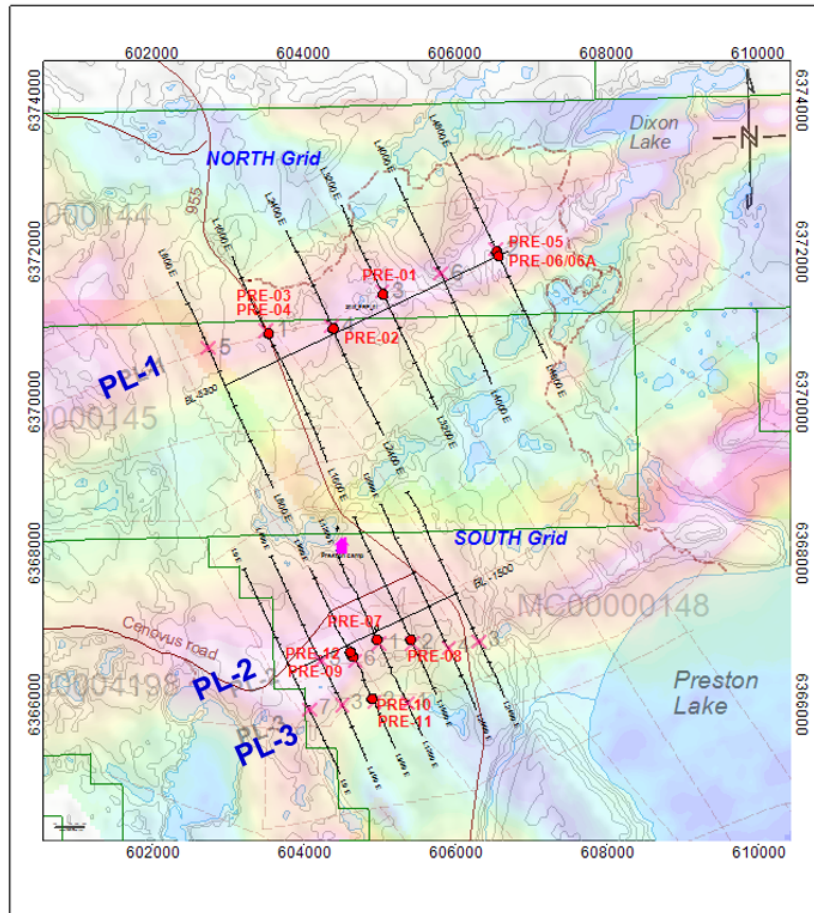
Figure 6.8: The survey grids of the Preston Lake Project Slingram TEM survey superimposed upon VTEM data (courtesy Orano Canada Inc.).
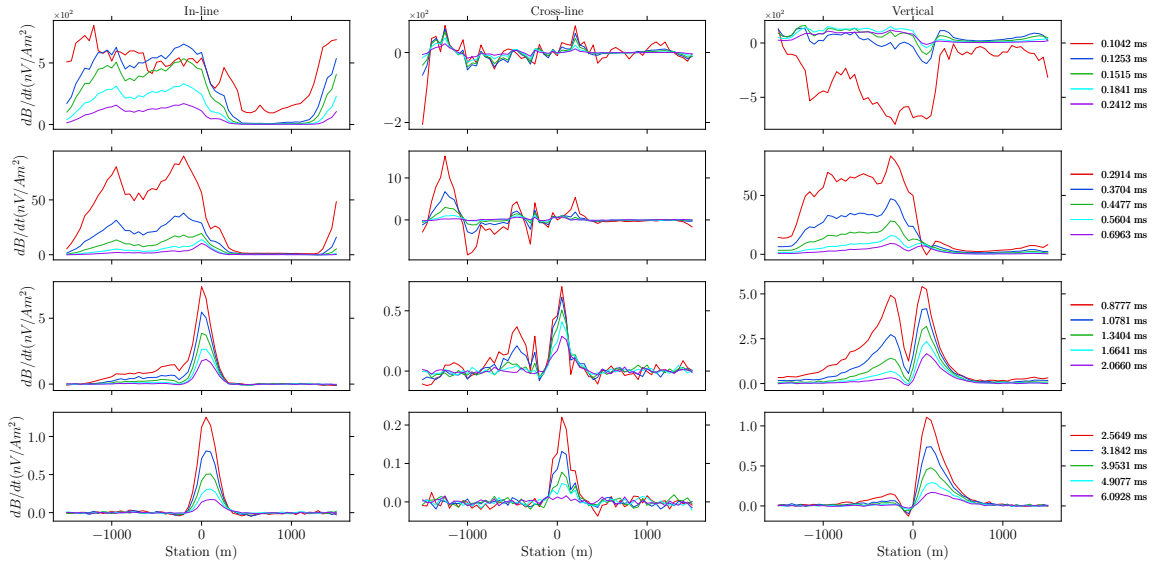
Figure 6.9: Three-component dB/dt data from Line 4800E of the Preston Lake Project.

Figures 6.9 and 6.10 show the three-component dB/dt and B-field responses of the real data collected on Line 4800E. As can be seen in the two figures, the early time channels are very noisy, especially for the dB/dt data. The noise may come from certain shallow conductive geologic structures. At later times starting from $t = 0.8777$ ms, the vertical responses of both dB/dt and B-field data show typical responses of a conductive plate dipping to the positive direction of the profile. Note that the B-field data clearly show the anomaly starting from the sixth channel while the dB/dt data are still quite noisy at that time. The anomaly persists until the last channel for both the dB/dt and B-field data while the B-field data are less noisy. Also, the dynamic range of the B-field data for the collected 20 channels is smaller than that of the dB/dt data. All these observations are consistent with previous comparisons of dB/dt and B-field data (Macnae and Kratzer, 2012; Asten and Duncan, 2012).
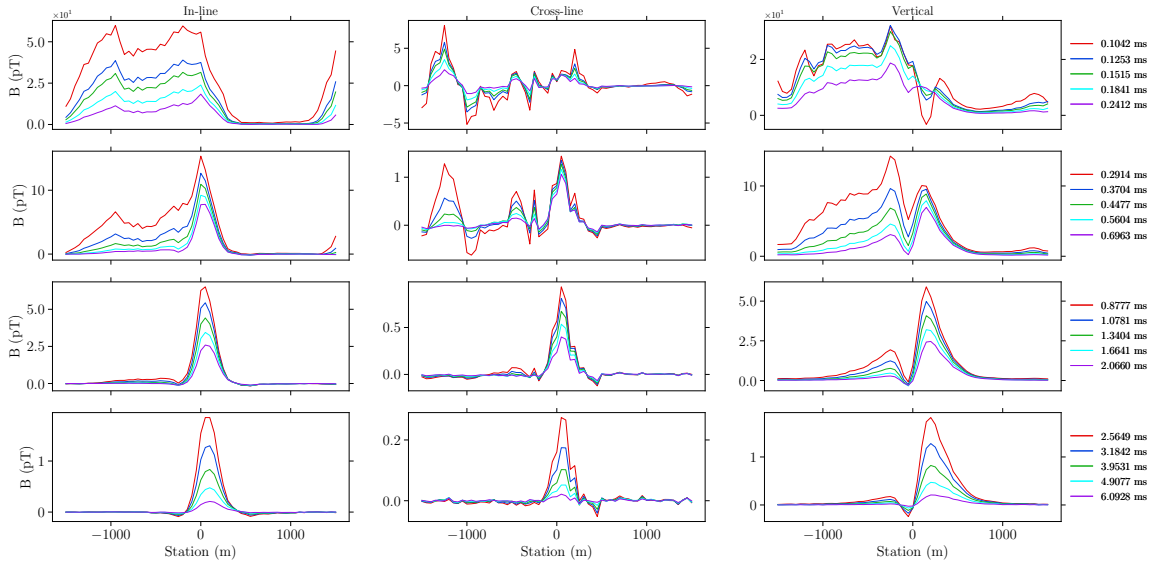
Figure 6.10: Three-component B-field data from Line 4800E of the Preston Lake Project.

6.3.2 Trial-and-error modeling

The method developed in Section 2.4 was used here to generate the mesh for the modeling of the Preston Lake Project. The survey area is generally flat and topography was not considered here for the modeling. Tetrahedral edges with a length of 10 m and regular tetrahedra with an edge length of 10 m were used for the refinements of the mesh at sources and receivers, respectively.

The project area is outside of the Athabasca Basin so that no sandstone layer exists. For the basement, it was still treated as a layered Earth model since no detailed regional geological information and physical property data were available. Through trial-and-error, it was found that a 20m thick conductor dipping 30 degrees to the right side of the profile buried at 100 m below the surface in a five-layer layered Earth model can generate responses that can match the real data reasonably well.

161

Table 6.3: Conductivities of each unit in the model shown in Figure 6.12.

Unit	Conductivity (S/m)	Unit	Conductivity (S/m)
Air	10^{-8}	Overburden	0.01
C1	1.3	C2	1.7
BSMT1	2×10^{-3}	BSMT2	10^{-4}
BSMT3	10^{-4}	Background	10^{-4}

The coordinates of the survey line were rotated such that the profile is along the y-axis, with the first and the last stations located at (0, -1500, 0) m and (0, 1500, 0) m, respectively. The strike of the fault was set to 80º in order to match the non-zero cross-line response.

Figure 6.11 is a screenshot taken from the FacetModeller software which shows the model built for the Preston Lake project. The overburden layer with a thickness of 30 m is located on the top of the model. Following the overburden layer, there are two layers of basement above the background (which is not shown in the figure). The first layer is 70 m thick and the second is 400 m thick. The strike length of the conductor is 2,200 m and the depth extent is 850 m. The top center of the conductor is located at (0, -100, -100) m. Figure 6.12 shows the tetrahedral mesh of the model created by FacetModeller (Figure 6.11). There are 1,172,593 edges and 999,076 cells generated by TetGen using only the maximum edge-radius ratio constraint of 1.15. The conductivities of each unit in the model are listed in Table 6.3.

The E-field FVTD method was used to calculate the dB/dt responses of the model, and the B-field response was obtained through numerical integration. For a more
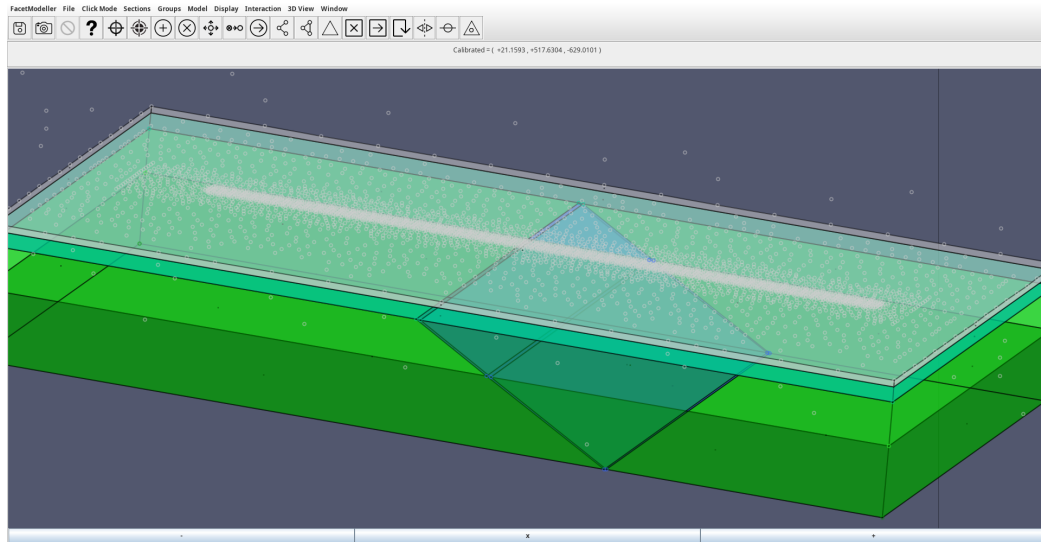
Figure 6.11: A screenshot taken from FacetModeller software showing the 3D model built for the Preston Lake model. The white nodes come from the surface mesh and they contain refinements designed for sources and receivers of Line 4800E.

accurate integration result, the modeling was carried out until 500 ms after the source was switched off. The multiplier and number of iteration steps in each section are set to 2 and 50, respectively, which led to 712 iteration steps in total.

Figure 6.13 shows the dB/dt responses calculated by the E-field FVTD method and the real data. It is clear that the real data are very noisy for the first 10 channels and consequently there is no good match between the two data-sets. After the first 10 channels, the data quality improves and a good match can be observed, especially on the right part of the profile for the vertical component data. For the vertical component, the modeled data have a better match with the real data for the right peak than the left peak, especially at middle times. For the in-line component, a good match is also only observed for middle to late times, and the magnitude of the modeled data is slightly larger than that of the real data. For the cross-line component, the

163
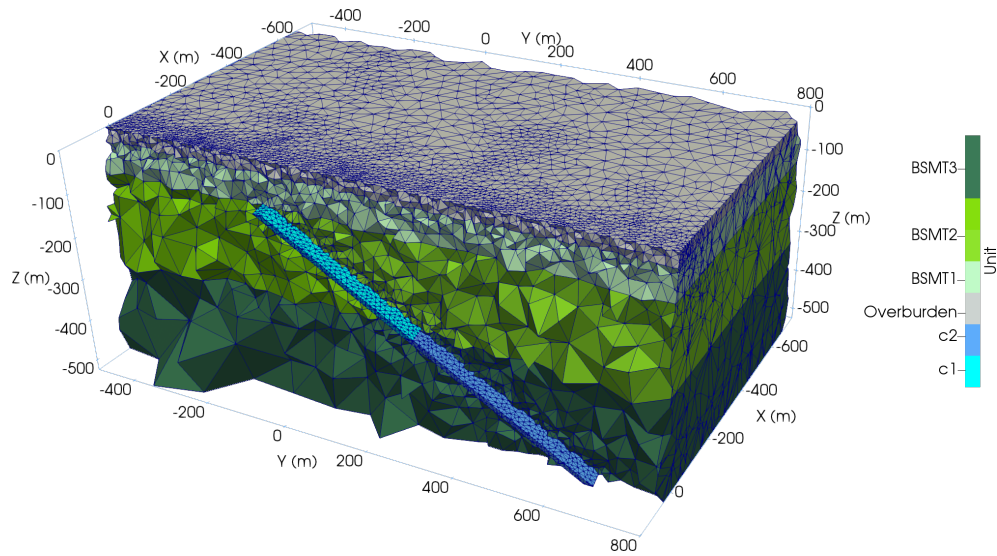
Figure 6.12: The unstructured tetrahedral mesh generated by TetGen for the model shown in Figure 6.11.

real data are noisy even at late times, but a good match can be seen for late times, confirming the necessity for keeping the conductor strike not completely perpendicular to the profile. No attempt was made in this model to match the early-time data due to the large noise existing in the field data, which might be caused by shallow conductive geological structures.

Figure 6.14 shows the comparison of the B-field responses obtained by the numerical integration of the dB/dt response calculated by the E-field FVTD method and the field data. Compared to Figure 6.13, the B-field responses are less noisy, and therefore a good match can be achieved starting from the sixth channel. The in-line component from the numerical solution is also larger than the real data, similar to what was observed for the dB/dt data. The cross-line component is less noisy compared to the dB/dt response and thus a better match is observed. The vertical component still cannot get a good match for the left peak, especially at middle times. The right

164
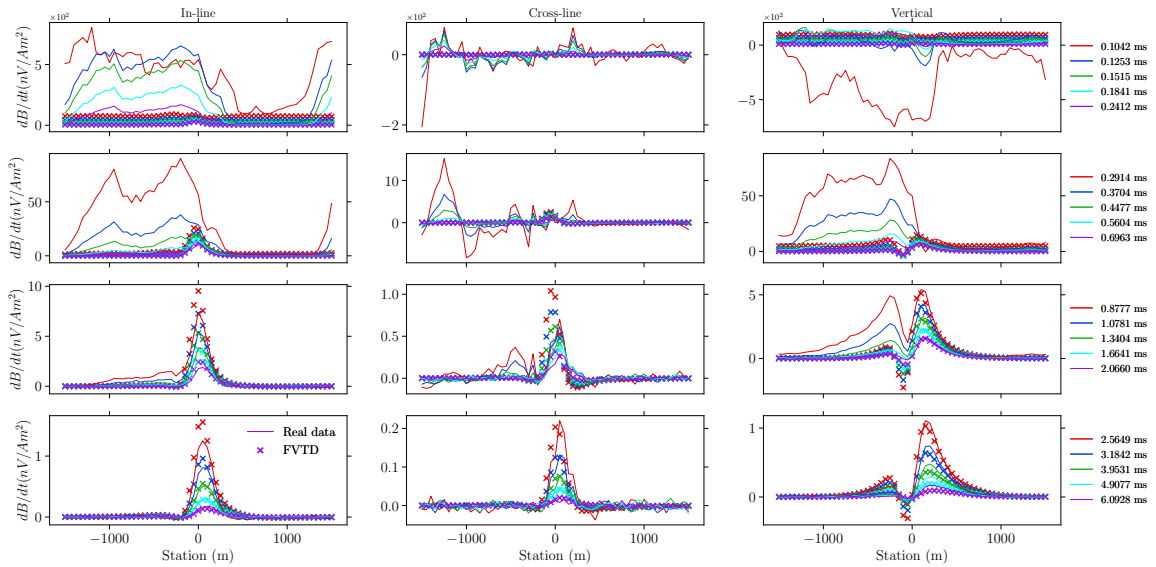
Figure 6.13: The dB/dt responses calculated by the FVTD method and the field data of Line 4800E of the Preston Lake Project.

peak of the numerical solution is now slightly smaller than the real data, which was not observed for the dB/dt response.

The dB/dt and B-field responses of the field data are recorded using different sensors simultaneously along the same profile with the same configuration. It is very obvious that the dB/dt data are noisier compared with the B-field data. The dB/dt and B-field responses of the numerical data are calculated for the same geophysical model and they can both match the field data reasonably well.
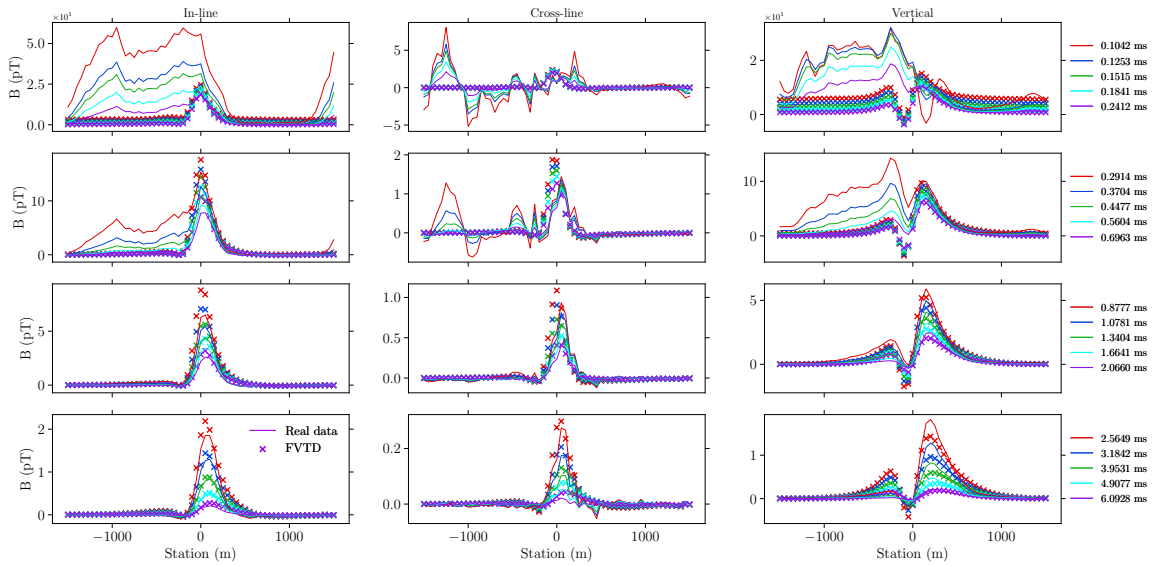
Figure 6.14: The dB/dt responses calculated by the FVTD method and from the field data of Line 4800E of the Preston Lake Project.

6.4 Close Lake project

6.4.1 Project introduction

The second example is taken from the Close Lake Project. The project area is located at the southeastern part of the Athabasca Basin and is marked by the green-shaded area near the eastern edge of the basin as shown in Figure 6.15. The world-class McArthur River (number 4 in Figure 6.15) and Cigar Lake (number 6 in Figure 6.15) uranium mines are located at the south and east, respectively, of the Close Lake Project area.

The area is approximately 500 m above sea level. The overburden layer thickness ranges from 20 m to 60 m approximately, which is mainly comprised of glacial tills. The basin sandstone in the project area is represented by Manitou Falls Formation

which can be further divided into three members from top to bottom: Manitou Falls Dunlop (MFd), Manitou Falls Collins (MFc), and Manitou Falls Bird (MFb). The Athabasca strata are generally flat lying. The unconformity depth for the project area ranges from 420 m to 770 m according to drilling data. The basement is comprised of metasedimentary units consisting predominantly of pelitic gneiss, psammo-pelitic gneiss, quartzite and calc-silicate. Brittle and ductile deformation can be observed around the graphitic shear zone known as the C1 conductor. The fault was clearly reactivated after the deposit of the basin sandstone because it extends all the way up through the sandstone basin. Uranium mineralization with a concentration greater than 0.5 ppm were developed above the unconformity near the graphitic shear zone. At the top of the basement, there is a paleoweathering layer with a thickness up to 50 m based on drilling data.

Exploration work dates back to 1978 for the project area, and multiple conductive trends have been identified by continuous geophysical exploration and diamond drilling campaigns in the past several decades. Figure 6.16 shows these conductors over the entire project area, superimposed on the late-time (channel 16 of the off-time response) responses measured by the time-domain airborne MEGATEM system.

In 2013, a Moving-Loop TEM survey was conducted in the southern part of the property (Figure 6.17). An IPHT/Supracon High Temperature "Jessy Deep" superconducting quantum interference device (SQUID) sensor, a Geonics EM-37 transmitter, and Electro-Magnetic Imaging Technology (EMIT) SMARTem24 digital receiver were used for the survey. The receiver recorded three-component B-field using
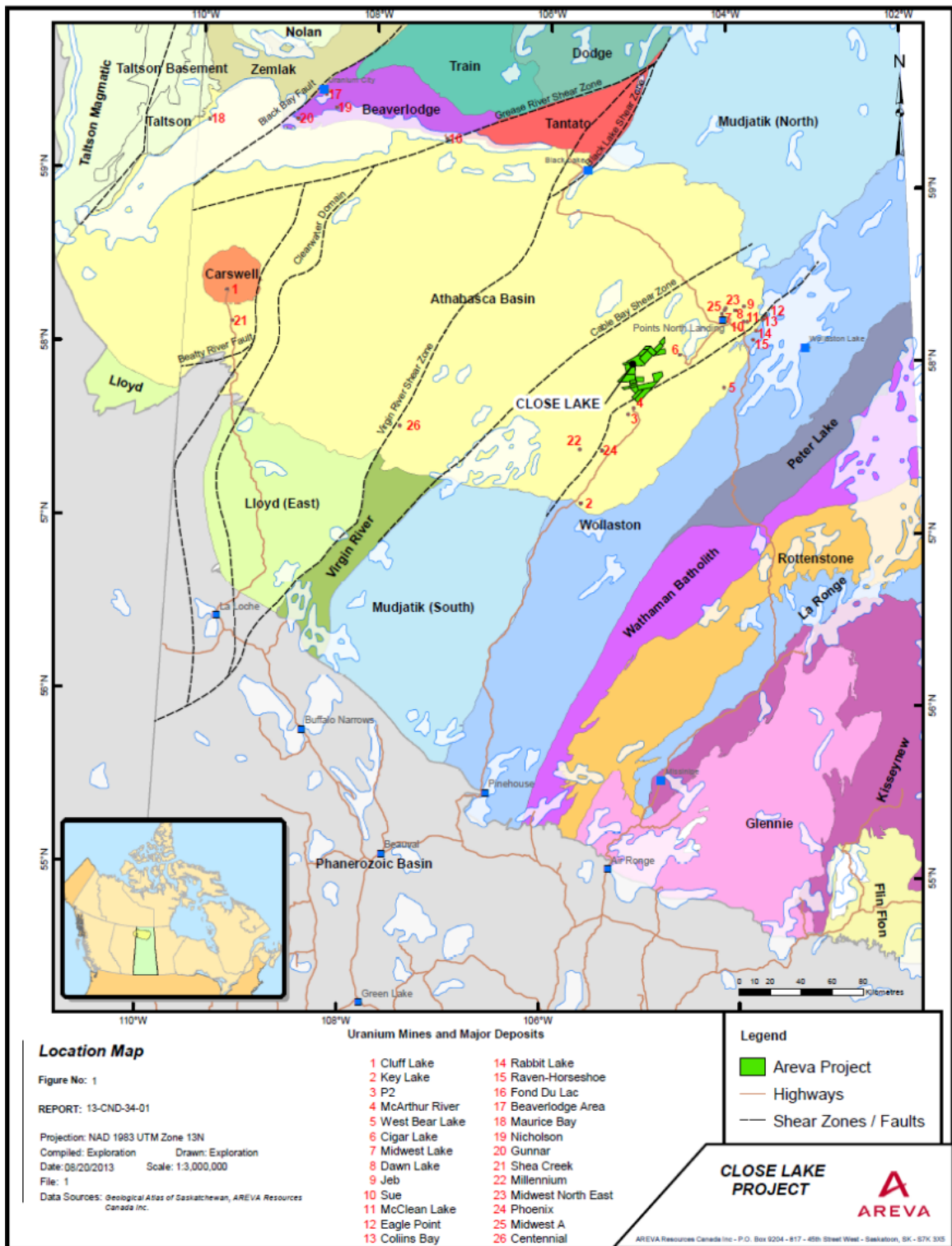
Figure 6.15: The geological map of the Athabasca Basin. Close Lake Project is located in the sourtheast part of the basin (Hutchinson and Zalustskiy, 2015).
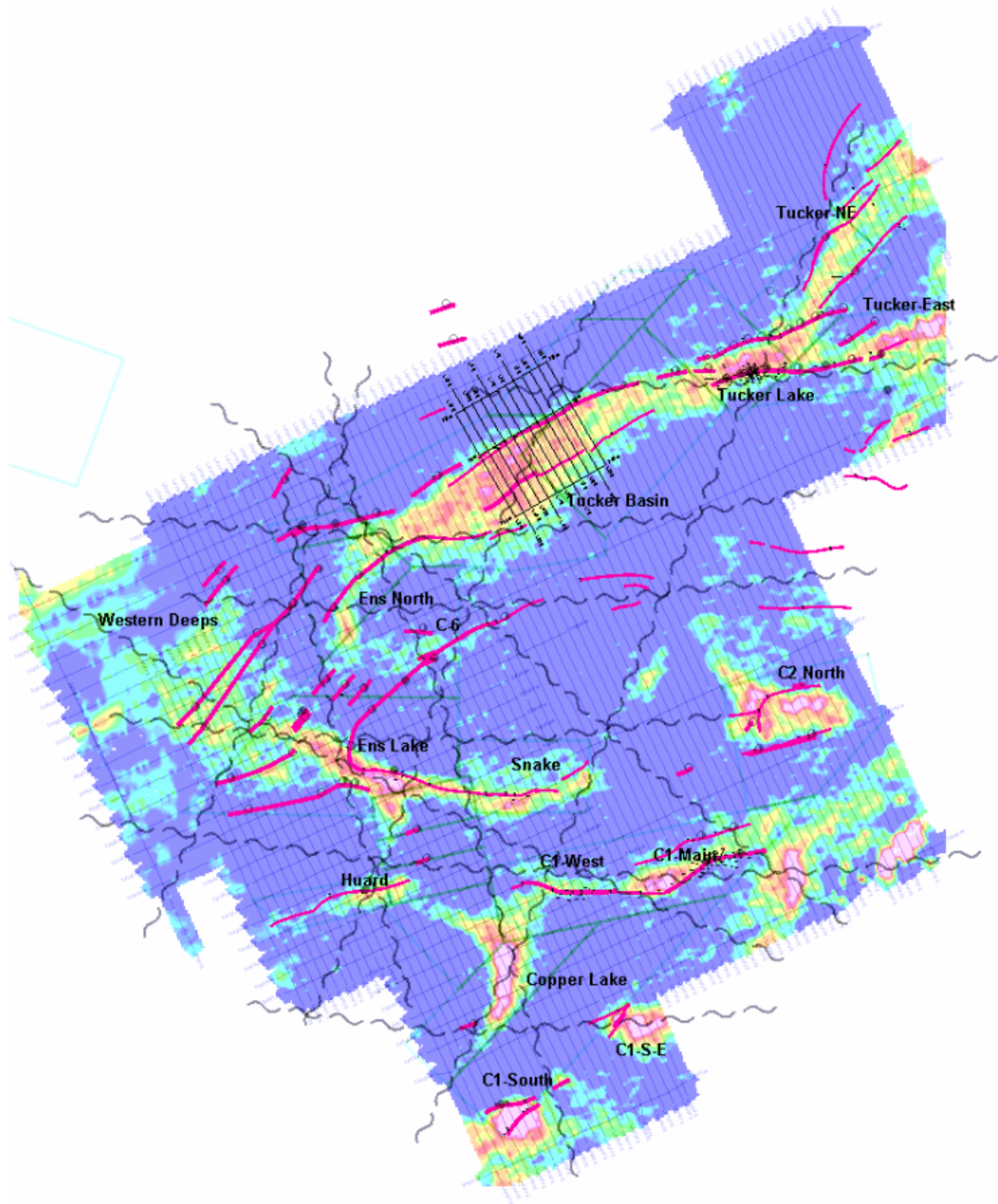
Figure 6.16: Major conductive trends at the Close Lake Project area superimposed on the late-time responses (channel 16 of the off-time respones) of the 2014 airborne MEGATEM time-domain EM survey (Bingham, 2004).
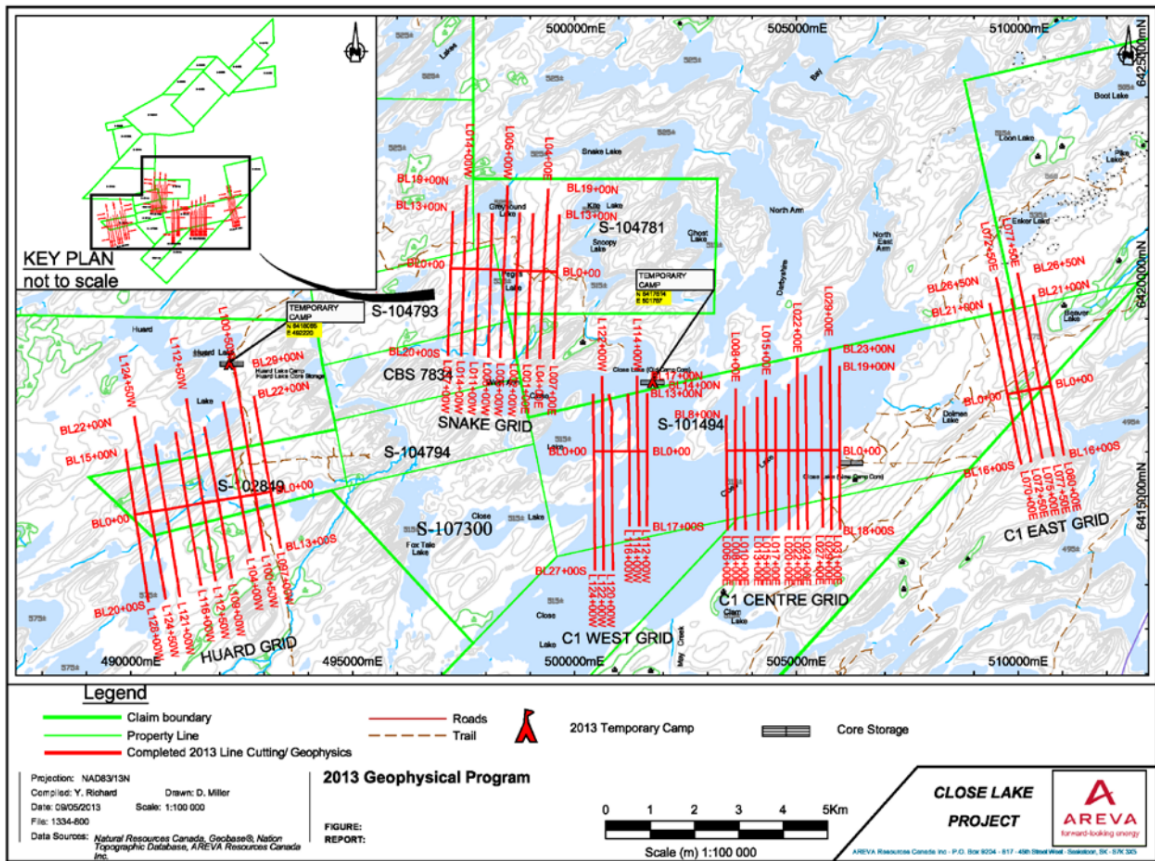
Figure 6.17: The 2013 moving-loop TEM survey grids for the Close Lake Project (Richard, 2013).

the SQUID sensor. The synchronization between the receiver and transmitter was performed using a crystal clock at a base repetition rate of 5 Hz, resulting in 29 logarithmically-spaced secondary channels ranging from 0.1 ms to 42.7 ms. For the transmitting waveform, the turn-off stage was 0.42 ms and the turn-on stage was unspecified. In total, 40.5 km survey were carried out over five grids: C1-East Grid, C1-Center Grid, C1-West Grid, Snake Grid and Huard Grid. Among them, C1-West, C1-Center, and C1-East grids were specifically designed to locate and characterize the C1 conductor. A 400×400 m loop source was used for the above three grids and the station spacing was set to 100 m.

Later in 2015, a diamond drilling program was conducted to target the conductors along the C1 conductive trend as interpreted from the 2013 Moving-Loop TEM survey, particularly at the underexplored western and central portions of the C1 conductive trend. Figure 6.18 shows the 2015 (large red square) and historical (small black square) drill hole collar locations superimposed on the 2013 moving-loop TEM survey grids (C1-Center and part of C1-West). Figure 6.19 shows an interpretation map based on the drilling results. The red lines are the interpreted conductive trend based on historical data while the green line marks the C1 conductive trend based on the interpretation of the 2013 moving-loop TEM survey. The 2015 program consisted of 10 diamond drilling holes all reaching the basement with a total meterage of 5,828.4 m.

Geochemical analyses were carried out on samples taken from all the 10 drill holes. The spectral clay sampling was performed every three meters. A 10 cm long core sample was collected for every 10 to 20 m in the sandstone and basement units based on the lithology and alteration in order to measure physical properties. Resistivity and chargeability properties were measured with a Sample Core I.P. Tester (SCIP) manufactured by Instrumentation GDD Inc. The instrument uses a controlled electrical source and a direct current method to measure the resistivity and chargeability values of rock samples. Petrographic analyses were also conducted on all drill hole samples ($\leq$ 10 cm) to determine mineralogy and alteration. Down-hole gamma probing was used to analyze each hole immediately after drilling was completed. Down-hole resistivity probing was completed in some of the holes when there was no drill rod inside the
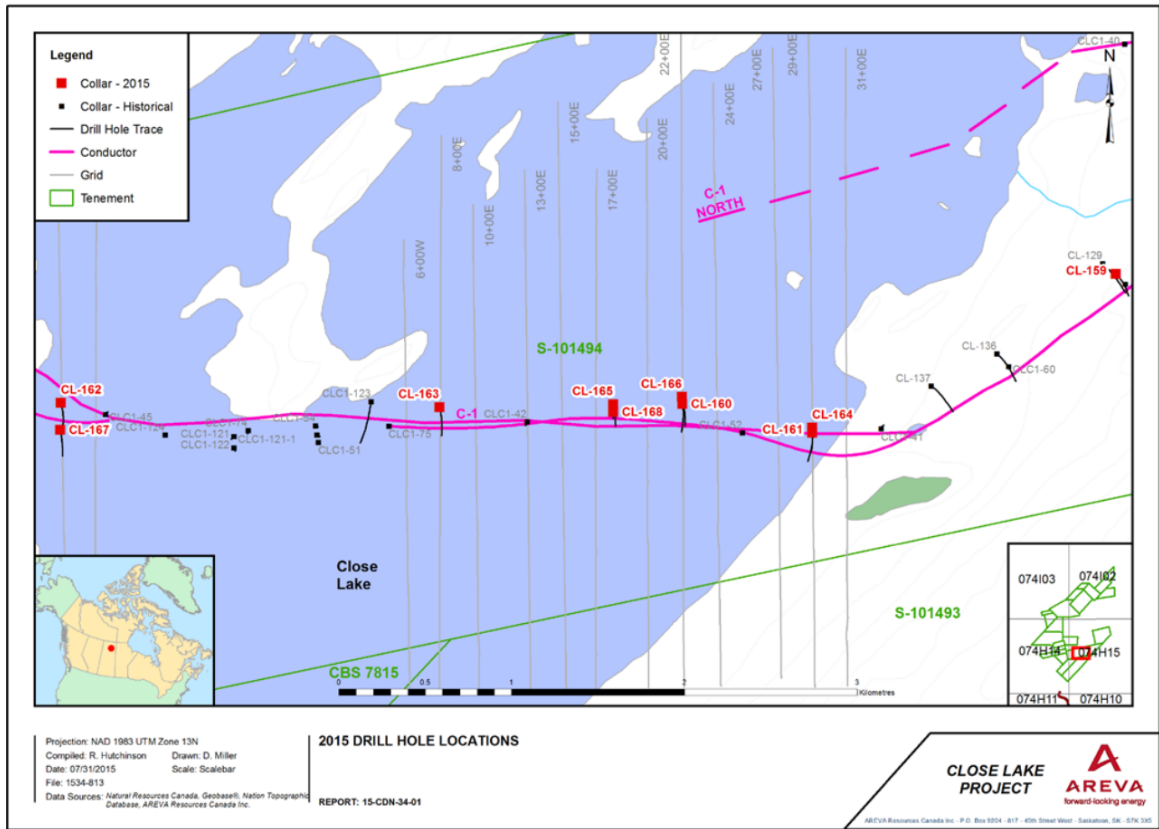
Figure 6.18: The 2015 diamond drilling map superimposed on the 2013 moving-loop TEM survey grids of the Close Lake Project (Hutchinson and Zalustskiy, 2015).
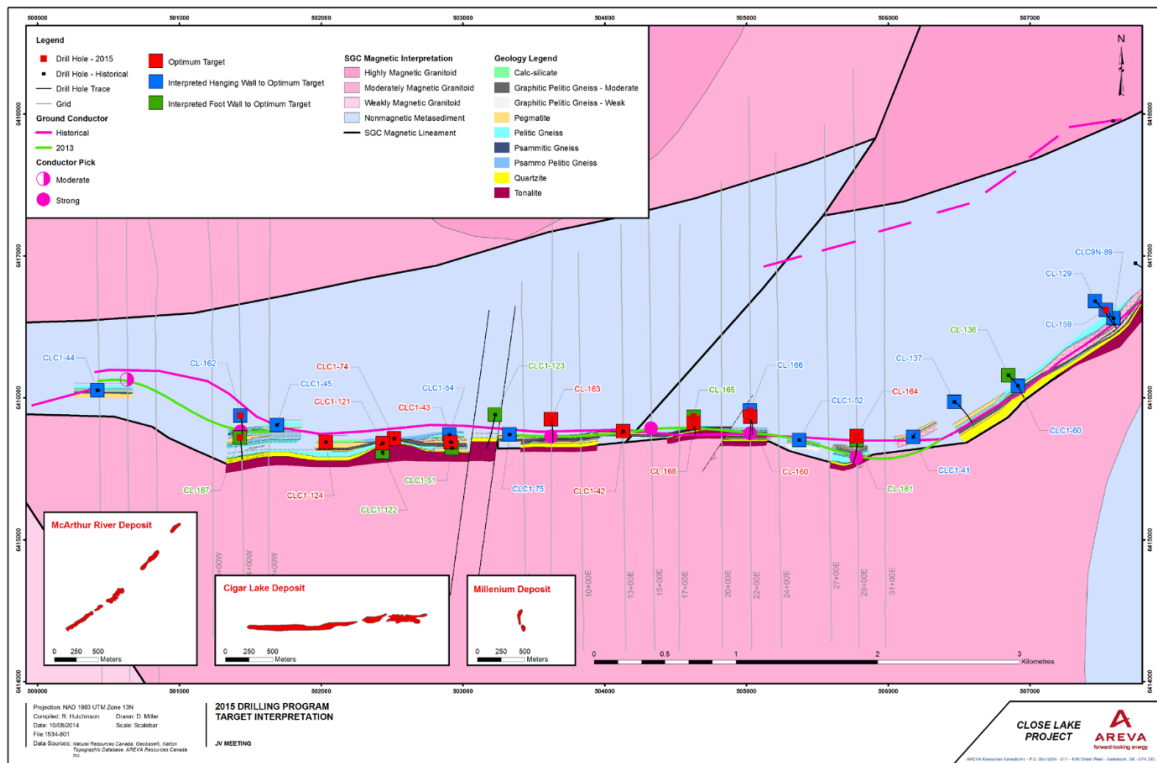
Figure 6.19: The interpretation of the 2015 and historical diamond drilling results (Hutchinson and Zalustskiy, 2015).

hole. Otherwise, the resistivity probing cannot be carried out. The down-hole probing was measured by a Dual Focused Resistivity Sonde manufactured by GeoVista. Six out of ten holes recorded graphitic pelitic gneisses around the unconformity.

For this project, trial-and-error modeling experiments were carried out for the 2013 moving-loop TEM survey data in order to better understand how the C1 conductor and other basin and basement structures influence the EM data. C1-West and C1-Center grids were chosen to be modeled.

Table 6.4: Coverage area of the C1-Center grid in the 2013 moving-loop TEM survey of the Close Lake Project.

Line	First station	Last station	Profile length (km)
800E	1300S	1100N	2.4
1500E	1300S	1300N	2.6
2200E	1300S	1800N	3.1
2900E	1300S	2000N	3.3

6.4.2   C1-Center Grid

Figure 6.20 plots the grid coordinates of each profile on top of the UTM coordinates. The blue rectangles at the beginning and the end of each profile represent the loop source used for the first and the last stations in the respective profiles. The red lines connect the first and last stations in each profile. The receivers are located 600 m to the north of the center of the loop source along the profile and the location of the station is the center of the source and receiver. Table 6.4 lists the coverage area of each profile in the C1-Center Grid.

6.4.2.1   Modeling of Line 2200E

The data from a single line, Line 2200E, was selected to be modeled first in order to get a general understanding of the survey area. Line 2200E was chosen because it has one of the lowest noise levels among all four lines in C1-Center Grid while the two drill holes drilled on the profile all hit graphite at the fault zone around the unconformity.

Figure 6.21 shows the three-component B-field data of Line 2200E. The vertical
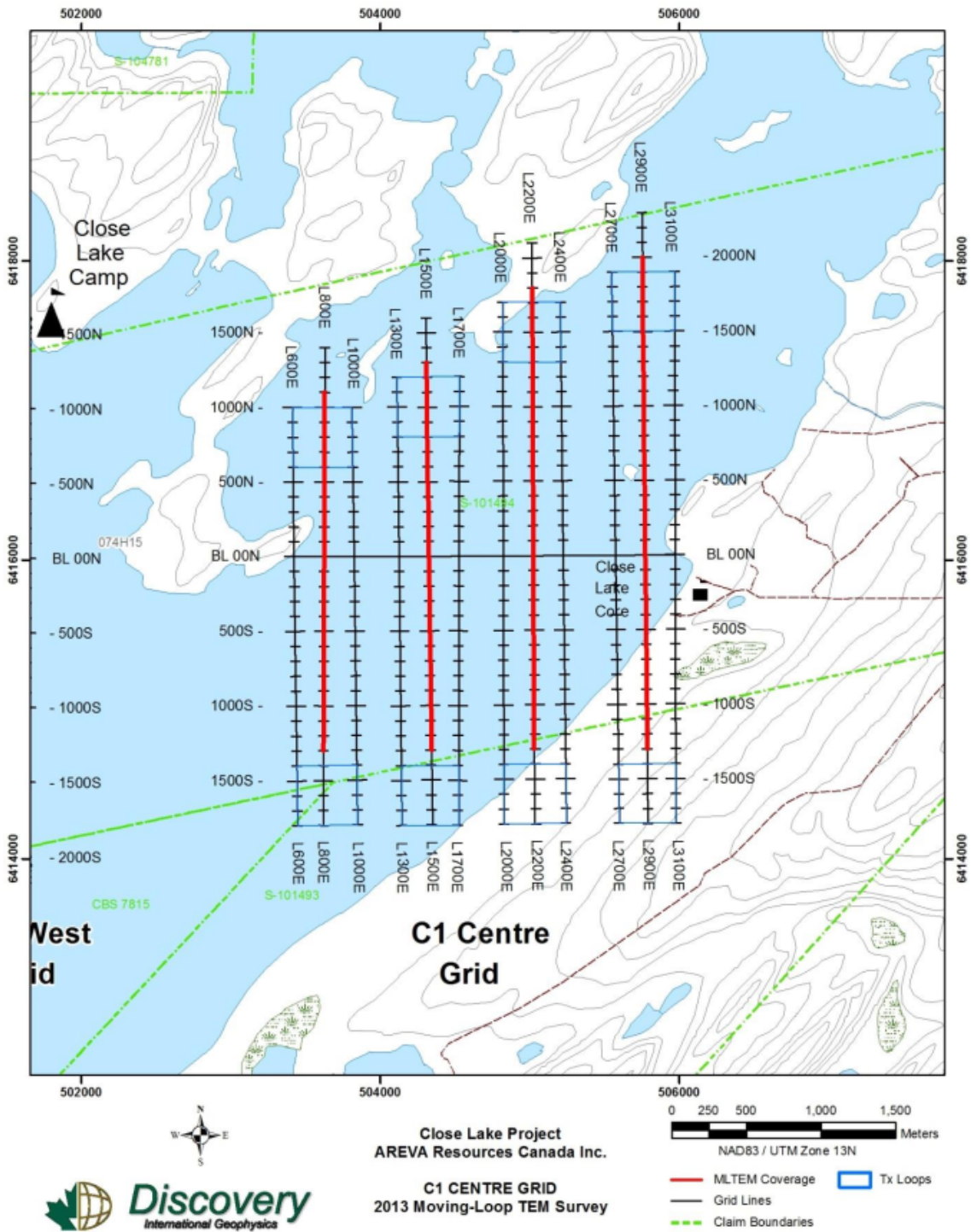
Figure 6.20: The C1-Center Grid of the Close Lake Project 2013 moving-loop TEM survey (Palomino, 2013).

component of the field data has the lowest noise level while the y-component data has the highest noise level, especially for late-time gates. The large noise present in the y-component data can be attributed to the fact that it has the smallest magnitude in all the three components. This is expected since the conductor is largely parallel to the east-west direction, and the y-component response would be zero if the conductor is perfectly parallel to the east-west direction. The x- and z-component data all suggest a north-dipping plate-type target buried in the subsurface Earth (see the model with 75° dip angle in Section A, Figure A.4). However, in early times, the x-component responses have two peaks with the right peak even larger than the left one, which is different from the responses of a simple, steeply north-dipping thin plate conductor. It indicates that there might be some conductive structure around the second peak. Also, the relatively large magnitude of the y-component response at stations close to $x = 500$ m also suggests the existence of a conductive feature which is not perpendicular to the profile direction. Despite being easily visible in the x- and y-component data, that conductive feature is not very obvious in the vertical component except that the peak decreases rapidly to a layered-Earth response in the early to middle times (gates 1-16) while the decrease in later times seems to be smoother.

These conductive features observed in the horizontal components may correspond to the C1-North conductive trend as identified in earlier exploration campaigns (see Figure 6.16). In the 2013 moving-loop TEM survey report, this conductive trend was suggested to be a shallower structure rather than a basement conductor. An

176
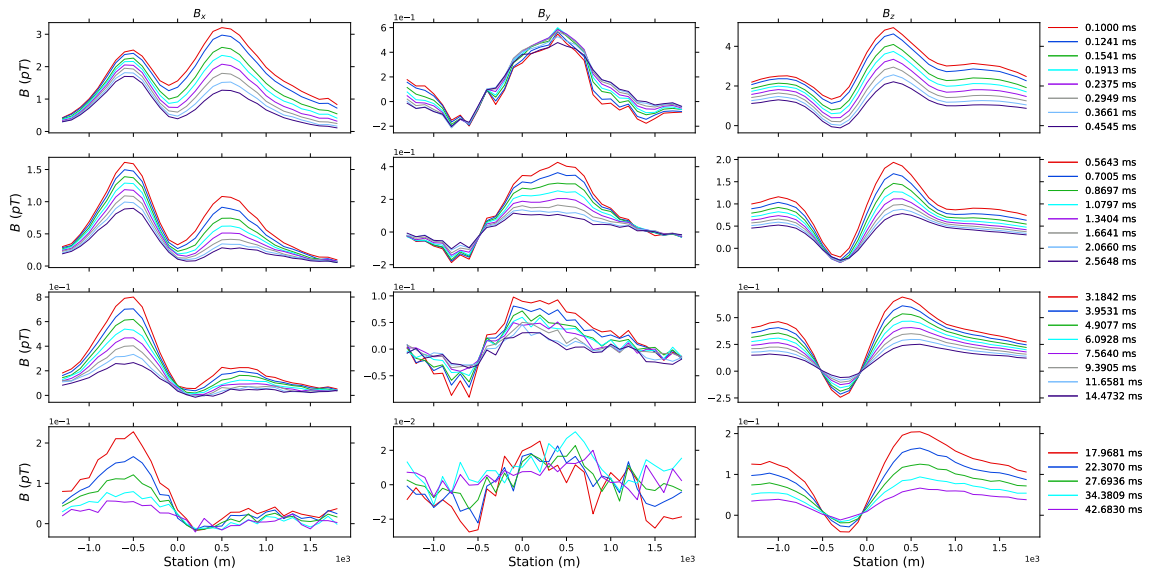
Figure 6.21: The in-line (left), cross-line (middle), and vertical (right) data of Line 2200E survey line from the Close Lake Project.

interpretation based on the modeling using the Maxwell software from EMIT (2005) only verified the existence of this conductor in the C1-East Grid, and the data from Line 2200E was modeled with a single conductor (Figure 6.22). It is worth noting that this interpretation only takes the vertical component into account, and only the last 8 channels of data were used while the total number of channels collected was 29.

For Line 2200E, two holes, CL-160 and CL-166, were drilled in the 2015 Diamond Drilling Program, and they all hit the graphitic shear zone (Figure B.2). The two drill holes are nearly parallel to each other and they all stop shortly after passing the graphitic shear zone. There were 31 and 26 physical property samples measured for Drill Holes CL-160 and CL-166, respectively. Table C.1 and C.4 give the resistivity values and the primary lithology information of the samples collected from Drill Holes CL-160 and CL-166, respectively. Each sample is 10 cm long and the sampling density
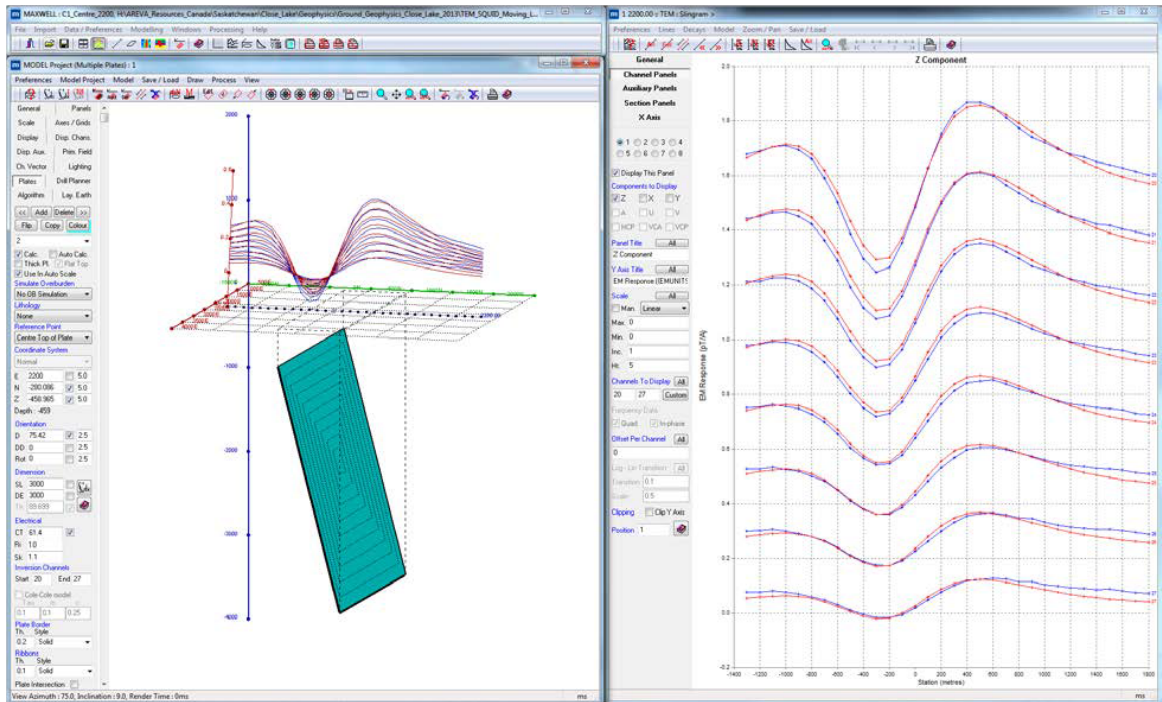
Figure 6.22: The interpretation of Line 2200E based on the modeling by Maxwell software (EMIT, 2005). The calculated responses of the plate model shown in the left panel (green) can match the last eight channels of the vertical component real data reasonably well (right panel) (Richard, 2013).

is not constant within each hole, with the densest sampling rate occurring around the unconformity. Samples from Drill Hole CL-160 do not contain graphite but there are samples which have low resistivity values (Samples 23 and 24). Samples collected from CL-166 starting from 514.65 m to 546.25 m are found to have graphite with a grade higher than 10%. These samples have low resistivity values with the lowest being 1.58 Ωm. Because the samples are not collected densely enough, it is possible that some of the rocks with even lower resistivity values were missed. Resistivity probing data were also collected in Drill Hole CL-166, and the resistivity values are close to those of the resistivity measurements made using the SCIP instrument.

The unstructured mesh was built using the procedures established in Section 2.4 in

Chapter 2. As can be seen from Figure 6.20, almost the entire survey line is on Close Lake which means that topography may not affect the data significantly. However, given the fact that a hill is present right to the south of the southern-most transmitting loop, as well as the ability of unstructured grids to represent topography, the topography data were still incorporated into the model. The digital elevation model (DEM) data with a resolution of 3 arc-second were downloaded from the Geospatial Data Extraction online service provided by the Canadian government. Higher resolution data were available for download as well, but it would make the interpolation process a computationally heavy task due to a significant increase in the data size for higher resolution DEM data. The downloaded topography data covers an area much larger than the area where C1-Center and C1-West grids are located.

According to Drill Holes CL-160 and CL-166, the ice/water column is about 7 m thick, which is followed by an approximately 50 m thick overburden layer. Unfortunately, there are no resistivity values available for these two units. Nonetheless, a 60 m horizontal layer was designed for the overburden to allow for possible investigations of its influence on the EM data. Following the overburden layer, another two horizontal layers were designed to represent the two sandstone units, namely, the MFc and MFb members. The unconformity is at an elevation of approximately 60 m and 65 m for Drill Holes CL-160 and CL-166, respectively. The graphitic fault zone is approximately at 50 m elevation. Drill Hole CL-166 encountered a paleoweathering layer after the unconformity that extends approximately another 50 m in depth while no paleoweathering layer is observed within Drill Hole CL-160.

In the Athabasca Basin, the basement gneiss is generally paleoweathered, and the paleoweathering layer thickness ranges from a few centimeters to more than 200 m (Jefferson et al., 2007). From the unconformity, the clay-altered, hematitic regolith gradually changes to chloritic altered rock, and finally, fresh basement rock. This layer is commonly more conductive compared to fresh rocks, partly due to an increased permeability and porosity during the weathering process (Darnet et al., 2019), and partly because of the hematitic and clay alteration. In order to investigate how the conductivity of this layer affects the EM data, a 50 m thick, horizontal layer was built in the model. It underlies the sandstone layers above the unconformity.

For basement regions away from the graphitic faults and deeper than the drill holes, there were no conductivity measurements available. Therefore, it was simply treated as horizontal layers. The graphitic fault was believed to be steeply dipping to the north, with its strike direction almost parallel to the east-west direction around the profile. Although the fault is not extending directly to the east and west, here it was still treated as a straight thin plate for the single profile modeling of Line 2200E for simplicity. It was set to be 50 m thick and its dip angle was 70$^{\text{o}}$. The strike length was set to 7 km. The depth extension was 2 km, with its top and bottom located at $z = 50$ m and $z = 1,830$ m, respectively.

For the modeling of Line 2200E, 20 m long tetrahedral edges were inserted for the refinements of the transmitter sources and regular tetrahedra with 20 m edge length were inserted for the refinements of receivers. A 2D surface mesh with these refinements was then generated using Triangle. The downloaded topography data

were interpolated on the newly generated 2D surface mesh. Figure 6.23 shows the 2D surface mesh after the topography interpolation. This surface mesh was then imported to FacetModeller to form the Earth-air interface. Figure 6.24 shows a screenshot taken from FacetModeller, which shows the 3D model built for Line 2200E. The first horizontal thin layer with gray color is the overburden layer. The following two horizontal layers with brownish colors represent the MFc and MFb members of the sandstone basin. The red horizontal layer beneath sandstone layers represents the paleoweathering layer which is cut into two parts by the dipping conductor shown in blue. The bottom three greenish horizontal layers represent the top parts of the basement. The air and bottom basement units are not shown in Figure 6.24 since they are significantly larger in size than those shown. The conductor is split vertically into four parts, with boundaries between each part consistent with the boundaries between different basement units. This allows for the adjustment of conductivities with depth. Note that with FacetModeller, the conductor can be split into as many parts as one wants if deemed necessary later during the modeling.

In this chapter, the main goal is to model the responses of geophysical models built based on geological and drilling information and to find out the best model that can match the real data. Therefore, the modeling efficiency is important and consequently some of the modeling parameters are tuned towards a better efficiency. Refinements of loop sources and receivers used larger tetrahedral edges and regular tetrahedra. Also, only the minimum edge-radius ratio constraint was used for generating the 3D unstructured Delaunay-Voronoï dual meshes. When it was set to 1.25, TetGen
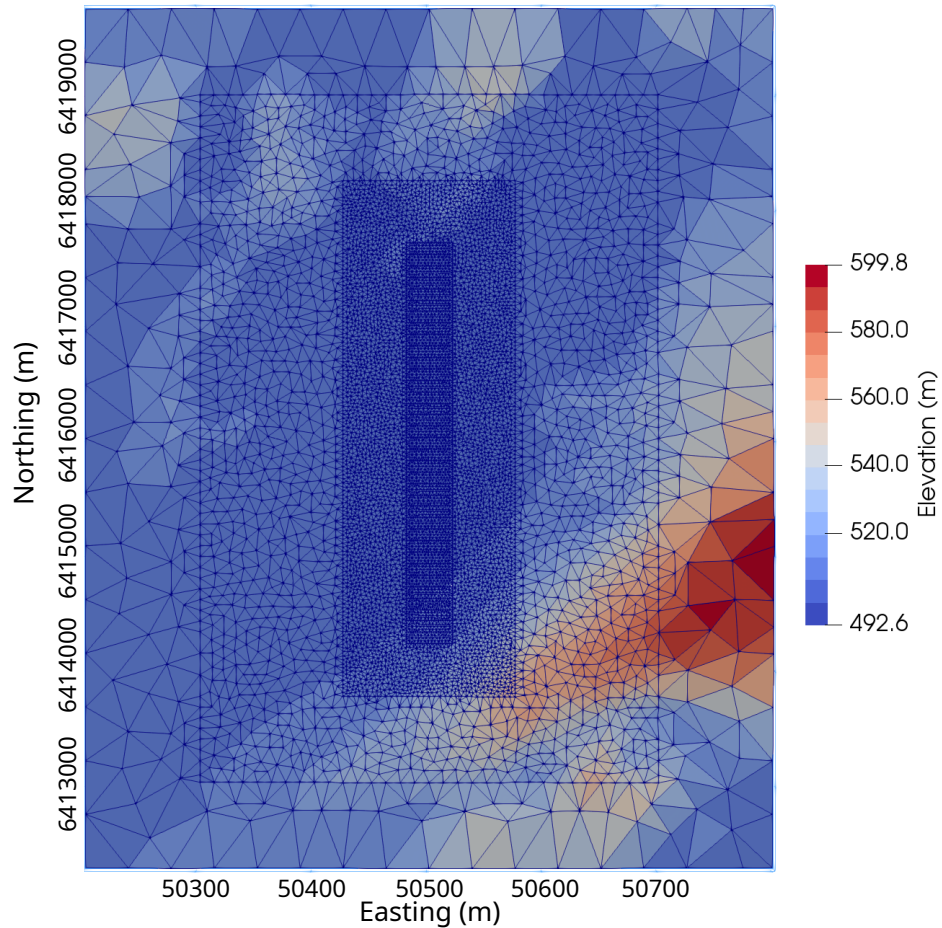
Figure 6.23: The central portion of the surface mesh designed for modeling of Line 2200E of Close Lake Project. The color represents the elevation of each cell, which is interpolated from the original DEM data.

generated a mesh with 922,677 tetrahedral edges and 795,969 cells. Figure 6.25 shows the unstructured tetrahedral mesh generated by TetGen based on the PLC exported from FacetModeller. The initial time step was set to 10^{-6} s and the time step was doubled every 50 times, resulting in a total number of 648 steps which can model 400 ms responses. The E-field method was chosen for the modeling and the dB/dt response was integrated backward in time numerically to get the B-field response. The transmitting waveform was accounted for by convolving the step-off response
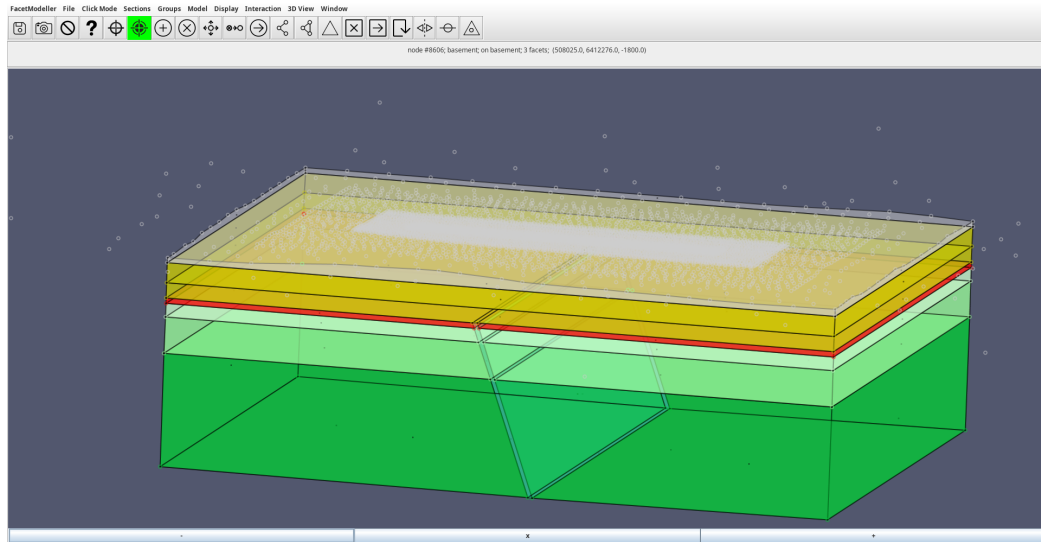
Figure 6.24: A FacetModeller software screenshot showing the 3D model built for Line 2200E. The white nodes come from the surface mesh which extends all the way to the model boundaries.

with the actual waveform used. The turn-on and turn-off edges were both assumed to be linearly changing with time. The turn-on stage length was not specified in the survey report and here it was assumed to be 2 ms. The turn-off stage is 0.42 ms and consequently the steady stage is 47.58 ms so that in total the transmitting waveform lasts for 50 ms (a 5 Hz repetition frequency is used for the transmitter).

The conductivity of each unit in the model can be determined from the rock sample resistivity measurement as well as the probing results. Appendix C.6 lists the average conductivity and standard deviation of measurements made for each unit. For Line 2200E, the rock sample resistivity measurements were carried out for both Drill Holes CL-160 and CL-166 but the probing result was only available in Drill Hole CL-166. The conductivity of the overburden was not available in both measurements so that it was always treated as MFc unless otherwise specified.

From Table C.7, the average resistivities of the sandstone layers MFc and MFb
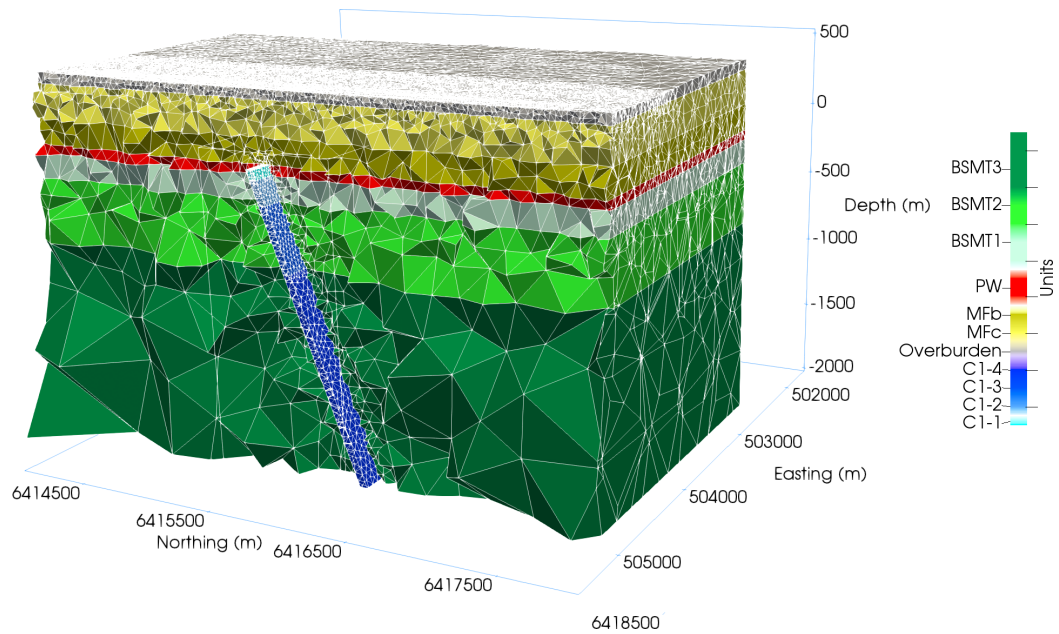
Figure 6.25: Unstructured tetrahedral mesh for the model created for the modeling of Line 2200E profile of the Close Lake Project. The letters 'R' and 'L' at the end of the unit names represent the right and left halves, respectively, divided by the conductor.

obtained from the rock sample physical property measurements in Drill Holes CL-160 and CL-166 are close to 2,000 Ωm. Meanwhile, the average resistivities of MFc and MFb members obtained from the probing result from Drill Hole CL-166 are all close to 4,000 Ωm. The paleoweathering layer right beneath the unconformity is more conductive than the sandstone basin and the fresh basement. The rock sample physical property measurements of Drill Holes CL-160 and CL-166 show that this layer has a resistivity below 500 Ωm while the probing of Drill Hole CL-166 suggests a higher resistivity value with its average being 865.68 Ωm. The pelitic gneiss located at the center of the fault zones commonly underwent heavy alteration and various levels of hematization and paleoweathering and hence possesses a low resistivity, especially when it contains high grade of graphite (can be more than 10%). Some of the rock

184

samples recorded resistivities as low as 1.58 Ωm (Sample 21 from Drill Hole CL-166, Table C.4) and 4.36 Ωm (Sample 28 from Drill Hole CL-168, Table C.6). It is the most conductive material in the entire model. The basement in general is more resistive than the sandstone basin according to the limited rock samples collected in the fresh, unaltered basement. For example, Sample 31 from Drill Hole CL-160 is fresh tonolitic gneiss and it has a resistivity of 63,242.50 Ωm; Samples 24 and 25 from Drill Hole CL-166 all have resistivities larger than 5,000 Ωm.

Based on the rock sample physical property measurements carried out in Drill Holes CL-160 and CL-166, as well as the probing result of CL-166, a model from now on referred to as Model M1 was first simulated. The conductivities of all units above the unconformity of Model M1 were set to 5×10^{-4} S/m. The conductivities of different parts of the C1 conductor, C1-1, C1-2, C1-3, and C1-4 were set to 0.2, 0.3, 0.4, and 0.5 S/m, respectively. The conductivity of the air was set to 10^{-8} S/m and the conductivities of all basement units and the paleoweathering layer were set to 10^{-4} S/m.

Figure 6.26 shows the three-component responses calculated by the E-field method for Model M1 and the real data. It can be noted that the responses from the last four receivers are not smooth especially for early times in y-component responses. This is caused by an inconsistency in the mesh refinements for these four receivers compared to the rest of the receivers in the profile. These four receivers do not overlie sources of previous stations and are refined only for the observation point. However, all the other receivers are refined on top of the refinement for sources since they overlie the

185
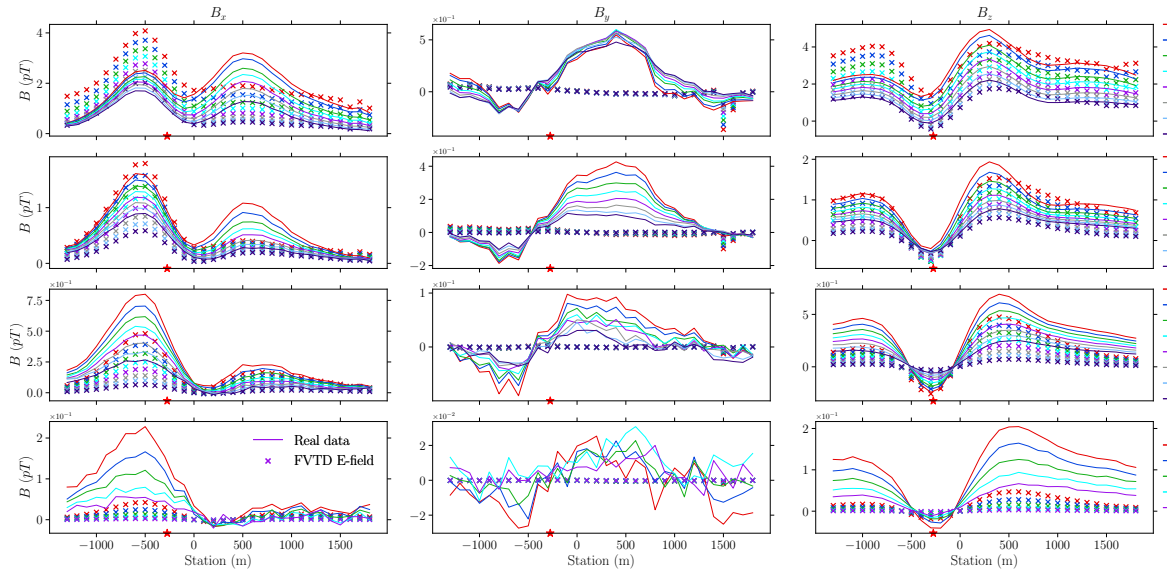
Figure 6.26: Comparison between three component responses of the numerical responses calculated for Model M1 and the real data of Line 2200E from Close Lake Project. The red star symbol marks the top center of the C1 condutor immediately under the profile for Model M1.

source wires of previous stations. This inconsistency can be easily tackled by refining the last four receivers with the same method as used for the previous ones. But the extra refinements can cause longer computation times. Also, these receivers normally do not bear the anomalous responses from our main conductor targets. Consequently, this fluctuation in the response was ignored for the modeling of Line 2200E.

It can be seen from Figure 6.26 that the x-component of the modeled data show typical responses of a steeply dipping thin conductor in a homogeneous half-space (see, e.g., Figure A.4 in Section A): a large peak which persists though all gates and appears at the left side of the conductor (when the receiver is on the right side of the loop source); and a second peak which is significantly smaller in magnitude compared with the first one on the right side of the conductor (more obvious in the middle to late times). The y-component of the modeled data are close to zero (except here for the

186

last four receivers due to reasons given above) which is a result of the conductor being strictly perpendicular to the profile in the model. The non-zero response observed in the real data suggests that the conductor is not perfectly perpendicular to the profile. For the vertical component, the modeled and real data have a fairly good match for the early to middle channels (shown in the first two rows of Figure 6.26). The responses on the left side of the trough are larger than the real data in early times, which is also observed for the x-component. For late channels, the numerical response is obviously smaller than the real data, which suggests that the background conductivity may be larger than the value chosen for the basement in Model M1.

In Model M1, the paleoweathering layer was not treated the same as basement layers in terms of conductivity. Another model, Model M2, was designed and modeled to investigate the effects of this thin conductive layer. The conductivity of the paleoweathering layer was now set to 2×10^{-3} S/m, and all the other units were kept the same as in Model M1. Figure 6.27 shows the three-component responses calculated by the E-field method for Model M2 and the real data. Compared to Figure 6.26, both the x-component and z-component responses from the first two rows are found to have increased. But the late-time responses have basically stayed the same, which are still significantly smaller than the real data. Other models which only changed the conductivity of the paleoweathering layer from 2×10^{-3} S/m in Model M2 to 5×10^{-3} S/m and 1×10^{-3} S/m, whose results are not presented here, show that the late-time responses remain nearly the same as what was observed for Models M1 and M2 while the early-time responses are even larger than those of Models M1 and M2, making it

187
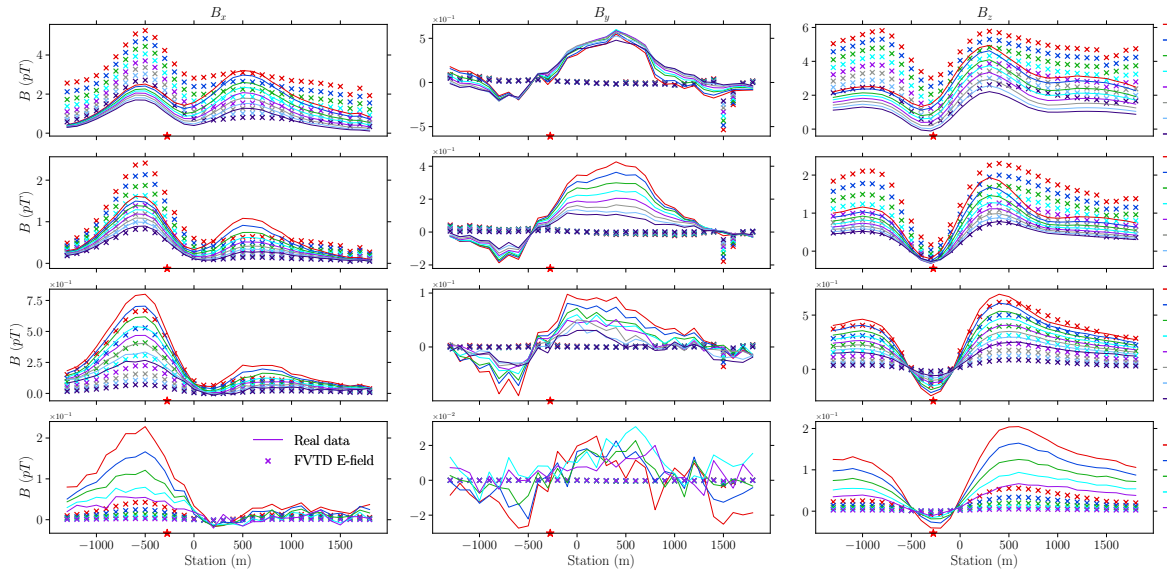
Figure 6.27: Same as Figure 6.26 but for Model M2.

significantly larger than the real data. The modeling of Model M2 indicates that the paleoweathering layer can only affect early-time responses and cannot make up the differences seen in late-time channels between the modeled and the real data.

Both in Models M1 and M2, the conductivities of the background and basement units were set to 10^{-4} S/m. However, the modeling experiments of Models M1 and M2 all suggest that there exists something more conductive which is responsible for the relatively large late-time responses. This necessitates the next modeling experiment using a model with higher conductivity values for the basement units. The new model was named M3, and it increased the conductivities of BM3 from 1×10^{-4} S/m to 1.5×10^{-3} S/m, decreased the conductivity of the left (south) paleoweathering layer from 2×10^{-3} S/m to 5×10^{-4} S/m in order to decrease the modeled responses left of the conductor. Also, because the late-time responses coming from the conductor in Models M1 and M2 are all smaller than the real data, conductivities of C2, C3, and

188
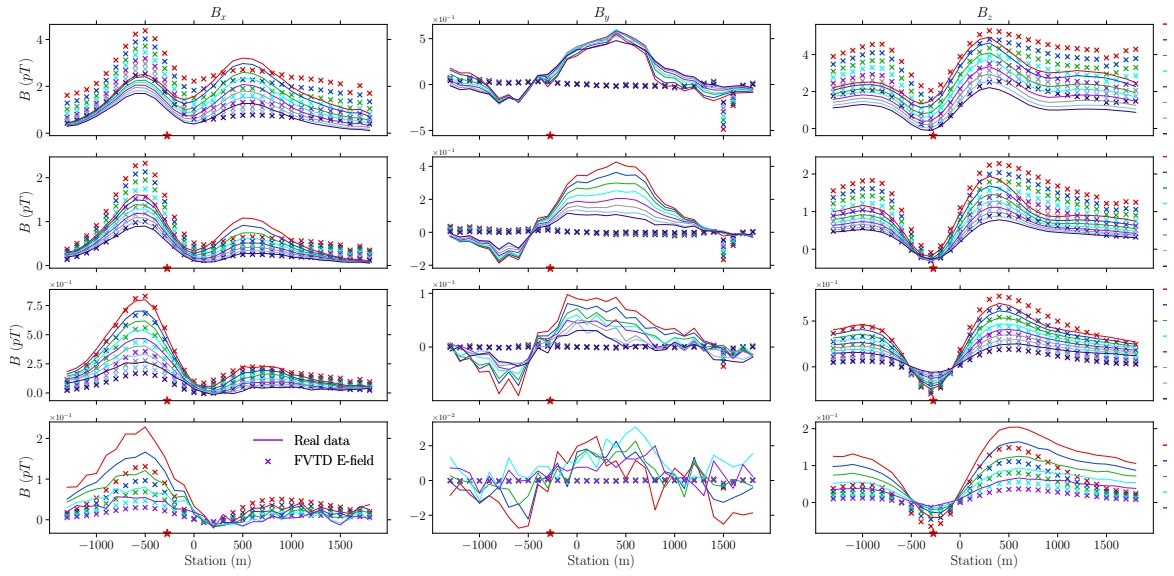
Figure 6.28: Same as Figure 6.26 but for Model M3.

C4 were changed from 0.3 S/m, 0.4 S/m, and 0.5 S/m to 0.5 S/m, 0.8 S/m, and 1.5 S/m, respectively.

Figure 6.28 shows the three-component responses calculated by the E-field method for Model M3 and the real data. Compared to Figure 6.26, the responses calculated for Model M3 have slightly larger early-time responses (the first two rows of Figure 6.28) while the responses from channels 17 to 24 are much closer to the real data compared to Model M2. But the calculated responses of the last five channels for Model M3 are still smaller than the real data, especially at stations further away from the conductor. This indicates that the conductivity of the background basement should be larger than 10^{-4} S/m which was used for Model 3. The increase in the conductivities of different parts of the conductor is responsible for the better match between the modeled data and the real data for stations directly under the influence of the conductor.

189

Another model, Model M4, was created to investigate how conductive the background basement should be in order to get a satisfactory match between the modeled data and the real data. After some trial-and-error modeling, it was found that the conductivities of the background basement and the third layer of the basement should be set to 2×10^{-3} S/m and 5×10^{-4} S/m, respectively. Besides, the conductivity of the paleoweathering layer north of the conductor was also decreased to 10^{-3} S/m in order to get a better match for early-time channels. Figure 6.29 shows the three-component responses calculated by the E-field method for Model M4 and the real data. It can be seen that the late-time responses are finally close enough to the real data. Also, because of the reduced conductivity for PaleoR unit, the vertical component responses at those stations right (north) of the conductor now also have a better match. For Model M4, the only noticeable mismatch between the vertical component real data and the modeled data are from the stations left (south) of the conductor from early time. The modeled data is larger than the real data for both the x- and z-components. For the x-component data, the mismatch still exists at stations around the second peak in the first two rows.

From the modeling experiments carried out for Models M1 to M4, it is found that a relatively conductive background basement is required in order to get a better match between the modeled and real data. However, the low conductivity is not supported by the limited rock samples collected in the shallower part of the basement if the conductivities of different parts of the basement unit are similar at different burial depths. Instead of having a conductive basement in the deeper part of a model,
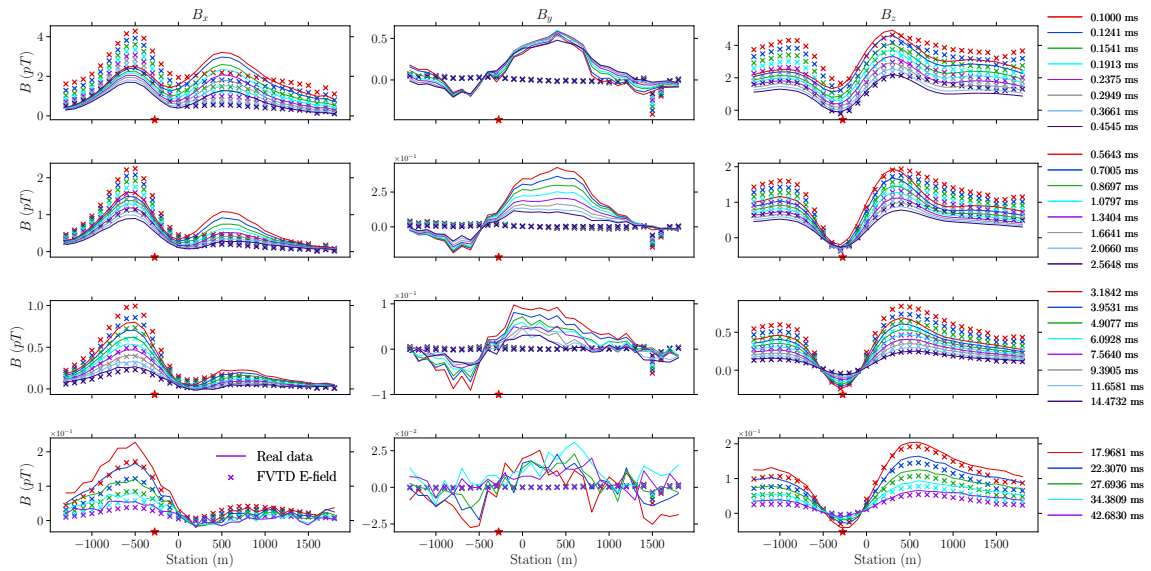
Figure 6.29: Same as Figure 6.27 but for Model M4.

would it be possible for a model with only a thin layer of very conductive material to produce the observed responses in the real data? A geological interpretation for the C1 conductive trend presented in the report of the 2015 Diamond Drilling Program is modeled to investigate this hypothesis. The geological interpretation of the C1 conductive trend is shown in Figure 6.30. The conductor was interpreted to be steeply dipping to the north in the shallower part of the basement beneath the unconformity but gradually bending to be horizontal.

Figure 6.31 shows the unstructured tetrahedral mesh created for the geological interpretation shown in Figure 6.30. This model is referred to as Model M_{B1} from now on. Since the main goal for the modeling of Model M_{B1} was to investigate how the bending conductor affects EM responses, other parts of the model were simplified compared to Models M1 to M4. The overburden layer was neglected and the basin only contains the MFc and MFb units. The entire background was treated as one

191
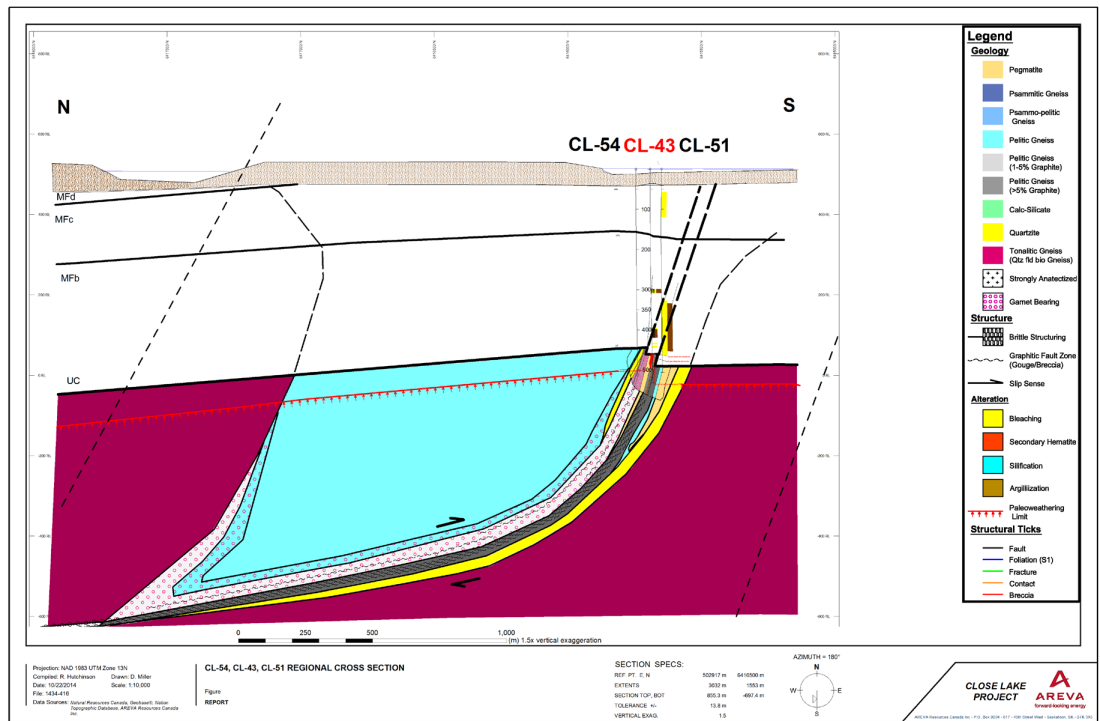
Figure 6.30: A geological interpretation of the C1 conductive trend where the conductor is interpreted to be steeply dipping to the north in the shallower part and then gradually bends to be horizontal in the deeper part (Hutchinson and Zalustskiy, 2015).

basement unit. The conductor was set to be dipping 70° to the north until it reaches to $z \approx -200$ m. It was then gradually bent to become almost horizontal at $z \approx -800$ m. The conductor stopped at approximately 200 m north to the receiver of the last station in the profile. The thickness of the conductor was kept at 50 m and the conductivity was set to 0.4 S/m. The conductivities of MFc, MFb, and the basement were set to 5×10^{-4} S/m, 2×10^{-4} S/m, and 10^{-4} S/m, respectively.

Figure 6.32 shows the three-component responses calculated by the E-field method for Model M_{B1} and the real data. The match between the modeled data and the real data for the first eight channels is better than that of Model M4. For example, the x-component response now has a clear second peak which is present in the real data.
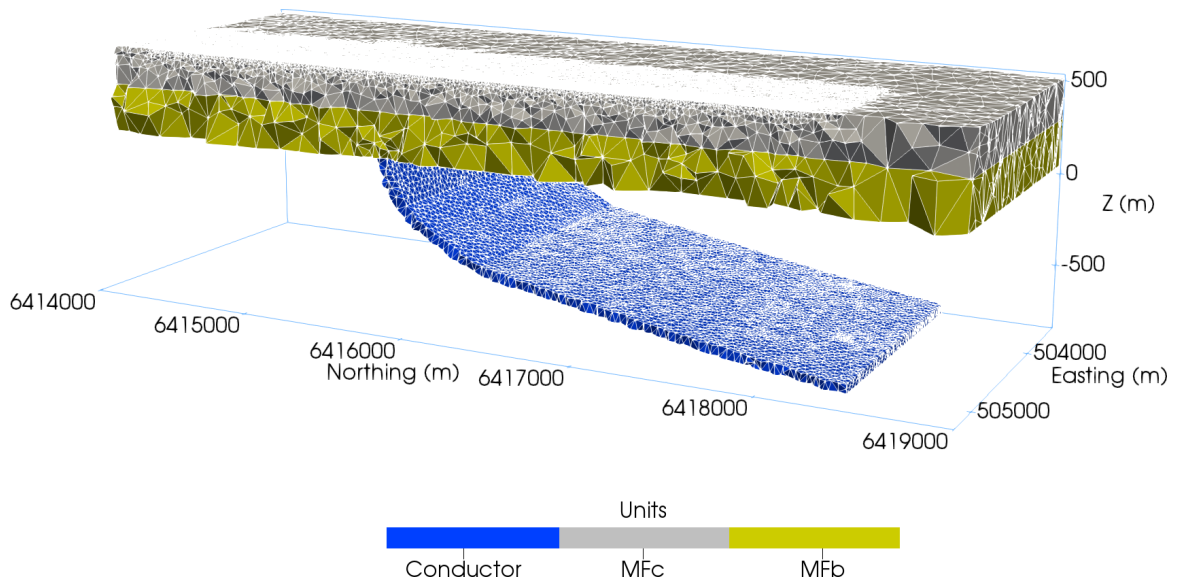
Figure 6.31: The unstructured tetrahedral mesh created for the modeling of the bending conductor model as shown in Figure 6.30. For this model the overburden was ignored and the basin only contains the MFc and MFb units. The basement is not shown in the figure for a better view of the bending conductor.

The responses of the vertical component left of the conductor is very close to the real data now whereas it was much larger than the real data for Model M4. The responses of the vertical component right of the trough also show a better match. However, the match quickly deteriorates after the eighth channel: the right peaks in both the x- and z-component responses are much larger than the real data. While the late-time responses of the real data resemble typical responses of a steeply dipping conductor, the responses calculated for Model M_{B1} do not. Although the horizontal part of the conductor in the deeper part can result in a large response that is comparable with the real data, their characteristics simply do not match. Therefore, judging from the measured EM data, the geological interpretation as shown in Figure 6.30 is not valid.
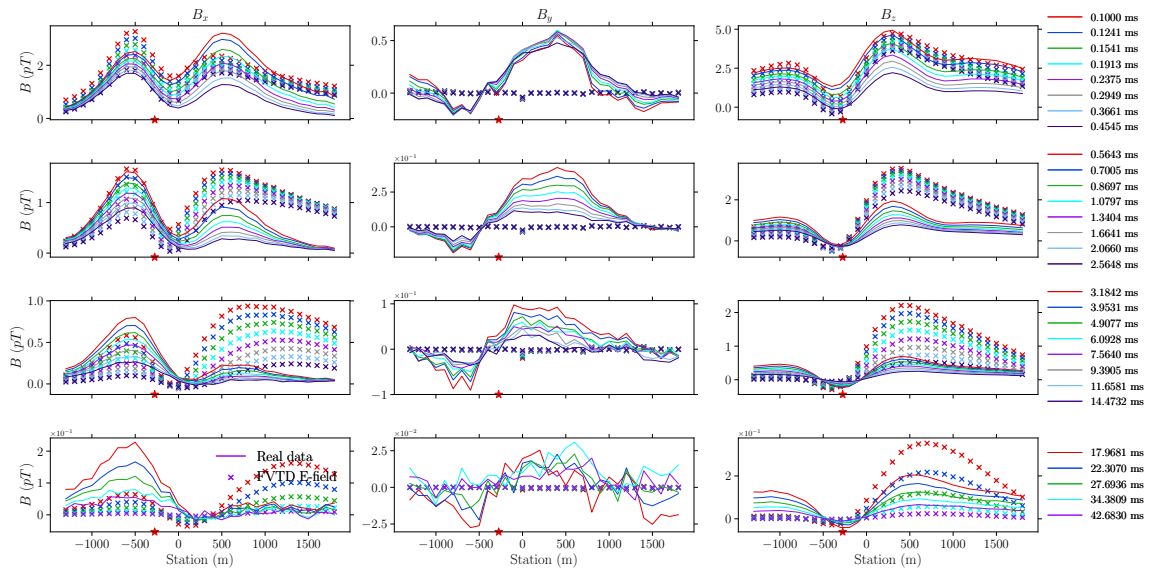
Figure 6.32: Same as Figure 6.26 but for Model M$_{B1}$.

6.4.2.2 Grid-scale modeling of C1-Center Grid

The four profiles in C1-Center Grid, Lines 800E, 1500E, 2200E, and 2900E, can be modeled together for a given model using a single mesh. Compared with the single profile modeling, modeling of the entire grid allows for the investigation of lateral variations of the conductor and its surrounding geological structures. For example, as shown in Figures 6.18 and 6.19, the C1 conductor is not strictly perpendicular to the east-west direction based on both EM interpretations and drilling results. The variation in the strike direction is likely responsible for the non-negligible y-component responses observed in the real data for Line 2200E. By modeling multiple profiles from the real data, a realistic conductor model can be built based on the records of multiple drill holes spreading throughout C1-Center, C1-East, and C1-West Grids.

Based on all the drilling data from the 2015 Diamond Drilling Program (see Ap-

194

pendix B) as well as historical drilling from 1988 to 2006, a thin, steeply dipping but laterally varying structure was built to represent the C1 conductor. During the building of the model, control points were taken from the drilling data and were used to control how the conductor is varying laterally. A few extra points were added in order to make the conductor vary smoothly along the strike direction. A surface mesh with all the refinements required for the transmitting sources and receivers in the four survey profiles in C1-Center Grid was generated first (Figure 6.33). The same refinement strategy as used in the modeling of Line 2200E was adopted here. The surface mesh was then imported into FacetModeller to build the 3D PLC representing the 3D model. Figure 6.34 is a screenshot taken from FacetModeller after the model building was complete. The gray dots are the nodes coming from the surface mesh shown in Figure 6.33.

In order to be able to adjust the conductivities of the conductor both horizontally and vertically, the C1 conductor was divided into four parts horizontally and three parts vertically. The horizontal division were made to create a vertical interface between adjacent survey lines such that the part of the conductor right beneath a survey profile would have constant conductivities horizontally. The vertical division interfaces were consistent with those of the basement units interfaces, i.e., when there is a vertical interface for the basement, there is also an interface for the conductor. Compared with models made for Line 2200E, this model still has the same paleoweathering layer but the first and the second layers of the basement in previous models were combined into one layer. The last layer of the basement was kept the

195
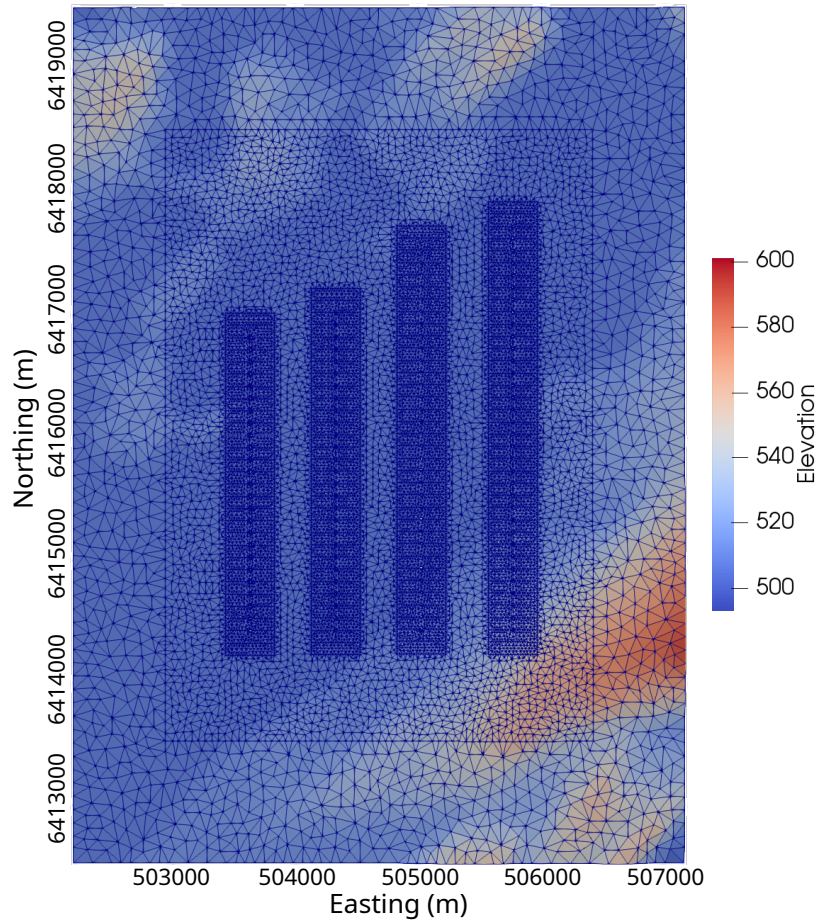
Figure 6.33: The central portion of the surface mesh designed for the modeling of C1-Center Grid. The color represents the elevation of each cell, which was interpolated from the original DEM data.

same as the one in previous models.

No drilling data exists for the C1-North conductor in the area within the C1-Center grid. The locations of this conductor were inferred from the geological interpretation as shown in Figure 6.19 and adjusted based on trial-and-error modeling. The dip angle of the C1-North conductor was set to be the same as the C1 conductor, namely, 70°. In total, there were 27 unique regions existing in the model. The PLC generated by FacetModeller was then given to TetGen to generate the final Delaunay-Voronoï dual meshes. Again, $\alpha = 1.25$ was used for generating the mesh and the number

196
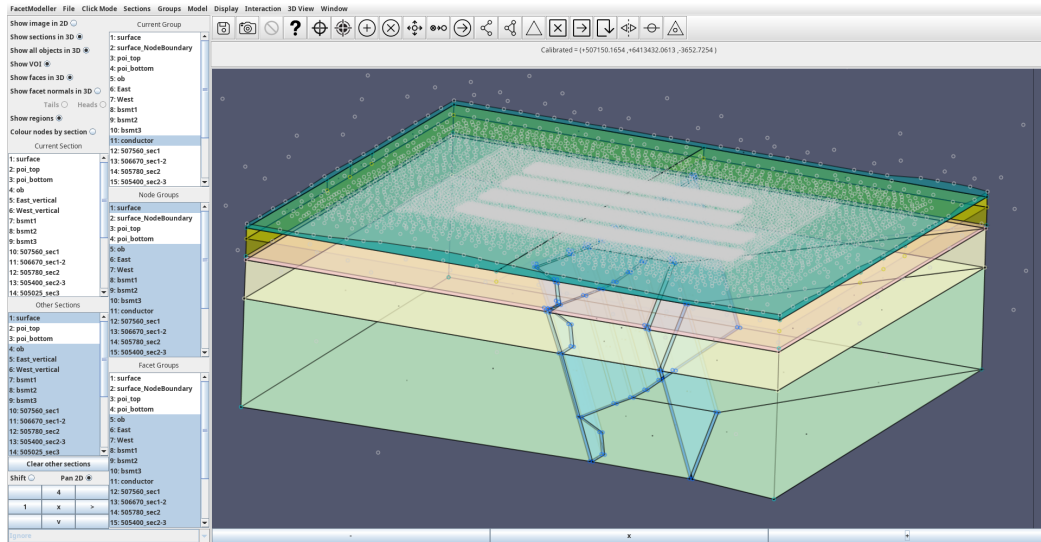
Figure 6.34: A screenshot taken from the FacetModeller software showing the 3D model built for the C1-Center Grid. The white nodes come from the surface mesh shown in Figure 6.33, which extends all the way to the model boundaries.

of tetrahedral cells and edges were 1,266,475 and 1,468,146, respectively. The mesh size is slightly larger than those generated for Models M1 to M4 because of more refinements for sources and receivers in the surface mesh. Figure 6.35 shows part the unstructured tetrahedral mesh generated by TetGen.

The two conductors, C1 shown in blue and C1-North shown in cyan colors, as explained above, were divided into 12 and 3 parts, respectively. Figure 6.36 shows the shape of the two conductors and how they were divided by marking each distinct unit with a unique color. The conductivities of the conductors and other units in the model, hereafter referred to as Model C1-Center-A, were chosen based on trial-and-error and experiences of modeling Line 2200E. The conductivities for each unit are listed in Table 6.5. In total, there were 118 stations in the four profiles in C1-Center Grid. When using the same computing platform as used in previous chapters, it took
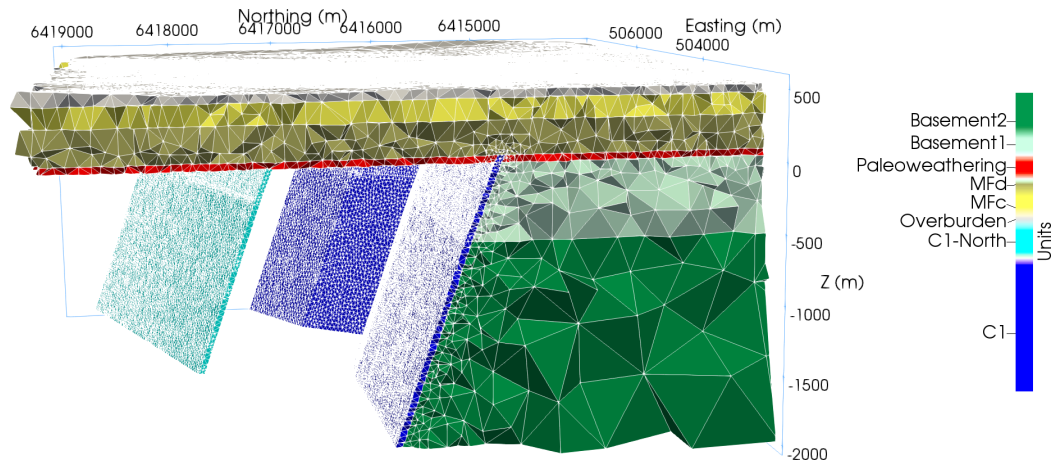
Figure 6.35: Unstructured tetrahedral mesh for the modeling of C1-Center Grid of the Close Lake Project. Note that not all basement units are shown in order to expose C1 and C1-North conductors shown in blue and cyan colors.

approximately 8 hours and 30 minutes to finish the modeling of 400 ms secondary field when the initial time step was 10^{-6} s and the time step doubles every 50 steps. For comparison, it took 1 hour and 36 minutes using the same computing platform to finish the modelings of Models M1 to M4.

Figures 6.37 to 6.40 show the comparison of the three-component responses calculated by numerical modeling and from real data for Lines 800E to 2900E. First, it can be seen that the match between the modeled data and the real data is generally good for all four profiles, with a better match observed at late times. The early-time vertical responses of the modeled data are all slightly larger than the real data at stations to the left of the conductor. With the conductor now having varying strike directions, the previously near zero y-component responses in the modeled data seen in the single profile modeling of Line 2200E are now larger with comparable magnitudes to the real data. For example, the y-component response of the modeled data

Table 6.5: Conductivities of each unit in Model C1-Center-A designed for the modeling of C1-Center Grid from Close Lake Project.

Unit	Conductivity (S/m)	Unit	Conductivity (S/m)
C1-1	0.1	C1-2	0.4
C1-3	0.4	C1-4	0.4
C1-5	0.8	C1-6	0.8
C1-7	0.7	C1-8	0.5
C1-9	2	C1-10	2
C1-11	1.5	C1-12	2
C1N-1	0.3	C1N-2	0.2
C1N-3	0.1	Overburden	5×10^{-4}
MFc South	5×10^{-4}	MFc North	5×10^{-4}
MFb	5×10^{-4}		
PW South	5×10^{-4}	PW North	10^{-3}
BSMT1 South	10^{-4}	BSMT1 North	10^{-4}
BSMT2 South	10^{-3}	BSMT2 North	10^{-3}
Air	10^{-8}	Background	2×10^{-3}

in Figure 6.39, compared to Figure 6.28, has two troughs with one peak in between, which is very similar to what is observed for the real data. The left trough is caused by the conductor's strike direction changing from being parallel to the east-west direction west of the profile to slightly south-eastward of the profile until some point after passing Line 2900E. The peak in the middle and the northern trough are both caused by C1-North conductor because its strike is approximately along ENE-WSW. After adding the C1-North conductor, the x-component response also shows a clear peak north of the first peak, which makes the modeled data now much closer to the real data compared to Figure 6.28. For the vertical component, the responses south of the conductor are still larger than the real data, but the right peak is narrower than that of Figure 6.28. The change of modeled responses from Model M4 to Model C1-Center-A clearly suggests the existence of the C1-North conductor.

199
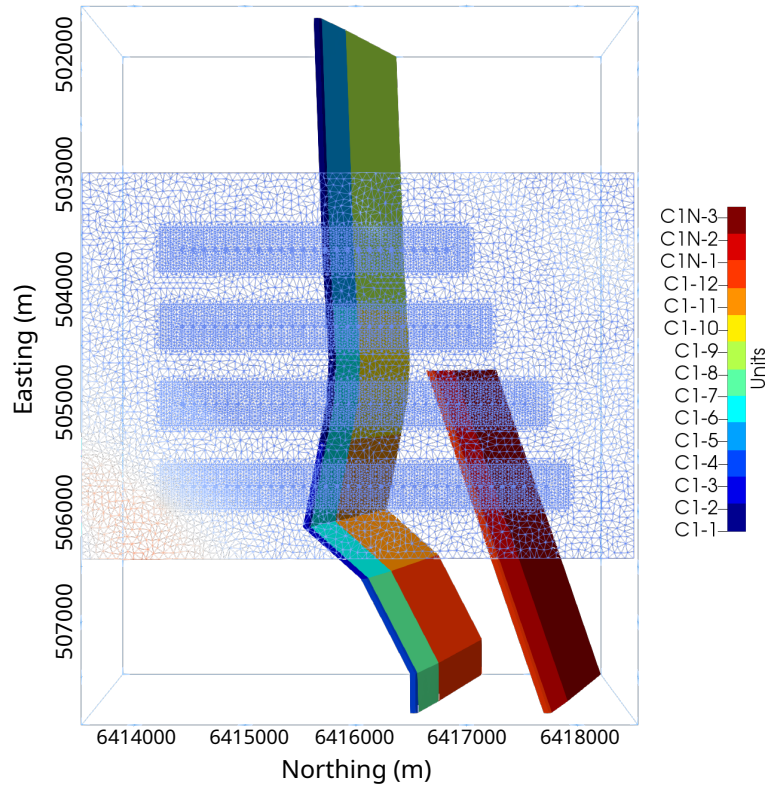
Figure 6.36: Bird's eye view of the C1 and C1-North conductors under the surface mesh which shows the four profiles in C1-Center Grid. Note that the colors used here are different from those used in Figure 6.25, and they are only used for the purpose of visualizing different parts of C1 and C1-North conductors.

The responses coming from the C1-North conductor are larger at Line 2900E compared to Line 2200E. For instance, the second peak of the x-component response at Line 2900E lasts longer than Line 2200E. Also, the z-component response at early times has a weak peak around $x = 1000$ m while the peak can be hardly seen in Line 2200E. However, compared to the C1 conductor, the conductivity or the scale of the C1-North conductor should be smaller because its responses only affect early-time gates in Lines 2200E and 2900E. In Model C1-Center-A, the C1-North conductor is considered to have the same thickness, dip angle, and depth extension, but has a smaller conductivity compared to the C1 conductor. Model C1-Center-A yields a

200

satisfactory match between the real data and the modeled data, suggesting that a smaller conductivity for the C1-North conductor is feasible if its scale is kept the same as the C1 conductor.

However, the right peak of the x-component response from both the modeled data and the real data demonstrate a higher amplitude at early times is unexpected, considering that C1-North actually has a smaller conductivity. This can be explained by examining the x-component responses of typical steeply dipping conductors. As presented in Appendix A, the conductor with a dip angle of 75º or 80º has two peaks in the x-component especially in the middle to late times, which would also be true for the C1 conductor since it is also steeply dipping. For Lines 2200E and 2900E, the first peak of the x-component responses caused by the C1-North conductor may be occurring at the same stations at which the second peak of the responses caused by the C1 conductor occur. Consequently, the right peak in the x-component responses becomes larger than the first one.

The responses of Lines 800E and 1500E are simpler than those seen in Lines 2200E and 2900E due to the absence of the C1-North conductor. The C1 conductor is generally along the east-west direction under Lines 800E and 1500E (Figure 6.19) and consequently the y-component responses in these two lines are noisier than those from Lines 2200E and 2900E. Therefore, a good match can only be found for the x- and z-component responses.

From the grid-scale modeling where both C1 and C1-North conductors are present in the model, a good match between the modeled and real data is achieved. It has

201
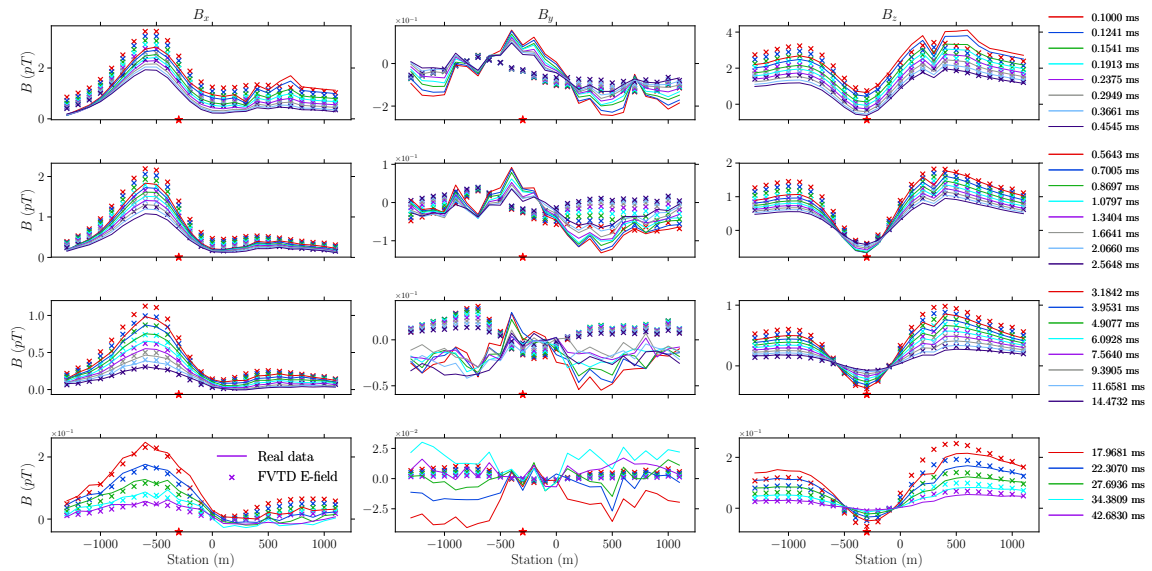
Figure 6.37: Three-component responses calculated by the FVTD method and the real data on Line 800E. The red star symbols mark the top centers of the C1 conductor (left) and the C1-North conductor (right) immediately under Line 800E.
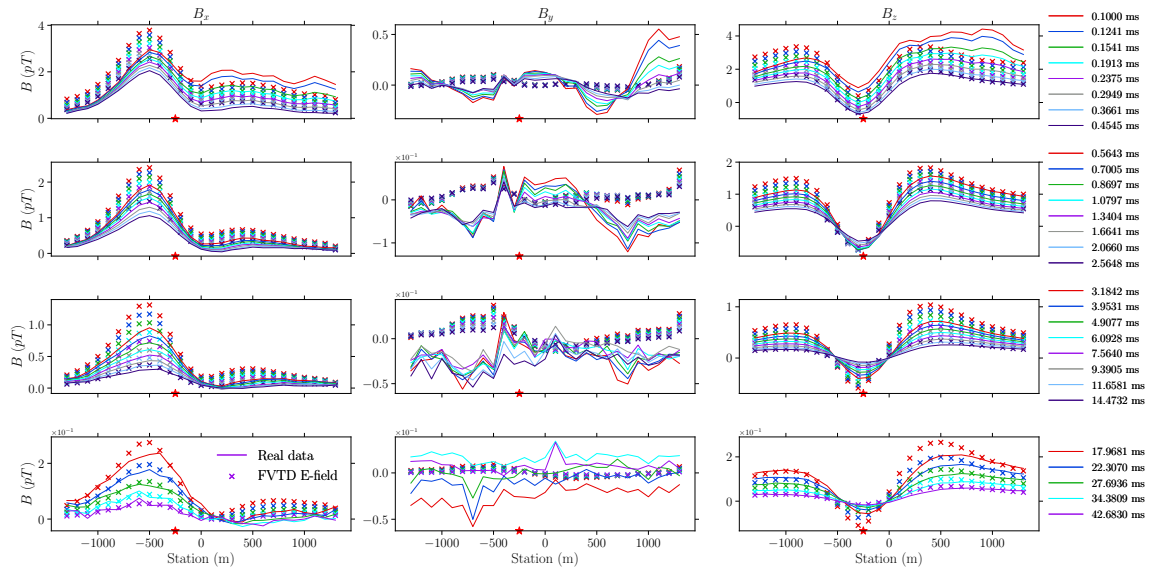
Figure 6.38: Same as Figure 6.37 but for Line 1500E.

been shown that the EM data collected in the C1-Center Grid contains useful information about the existence of the C1-North conductor, which was totally missed in the interpretation of the real data by thin plate modeling using Maxwell software and
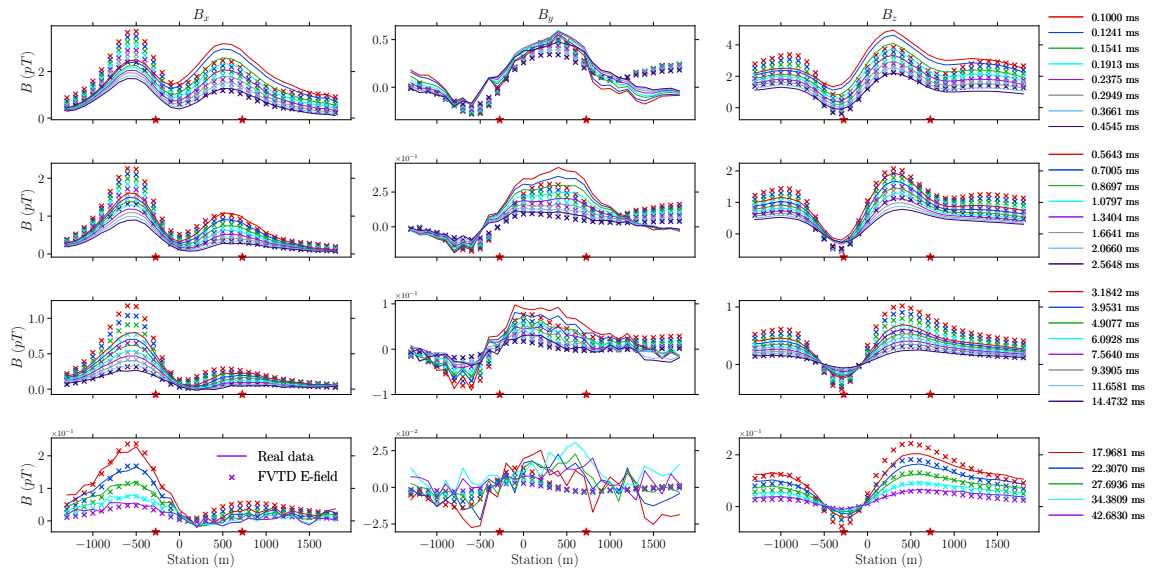
Figure 6.39: Same as Figure 6.37 but for Line 2200E.
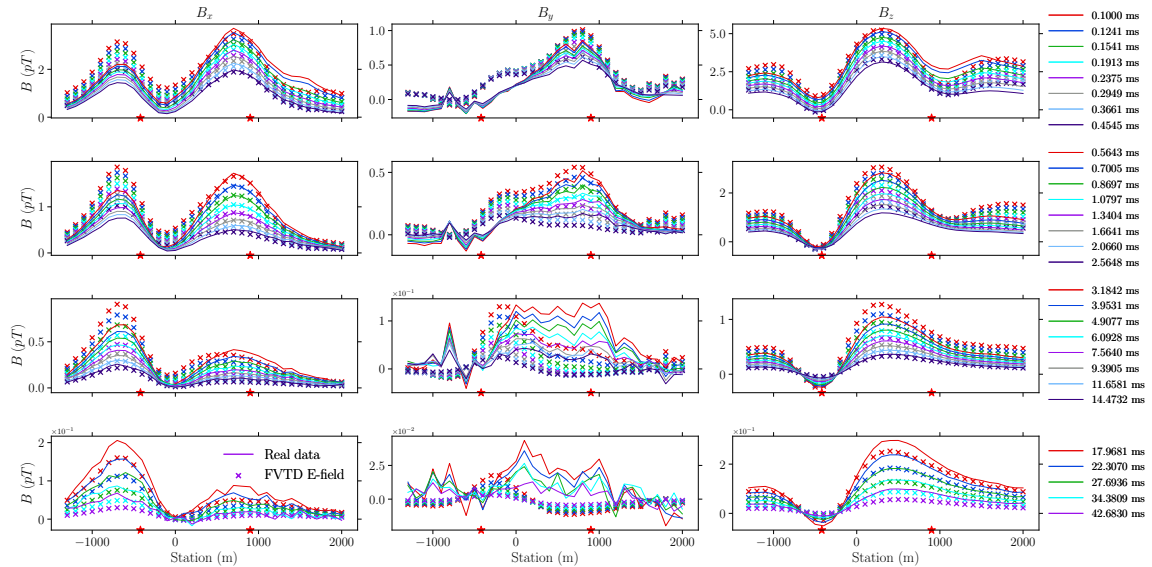
Figure 6.40: Same as Figure 6.37 but for Line 2900E.

only considering the last eight channels of the vertical component data. This modeling experiment shows the importance of modeling three-component data from early to late channels because the C1-North conductor only causes noticeable anomalies in the early times and the anomaly is most obvious in the horizontal components.

6.4.3 C1-West Grid

The C1 conductor extends from the C1-Center Grid further to the west beyond C1-West Grid. There are two lines in C1-West Grid, Line 1400W and Line 2200W (Figure 6.41), which were also surveyed in the 2013 Moving-Loop TEM Program. Drill Hole CL-162 was drilled to target the C1 conductor at Line 1400W as identified in the 2013 Moving-Loop TEM survey but no graphitic conductor was encountered. Then a borehole EM survey was conducted immediately following the drilling to better locate the C1 conductor. Based on the borehole EM data, Drill Hole CL-167 was subsequently drilled to locate the interpreted conductor but also failed (see Figure B.4). In this section, the ground data will be modeled to understand where the C1 conductor is located under C1-West Grid. Besides Drill Holes CL-162 and CL-167 which were drilled at Line 1400W, Drill Hole CLC1-44 (Figure 6.19) was drilled at Line 2400W in the 1988 Diamond Drilling Program (Lavoie et al., 1988). Drill Hole CLC1-44 successfully reached the fault zone and graphite was recorded. In the models in this section, the C1 conductor directly under Lines 1400W and 2200W was built based on the information provided by these three drill holes. Drill holes existing at the C1-Center Grid were also used to build the eastern part of the conductor.
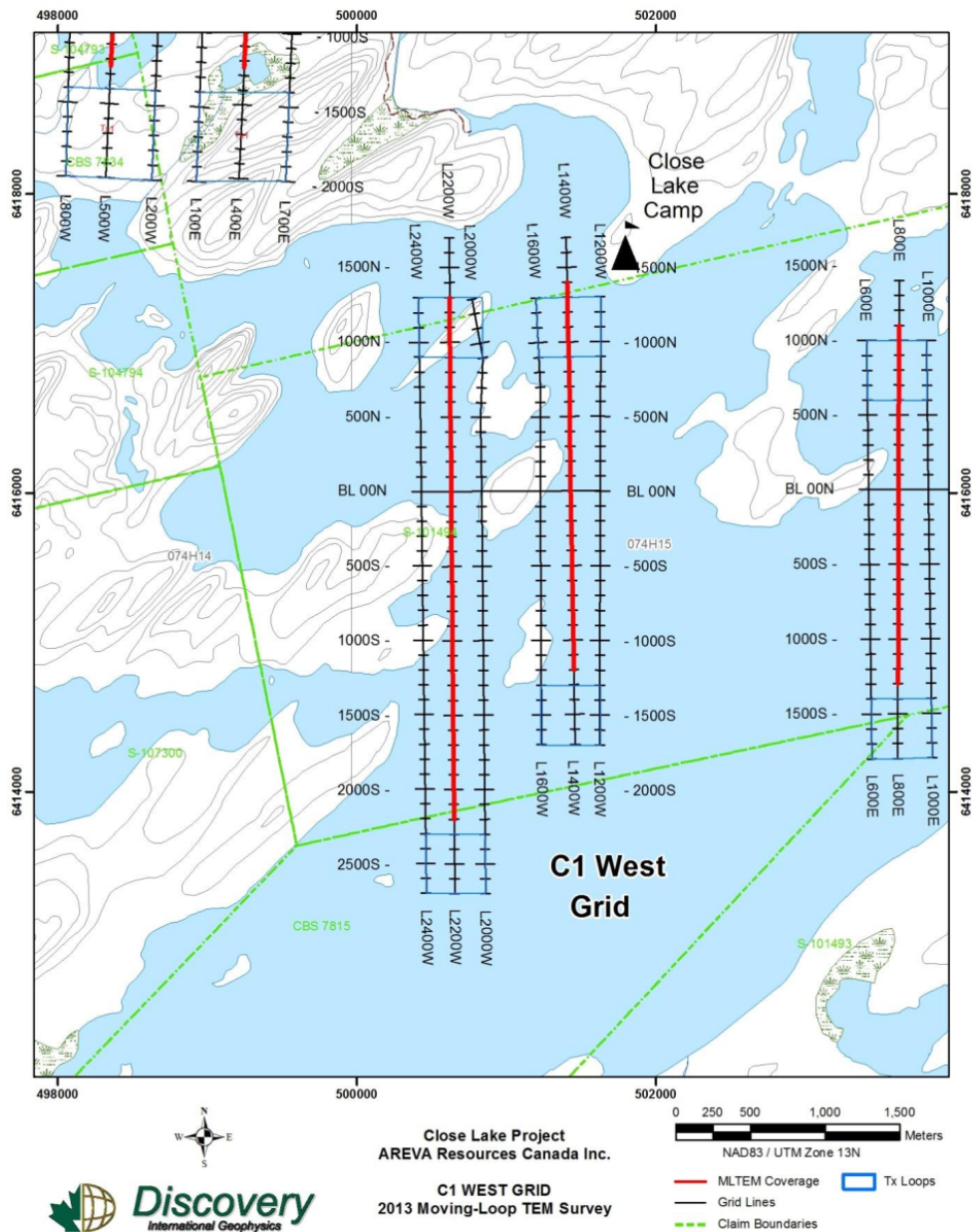
Figure 6.41: The C1-West Grid of the Close Lake Project 2013 Moving-Loop TEM Program (Palomino, 2013).

First, the surface mesh was created for the model considered here: Model C1-West-A. Again, tetrahedral edges with a length of 20 m were inserted in the surface mesh for the refinements of transmitter loop sources, and regular tetrahedra with an
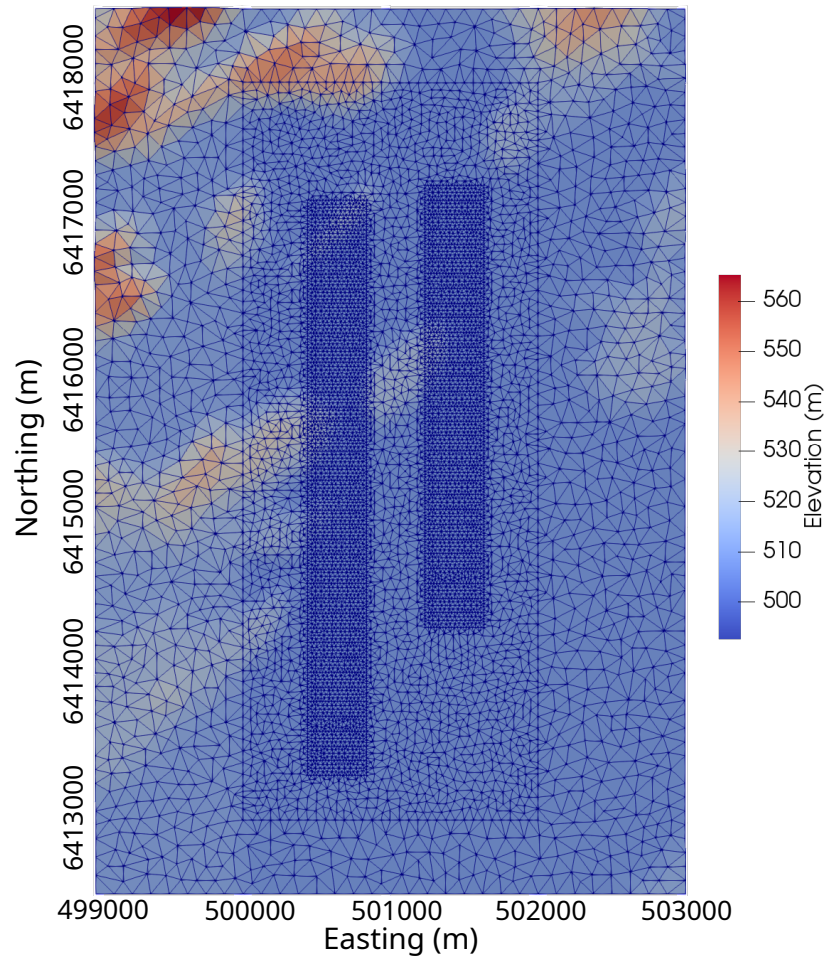
Figure 6.42: The surface mesh with topography data interpolated and refinements added for transmitters and receivers.

edge length of 20 m were inserted for the refinements of receivers. Figure 6.42 shows the surface mesh created using Triangle for C1-West Grid, which has topography interpolated.

The water and overburden columns as recorded in Drill Holes CL-162 and Cl-167 are approximately 60 m in total. MFc and MFb members follow the overburden layer. Their thicknesses, according to Drill Holes CL-162 and CL-167, are approximately 90 m and 280 m, respectively. While only 20 m paleoweathering layer was recorded in

206

Drill Hole CL-162, Drill Hole CL-167 recorded more than 75 m of it. To simplify, the paleoweathering layer was considered to be 60 m here.

In order to be able to adjust conductivities of the conductor for each profile, the conductor in Model C1-West-A was further split into 16 parts: four parts vertically and four parts horizontally (see Figure 6.45). Figure 6.43 shows the central parts of C1-West-A built using FacetModeller. Beyond the paleoweathering layer, there is no drilling information for the basement so that it was treated similarly as what was done for the modeling of C1-Center Grid. Specifically, the basement was divided into four horizontal layers, with the three interfaces located at $z = -230$ m, $z = -780$ m, and $z = -2000$ m, respectively. Beyond the third layer of the basement, it was the background basement where the conductor ceased to exist. The first horizontal interface of the C1 conductor is the same as the interface between the paleoweathering layer and the first basement layer, and the next two interfaces are the same as the interfaces between the first three basement units. The dip angle of the C1 conductor was changed from 70º from the modeling of C1-Center Grid to 90º in order to achieve a better match between the modeled data and the real data.

Again, $\alpha = 1.25$ was used as the only constraint when generating unstructured tetrahedral meshes using TetGen. In total, the tetrahedral mesh has 820,015 edges and 707,235 cells, respectively. Figure 6.44 shows the unstructured tetrahedral mesh generated by TetGen for the PLC shown in Figure 6.43.

Trial-and-error modeling shows that the conductivities of each layer of the basin or basement units cannot be uniform if a good match between the modeled data and the
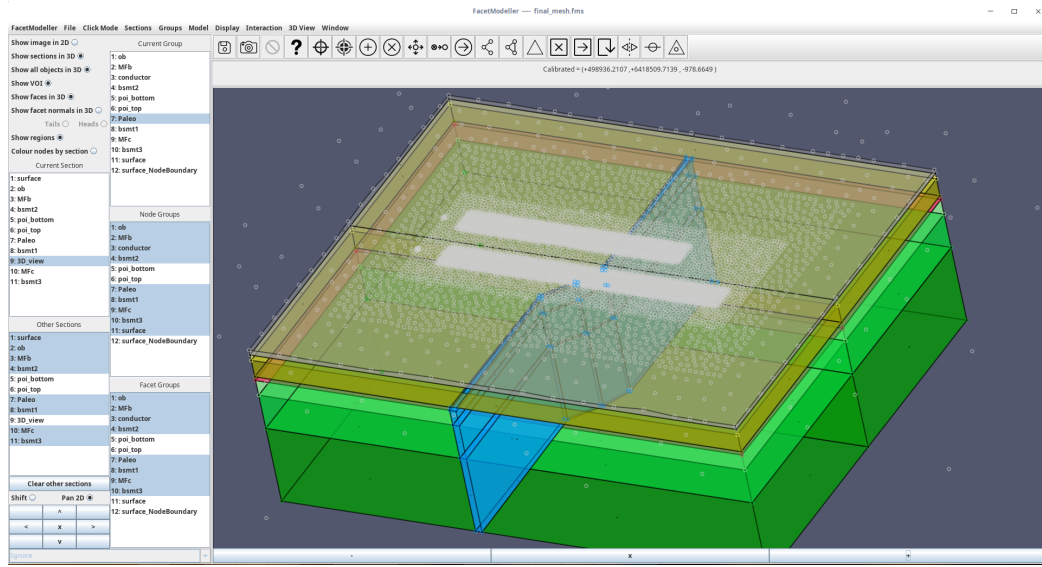
Figure 6.43: A screenshot taken from the FacetModeller software showing the 3D model built for Model C1-West-A. The white nodes come from the surface mesh shown in Figure 6.42, which extends all the way to the model boundaries.

real data is expected. Therefore, the MFc and MFb members of the sandstone basin were further divided into two parts horizontally with the center of the two profiles as the division interface. The paleoweathering, Basement1, Basement2, and Basement3 units (Figure 6.44) were each split into four parts, two north of the conductor and two south of the conductor, with the same interface as used for the sandstone layers dividing them further into east and west ones. The conductivities adopted for Model C1-West-A are listed in Table 6.6.

Figures 6.46 and 6.47 show the three-component responses calculated by the E-field method for Model C1-West-A and the real data at Lines 1400W and 2200W, respectively. For Line 1400W, the x-component of the real data at early times show a wider peak around the conductor as opposed to the modeled data where the peak is typical of a thin dipping conductor. At later times, the peak from the real data narrows

Table 6.6: Conductivities of each unit adopted for Model C1-West-A.

Unit	Conductivity (S/m)	Unit	Conductivity (S/m)
C1-1	0.08	C1-2	0.08
C1-3	10^{-3}	C1-4	10^{-3}
C1-5	0.1	C1-6	0.1
C1-7	0.01	C1-8	0.01
C1-9	0.2	C1-10	0.2
C1-11	2	C1-12	2
C1-13	0.4	C1-15	0.4
C1-14	1.5	C1-16	1.5
Overburden	5×10^{-4}		
MFc West	5×10^{-4}	MFc East	5×10^{-4}
MFb West	4×10^{-4}	MFb East	2×10^{-4}
PW SW	10^{-3}	PW NW	2×10^{-4}
PW SE	8^{-4}	PW NE	2×10^{-4}
BSMT1 SW	5×10^{-4}	BSMT1 NW	10^{-5}
BSMT1 SE	2×10^{-4}	BSMT1 NE	2×10^{-5}
BSMT2 SW	3×10^{-4}	BSMT2 NW	1×10^{-4}
BSMT2 SE	7×10^{-4}	BSMT2 NE	4×10^{-4}
BSMT3 SW	1.5×10^{-3}	BSMT3 NW	1.5×10^{-3}
BSMT3 SE	1.5×10^{-3}	BSMT3 NE	1×10^{-3}
Air	10^{-8}	Background	2×10^{-3}
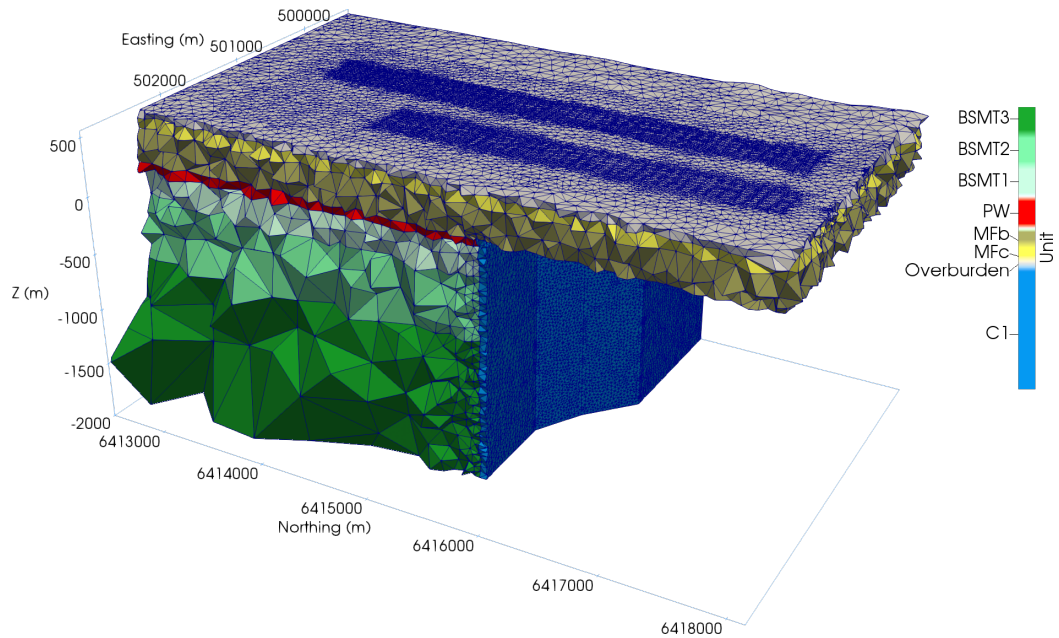
Figure 6.44: Unstructured tetrahedral mesh generated for Model C1-West-A for the modeling of C1-West Grid of the Close Lake Project.

down and is hence closer to the modeled data. The broader anomalous response observed at early times indicates that there may exist other conductive features at shallower depth. The y-component of the modeled data can only match the real data in terms of anomalous patterns at early times. The real data show a larger conductive response than the modeled data. At later times the magnitude of the modeled data becomes closer to that of the real data while still keeping the same pattern. The real data for the last five time gates are very noisy so that meaningful comparisons cannot be achieved. For the vertical component, the match between the modeled data and the real data is better than those of the horizontal components. Note that the shallower parts of the conductor immediately below Line 1400W (C1-3, C1-4, C1-7, and C1-8 in Figure 6.45) are set to be less conductive than the other parts of the C1 conductor (see Table 6.6). Other modeling experiments show that those conductor
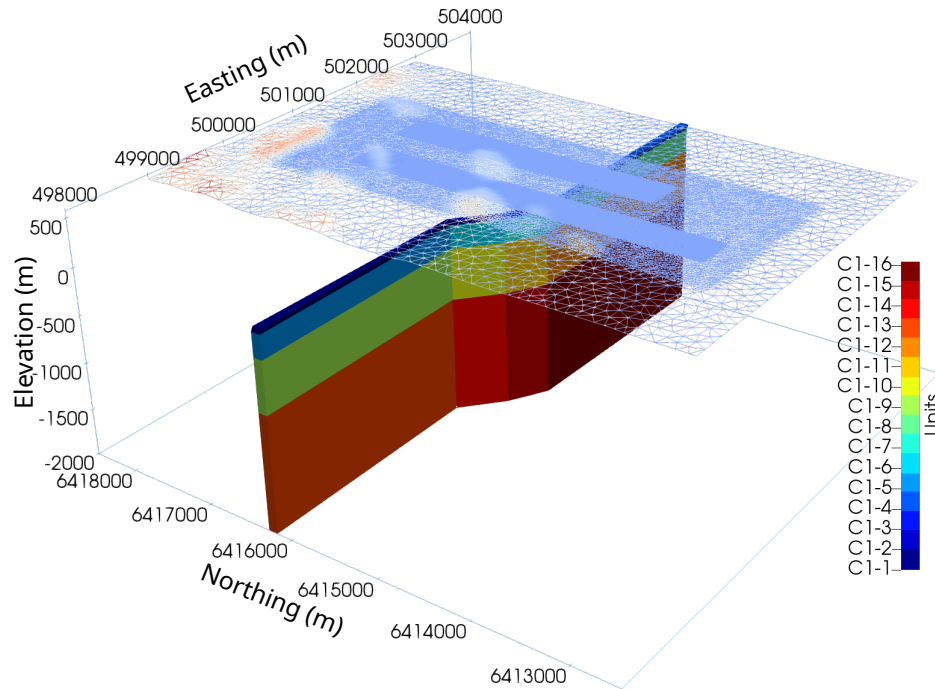
Figure 6.45: A bird's eye view of the conductor shown in Figure 6.44 with the surface mesh showed on top of it. Note that the colors used in this Figure are only intended for distinguishing different parts of the conductor and they are not consistent with the colors used in Figure 6.44.

regions cannot be kept as conductive as other parts of the C1 conductor. Otherwise, a good match cannot be achieved because the modeled data will demonstrate a stronger conductive pattern than the real data: a deeper trough with higher shoulders.

Both Drill Holes CL-162 and CL-167 did not encounter any graphite. In the resistivity probing, the resistivity recorded in Drill Hole CL-162 around the unconformity is largely above 1000 Ω m, and the resistivity recorded in Drill Hole CL-167 briefly reduces to an average of 775.17 Ω m around the unconformity before it quickly increases to well over 10,000 Ω m in the basement (Hutchinson and Zalustskiy, 2015). These resistivity probing results and the absence of graphite in the drill core logs all suggest that the C1 conductor under Line 1400W does not exist immediately below the unconformity. The modeling of Model C1-West-A confirms that the conductor

below Line 1400W starts at a deeper depth. Nonetheless, the good match seen at later channels suggests that the C1 conductor still exists and extends deep into the basement under Line 1400W.

For Line 2200W and for the x-component, the match between the modeled response and the real data is arguably better than that of Line 1400W. The patterns are similar and the magnitudes are almost identical for stations close to the conductor at early to middle times. The match deteriorates at later times due to an increased noise level in the real data. Compared to the x-component, the y-component responses in the real data are even noisier, starting from the first gate. The real data vaguely demonstrates a trough at stations left of the conductor while the trough is very obvious in the modeled data. Also, the amplitude of the trough is larger for the modeled data. For the z-component, the match is also good at early times as observed for the x-component. Even the responses from stations far from the conductor are very close, which means that the conductivities chosen for shallower units such as overburden, MFc and MFb members of the sandstone basin are appropriate. The northern stations (right part of the profile) of the real data have smaller responses compared to the southern (left part of the profile) stations but it is the opposite in the modeled data. In reality, the basement north to the conductor might be significantly more resistive than the basement to the south of the conductor. However, the match of the last five channels seems to be improved despite an increased noise level in the real data.
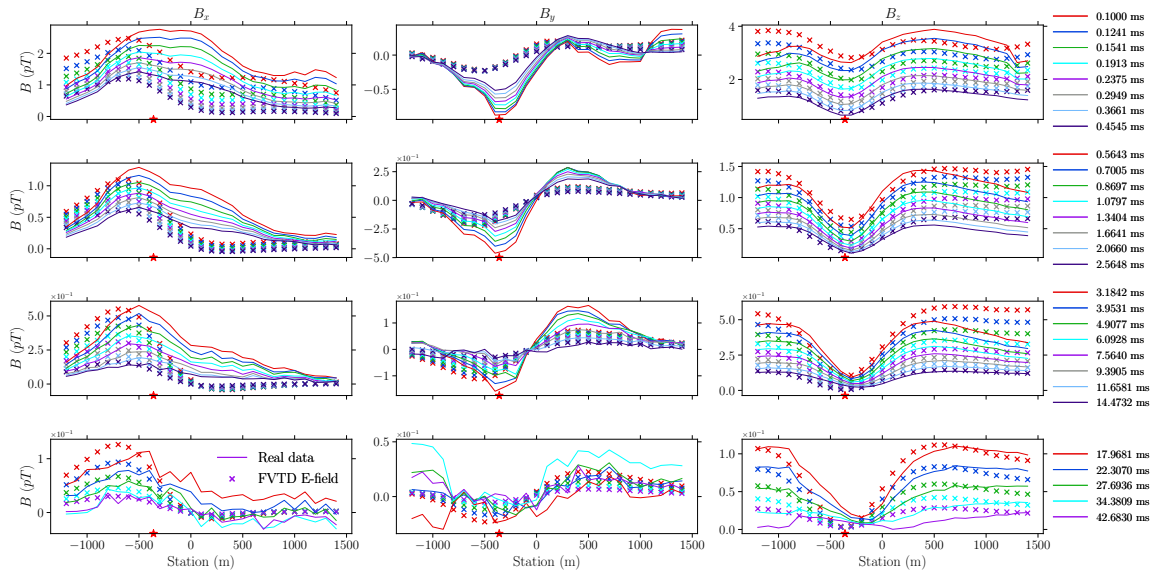
Figure 6.46: Three-component responses calculated by the FVTD method for Model C1-West-D and the real data at Line 1400W. The red star symbol marks approximately the top center of the C1 conductor immediately below the survey line.
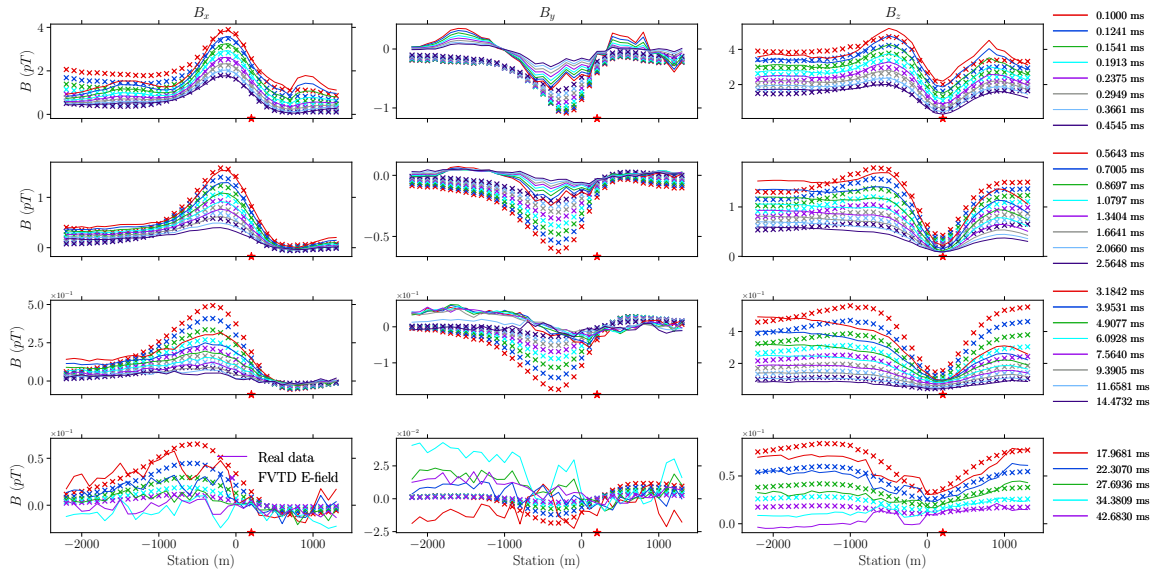
Figure 6.47: Same as Figure 6.46 but for Line 2200W.

6.5 Conclusion

The modeling method developed in this thesis has been successfully applied to the modeling of real-life graphitic fault models in the Athabasca Basin. With the unstruc-

tured Delaunay-Voronoï dual meshes, the thin, steeply dipping graphitic conductors can be easily handled with a mesh that has a relatively small number of cells. The meshing procedure developed in Section 2.4 makes the model building process very easy. Geological structures such as overburden, sandstone and basement units can be easily included in the created 3D model. Compared with fast algorithms such as Maxwell (EMIT, 2005) and MultiLoop (Lamontagne, 2007), the 3D FV modeling method developed in this thesis models the complete, real-life Earth model and can calculate all three-component EM data accurately at any given time within a EM survey. Interpretations based on trial-and-error FVTD modeling which uses all three components and all channels of the collected EM data have been shown to be able to generate geological models much closer to the real geology as revealed by drilling data and to extract useful information in the data that can be easily missed by interpretations based on trial-and-error modeling using those fast algorithms. Because the complete Earth model can be modeled, the investigation on how geological units other than the conductor influence the EM data is also possible.

Chapter 7

Conclusion

In this thesis, a FVTD modeling method that can solve both the electric-field Helmholtz equation as well as the Helmholtz equation and the conservation law of charge equation expressed in terms of the magnetic vector and electric scalar potentials is developed. The method uses the unstructured Delaunay-Voronoï dual meshes and therefore enjoys all the benefits provided by using unstructured grids when modeling realistic geological models. The numerical discretization of Maxwell's equations is carried out in two steps: semi-discretization and full discretization. First, the FV method is used to discretize the continuous spatial partial differential operators into discrete operators based on the dual mesh discretization of space. Those discrete operators are essentially sparse matrices which can be later used to rewrite the continuous PDEs into a semi-discretized ODE system. Second, the full discretization discretizes the time derivatives in the semi-discretized ODE system using a standard time-stepping method, namely, the backward Euler method. Through time stepping, the electric

and potential fields are advanced in time. A good modeling efficiency is achieved by using a direct solver because the factorization results can be reused for multiple iteration steps when the time step is unchanged across successive iterations.

Solving the E-field Helmholtz equation using the FV method is simpler compared with solving the $A - \phi$ system because only the double curl operator needs to be discretized for the E-field method and the number of unknowns in the E-field method is less than that of the $A - \phi$ system. Also, for loop sources, the $A - \phi$ method requires the calculation of initial values for **A** which is used as the initial condition while the E-field method does not need to do so. The initial condition for the magnetic vector potential can either be calculated by analytic solutions or by the FV method developed here, but higher accuracy can be achieved by using the former. On the other hand, the $A - \phi$ system is better conditioned which makes it possible to use iterative solvers although it is not implemented in this thesis. Also, with the $A - \phi$ method, the electric field can be decomposed into galvanic and inductive parts, which is helpful to understand the physics behind the EM diffusion phenomenon for a given subsurface model. Lastly, the $A - \phi$ method can be used to directly obtain the solution for B-field responses while the E-field method needs to numerically integrate the dB/dt response in time in order to get B-field solutions. The E-field method, when used to calculate the B-field response through numerical integration, requires extra care. Extra modeling or numerical extrapolation of the dB/dt response to a time later than the last channel as recorded in real data is needed in order to get an accurate B-field response at late times. In general, the potential method demonstrates a better

accuracy despite being more expensive to compute in terms of both the memory consumption and computing time.

Compared to solving the frequency-domain problems using $\mathbf{A} - \phi$ potentials, the magnetic vector potential $\mathbf{A}$ has to be gauged in order to get consistent solutions for the magnetic field in the time domain. Only the Coulomb gauge condition is considered in this thesis and there are two methods used to enforce this gauge condition: the implicit method and the explicit method. Both the explicit and the implicit methods can generate satisfactory results when compared to analytic solutions for a homogeneous half-space model. The comparison of the modeling results for a 3D conductive block model calculated by the FE code and the FV codes developed here also shows that the results of the two methods are in a very good agreement with each other. The memory consumption when using the implicit gauge enforcement method is approximately three times the amount used by the E-field method, which is consistent with what was found for the frequency-domain problems. The explicit enforcement method requires slightly less memory compared to the implicit enforcement method despite having more equations.

Homogeneous half-space models with different conductivities, different transmitter and receiver configurations are used in the thesis for the validation of the numerical methods developed. Also, responses are computed for complex models with real-life topography and anomalous bodies with complicated geometry and the results are compared to those of other numerical methods. All the comparison results show that the FVTD method developed in this thesis can generate accurate results which

are comparable to other numerical methods such as the FETD method in terms of both accuracy and efficiency. The accuracy of the FVTD method depends on many factors such as the truncation boundary, the mesh quality, and the time-stepping scheme. Taking the E-field method as an example, the effects of these factors are investigated to obtain an optimal setup for the modeling of real data. It is found that the truncation boundary of a 3D model should be sufficiently far away from the center of the mesh so that late-time responses can still be correct. Generally, a more refined, higher quality unstructured mesh leads to results with higher accuracy. For the time-stepping schemes, testing shows that the time steps cannot increase too rapidly if an accurate result is wanted.

The $A - \phi$ method is used to visualize the inductive and galvanic parts of the electric field for models with a thin, plate-like conductor buried in a less conductive homogeneous half-space. The current gathering (current channeling) between the conductor and the less conductive host can be clearly observed. The galvanic part of the electric field, responsible for the current gathering, is caused by the charge buildups at the conductor boundaries due to the existence of a conductivity contrast between the conductor and the host across which current is flowing. When inductive sources are used and the model comprises a conductive target in a less conductive background, the inductive part can provide the dominant contribution to the total electric field at many times. However, the total field and inductive part can be quite different from each other, and the galvanic part can be a critical factor in obtaining what would otherwise be categorized as an inductive response. Therefore, algorithms

218

that do not take the conductive background into consideration, thus ignoring the current gathering effects, may yield misleading results if used without caution.

A three-step procedure is developed in this thesis to create the unstructured Delaunay-Voronoï dual meshes for complex geological models. The created mesh incorporates topography data over survey areas and specific mesh refinements for sources and receivers required by the FVTD method. The geological model is built under a GUI environment provided by the software FacetModeller, which makes the entire process intuitive and easy.

The last part of the thesis models the moving-loop TEM data collected in the Athabasca Basin targeting graphitic fault zones with the FVTD method and mesh creation procedure developed in this thesis. Topography, complex geometries of thin, dipping graphitic faults are incorporated into the model using unstructured Delaunay-Voronoï dual meshes. The modeling method here considers not only the most conductive unit of the model, i.e., the graphitic fault zone, but also other geological units which are less conductive. Such a complete modeling of the geological models enables the data interpretation that uses all three components and all channels of the field data, in contrast to only late-time channels with those fast algorithms. Also, the 3D modeling method here shows that the modeling of conductors which are bending to arbitrary directions is convenient and useful to interpret the spatial extension of the conductors. By splitting the conductor into different parts both horizontally and vertically and assigning different parts of the conductor with different conductivities, a better match between the modeled data and the real data in trial-and-error modeling

219

can be obtained compared to only considering the entire conductor as a uniform body, as what is normally done with those fast algorithms.

As shown by the modeling of the Close Lake Project, preexisting drill logs or other types of geophysical surveys over the project area can be very helpful for the trial-and-error modeling. The sandstone layers in the Athabasca Basin are generally flat-lying such that the stratigraphy revealed by neighboring drill logs can be used as good references. Interpretations of early-stage EM surveys such as airborne EM and fixed-loop EM surveys, when they exist, can help to determine where does the conductor extend laterally. Those data interpretations may not be accurate enough but can serve as a good starting model. The model can then be gradually tuned during the trial-and-error modeling process which eventually results in a model that is supposed to be close to reality once a good match between the modeled data and real data is achieved. The conductivities of all the geological units in the subsurface Earth model can be determined from preexisting physical property measurements collected during previous drilling campaigns. Having a good estimation of the conductivity of each unit of the geological model is critical in efficiently getting a satisfactory match between the modeled data and the real data. A lack of physical property measurements can add difficulties in the trial-and-error modeling, but a good match can still be achieved through trial-and-error modeling, as suggested by the modeling for the Preston Lake Project.

The modeling of the Close Lake Project shows that early-time data can be critical in identifying shallower conductors or conductors with a smaller conductivity. Also,

the modeling of all three components of the field data can give useful information on the lateral extent of the conductor, which is important in the subsequent drill targeting. Because the fast algorithms only assume a perfectly resistive background, and a plate-like shape for the conductor within which the conductivity is uniform, they cannot make use of early-time responses and all three components of the field data. Consequently, important information about the conductor can be missed by the interpretation based on these fast algorithms. For example, the existence of the C1-North conductor is clearly indicated by the field data collected on Lines 2200E and 2900E over the C1-Center Grid of the 2013 moving-loop TEM survey for the Close Lake Project according to the 3D modeling. However, it was totally missed in the original survey report where the interpretation was conducted based on only modeling the last eight channels of the vertical-component real data. The 3D modeling method developed here should therefore be considered when interpreting three-component field data from early to late times.

In this thesis, iterative solvers are not implemented for the $A - \phi$ method. This would be a natural extension of the thesis work in the future. Iterative solvers require less memory compared to direct solvers. The memory consumption can be critical for successful 3D forward modelings especially when the model is discretized with a large number of cells. Time-domain problems are solved using time-stepping methods, and solutions of the previous step can be used as initial solutions for the current step for the iterative solver, which could significantly speed up the convergence of the iterative solver. Proper pre-conditioners should be investigated in order to further improve the

efficiency of the iterative solvers. Because the FV method uses the Delaunay-Voronoï dual mesh which is a generalization of the conventional Yee's grid, it is possible to use the explicit method to solve the time-integrated Maxwell's equations. The calculation of each iteration step for the explicit method essentially is just a matrix-vector product which is easy to parallelize and does not require a large amount of memory. This means the explicit method can be potentially more efficient compared to the implicit method as implemented in this thesis. Although there are foreseeable obstacles such as non-trivial stability conditions, it would still be worth investigating in future work.

Bibliography

Allaire, G., and S. M. Kaber, 2008, Numerical linear algebra: Springer.

Amestoy, P. R., A. Guermouche, J.-Y. L'Excellent, and S. Pralet, 2006, Hybrid scheduling for the parallel solution of linear systems: Parallel Computing, **32**, 136–156.

Annan, A. P., 1974, The equivalent source method for electromagnetic scattering analysis and its geophysical application: PhD thesis, Memorial University of Newfoundland.

Ansari, S., C. Farquharson, and S. MacLachlan, 2017, A gauged finite-element potential formulation for accurate inductive and galvanic modelling of 3-D electromagnetic problems: Geophysical Journal International, **210**, 105–129.

Ansari, S., and C. G. Farquharson, 2014, 3D finite-element forward modeling of electromagnetic data using vector and scalar potentials and unstructured grids: Geophysics, **79**, E149–E165.

Ascher, U. M., 2008, Numerical Methods for Evolutionary Differential Equations: SIAM.

Asten, M. W., 1987, Full transmitter waveform transient electromagnetic modeling and inversion for soundings over coal measures: Geophysics, **52**, 279–288.

Asten, M. W., and A. C. Duncan, 2012, The quantitative advantages of using B-field sensors in time-domain EM measurement for mineral exploration and unexploded ordnance search: Geophysics, **77**, WB137–WB148.

Badea, E., M. E. Everett, G. Newman, and O. Biro, 2001, Finite-element analysis of controlled-source electromagnetic induction using Coulomb-gauged potentials: Geophysics, **66**, 786–799.

Balch, S. J., T. J. Crebs, A. King, and M. Verbiski, 1998, Geophysics of the Voisey's Bay Ni-Cu-Co Deposits: SEG Technical Program Expanded Abstracts., 784–787.

Bingham, D. C., 2004, A report on combined MEGATEM® airborne em and magnetic surveys over the close lake project: Technical Report 74H14-0051, Areva Resources Canada Inc.

Bíró, O., and K. Preis, 1989, On the use of the magnetic vector potential in the finite-element analysis of three-dimensional eddy currents: IEEE Transactions on Magnetics, **25**, 3145–3159.

——, 1990, Finite element analysis of 3-d eddy currents: IEEE Transactions on Magnetics, **26**, 418–423.

Bíró, O., K. Preis, and K. R. Richter, 1996, On the use of the magnetic vector potential in the nodal and edge finite element analysis of 3d magnetostatic problems: IEEE Transactions on Magnetics, **32**, 651–654.

Börner, R.-U., O. G. Ernst, and S. Güttel, 2015, Three-dimensional transient electro-

magnetic modelling using Rational Krylov methods: Geophysical Journal International, **202**, 2025–2043.

Bossavit, A., 1988, Whitney forms: a class of finite elements for three-dimensional computations in electromagnetism: IEE Proceedings A Physical Science, Measurement and Instrumentation, Management and Education, Reviews, **135**, 493.

——, 1999, On the Lorenz gauge: COMPEL - The International Journal for Computation and Mathematics in Electrical and Electronic Engineering, **18**, 323–336.

Bryant, C. F., C. R. Emson, and C. W. Trowbridge, 1990, A General Purpose 3-D Formulation for Eddy Currents Using the Lorentz Gauge: IEEE Transactions on Magnetics, **26**, 2373–2375.

Chew, W. C., 2014, Vector potential electromagnetics with generalized gauge for inhomogeneous media: Formulation: Progress in Electromagnetics Research, **149**, 69–84.

Commer, M., G. M. Hoversten, and E. S. Um, 2015, Transient-electromagnetic finite-difference time-domain earth modeling over steel infrastructure: Geophysics, **80**, E147–E162.

Commer, M., G. A. Newman, J. J. Carazzone, T. A. Dickens, K. E. Green, L. A. Wahrmund, D. E. Willen, and J. Shiu, 2008, Massively parallel imaging of hydrocarbons using the IBM Blue Gene/L supercomputer: IBM Journal of Research and Dev, **52**, 93–103.

Cox, L., G. Wilson, and M. Zhdanov, 2012, 3D inversion of airborne electromagnetic data: Geophysics, **77**, WB59–WB69.

Darnet, M., C. Dezayes, J. Girard, J. Baltassat, C. Lerouge, T. Reuschlé, N. Coppo, F. Bretaudeau, J. Porte, and Y. Lucas, 2019, Geophysical signature of the transition zone between the sedimentary cover and the basement: an analogue approach to help de-risking geothermal prospects: arXiv preprint arXiv:1905.07897.

Duckworth, K., T. D. Nichols, and E. S. Krebes, 2001, Examination of the relative influence of current gathering on fixed loop and moving source electromagnetic surveys: Geophysics, **66**, 1059–1066.

Dyck, A. V., B. M., and M. A. Vallee, 1980, User manual for programs PLATE and SPHERE: Research in Applied Geophysics, No. 14, University of Toronto, Canada.

Edwards, R. N., 1978, On the theory of magnetometric resistivity (MMR) methods: Geophysics, **43**, 1176.

EMIT, 2005, Modeling, presentation and visualization of EM and electrical geophysical data: Technical report.

Everett, M. E., 2013, Near-Surface Applied Geophysics: Cambridge University Press.

Ezersky, M., A. Legchenko, A. Al-zoubi, E. Levi, E. Akkawi, and K. Chalikakis, 2011, TEM study of the geoelectrical structure and groundwater salinity of the Nahal Hever sinkhole site , Dead Sea shore , Israel: Journal of Applied Geophysics, **75**, 99–112.

Farquharson, C. G., 2008, Constructing piecewise-constant models in multidimensional minimum-structure inversions: Geophysics, **73**, K1–K9.

Farquharson, C. G., K. Duckworth, and D. W. Oldenburg, 2006, Comparison of integral equation and physical scale modeling of the electromagnetic responses of

models with large conductivity contrasts: Geophysics, **71**, G169–G177.

Farquharson, C. G., and M. P. Miensopust, 2011, Three-dimensional finite-element modelling of magnetotelluric data with a divergence correction: Journal of Applied Geophysics, **75**, 699–710.

Farquharson, C. G., and D. W. Oldenburg, 2004, A comparison of automatic techniques for estimating the regularization parameter in non-linear inverse problems: Geophysical Journal International, **156**, 411–425.

Feynman, R. P., B. B. Leighton, and M. Sands, 2010, The Feynmen Lectures on Physics, new millennium ed.: Basic Books, **II**.

Fitterman, D. V., and W. L. Anderson, 1987, Effect of transmitter turn-off time on transient soundings: Geoexploration, **24**, 131–146.

Francés, A. P., M. W. Lubczynski, J. Roy, F. A. Santos, and M. R. M. Ardekani], 2014, Hydrogeophysics and remote sensing for the design of hydrogeological conceptual models in hard rocks sardón catchment (Spain): Journal of Applied Geophysics, **110**, 63 – 81.

Haber, E., 2014, Computational Methods in Geophysical Electromagnetics: SIAM.

Haber, E., U. Ascher, and D. W. Oldenburg, 2002, 3D forward modelling of time domain electromagnetic data, *in* SEG Technical Program Expanded Abstracts 2002: Society of Exploration Geophysicists, 641–644.

Haber, E., and U. M. Ascher, 2001, Preconditioned all-at-once methods for large , sparse parameter estimation problems: Inverse Problems, **17**, 1847–1864.

Haber, E., U. M. Ascher, D. a. Aruliah, and D. W. Oldenburg, 2000, Fast simulation of

3D electromagnetic problems using potentials: Journal of Computational Physics, **163**, 150–171.

Harrington, R. F., 2001, Time-harmonic Electromagnetic fields: Wiley-IEEE Press.

Hutchinson, R., and V. Zalustskiy, 2015, Close lake project 2015 annual drilling report: Technical Report MAW01818, Areva Resources Canada Inc.

Irvine, R., and K. Witherly, 2006, *in* Advances in airborne EM acquisition and processing for uranium exploration in the Athabasca Basin, Canada: 1258–1262.

——, 2007, Reconciling airborne and ground geophysical outcomes in the athabasca basin, saskatchewan, canada: ASEG Extended Abstracts, **2007**, 1–5.

Iserles, A., 2009, A first course in the numerical analysis of differential equations, second ed.: Cambridge University Press.

Jackson, J. D., 1998, Classical electrodynamics, third ed.: John Wiley & Sons, Inc.

——, 2002, From Lorenz to Coulomb and other explicit gauge transformations: American Journal of Physics, **70**, 917–928.

Jahandari, H., S. Ansari, and C. G. Farquharson, 2017, Comparison between staggered grid finite-volume and edge-based finite-element modelling of geophysical electromagnetic data on unstructured grids: Journal of Applied Geophysics, **138**, 185–197.

Jahandari, H., and C. Farquharson, 2015, Finite-volume modelling of geophysical electromagnetic data on unstructured grids using potentials: Geophysical Journal International, **202**, 1859–1876.

Jahandari, H., and C. G. Farquharson, 2014, A finite-volume solution to the geophysical electromagnetic forward problem using unstructured grids: Geophysics, **79**,

E287–E302.

Jefferson, C. W., D. J. Thomas, S. S. Gandhi, P. Ramaekers, G. Delaney, D. Brisbin, C. Cutts, D. Quirt, P. Portella, and R. A. Olson, 2007, Unconformity-Associated Uranium Deposits of the Athabasca Basin, Saskatchewan and Alberta, *in* Mineral deposits of Canada: a synthesis of major deposit-types, district metallogeny, the evolution of geological provinces, and exploration methods: Geological Association of Canada, Mineral Deposits Division, Special publication no. 5, 273–305.

Jin, J.-M., 2015, The finite element method in electromagnetics, third ed.: John Wiley & Sons, Inc.

Jiracek, G. R., 1990, Near-surface and topographic distortions in electromagnetic induction: Surveys in Geophysics, **11**, 163–203.

Jones, D., S. Ansari, C. Farquharson, and R. Hearst, 2016, Synthesizing time-domain electromagnetic data for graphitic fault zones and associated uranium deposits in the athabasca basin, canada, *in* SEG Technical Program Expanded Abstracts 2016: 2206–2210.

Keller, C., 2019, *in* Advancements in 3D time-domain electromagnetic inversion in the Athabasca Basin, Canada: A unique case study from the West McArthur project: 2133–2137.

Kordy, M., P. Wannamaker, V. Maris, E. Cherkaev, and G. Hill, 2016, 3-D magnetotelluric inversion including topography using deformed hexahedral edge finite elements and direct solvers parallelized on SMP computers - Part I: forward problem and parameter Jacobians: Geophysical Journal International, **204**, 74–93.

Lamontagne, Y., 2007, Deep Exploration with EM in Boreholes: Proceedings of Exploration 07: Fifth Decennial International Conference on Mineral Exploration, 401–415.

Lamontagne, Y., J. Macnae, and B. Polzer, 1988, Multiple conductor modeling using program multiloop, *in* SEG Technical Program Expanded Abstracts 1988: Society of Exploration Geophysicists, 237–240.

Lamontagne, Y., and G. F. West, 1971, EM RESPONSE OF A RECTANGULAR THIN PLATE: Geophysics, **36**, 1204–1222.

Lavoie, S., P. Bruneton, and R. Koch, 1988, Close Lake project final report 1988: Technical Report 74H14-0027, Cogema Canada Limited. (Volume I).

Lelièvre, P. G., A. Carter-McAuslan, C. Farquharson, and C. Hurich, 2012, Unified geophysical and geological 3D Earth models: The Leading Edge, **31**, 322–328.

Lelièvre, P. G., A. E. Carter-McAuslan, M. W. Dunham, D. J. Jones, M. Nalepa, C. L. Squires, C. J. Tycholiz, M. A. Vallée, and C. G. Farquharson, 2018a, FacetModeller: Software for manual creation, manipulation and analysis of 3D surface-based models: SoftwareX, **7**, 41–46.

Lelièvre, P. G., C. G. Galley, and C. G. Farquharson, 2018b, Podium: a suite of software utilities for preparation of data for inversion on unstructured meshes (version 1.0): https://www.esd.mun.ca/~farq/.

Levy, G., 1984, Correction of measured transient electromagnetic responses for finite transmitter turn-off duration: Technical Report Geonics Technical Note TN-16, Geonics Limited.

Li, J., C. G. Farquharson, and X. Hu, 2017, 3D vector finite-element electromagnetic forward modeling for large loop sources using a total-field algorithm and unstructured tetrahedral grids: Geophysics, **82**, E1–E16.

Li, J., X. Lu, C. G. Farquharson, and X. Hu, 2018, A finite-element time-domain forward solver for electromagnetic methods with complex-shaped loop sources: Geophysics, **83**, E117–E132.

Li, S., H. Sun, X. Lu, and X. Li, 2014, Three-dimensional Modeling of Transient Electromagnetic Responses of Water-bearing Structures in Front of a Tunnel Face: Journal of Environmental & Engineering Geophysics, **19**, 13–32.

Li, Y., S. Sun, Q. I. Dai, and W. C. Chew, 2015, Vectorial solution to double curl equation with generalized coulomb gauge for magnetostatic problems: IEEE Transactions on Magnetics, **51**, 1–6.

Liu, G., 1998, Effect of transmitter current waveform on airborne TEM response: Exploration Geophysics, **29**, 35–41.

Lu, X., X. Li, Z. Qi, and H. Sun, 2013, A Parallel 3-D Finite Difference, Time Domain Method for Modeling of Transient Electromagnetic Diffusion Phenomena in Tunnels: Near Surface Geophysics Asia Pacific Conference, Beijing, China, 17-19 July, 2013, 488–491.

Mackie, R. L., T. R. Madden, and P. E. Wannamaker, 1993, Three-dimensional magnetotelluric modeling using difference equations - theory and comparisons to integral equation solutions: Geophysics, **58**, 215–226.

Macnae, J., and T. Kratzer, 2012, Joint sensing of B and dB/dt responses: 23rd

International Geophysical Conference and Exhibition, 1–4.

Macnae, J. C., R. Smith, B. D. Polzer, P. S. Klinkert, and Y. Lamontagne, 1991, Conductivitydepth imaging of airborne electromagnetic stepresponse data: Geophysics, **56**, 102–114.

Manges, J. B., and Z. J. Cendes, 1995, A Generalized Tree-Cotree Gauge for Magnetic Field Computation: IEEE Transactions on Magnetics, **31**, 1342–1347.

Miller, G. L., D. Talmor, S.-H. Teng, N. Walkington, and H. Wang, 1996, Control volume meshes using sphere packing: Generation, refinement and coarsening.

Miorelli, F., R. L. Mackie, F. Gilbert, and W. Soyer, 2019, *in* Foothills structural model de-risking with 3D magnetotellurics: 1090–1094.

Nam, M. J., H. J. Kim, Y. Song, T. J. Lee, and J. H. Suh, 2009, Three-dimensional topographic and bathymetric effects on magnetotelluric responses in Jeju Island, Korea: Geophysical Journal International, **176**, 457–466.

Newman, G. a., and D. L. Alumbaugh, 1995, Frequency-domain modelling of airborne electromagnetic responses using staggered finite differences: Geophysical Prospecting, **43**, 1021–1042.

Newman, G. A., and G. W. Hohmann, 1988, Transient electromagnetic responses of high-contrast prisms in a Layered Earth Model: Geophysics, **53**, 691–706.

Newman, G. A., G. W. Hohmann, and W. L. Anderson, 1986, Transient electromagnetic response of a three-dimensional body in a layered earth: Geophysics, **51**, 1608–1627.

Oldenburg, D. W. D., E. Haber, and R. Shekhtman, 2013, Three dimensional inversion

of multisource time domain electromagnetic data: Geophysics, **78**, E47–E57.

Oristaglio, M., and G. Hohmann, 1984, Diffusion of electromagnetic fields into a two-dimensional earth: A finite-difference approach: Geophysics, **49**, 870–894.

Palomino, A. D., 2013, Close Lake project SQUID Moving-Loop TEM survey logistics report: Technical report, Discovery Int'l Geophysics Inc.

Pasion, L. R., S. D. Billings, D. W. Oldenburg, and S. E. Walker, 2007, Application of a library based method to time domain electromagnetic data for the identification of unexploded ordnance: Journal of Applied Geophysics, **61**, 279–291.

Powell, B., G. Wood, and L. Bzdel, 2007, Advances in Geophysical Exploration for Uranium Deposits in the Athabasca Basin: Proceedings of Exploration 07: Fifth Decennial International Conference on Mineral Exploration, 771–790.

Puzyrev, V., J. Koldan, J. de la Puente, G. Houzeaux, M. Vázquez, and J. M. Cela, 2013, A parallel finite-element method for three-dimensional controlled-source electromagnetic forward modelling: Geophysical Journal International, **193**, 678–693.

Qiu, C., S. Güttel, X. Ren, C. Yin, Y. Liu, B. Zhang, and G. Egbert, 2019, A block rational Krylov method for 3-D time-domain marine controlled-source electromagnetic modelling: Geophysical Journal International, **218**, 100–114.

Ren, Z., T. Kalscheuer, S. Greenhalgh, and H. Maurer, 2013, A goal-oriented adaptive finite-element approach for plane wave 3-D electromagnetic modelling: Geophysical Journal International, **194**, 700–718.

Richard, Y., 2013, Close lake project 2013 geophysical report: Technical Report MAW00516, Areva Resources Canada Inc.

Roux, L., and J. Macnae, 2007, SQUID sensors for EM systems: Proceedings of Exploration 07: Fifth Decennial International Conference on Mineral Exploration, 417–423.

Sazonov, I., O. Hassan, K. Morgan, and N. P. Weatherill, 2008, Comparison of two explicit time domain unstructured mesh algorithms for computational electromagnetics, *in* Partial Differential Equations: Modeling and Numerical Simulation: Springer, 95–112.

Shewchuk, J. R., 1996, Triangle: Engineering a 2D Quality Mesh Generator and Delaunay Triangulator, *in* Applied Computational Geometry: Towards Geometric Engineering: Springer-Verlag, volume **1148** *of* Lecture Notes in Computer Science, 203–222. (From the First ACM Workshop on Applied Computational Geometry).

Si, H., 2015, TetGen, a Quality Tetrahedral Mesh Generator: AMC Transactions on Mathematical Software, **41**, 11.

Smiarowski, A., and J. Macnae, 2013, Detection of a perfect conductor with an airborne electromagnetic system: The Gemini field test: Geophysics, **78**, E249–E259.

Smith, R. S., R. Koch, G. Hodges, and J. Lemieux, 2011, A comparison of airborne electromagnetic data with ground resistivity data over the Midwest deposit in the Athabasca basin: Near Surface Geophysics, **9**, 319–330.

Spies, B. R., and F. C. Frischknecht, 1991, Electromagnetic sounding, *in* Electromagnetic Methods in Applied Geophysics: Volume 2, Application, Parts A and B: Society of Exploration Geophysicists, 285–425.

Um, E. S., D. L. Alumbaugh, and J. M. Harris, 2010a, A lorenzgauged finiteele-

ment solution for transient csem modeling, *in* SEG Technical Program Expanded Abstracts 2010: 748–752.

Um, E. S., M. Commer, G. a. Newman, and G. M. Hoversten, 2015, Finite element modelling of transient electromagnetic fields near steel-cased wells: Geophysical Journal International, **202**, 901–913.

Um, E. S., J. M. Harris, and D. L. Alumbaugh, 2010b, 3D time-domain simulation of electromagnetic diffusion phenomena: A finite-element electric-field approach: Geophysics, **75**, F115–F126.

Vallée, M. A., R. S. Smith, and P. Keating, 2011, Metalliferous mining geophysics State of the art after a decade in the new millennium: Geophysics, **76**, W31–W50.

Walker, P., and Y. Lamontagne, 2007, Electromagnetic Modelling of the Cree Lake Extension, Millenium Deposit, with MultiLoop III: Proceedings of Exploration 07: Fifth Decennial International Conference on Mineral Exploration, 1077–1080.

Walton, S., O. Hassan, and K. Morgan, 2017, Advances in co-volume mesh generation and mesh optimisation techniques: Computers and Structures, **181**, 70–88.

Wang, T., and G. Hohmann, 1993, A finite-difference, time-domain solution for three-dimensional electromagnetic modeling: Geophysics, **58**, 797–809.

Ward, S. H., and G. W. Hohmann, 1988, Electromagnetic Theory for Geophysical Applications, *in* Electromagnetic Theory for Geophysical Applications: 4, 130–311.

Weiss, C. J., 2010, Triangulated finite difference methods for global-scale electromagnetic induction simulations of whole mantle electrical heterogeneity: Geochemistry, Geophysics, Geosystems, **11**.

———, 2013, Project APhiD: A Lorenz-gauged A-Φ decomposition for parallelized computation of ultra-broadband electromagnetic induction in a fully heterogeneous Earth: Computers and Geosciences, **58**, 40–52.

West, G., and J. Macnae, 1991, Physics of the electromagnetic induction exploration method, *in* Electromagnetic Methods in Applied Geophysics: Volume 2, Application, Parts A and B: Society of Exploration Geophysicists, 5–46.

Weymer, B. A., M. E. Everett, T. S. [de Smet], and C. Houser, 2015, Review of electromagnetic induction for mapping barrier island framework geology: Sedimentary Geology, **321**, 11 – 24.

Weymer, B. A., M. E. Everett, C. Houser, P. Wernette, and P. Barrineau, 2016, Differentiating tidal and groundwater dynamics from barrier island framework geology: Testing the utility of portable multifrequency electromagnetic induction profilers: Geophysics, **81**, E347–E361.

Williams, N. C., 2008, Geologically-constrained UBC-GIF gravity and magnetic inversions with examples from the Agnew-Wiluna greenstone belt, Western Australia: PhD thesis, The University of British Columbia.

Xie, Z. Q., O. Hassan, and K. Morgan, 2011, Tailoring unstructured meshes for use with a 3D time domain co-volume algorithm for computational electromagnetics: International Journal for Numerical Mthods in Engineering, **87**, 48–65.

Yang, D., and D. W. Oldenburg, 2012, Three-dimensional inversion of airborne time-domain electromagnetic data with applications to a porphyry deposit: Geophysics, **77**, B23–B34.

Yee, K. S., 1966, Numerical solution of initial boundary value problems involving maxwell's equations in isotropic media: IEEE Transactions on Antennas and Propagation, **14**, 302–307.

Yin, C., Y. Qi, and Y. Liu, 2016, 3D time-domain airborne EM modeling for an arbitrarily anisotropic earth: Journal of Applied Geophysics, **131**, 163–178.

Young, M. E., P. G. Macumber, M. D. Watts, and N. Al-Toqy, 2004, Electromagnetic detection of deep freshwater lenses in a hyper-arid limestone terrain: Journal of Applied Geophysics, **57**, 43–61.

Zanchi, A., S. Francesca, Z. Stefano, S. Simone, and G. Guerra, 2009, 3D reconstruction of complex geological bodies: Examples from the Alps: Computers & Geosciences, **35**, 49–69.

Zeng, S., X. Hu, J. Li, C. G. Farquharson, P. C. Wood, X. Lu, and R. Peng, 2019, Effects of full transmitting-current waveforms on transient electromagnetics: Insights from modeling the Albany graphite deposit: Geophysics, **84**, E255–E268.

Zhou, J., W. Liu, X. Li, and Z. Qi, 2018, 3D transient electromagnetic modeling using a shift-and-invert Krylov subspace method: Journal of Geophysics and Engineering, **15**, 1341–1349.

Appendix A

Moving-loop TEM responses of typical thin, dipping conductors

The characteristics of the EM response of dipping, thin conductors for a moving-loop configuration are important references for identifying graphitic faults in the Athabasca Basin. Here, the responses of dipping, thin conductors with different dip angles are investigated. These conductors are assumed to have the same thickness and conductivity, which are set to 1 S/m and 50 m, respectively. The conductors are considered to be buried in a resistive homogeneous half-space background, with the conductivity of the background being set to 10^{-4} S/m.

A 3,400 m long profile which is parallel to the y-direction is considered here with the station spacing being set to 100 m. So, in total, there are 35 stations in the profile. To make the example more relevant to the modeling of the Close Lake Project presented in Chapter 6, the conductor here is considered to be buried 500 m below

the surface. The strike is along the x-direction and the top center of the conductor is located at (0, 0, -500) m. The same source and receiver configuration as used in the Close Lake Project are used here. Specifically, a 400×400 m loop source is used and the receiver is 600 m north to the center of the loop source. Also, the same waveform and time gates as used in the Close Lake Project are adopted here. There are 9 models considered and they cover dip angles from 30° to 150°.

Figure A.1 shows the three-component B-field responses of the 30° dipping conductor. For the x-component response, it has only one peak in the early to middle times about 200 m left of the conductor. Then another peak gradually emerges at the right of the conductor. The peak slowly moves to the right with time, and the peak is nearly 1000 m right of the conductor for late channels while the left peak generally stays at its original location. For the vertical component, a trough is observed near the conductor and the responses in early times are close to being symmetric, with the left shoulder larger than the right one. However, the right shoulder is larger than the left one in late times. In the first eight channels, the minimum vertical component (center of the trough) is located one station to the right ($x = 100$ m) of the top center of the conductor although the response at $x = 0$ m is very close to that of the next right station. Then it gradually switched to $x = -100$ m in the next eight channels (second row of Figure A.1), and it becomes even more obvious for channels 17 to 24 (third row of Figure A.1).

Figure A.2 shows the three-component B-field responses of the 45° dipping conductor. Both the x- and z-component responses are similar to those observed from

239
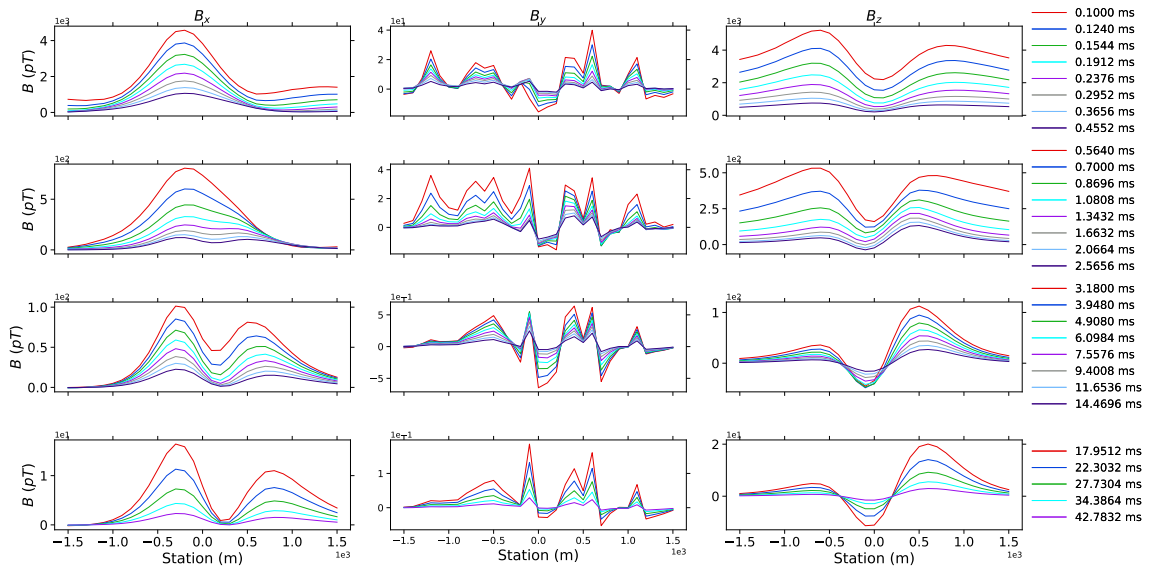
Figure A.1: Three-component responses of the conductor with a 30° dip angle.

Figure A.1. The right peak in the x-component now becomes larger than the left one, which is different from the previous conductor. The z-component response now has a smaller amplitude compared to Figure A.1, especially for the late-time channels. This can be explained by the fact that now the lower part of the conductor is buried deeper. Also, the left shoulder of the vertical component now is even smaller compared to the right one.

Figure A.3 shows the three-component B-field responses of the 60° dipping conductor. The right peak in the x-component is even larger than the left one in late times. The left shoulder of the vertical component in late times now is almost invisible and the magnitude further decreases compared to the 45° dipping conductor. The trough in early times is further to the right and in late times it is further to the left.

Figure A.4 shows the three-component B-field responses of the 75° dipping conductor. It is interesting to see that the response is very similar to that of the 30°

240
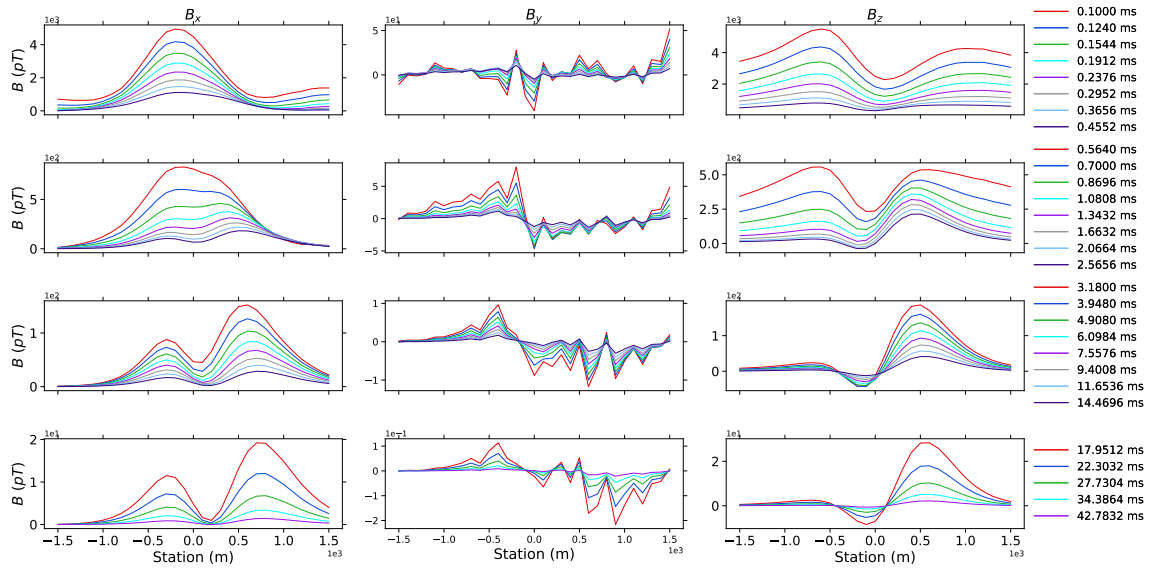
Figure A.2: Three-component responses of the conductor with a 45° dip angle.
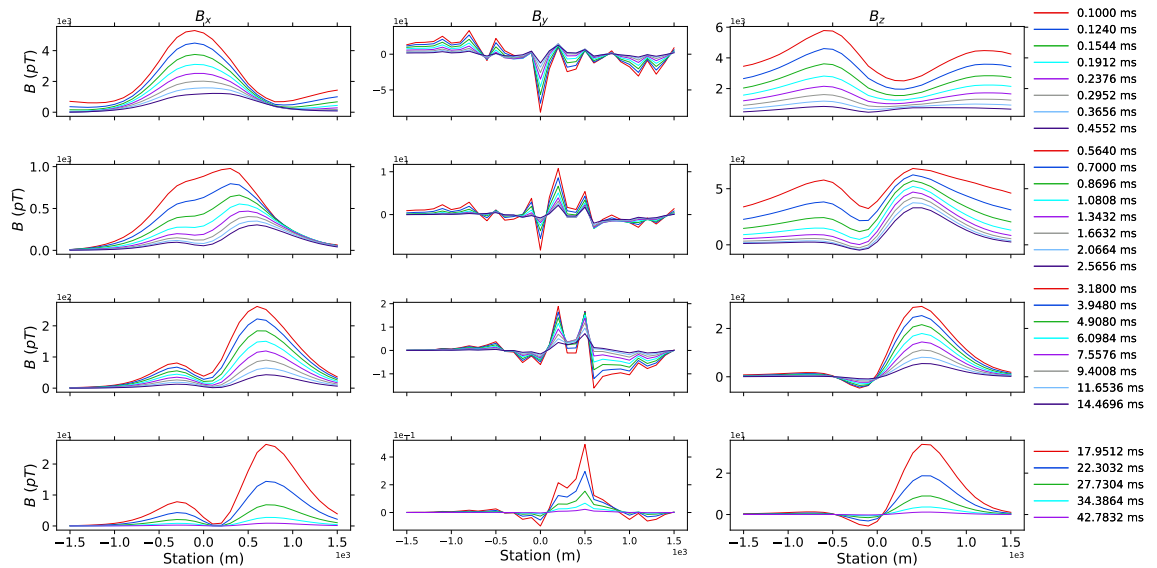
Figure A.3: Three-component responses of the conductor with a 60° dip angle.
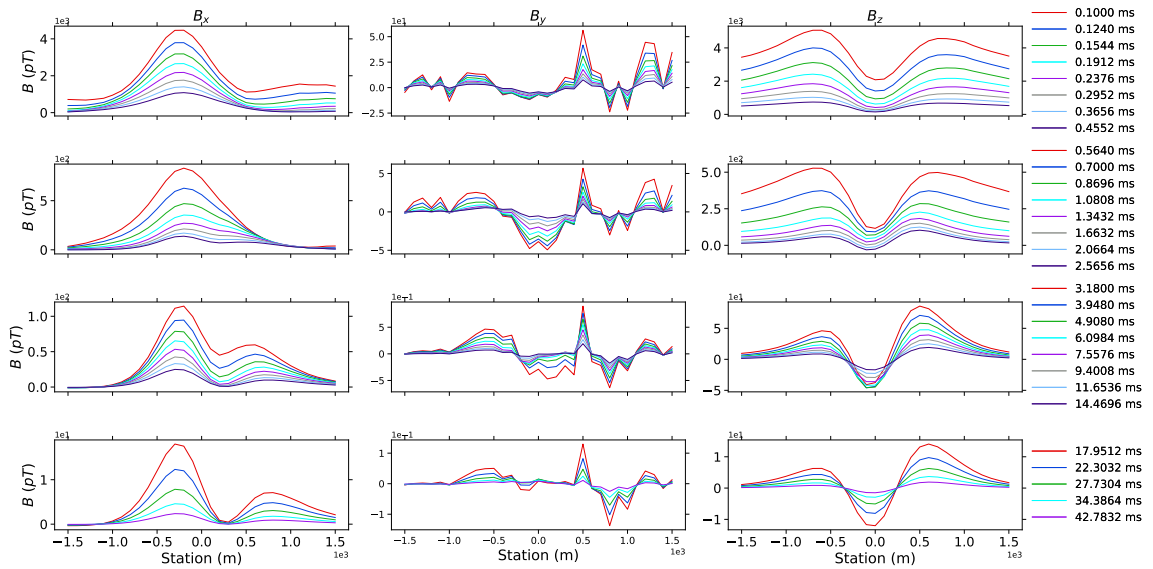
Figure A.4: Three-component responses of the conductor with a 75° dip angle.

dipping conductor. The right peak in the x-component response is less significant compared to the 30° dipping conductor. The magnitude of the vertical component response is smaller than that of the 30° dipping conductor except for the very early times, indicating that the decay of the 75° dipping conductor is faster than the 30° dipping conductor. With a larger dip angle, the minimum vertical response (center of the trough) in the profile is always located at the center of the plate from early to late times.

As the dip increases to 80° (Figure A.5), the right peak in the x-component is slightly smaller compared to the 75° dipping conductor, the change in the vertical component is minor.

When the conductor becomes vertical, as shown in Figure A.6, the right peak in the x-component is only a fraction of the left peak. The vertical component responses are now more symmetric and the left shoulder is only slightly larger than the right one
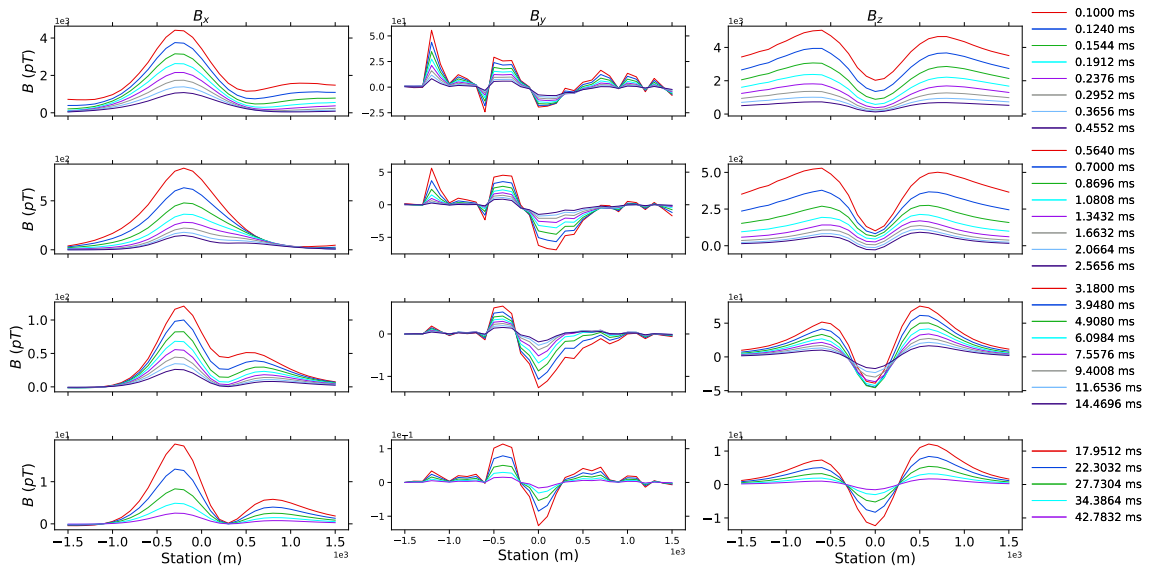
Figure A.5: Three-component responses of the conductor with a 80º dip angle.

in late times. The center of the trough in the vertical component is always pointing to the top center of the conductor.

When the dip angle increases to 120º (Figure A.7), the second peak in the profile is only vaguely noticeable in the very early times. The *z*-component responses are nearly symmetric to that of the 30º dipping conductor. Similar observations can be made between the 135º dipping conductor (Figure A.8) and the 45º dipping conductor. However, the vertical component of the 150º dipping conductor is noticeably different from that of the 30º dipping conductor. The right shoulder of the 150º dipping conductor (Figure A.9) almost disappears while the left shoulder of the 30º dipping conductor is clearly visible.
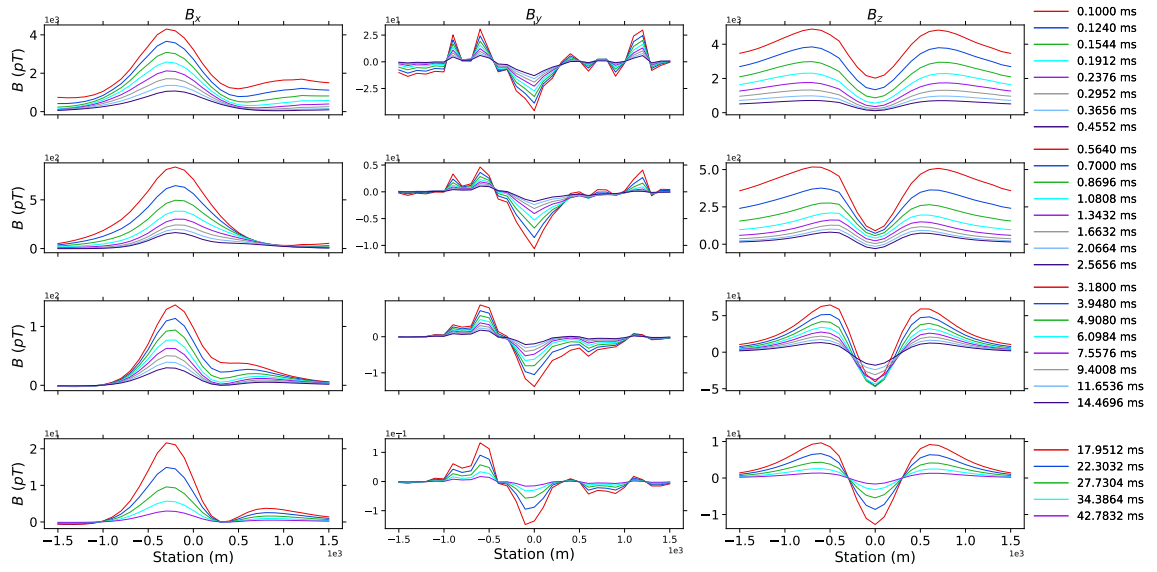
Figure A.6: Three-component responses of the conductor with a 90° dip angle.
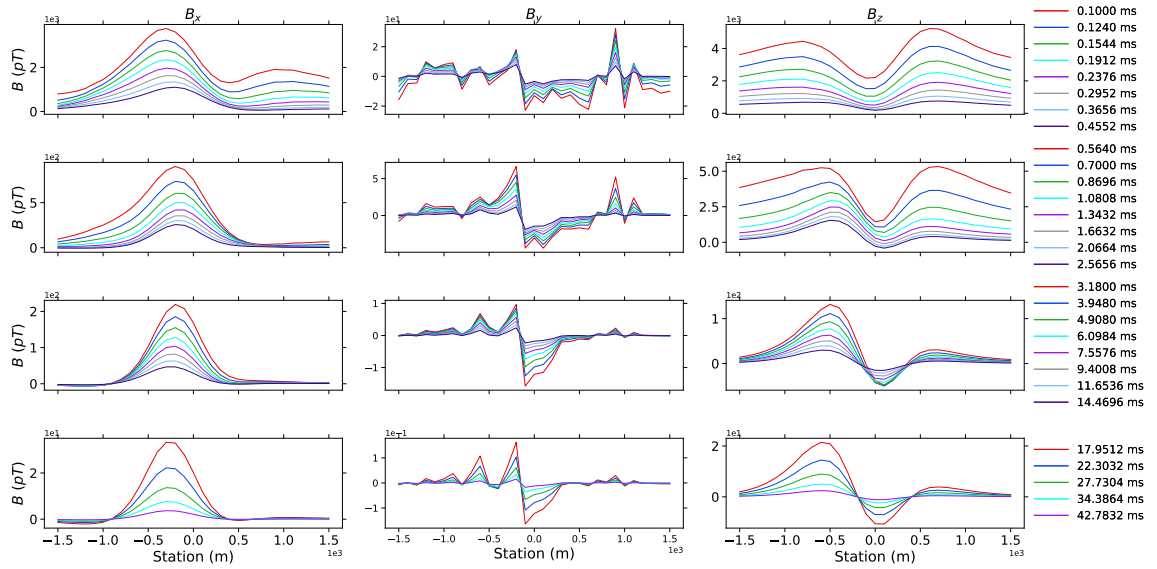
Figure A.7: Three-component responses of the conductor with a 120° dip angle.
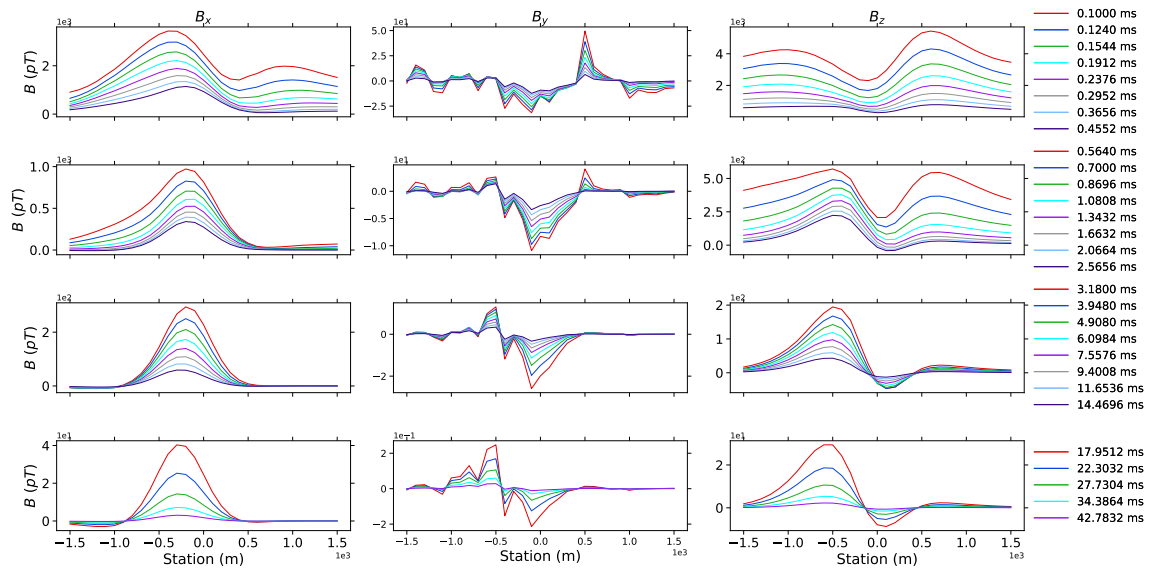
Figure A.8: Three-component responses of the conductor with a 135° dip angle.
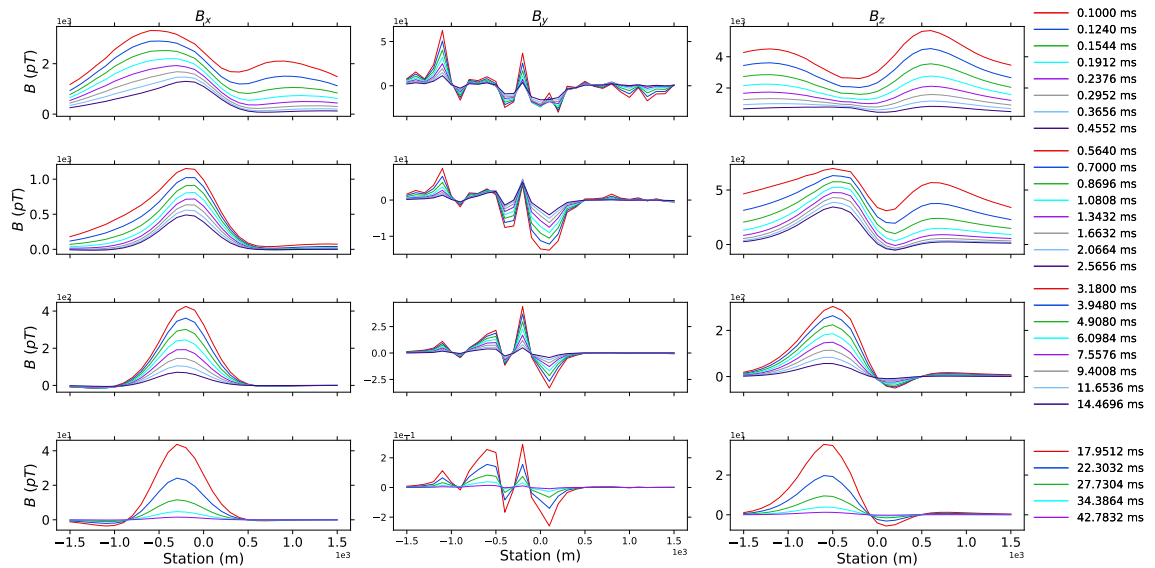
Figure A.9: Three-component responses of the conductor with a 150° dip angle.

245

Appendix B

Vertical sections of Drill Holes

CL-159 to CL-168

Figures B.1 to B.6 show the vertical geological interpretation section of all the drill holes drilled in the 2015 Diamond Drilling Program. These figures are directly taken from the project's report (Hutchinson and Zalustskiy, 2015).
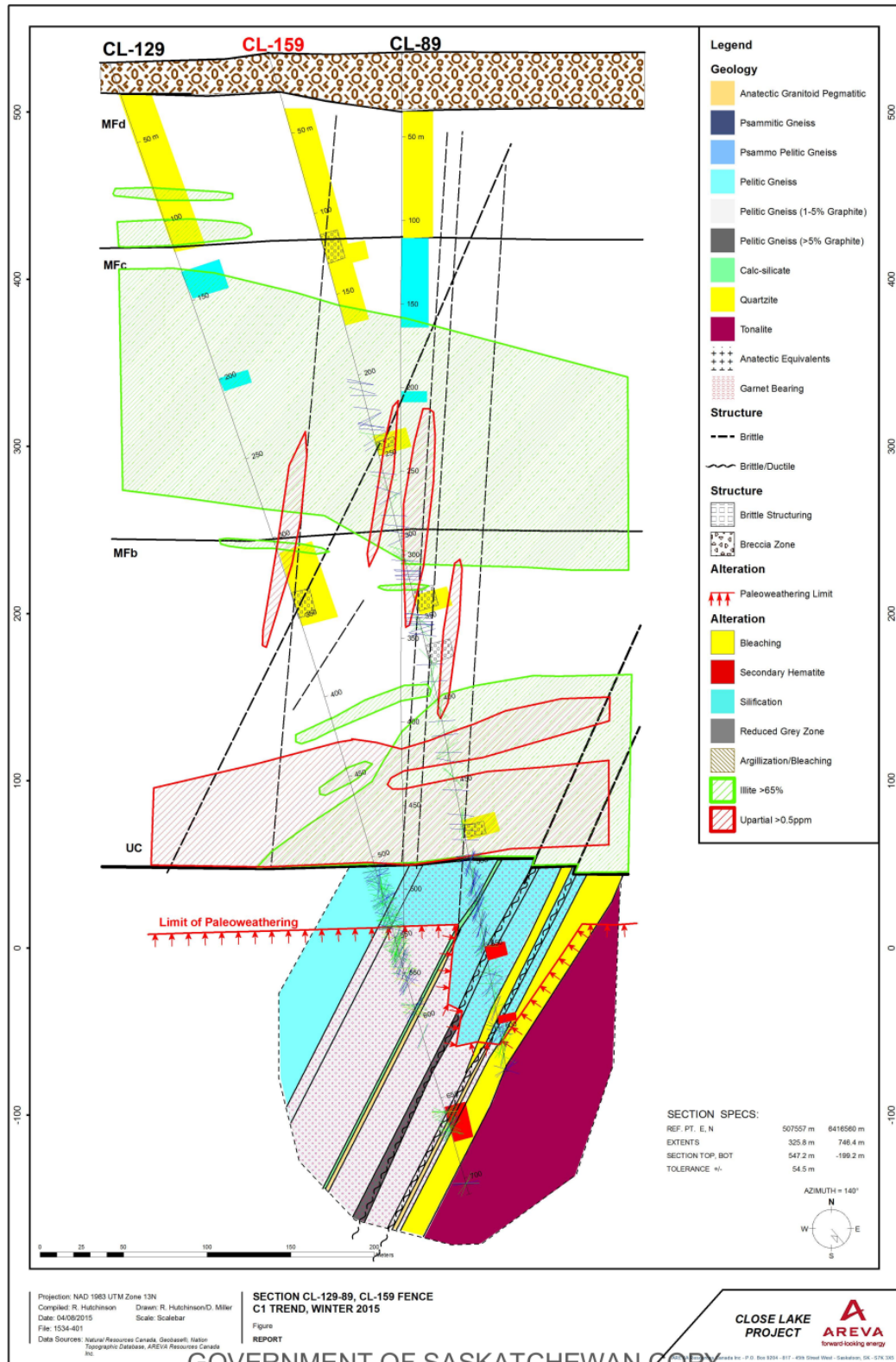
Figure B.1: Vertical section based on Drill Hole CL-159.
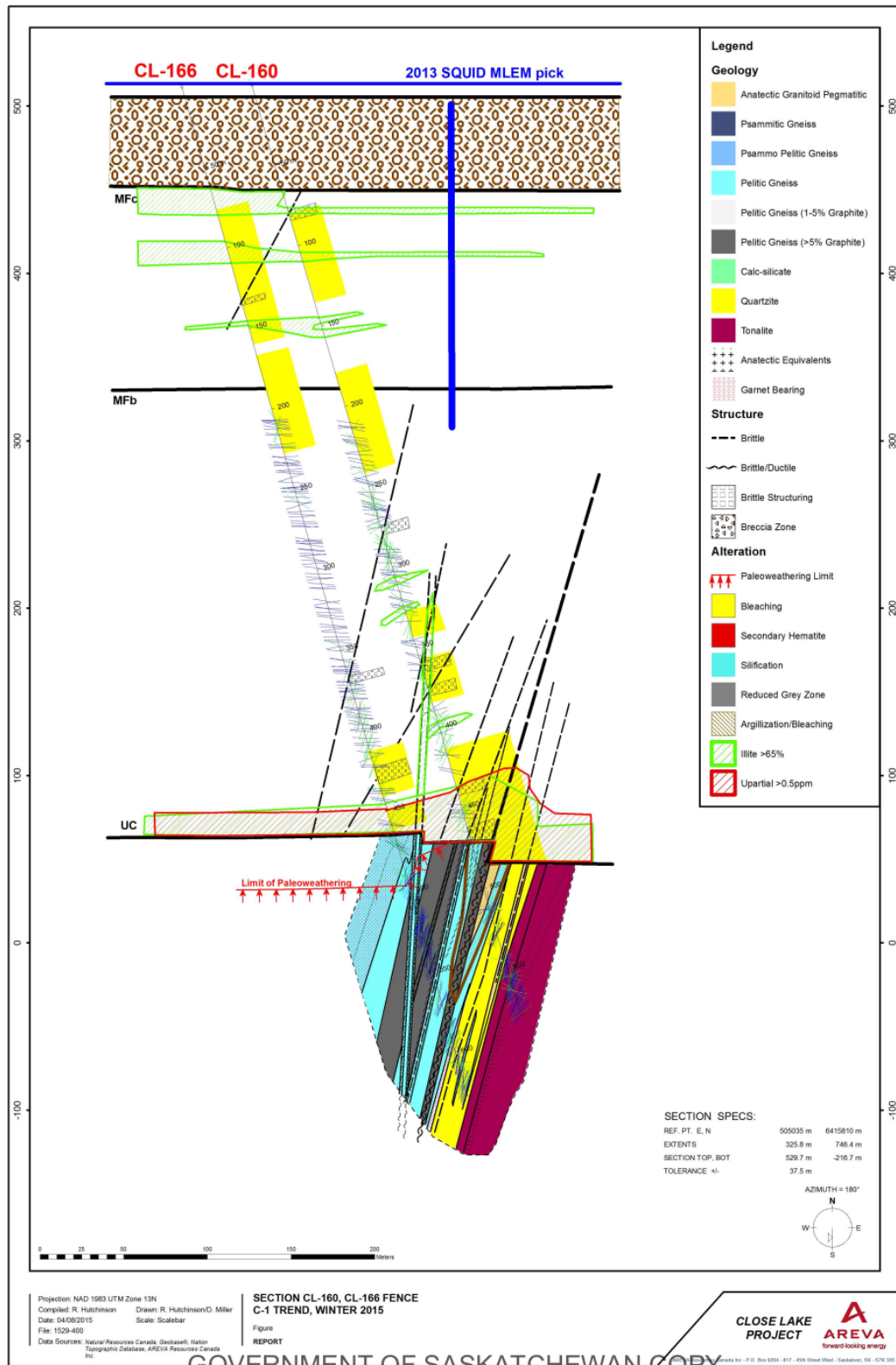
Figure B.2: Vertical section based on Drill Holes CL-160 and CL-166.
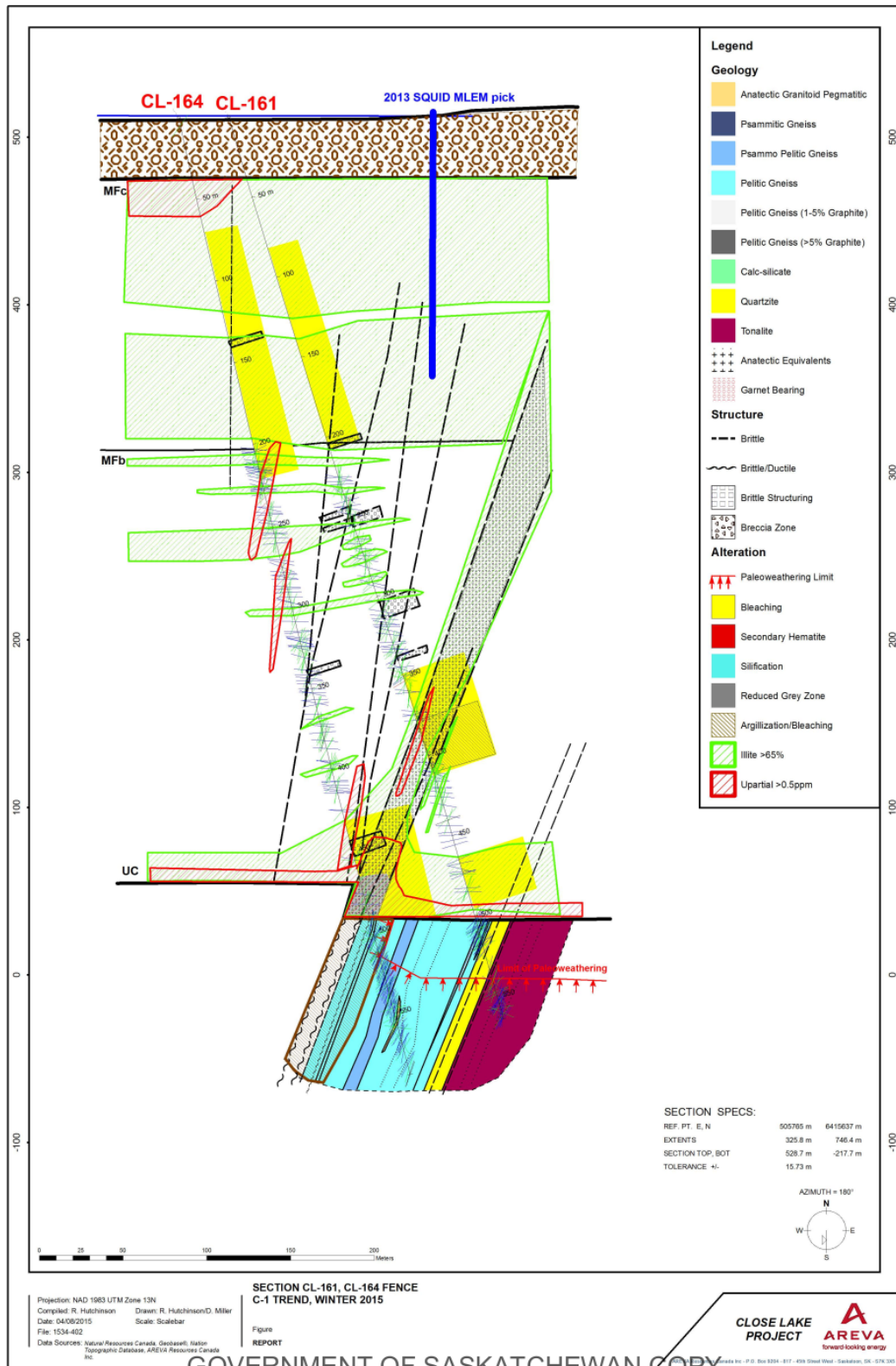
Figure B.3: Vertical section based on Drill Holes CL-161 and CL-164.
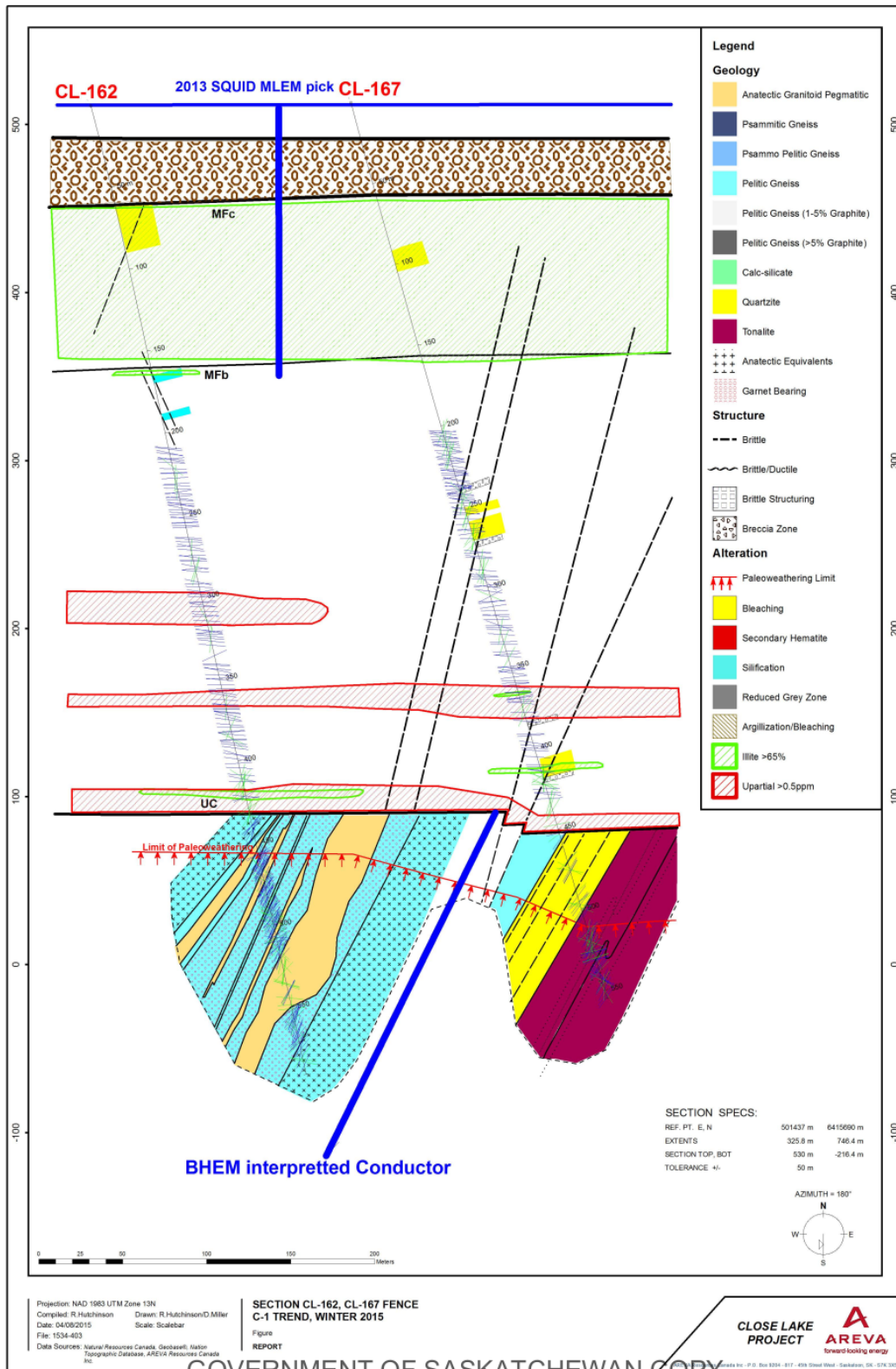
Figure B.4: Vertical section based on Drill Holes CL-162 and CL-167.
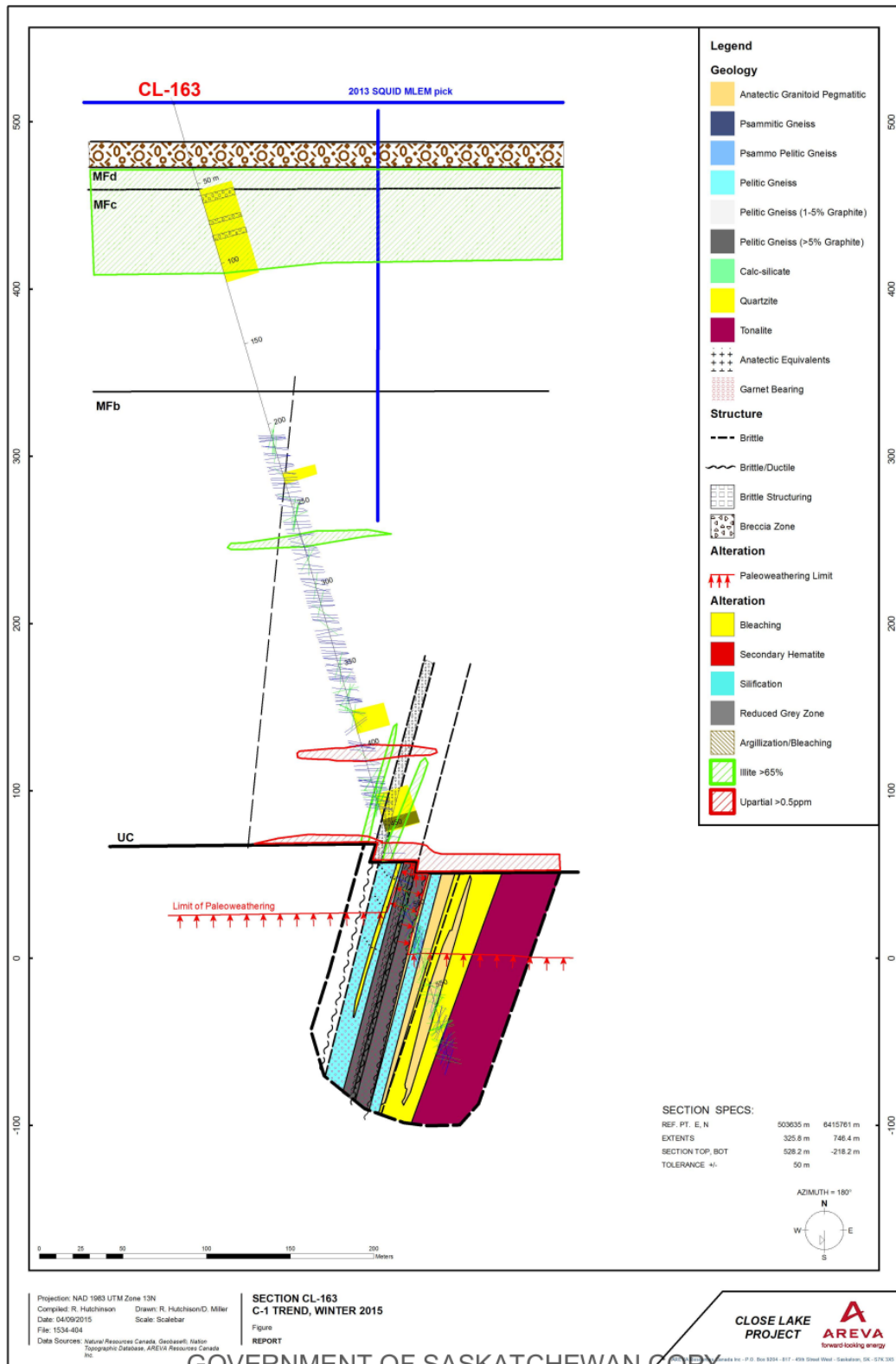
Figure B.5: Vertical section based on Drill Hole CL-163.
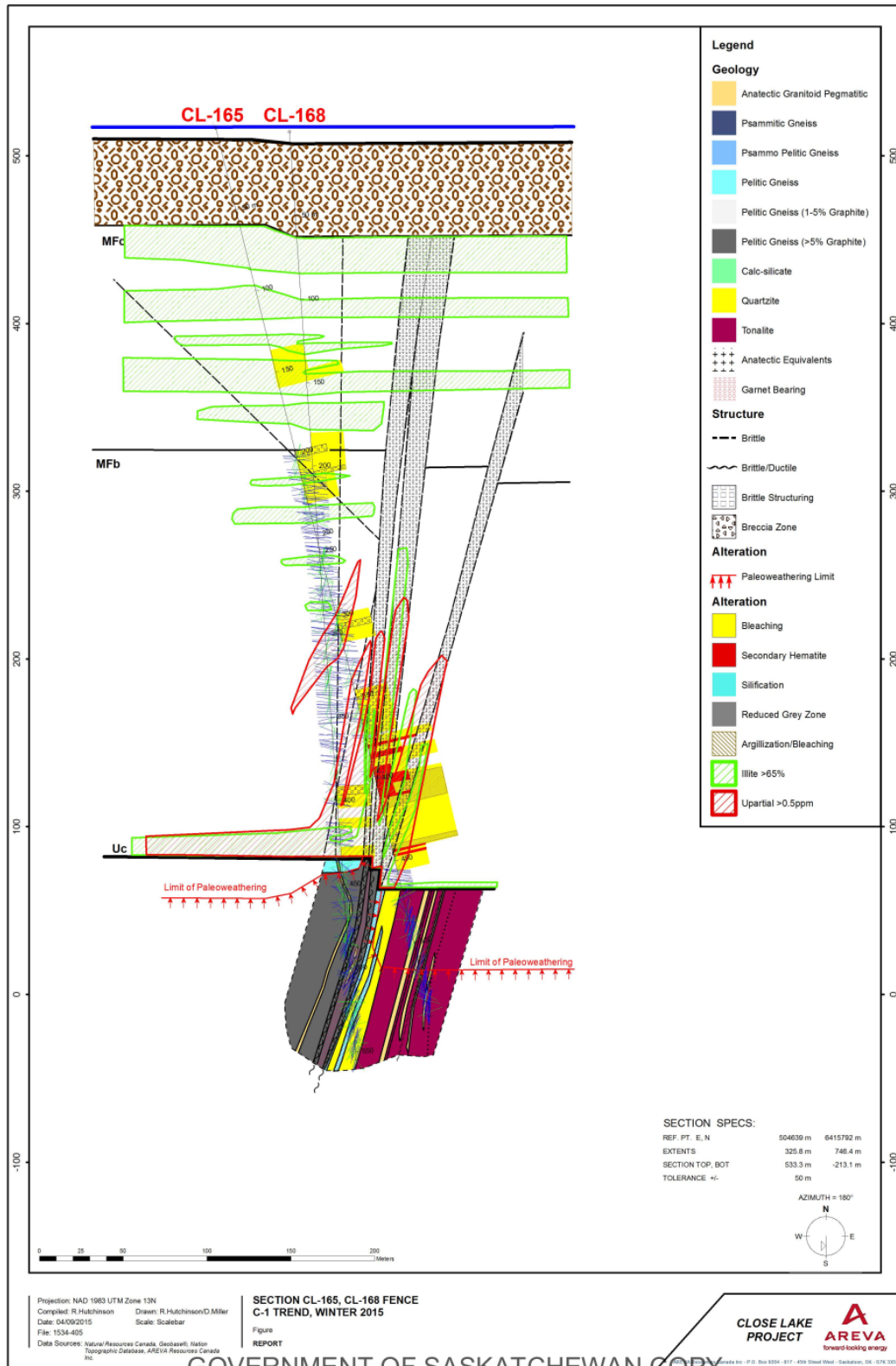
Figure B.6: Vertical section based on Drill Holes CL-165 and CL-168.

Appendix C

Lithology and conductivity measurements of Drill Holes CL-159 to CL-168

In this section, the lithology and conductivity data measured during the 2015 diamond drilling campaign will be presented. All the data are taken from the survey report (Hutchinson and Zalustskiy, 2015).

C.1   CL-160

Table C.1 lists the primary lithology and resistivity measurements of the rock samples collected for Drill Hole CL-160. The following paragraph is the original geological comments as they appeared in the report. The abbreviations in the comments are

replaced with original words in order to remove ambiguity.

Overburden to 66 m. Poorly altered and weakly fractured sandstone was intersected to 331 m. The moderate-strong bleaching; increased fracturing; core loss from 376.8 m & to 473.4 m. The sandstone displays lower friability; desilicification and strong limonitization. The unconformity is sharp and altered. Strong bleachig and local moderate argillization and chloritization with a few gouges are noted in the altered pelitic sequence within the upper basement. A thick strongly altered graphitic horizon is noted from 486.8-496.5 m with graphitic fault zones observed from 486.4-490 m; 492-500.8 m. Quartzite with pegmatitic zones is noted to 549.1 m. Below quartzite to 579 m tonalitic gneiss is noted. Maximum peak (natural gamma) of 350.72 at 310.6 m.

C.2   CL-163

Table C.2 lists the primary lithology and resistivity measurements of the rock samples collected for Drill Hole CL-163. The following paragraph is the original geological comments as they appeared in the report. The abbreviations in the comments are replaced with original words in order to remove ambiguity.

Overburden to 39.9 m. Overall very poorly bleached and poorly structured sandstone of the MFc and MFb members. A dissolution zone was noted within the lower sandstone from 443-454.5 m. Secondary hematite noted proximal to the unconformity which displayed elevated RA (400 cps SPPY). Sharp hematized unconformity

Table C.1: Primary lithology and resistivity values of samples from dirll hole CL-160.

Sample ID	Center (m)	Resistivity Ωm	Lithology	Notes
1	67.15	1651	MFc	
2	79.35	2319.87	MFc	
3	109.95	2701.53	MFc	
4	130.75	1500.93	MFc	
5	149.90	2884.56	MFc	
6	170.35	2742.4	MFc	
7	190.05	2491.05	MFc	
8	209.25	1957.94	MFc	
9	230.05	2395.47	MFc	
10	250.05	2923.43	MFb	
11	269.95	1302.47	MFb	
12	291.75	3039.24	MFb	
13	300.55	2111.91	MFb	
14	320.15	1880.85	MFb	
15	339.95	1006.15	MFb	
16	360.30	1480.37	MFb	
17	387.63	1462.13	MFb	
18	399.45	2060.24	MFb	
19	420.25	834.05	MFb	Hematization
20	439.15	805.072	MFb	Hematization
21	460.05	872.67	MFb	Hematization
22	466.05	667.77	MFb	Hematization
23	475.25	98.35	Altered Pelitic Gneiss	
24	483.55	133.62	Altered Pelitic Gneiss	
25	511.90	377.535	Altered Pelitic Gneiss	
26	522.85	5404.92	Quartzite/Silicified Gneiss	
27	534.05	1747.69	Quartzite/Silicified Gneiss	
28	549.35	3999.8	Transitional Gneiss	Silicified
29	557.05	631.03	Transitional Gneiss	
30	567.25	742.791	Tonalitic Gneiss	
31	576.10	63242.5	Tonolitic Gneiss	Very fresh

at 472.1 m. The upper basement was composed of pelitic gneiss with graphitic fault zone from 482-498.6 m. Hematized pelitic gneiss with local anatectic granitoid noted to 541.1 m with quartzite intersected to 580.0 m. Competent and unaltered tonalitic gneiss noted below to the EOH (end of hole) at 597.0 m. Maximum peak (natural gamma) 2945 cps at 471.5 m associated with secondary hematized zone proximal to the unconformity.

Table C.2: Primary lithology and resistivity values of samples from dirll hole CL-163.

Sample ID	Depth (m)	Resistivity Ωm	Lithology	Notes
1	42.1	509.76	MFd	Weakly hematized
2	50	514.04	MFd	Weakly hematized
3	60.1	592.53	MFc	Weak diagenetic hematization
4	70.1	934.363	MFc	Weak diagenetic hematization
5	80.6	645.81	MFc	Weak diagenetic hematization
6	100	1219.18	MFc	Weakly hematized / weak limonite
7	119.7	1427.71	MFc	Weakly hematized / weak limonite
8	140.2	1293.47	MFc	Weakly hematized
9	160.1	1316.00	MFc	Weakly hematized
10	180	1396.66	MFb	Weakly to moderately hematized
11	220.1	2072.01	MFb	Weakly to moderately hematized
12	260.2	1605.43	MFb	Strongly hematized
13	279.95	1344.57	MFb	Strongly hematized
14	N/A	N/A	N/A	
15	320.3	2897.36	MFb	Strongly hematized
16	339.5	2643.94	MFb	Strongly hematized
17	360.1	1580.03	MFb	Strongly hematized
18	380.1	1183.36	MFb	Strongly hematized
19	399.8	1364.11	MFb	Trace to moderate limonization
20	420	925.54	MFb	Moderately to strongly hematized
21	439.1	1291.52	MFb	Moderately to strongly hematized

Continued from previous page

Sample ID	Depth (m)	Resistivity Ωm	Lithology	Notes
22	460.7	1041.91	MFb	Moderately to strongly limonitized
23	473.25	1016.93	Pelitic Gneiss	Paleoweathered, strong hematization
24	480.3	484.93	Pelitic Gneiss	Strongly hematized
25	492.4	75.55	Graphitic Pelitic Gneiss	Graphitic pelitic gneiss > 10%
26	502.6	185.93	Graphitic Pelitic Gneiss	Strong-moderate graphite > 10%
27	507.1	641.215	Graphitic Pelitic Gneiss	Strong-moderate graphite > 10%
28	515	1487.18	Pegmatite	Paleoweathered anatectic granitoid pegmatitic
29	521	416.96	Pelitic Gneiss	Paleoweathered, strong hematization
30	532.7	715.63	Pegmatite	Trace to strong hematization
31	535.85	691.38	Pegmatite	Trace to strong hematization
32	540.3	692.84	Pegmatite	Trace to strong hematization
33	546.7	2158.08	Silicified Paragneiss	Trace hematization resistivity
34	551.2	602.79	Pegmatite	Weak to moderate hematization
35	553.8	2439.36	Pegmatite	Weak to moderate hematization
36	560	525.30	Pegmatite	Weak to moderate hematization
37	574.5	14163.39	Silicified Paragneiss	Weak hematization
38	582.3	498.20	Tonalitic Gneiss	Unaltered
39	591.3	235474.52	Tonalitic Gneiss	Unaltered

C.3 CL-165

Table C.3 lists the primary lithology and resistivity measurements of the rock samples collected for Drill Hole CL-163. The following paragraph is the original geological comments from the drilling report. The abbreviations in the comments are replaced with original words in order to remove ambiguity.

Overburden to 59.7 m. Overall weakly bleached; poorly structured sandstone of the MFc member, with the lower sandstone of the MFb member being strongly bleached and structured. A thick fault zone was intersected 375.0 m to 444.0 m. The fault displays strong bleaching; de-silicification, locally pervasive argillization and hydrothermal hematite alteration. The unconformity intersected at 467.3 m is sharp and unaltered. Directly below the unconformity the basement was composed of altered tonalitic orthogneiss. Below 520.8 m to the EOH; fresh and unaltered tonalitic gneiss was observed. Maximum peak (natural gamma) 756.14 cps at 519.0 m associated with an anatectic granitoid within the basement.

Table C.3: Primary lithology and resistivity values of samples from dirll hole CL-165.

Sample ID	Depth (m)	Resistivity Ωm	Lithology	Notes
1	60.4	590.29	MFc	Weak to moderate hematization until Sample 6
2	70	1422.38	MFc	
3	80.1	1111.06	MFc	
4	100	2712.84	MFc	
5	119.5	1944.38	MFc	
6	139.4	1749.68	MFc	
7	160.9	1013.86	MFc	Weak hematization, localized limonite
8	180	1162.15	MFc	Weak hematization, localized limonite
9	200	2113.97	MFb	Weak to moderate hematization
10	220	1954.03	MFb	
11	240	1250.87	MFb	
12	260.4	1540.79	MFb	
13	280.2	3120.20	MFb	
14	301.3	1866.69	MFb	
15	321	2088.37	MFb	
16	339.5	1404.80	MFb	
17	360	1367.48	MFb	
18	386.7	837.77	MFb	Fault Zone
19	400.1	1372.49	MFb	
20	422.7	576.22	MFb	Fault Zone
21	445.4	452.61	MFb	Fault Zone

Continued from previous page

Sample ID	Depth (m)	Resistivity Ωm	Lithology	Notes
22	460	2870.72	MFb	
23	473.3	3018.40	Tonalitic Gneiss	Paleoweathered/Red Zone
24	483.2	1210.27	Tonalitic Gneiss	Paleoweathered/Red Zone
25	495.05	248.24	Pelitic Tonalitic Gneiss	Paleoweathered
26	498.6	80.98	Pegmatite	Paleoweathered
27	508.05	83.23	Pelitic Tonalitic Gneiss	Paleoweathered
28	514.15	86.23	Pelitic Tonalitic Gneiss	Paleoweathered
29	520.1	7282.55	Pegmatite	Fresh/Unaltered
30	525.2	7277.22	Tonalitic Gneiss	Fresh/Unaltered
31	536.5	7227.76	Tonalitic Gneiss	Fresh/Unaltered
32	544.85	9292.24	Tonalitic Gneiss	Fresh/Unaltered

C.4 CL-166

Table C.4 lists the primary lithology and resistivity measurements of the rock samples collected for Drill Hole CL-163. The following paragraph is the original geological comments from the drilling report. The abbreviations in the comments are replaced with original words in order to remove ambiguity.

Overburden to 57.6 m. Overall poorly altered & structured sandstone of the MFc member, with the lower sandstone of the MFb member below 410.7m being moderately bleached and locally structured (420.3-422.2 m). A sharp poorly altered unconformity at 451.9 m. Normal paleoweathering profile noted to 510.0 m. Directly below the unconformity the basement was composed of strongly hematized pelitic gneiss to 457.8 m. Below 457.8 m quartzite/silicified paragneiss noted which persisted to 501 m. Below the silcified paragneiss moderately. hematized and weakly to moderately. chloritized tonalitic gneiss was noted to 525.5 m. Fresh and unaltered tonalitic gneiss was intersected below & continues to the EOH at 555 m. Max 415.67 cps at 451.7 m.

Table C.4: Primary lithology and resistivity values of samples from dirll hole CL-166.

Sample ID	Depth (m)	Resistivity (Ωm)	Lithology	Notes
1	62.15	1541.53	MFc	
2	79.75	1423.68	MFc	
3	100.35	2091.08	MFc	
4	120.05	2787.72	MFc	
5	140.05	3675.10	MFc	
6	179.75	2118.93	MFc	
7	240.05	1767.42	MFb	
8	280.05	3278.77	MFb	
9	300.05	2110.52	MFb	
10	340.05	1290.53	MFb	
11	420.65	2209.31	MFb	
12	460.05	4474.26	MFb	
13	468.35	519.30	Pelitic Gneiss	Paleoweathered resistivity
14	477.05	445.02	Pelitic Gneiss	Paleoweathered
15	486.75	418.30	Pelitic Gneiss	Paleoweathered
16	495.85	119.74	Pelitic Gneiss	Paleoweathered
17	505.45	171.07	Pelitic Gneiss	Altered
18	514.65	58.75	Pelitic Gneiss	Altered, locally graphite-bearing
19	522.45	75.81	Graphitic Pelitic Gneiss	Altered, graphite > 10%
20	533.65	207.70	Graphitic Pelitic Gneiss	Altered, graphite > 10%
21	546.25	1.58	Graphitic Pelitic Gneiss	Altered, graphite > 10%

Continued from previous page

Sample ID	Depth (m)	Resistivity (Ωm)	Lithology	Notes
22	565.25	180732	Altered Pelitic Gneiss	
23	587.65	647.95	Pelitic Gneiss	
24	603.15	5946.76	Silicified Paragneiss	
25	610.85	5217.65	Garnet Pelitic schist	
26	625.15	3378.91	Silicified Paragneiss	

C.5 CL-168

Table C.6 lists the primary lithology and resistivity measurements of the rock samples collected for Drill Hole CL-163. The following paragraph is the original geological comments from the drilling report. The abbreviations in the comments are replaced with original words in order to remove ambiguity.

Overburden to 63.0 m. Overall weakly bleached; poorly structured sandstone of the MFc member, with the lower sandstone of the MFb member very locally bleached and structured. A thin fracture zone was intersected 392-396.5 m displaying strong bleaching; de-silicification. The unconformity intersected at 434.6 m within a strong fractured rubble zone. Normal paleoweathering profile noted to 442.4 m. Below the unconformity the basement was composed of graphitic pelitic and garnet bearing pelitic gneisses with graphitic faults intersected 490.0-494.5 m; 512.4-516.8 m. Below 532.1 m to the EOH silicified paragneiss & quartzite was observed. Maximum peak (natural gamma) of 2163.29 cps at 520.6 m associated with limonitic fractures within the silicified paragneiss.

C.6 Resistivity mean and standard deviation

Table C.5: Average resistivity and standard deviation of each unit in Drill Hole CL-159 obtained from the probing data.

Lithology	Min (Ωm)	Max (Ωm)	Average (Ωm)	Standard Deviation (Ωm)	Thickness (m)
MFd	13.15	5241.19	1261.16	620.16	80.80
MFc	329.91	7689.98	1865.43	825.30	181.60
MFb	440.41	5921.74	2229.50	899.21	210.60
Fault Zone	165.93	1738.89	414.14	211.71	11.40
Pelitic Gneiss	34.23	10921.10	685.67	1172.64	34.80
Quartzite	328.00	6974.90	2386.38	1510.45	25.00

Table C.6: Primary lithology and resistivity values of samples from dirll hole CL-168.

Sample ID	Depth (m)	Resistivity (Ωm)	Lithology	Notes
1	63	868.74	MFc	
2	70	1436.25	MFc	
3	90	3307.03	MFc	
4	110.5	1840.24	MFc	
5	130.1	3263.48	MFc	
6	149.85	2258.09	MFc	
7	170.6	1975.50	MFc	
8	185.5	2420.33	MFc	
9	200.5	1354.41	MFb	
10	219.85	1655.76	MFb	
11	238.4	1471.95	MFb	
12	260.3	2261.98	MFb	
13	281.05	2940.11	MFb	
14	300.8	2072.84	MFb	
15	320.15	1741.80	MFb	
16	340.9	2591.13	MFb	
17	360	2294.91	MFb	
18	379.7	2169.61	MFb	
19	399.55	1208.88	MFb	
20	419.8	1434.94	MFb	
21	435.4	853.04	Pelitic Gneiss	Paleoweathered

Continued from previous page

Sample ID	Depth (m)	Resistivity (Ωm)	Lithology	Notes
22	443.5	883.96	Graphitic Pelitic Gneiss	
23	450.65	1145.81	Pegmatite	
24	457.3	116.27	Graphitic Pelitic Gneiss	
25	459.9	395.134	Graphitic Pelitic Gneiss	
26	470	106.87	Graphitic Pelitic Gneiss	
27	481.2	256.42	Graphitic Pelitic Gneiss	
28	483	4.36	Graphitic Pelitic Gneiss	
29	489.8	282.19	Graphitic Pelitic Gneiss	
30	497.4	476.35	Graphitic Pelitic Gneiss	
31	503.5	265.82	Graphitic Pelitic Gneiss	
32	506.3	3664.36	Graphitic Pelitic Gneiss	
33	512.2	N/A	N/A	Destroyed
34	519	8182.95	Silicified Paragneiss	
35	525.3	4885.11	Silicified Paragneiss	
36	528	1668.56	Pelitic Gneiss	
37	531	2282.61	Silicified Paragneiss	
38	533.1	5227.83	Silicified Paragneiss	
39	544.9	18155	Silicified Paragneiss	

Table C.7: Average resistivity and standard deviation of each unit obtained from rock sample physical property measurement with a SCIP instrument.

Drill Hole ID	MFc (Ωm)	MFb (Ωm)	Paleoweathering (Ωm)	Basement (Ωm)
CL-160	2,293.86/462.01	1,572.80/757.38	203.17/124.14	12,628.12/22,701.00
CL-163	1,061.29/313.15	1,612.20/591.03	851.5/434.35	25,796.15/70,005.29
CL-165	1,463.33/618.00	1,592.54/763.34	787.89/1,074.97	7,769.94/879.16
CL-166	2,273.01/768.55	2,521.80/1,059.64	375.59/152.28	39,184.65/70,797.31
CL-168	2171.21/785.59	1,933.19/516.02	853.04/0.00	6,733.68/5,533.22

Table C.8: Average conductivity and standard deviation of each unit in Drill Hole CL-161 obtained from the probing date

Lithology	Min (Ωm)	Max (Ωm)	Average (Ωm)	Standard Deviation (Ωm)	Thickness (m)
MFc	1037.01	6691.58	3237.72	760.72	162.80
MFb	266.45	6147.46	2346.90	906.24	268.10
Fault Zone	626.16	3785.13	1633.86	566.13	resistivity 30.9
Pelitic Gneiss (PW)	486.49	1597.96	836.04	200.29	16.49
Quartzite	1209.58	22924.16	10611.54	4347.65	18.00
Granitic Gneiss (PW)	603.19	2183.58	924.51	422.37	2.00
Granitic Gneiss	617.11	23879.65	14179.20	7168.26	25.99

Table C.9: Average resistivity and standard deviation of each unit in Drill Hole CL-162 obtained from the probing data

Lithology	Min (Ωm)	Max (Ωm)	Average (Ωm)	Standard Deviation (Ωm)	Thickness (m)
MFc	14.48	8306.43	2145.44	1032.95	97.40
MFb	326.04	10674.64	3633.52	1458.18	272.60
Migmatite	750.39	5313.42	2877.23	741.39	29.69

271

Table C.10: Average conductivity and standard deviation of each unit in Drill Hole CL-166 obtained from the probing date

Lithology	Min (Ωm)	Max (Ωm)	Average (Ωm)	Standard Deviation (Ωm)	Thickness (m)
MFc	13.90	9961.10	4166.51	1371.63	124.90
MFb	376.49	9642.56	3860.35	1681.68	278.30
Pelitic Gneiss (PW)	198.24	2013.72	865.68	366.36	36.59
Pelitic Gneiss	133.70	456.44	207.60	60.70	26.20
Fault Zone	122.63	258.28	163.95	25.37	24.70
Graphitic Pelitic Gneiss	68.11	215.86	153.68	26.14	32.00

Table C.11: Average resistivity and standard deviation of each unit in Drill Hole CL-167 obtained from the probing date

Lithology	Min (Ωm)	Max (Ωm)	Average (Ωm)	Standard Deviation (Ωm)	Thickness (m)
MFc	541.40	7278.47	2342.44	1116.20	98.50
MFb	829.84	11286.34	3703.60	1744.15	289.4
Fault Zone	972.03	3042.04	1677.50	506.92	5.00
Pelitic Gneiss (PW)	262.46	2477.93	1347.72	508.83	5.79
Granitic Gneiss (PW)	186.74	10312.72	1781.34	2416.36	8.90
Granitic Gneiss	149.42	30000.00	18272.67	13187.99	44.79